ABSTRACT

Title of Document: BIMETALLIC NANOPARTICLES FOR ADVANCED ENERGY CONVERSION TECHNOLOGIES

Christopher Michael Sims
Doctor of Philosophy, 2015

Directed By: Professor Bryan W. Eichhorn
Department of Chemistry and Biochemistry

The increased demand for a more sustainable energy infrastructure has spurred the development of innovative energy conversion processes and devices, such as the proton exchange membrane fuel cell (PEMFC). PEMFCs are highly regarded as a clean alternative energy technology for various applications, such as motor vehicles or power generators. Factors limiting their commercial viability include the poisoning of the hydrogen oxidation reaction (HOR) electrocatalyst at the anode by carbon monoxide (CO), an impurity in the H_2 fuel feedstocks derived from hydrocarbons, and the high expense and inefficiency of the oxygen reduction reaction (ORR) electrocatalyst at the cathode.

The research described in this dissertation entails the synthesis and characterization of new bimetallic nanoparticle (NP) catalysts with controlled sizes, compositions, and architectures. By varying the NPs' compositions, structures, and electronic environments, we aimed to elucidate the physical and chemical

relationships that govern their ability to catalyze chemical reactions pertinent to PEMFC operation. The ongoing research and development of these NP-based catalytic systems is essential to realizing the viability of this energy conversion technology.

We describe the development of a simple method for synthesizing monometallic and bimetallic NPs supported on various reduced graphene oxide (rGO) supports. Electrochemical studies illustrate how the chemical nature of the rGO support impacts the catalytic behavior of the NP catalysts through unique metal-support interactions that differ depending on the elemental composition of the NP substrate.

In another study, we present the synthesis and characterization of Co_xPt_y NPs with alloy and intermetallic architectures and describe how their inherent characteristics impact their catalytic activities for electrochemical reactions. Co_xPt_y NPs with alloy architectures were found to have improved CO tolerance compared to their intermetallic counterparts, while the performance of the Co_xPt_y NPs for ORR catalysis was shown to be highly dependent on the NPs' crystal structure.

Finally, we present the synthesis and characterization of various bimetallic core-shell NPs. Preliminary data for CO oxidation and PrOx catalysis demonstrated how subsurface metals modify the electronic structure of Ni and enhances its catalytic performance for CO oxidation and the PrOx reaction.

BIMETALLIC NANOPARTICLES FOR ADVANCED ENERGY CONVERSION TECHNOLOGIES

By

Christopher Michael Sims

Dissertation submitted to the Faculty of the Graduate School of the
University of Maryland, College Park, in partial fulfillment
of the requirements for the degree of
Doctor of Philosophy
2015

Advisory Committee:
Professor Bryan W. Eichhorn, Chair
Professor Jeffery T. Davis
Professor Philip R. DeShong
Professor Andrei N. Vedernikov
Associate Professor Chunsheng Wang

© Copyright by
Christopher Michael Sims
2015

Acknowledgements

On my journey, I've been fortunate to encounter hundreds of people who've impacted me in many ways: big or small, directly or indirectly, complimentary or critical. Each one has shaped who I am and will become in some fashion. There's not enough space here to thank each person individually, but do know that each of your contributions is greatly appreciated!

First, I would like to express my profound gratitude to my advisor, Prof. Bryan Eichhorn, for his unwavering encouragement. There were times when I lost confidence in myself, but Bryan never failed to lift my spirits and remind me of my capabilities. I know that I wouldn't have finished my degree without his genuine support, and for that, I'm eternally grateful.

Thank you to my lab mates, former and current, for their friendship, support, and professional assistance: Drs. Selim Alayoglu, Tony Dylla, Zhufang Liu, Chunjuan Zhang, Sanem Kocak, Dennis Mayo, Domonique Downing, Aldo Ponce, Yang Peng, Will Gibbons, Hao Lei, Chris Snyder, and Yi Yu; Pavan Bellamkonda, Samantha DeCarlo, Aaron Geller, Jonathan Senn, Kim Huynh, Lauren Stevens, Luning Wang, and Noah Masika; Cody Sherlock, Sarah Gibbons, and Raheed Khan. I've seen several people come and go, but you've all made the lab a fun and productive place to work. Special thanks to Zhufang and Aldo for their wonderful guidance and advice when I was just starting out - I learned a lot about being a researcher from my time with you.

To my PhD committee members, Drs. Jeffery Davis, Philip DeShong, Andrei Vedernikov, and Chunsheng Wang: Thank you for providing informative instruction and intellectually stimulating conversations. To Dr. Herman Sintim, Dolores Jackson, Tia Smith-Best, Cathy Clark-Fisanich, Bill Griffin, Floyd Bates, Rey Richards, and Ben Roembke: Thanks for being there to offer help, address concerns, and/or provide friendly conversation. Thanks to Drs. Peter Zavalij, Karen Gaskell, Wen-An Chiou, Li-Chung Lai, Panju Shang, Sz-Chian Liou, and Jonathan Duay, as well as Eleanor Gillette for their technical and scientific support - my life as a researcher would've been far more difficult without their training and assistance. Thanks to Drs. Bonnie Dixon, Lee Friedman, and Gili Marbach-Ad for their efforts and guidance during my GAANN Fellowship, which helped me realize the extent of my love for teaching and mentoring.

Speaking of which, thanks to the US Department of Education for the GAANN Fellowship, which supported my research for two years. Thanks to the UMD Graduate School for the Ann G. Wylie Dissertation Fellowship, which helped me to focus on writing this document and finishing my degree. Huge thanks go to NIST for the Dolphus E. Milligan Fellowship, which supported my first two years at UMD and provided me with an amazing summer internship that really cemented my desire to perform research. Drs. Bryant Nelson, Marlon Walker, and Willie May have been constant sources of inspiration, guidance, and fun. I will have done well to become half as good a mentor as they have been for me.

I am forever indebted to my undergraduate institution, UMBC, and its Meyerhoff Scholarship Program for first making me aware of the PhD degree and

that I had the ability to earn one. Special thanks to Dr. Dale Whalen for introducing me to the world of research and for being an incredibly patient and supportive mentor, even in retirement. I also want to thank the Meyerhoff staff and students for creating a wonderful environment that truly felt like an extended family. It was through UMBC that I met many of my closest friends: Dr. Zach Rayfield, Terrell Higgins, Imhotep Jackson, Tarrick Clayton, Richard Moore, Neil Agarwal, and Ola Jolaoso - thanks for making "The Crew" a fun group to be a part of! Matt Dressler, Ian Arthur, Jake Finkelstein – thanks for sticking with me throughout my childhood and beyond, you were there when no one else was, and I wouldn't be here without you! To Rachael McCleary, thank you for being a muse of perseverance and your heartfelt efforts in pushing me to achieve my dreams! To all my friends: Thanks for always being around to simply hang out or have serious life discussions. Here's to many more years of friendship and success!

My greatest thanks must go to my parents, JoAnn and Michael Sims. Words can't express just how appreciative I am of their resolute love, encouragement, and guidance. Thank you for recognizing my aptitude for the STEM fields and pushing me to realize my potential in those areas. Thanks for also pushing me to delve into other interesting subjects such as history, foreign culture, and the fine arts. Thanks for instilling a sense of adventure and for allowing me to satisfy my curiosities. Because of your efforts, I have been able to develop a well-rounded view of the world and experience many of its wonders! I hope I've made you proud with my accomplishments so far and I hope to continue making you proud well into the future! This achievement is just as much yours as it is mine!

Table of Contents

List of Tables

List of Figures

List of Abbreviations

acac	acetylacetonate
AES	Auger Electron Spectroscopy
AP	as prepared
BEt_3H	Triethylborohydride
BGO	Borohydride-reduced Graphene Oxide
C@S	Core($Metal_1$)@Shell($Metal_2$)
CB	Carbon Black
C_f	Carbon (Functionalized)
C_g	Carbon (Graphitic)
CO-FTIR	Carbon Monoxide Probe – Fourier Transform Infrared Spectroscopy
CV	Cyclic Voltammetry
D band	Disorder Band
DFT	Density Functional Theory
ECSA	Electrochemical Surface Area
EDS	Energy Dispersive X-ray Spectroscopy
EG	Ethylene Glycol
E_{Inf}	Inflection Potential
E_{Onset}	Onset Potential
E_{Peak}	Peak Potential
Et_2O	diethyl ether
EtOH	ethanol
FCC	Face-Centered Cubic
FCT	Face-Centered Tetragonal
FGS	Functionalized Graphene Sheets
FWHM	Full Width at Half Maximum
G band	Graphitic Band
GC	Glassy Carbon
GO	graphene oxide
HCP	Hexagonal Closest-Packed

HOR	Hydrogen Oxidation Reaction
iPrOH	isopropanol
LEED	Low Energy Electron Diffraction
MeOH	methanol
NGO	Nitrogen-doped (Hydrazine-reduced) Graphene Oxide
NP	Nanoparticle
OA	oleic acid
OAm	oleylamine
ORR	Oxygen Reduction Reaction
PEMFC	Proton Exchange (Polymer Electrolyte) Membrane Fuel Cell
Ph_2O	diphenyl ether
PrOx	Preferential Oxidation of Carbon Monoxide
PVP	polyvinylpyrrolidone
RBF	Round Bottom Flask
RDE	Rotating Disk Electrode
rGO	Reduced Graphene Oxide
RHE	Reversible Hydrogen Electrode
SCE	Saturated Calomel Electrode
SLG	Single Layer Graphene
STEM	Scanning Transmission Electron Microscopy
TEM	Transmission Electron Microscopy
TPR	Temperature Programmed Reaction
WGS	Water Gas Shift
XAS	X-ray Absorption Spectroscopy
XPS	X-ray Photoelectron Spectroscopy
XRD	(Powder) X-ray Diffraction

Chapter 1: Introduction and Background

1.1 Introduction

The increased demand for a more sustainable energy infrastructure has spurred the development of innovative energy conversion processes and devices. One such energy conversion device that holds much promise is the proton exchange membrane fuel cell (PEMFC), which operates by transforming the chemical energy from its fuel into usable electrical energy. Figure 1.1 illustrates the standard operation of a PEMFC using H_2 as a fuel.[1]

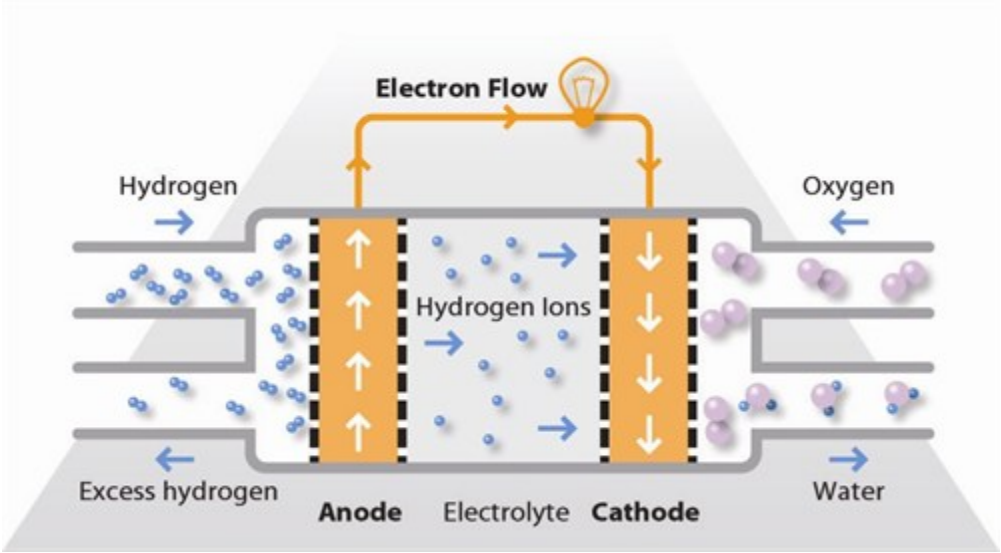

Figure 1.1 Diagram of a PEMFC using H_2 as the fuel. Adapted from reference [1]

H_2 fuel feeds into the anode, where it is catalytically split into protons and electrons. This process is known as the hydrogen oxidation reaction (HOR). From here, the electrons travel through an external circuit to the cathode, generating the current to be used for electrical energy. The protons travel through the electrolyte

membrane to the cathode, where they meet the electrons arriving from the circuit and O_2 molecules (typically from air). Here, the catalyst promotes the oxygen reduction reaction (ORR), producing water as byproduct. The overall reaction is shown below (Eq. 1-3):

Anode (HOR): $H_2 \rightarrow 2H^+ + 2e^-$ $E^o = 0.0\,V$ (1)

Cathode (ORR): $O_2 + 4H^+ + 4e^- \rightarrow 2H_2O$ $E^o = 1.23\,V$ (2)

Overall: $2H_2 + O_2 \rightarrow 2H_2$ $E^o = 1.23\,V$ (3)

While PEMFCs have received much attention as a potential future energy conversion technology because of their excellent energy conversion efficiencies, good power densities, and low operating temperatures, there are several hurdles that have prevented PEMFCs from reaching mass-market. Here, we focus on the issues concerning the catalysts at either electrode.

Pt nanoparticles (NPs) are currently used in PEMFCs to catalyze both the HOR and ORR due to its high activity for both of these processes.[2] However, there are still several concerns. First, the expense of the metal hinders the viability of its long-term use in this application.[3] On the cathode side, the kinetics for the ORR on Pt are slow, necessitating a large increase in efficiency for commercialization.[4] On the anode side, Pt is an excellent catalyst for the HOR, but is susceptible to CO impurities in the H_2 fuel (low CO tolerance).[5] The primary means of H_2 fuel production comes from steam reformation of hydrocarbons, a process that produces CO impurities as byproducts.[6] The CO molecules bind tightly to the Pt surface, blocking active sites

and preventing the HOR from occurring under efficient conditions.[7] Unfortunately, even trace amounts of CO can greatly impede the catalytic activity.[8] As such, there are 4 primary goals for improving catalysts within a PEMFC system:

- Cutting the overall cost of the catalysts
- Improving the catalytic activity for the ORR
- Increasing the CO tolerance of the HOR catalysts
- Reducing the amount of CO impurities in the H_2 fuel

Over the last several years, researchers have devised many solutions towards overcoming these challenges, many of which involve the replacement of monometallic Pt NPs with architecturally controlled bimetallic NPs. The ongoing research and development of these bimetallic systems is essential to achieving the viability of this energy conversion technology. The goal of the research described here is to develop new, less expensive bimetallic NP catalysts, of controlled sizes, compositions, and architectures, with high activity for the chemical reactions pertinent to PEMFC operation.

1.2 Research and Development of Bimetallic Nanoparticles for Catalysis

Research into bimetallic NPs for catalytic applications has its origins in the studies of bimetallic clusters during the 1960s and 70s. Sinfelt and coworkers were among the first to realize that bimetallic systems could have markedly different activity for particular catalytic processes vs. their individual monometallic components.[9,10] These early studies resulted in two important observations related to the catalytic activities of bimetallic compounds: 1) at the cluster-scale, the surface composition of a bimetallic system can greatly differ from the bulk; and 2) the

bonding properties of the component atoms are altered to some degree through their mutual interaction.[11] These observations paved the way for studies aimed towards elucidating the surface structures of bimetallic systems and determining the underlying factors influencing their catalytic activities.

As heterogeneous catalytic chemistry occurs on the surface of a catalyst, surface scientists soon began to study how the nature of the catalyst surface influenced the resultant catalytic activity. These early studies, pioneered by the research groups of Ertl,[12-16] and Somorjai,[17-20] used techniques such as low energy electron diffraction (LEED) or Auger electron spectroscopy (AES) to determine the adsorption properties of gas-phase molecules, atoms, and intermediates on various metal surfaces. Their results not only illustrated how the mobility of these species on the surfaces correlated with catalytic activity, but also the influence of the metal's identity and surface geometry on these adsorbate-metal interactions. The results provided a basic mechanistic understanding of why certain catalytic processes were preferred on some metals instead of others.

Building on these early studies of monometallic surfaces, research moved onto bimetallic systems in an effort to determine why the combination of two metals often resulted in higher catalytic activities than their monometallic components individually. Goodman and coworkers used X-ray photoelectron spectroscopy (XPS) to extensively study metallic monolayers grown on single crystal metal surfaces of a second, different metal (M_1/M_2).[21-23] Their experiments showed that the binding energies of the surface metals shifted from their normal values when arranged in this fashion, with the magnitudes of the shifts wholly dependent on the identity of the

substrate metal. Their results were among the first illustrations of metal-induced electronic structure modification.

The Goodman group later studied Pd and Cu overlayers on single crystal surfaces of various metals (Pd/M, Cu/M), where they discovered correlations between overlayer binding energy, CO adsorption energy, and the identity of the substrate metal.[24] For the Pd overlayers, it was found that CO adsorption decreased not only as the substrate metal became increasingly electron-poor (Ta < W < Re < Ru), but also that the CO binding energy on each Pd/M sample was lower than that of a monometallic Pd surface. For Cu overlayers, they found that CO adsorption increased as the substrate metal became increasingly electron-rich (Re < Ru < Pt). These trends revealed that charge transfer occurred between the surface metal and its substrate based on occupancy of the valance *d*-band. For the relatively electron-rich (more occupied) Pd, electrons were transferred to the more electron-poor (less occupied) substrates, resulting in decreased CO adsorption. Likewise, the relatively electron-poor Cu accepted charge from the more electron-rich substrates (Ru, Pt), resulting in increased CO adsorption. These results laid the groundwork for understanding how bimetallic systems could be tailored for specific chemical interactions relevant to catalytic processes.

While bimetallic systems were long known to offer improved catalytic activity vs. their monometallic counterparts for chemical reactions relevant to fuel cell technologies, it was not until the 1990s that the underlying reasons behind these phenomena were well understood. To elucidate the enhanced performance of bimetallic Pt-Ru electrodes for CO-tolerant HOR, Gasteiger, Markovic, and Ross

studied the electrocatalytic activities of well-characterized Ru, Pt, and bimetallic Pt-Ru electrodes.[25] In their studies, the onset potential for CO oxidation was found to occur at lower potential on a pure Ru electrode vs. a pure Pt electrode; however, the rate of CO oxidation was higher on the pure Pt electrode once the onset potential threshold was reached. For the bimetallic Pt-Ru electrode, the CO oxidation onset potential was lower than either the monometallic Ru or Pt electrodes, as expected; however, the CO oxidation rate was similar to that of the pure Pt electrode. The lower onset potential was attributed due to Ru's ability to adsorb oxygen-containing species (such as H_2O or OH) better than Pt, but the marked increase in electrocatalytic activity could not result from a simple combination of the two elements' properties. This observed performance enhancement was ascribed to a synergistic effect, which would come to be known as the "bifunctional mechanism". In the bifunctional mechanism for the bimetallic Pt-Ru surface, oxygen-containing species preferably bind to the Ru surface, which facilitates the removal of CO species bound to the Pt surface. This removal of CO leaves more active sites available for H_2, resulting in the enhanced HOR activity of bimetallic Pt-Ru electrodes vs. pure Pt. A schematic of the bifunctional mechanism for a bimetallic Pt-Ru surface is seen in Figure 1.2.

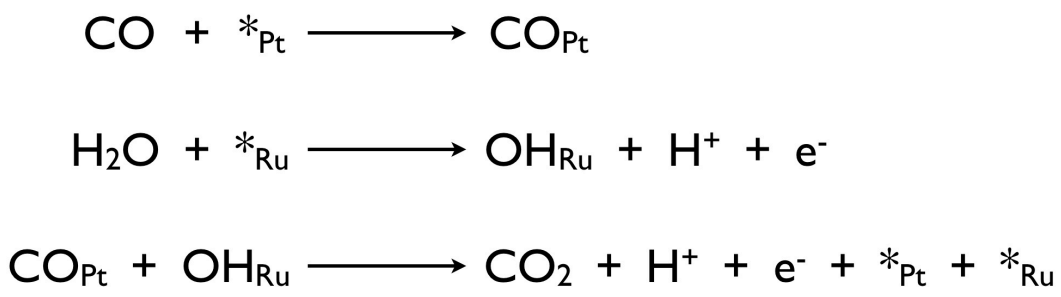

Figure 1.2 Schematic of the bifunctional mechanism on a bimetallic Pt-Ru surface. Asterisks represent metal sites available for adsorbate binding.

These same researchers later studied the Pt-Sn bimetallic system and found the bifunctional mechanism also occurred, with the Pt-Sn system having increased CO tolerance over Pt-Ru due to the lack of CO binding on Sn.[26-28] This improvement was credited to less CO coverage on the electrode, increasing the availability of oxygen-containing species for CO oxidation and hence, creating more active sites for the HOR to occur. Mukerjee and McBreen, with coworkers, verified the results (bifunctionality) of Gasteiger, Marvokic, and Ross with their *in situ* X-ray absorption spectroscopy (XAS) studies of bimetallic Pt-Ru,[29] Pt-Sn,[30-32] and Pt-Mo[32-34] electrocatalysts, which also showed high CO tolerances due to the bifunctional mechanism.

In some cases, the CO tolerance enhancement seen in bimetallic systems is not due to the bifunctional mechanism, but to other phenomena. In their studies of various Pt-based bimetallic electrodes, Watanabe and coworkers also observed enhanced CO tolerance vs. monometallic Pt.[35] However, they demonstrated that the electrode surface was mostly (if not fully) comprised of Pt in many cases, with the

second metal absent from the surface layer. Due to the absence of the second metal on the surface, the bifunctional mechanism could not be applied to explain the high CO tolerance seen in these systems. Using XPS, they showed that the Pt binding energies shifted positively in CO-tolerant bimetallic systems, and negatively in non CO-tolerant systems. Similarly to the surface science studies of Goodman and coworkers, these binding energy shifts directly correlated with the levels of CO adsorption onto the electrode surface. For the more CO-tolerant catalysts, there was increased Pt *d*-vacancy (increasingly electron poor), resulting in reduced CO binding and less CO coverage. The opposite was found to occur for the non CO-tolerant electrodes. In these studies, the CO tolerance enhancement was simply due to electronic structure modifications, which resulted in reduced CO coverage on the catalyst, leaving more active sites available for the HOR to occur.

Given the increasing wealth of experimental information relating elemental composition, adsorption phenomena, electronic structure, and catalysis, theoreticians began to develop models based on these observations.[36] Hammer and Norskov used density functional theory (DFT) calculations to correlate the binding energies of several different adsorbates (such as CO, H_2, and O_2) with the average *d*-orbital energy (the *d*-band center) of transition metal surfaces.[37,38] These findings "led to the development of the *d*-band theory, which relates the electronic structure of a metal to its chemical activity and catalytic performance."[39] The *d*-band theory was naturally applied to various bimetallic systems, with studies spanning several different metal combinations and structures (overlayer and bimetallic surfaces).[40] These studies supplied a comprehensive collection of bimetallic systems with calculated binding

energies for wide variety of adsorbates relevant to various catalytic processes. This approach enables the catalytic activity of bimetallic surfaces to be predicted based solely on its electronic properties.

Concurrently, chemists made several advancements in the syntheses of various bimetallic NPs, with the goal of combining the catalytic improvements seen in bimetallic surfaces and electrodes with the elevated number of catalytically active surface sites inherent to small NPs. The research groups of Toshima,[41,42] Bradley,[43,44] Cheon,[45-47] Schaak[48-50] and others developed new strategies for preparing and characterizing bimetallic NPs of various compositions and architectures (which will be discussed in sections 1.3 and 1.5). Building on their work, the research groups of DiSalvo & Abruna,[51-55] Strasser,[56-58] Eichhorn,[59-64] Sun,[65-67] Markovic,[68-71] and Somorjai[72-74] greatly contributed to the field by preparing many different bimetallic NP structures and evaluating their activities for many different catalytic processes. Their research greatly advanced our understanding of the physical and chemical characteristics within bimetallic NPs that govern their ability to catalyze various processes.

Over the past decade, theoretical predictions and experimental observations began to merge and many bimetallic NP systems were experimentally shown to have high catalytic activities as predicted by calculations.[69,75] Based on these successes, predictive models have driven much of the recent research of bimetallic catalysts and will continue to do so well into the future. Since these models are derived for very distinct bimetallic compositions and architectures, the synthesis of bimetallic NPs

with specific and reproducible structures is of upmost importance to the rational design of materials with high activities for desired catalytic processes.

1.3 Bimetallic Nanoparticle Syntheses and Architectures

While there are many techniques for producing bimetallic NPs with controlled sizes, shapes, and architectures, solution phase nucleation is the most commonly used synthesis method.[76] In the most basic synthesis scheme, metal precursor complexes are dissolved in an appropriate solvent and heated to induce NP formation. When heated, the precursors break down into monomeric metal atoms, which increase in concentration over time. Once the concentration of monomers reaches a critical concentration, they nucleate to form small metallic clusters. The formed clusters then grow by adding existing monomers, or by coalescing with each other. Eventually, the particles grow large enough in size that they precipitate out of solution.[77] In practice, the synthesis process is often more complex. In cases where the metal precursors are ionic, a reducing agent (which can also be the solvent) is employed to reduce the metal ions to their zero-valent state, a necessary step before colloid formation occurs.[78] The use of surface stabilizing agents is also quite common in the synthesis process, where their direct physical contact with the metal atoms allows for greater control over particle growth.[42] In some cases, the particles are grown directly on the solvent-suspended catalytic support,[79] which can greatly simplify the production process, but often comes at the cost of reduced synthetic control.

There are numerous parameters that affect the outcome of a NP synthesis: selection of precursor compounds, stabilizing agents, reducing agents, and solvent, concentrations of these entities, reaction temperature, reaction duration, order and

temperature of reagent addition, etc. While the sheer number and flexibility of these variables often complicates the synthesis of a particularly desired bimetallic NP, they allow one to exert a considerable amount of control over the desired outcome and produce complex NPs with consistent and repeatable results. The ability to selectively produce bimetallic NPs with specific sizes, compositions, and architectures allows for the design of materials with improved activities for pertinent catalytic transformations.

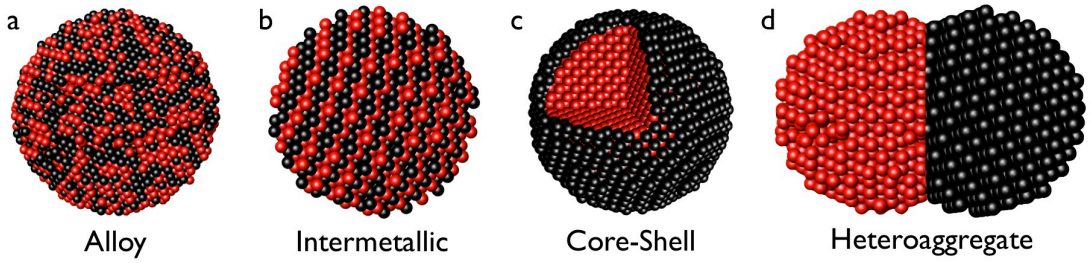

Figure 1.3 Examples of bimetallic nanoparticle architectures. Red represents one metal, while black represents a second metal

Figure 1.3 provides schematic representations of the most commonly seen bimetallic NP architectures. The most studied architecture is the alloy structure, seen in Figure 1.3a. Here, the component metals are randomly distributed throughout the NP, with no long-range order. They are sometimes referred to as "disordered" alloys to emphasize this fact. Some alloys, such as NiCo,[80] "innately" take the form of solid solutions due to their preference for heteroleptic bonding and are easily synthesized through mild co-reduction/nucleation methods. Other alloys are normally inaccessible under standard thermodynamic conditions due to their preference for homoleptic bonding. Very high reaction temperatures, powerful reducing agents, and/or careful

selection of metal precursors are often required to prepare alloys with this nature. The NiRu alloy NPs synthesized by Chen *et al.* are an example where the thermodynamically unfavored NP product is trapped by the fast kinetics of NP formation with the strongly reducing $NaBH_4$.[81]

Closely related to the alloy architecture is the intermetallic architecture seen in Figure 1.3b. Unlike alloy NPs, intermetallic NPs have well-defined structures, atomic stoichiometries, and discrete local environments. The distinction between an alloy and an intermetallic are well defined (stability, electronic structure, etc.) and result in unique chemical properties. Intermetallic NPs can also be formed from co-reduction/nucleation methods. In some cases, the fast kinetics of the NP synthesis can prevent the spontaneous formation of intermetallic NPs, despite the high thermodynamic stability typically associated with this architecture. For example, the PdCu NPs reported by Bradley and coworkers exist as alloys despite the intermetallic structure being thermodynamically favored at standard conditions.[43] Accordingly, intermetallic NPs are often produced by the thermal annealing of their alloy counterparts. The PtSn NPs in the work by Liu et al are kinetically trapped alloys prior to heat-treatment, which induces their transformation into their thermodynamically stable intermetallic phase.[82] Intermetallic NPs can also be formed by heat-treating monometallic NP mixtures, as seen in the work of the Schaak group, where their $AuCu_3$ intermetallic NPs were prepared in this fashion.[50]

The core-shell architecture, shown in Figure 1.3c, has received considerable interest in recent years. The core-shell arrangement is best imagined as a monometallic nanoparticle (the core) that is coated by a second metal (the shell) with

one or more layers. Unlike the other bimetallic architectures discussed here, the surface of a core-shell NP is usually comprised of only one metal. Due to this unique arrangement, the physical and electronic properties of core-shell NPs are unusual and distinct from those of their monometallic, alloy, or intermetallic counterparts. This phenomenon typically manifests through the unique behavior often seen in core-shell NP catalysts. Several examples of core-shell NPs exist in the literature, including Pt@Pd,[41] Ru@Pt,[83] Co@Pt,[84] and Fe@Co,[85] among others.

The most common methods for synthesizing core-shell NPs are summarized in Figure 1.4. The synthesis of core-shell NPs typically begins with the preparation of monometallic NPs which function as seeds for shell formation. From here, two mechanisms apply: sequential deposition and transmetalation. Ru@Pt NPs follow the sequential deposition method, where the reaction conditions are controlled such that Pt preferentially binds to the Ru NP core to form a Pt shell, rather than form additional monometallic Pt particles (Figure 1.4a).[64] In the transmetalation mechanism, surface atoms of the core metal are oxidatively displaced by the reduction of the second metal to form a shell. This mechanism describes the formation of the Co@Pt NPs reported by Park and Cheon (Figure 1.4b).[45,46] Additional methods for making core-shell NPs include delayed nucleation and surface segregation. The delayed nucleation method begins similarly to the co-reduction/nucleation methods used for making an alloy or intermetallic NP, except here, the second metal nucleates after the first metal has already formed monometallic NPs. Guo *et al.* prepared Ag@Ni NPs that followed this synthesis pathway (Figure 1.4c).[86] Finally, core-shell NPs can also be fabricated from alloy or intermetallic

particles through a process known as surface-segregation. Typically mediated by an adsorbate, in surface segregation, one metal is preferentially drawn to the NP surface, leaving the second metal embedded in the NP center. The PtSn@Pt NPs synthesized by Liu *et al.* used CO conditioning to draw Pt atoms to the PtSn NP surface (Figure 1.4d).[82]

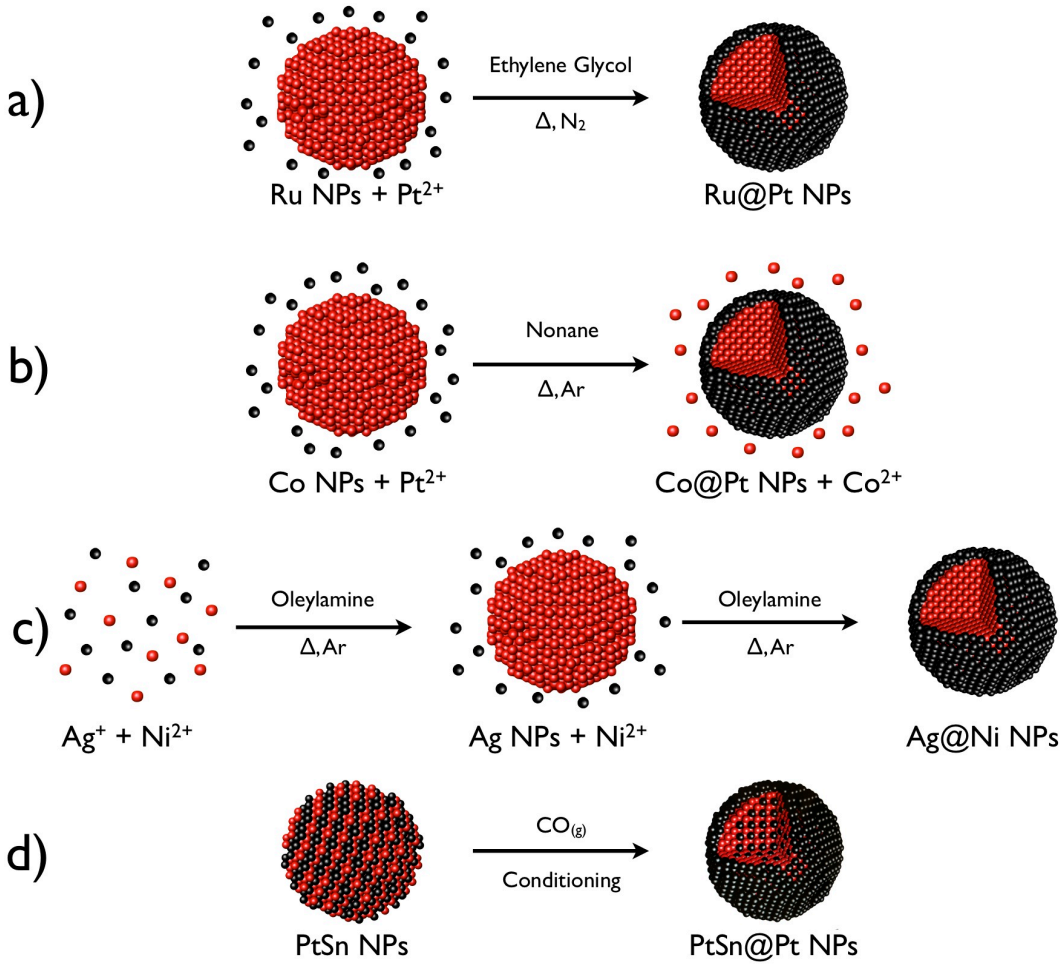

Figure 1.4 Schematic of the (a) sequential deposition, (b) transmetalation, (c) delayed nucleation, and (d) surface segregation methods of core-shell NP synthesis

The last architecture discussed is the heteroaggregate, as seen in Figure 1.3d. The heteroaggregate shares features with both the alloy/intermetallic and the core-

shell architectures. Similar to the alloy/intermetallic, its surface is bimetallic, but it has very distinct monometallic domains like the core-shell structure. Heteroaggregates often exhibit properties (and catalytic activities) similar to monometallic mixtures of their components, as shown in the catalysis studies of AuPt heteroaggregates synthesized by Zhou *et al.*[62] Heteroaggregate NPs are commonly produced in a similar fashion as core-shell NPs beginning with a monometallic NP seed.[59,87,88] In the core-shell architecture, reaction parameters are adjusted such that the second metal preferably binds to the seed, whereas for the heteroaggregate, the second metal preferentially binds to itself after initially using the seed as a foundation. Examples of heteroaggregates made in this fashion are the Au-Ge, and Ag-Ge heterodimers recently reported by Read *et al.*[88] Here, they selectively obtain the formation of heterodimers, rather than the formation of monometallic or core-shell NPs, by controlling the Ge nucleation and growth processes through careful manipulation of reaction time and temperature.

1.4 Support Materials for Nanoparticle Catalysts

NP catalysts typically require the use of high surface area support materials to immobilize the NPs, transport electrons, and provide good diffusion of reactants. The physical and chemical characteristics of these supports can change how the NP interacts with the material. This altered metal-support interaction can dramatically affect the NPs' electronic structure and their activity towards a particular catalytic process.[89] Physical and chemical characterizations of graphene-like support materials and discussions of how they alter the catalytic performance of their supported NPs are

important components of Chapters 2 and 3. A brief overview of the NP support materials mentioned in this dissertation is given below.

For PEMFC applications, carbon black powder (CB) has been the support material of choice for several years.[90] CB has several properties conducive to electrochemical applications, including high electronic conductivity, high porosity and surface area, and good chemical inertness. Electrocatalysts comprised of Pt-based NPs supported on CB remain the industry standard for PEMFC applications. As discussed in Chapter 4, we support our Co_xPt_y NPs on CB to create HOR and ORR electrocatalysts.

In recent years, graphene has received much interest as a new support material for electrochemical applications. Graphene potentially has many advantages over CB, such as improved electronic conductivity and increased surface area.[91,92] While the production of pristine graphene on the industrial level is currently uneconomical, reduced graphene oxides (rGOs), a graphene-like analogue, are available at large scales.[93] rGOs are mostly comprised of graphene domains, but are interspersed with functional groups, heteroatoms, and defects. Despite the presence of these components, rGOs retain most of graphene's desired properties and are equally capable for most electrochemical applications. Initially viewed as undesirable, the various functional groups present in rGOs provide an opportunity to exert more control over the support material's role in electrocatalytic processes.[94,95] Schematic models of both pristine graphene and rGO are shown in Figure 1.5, with more detailed discussions of graphene and rGOs to be presented in Chapters 2 and 3.

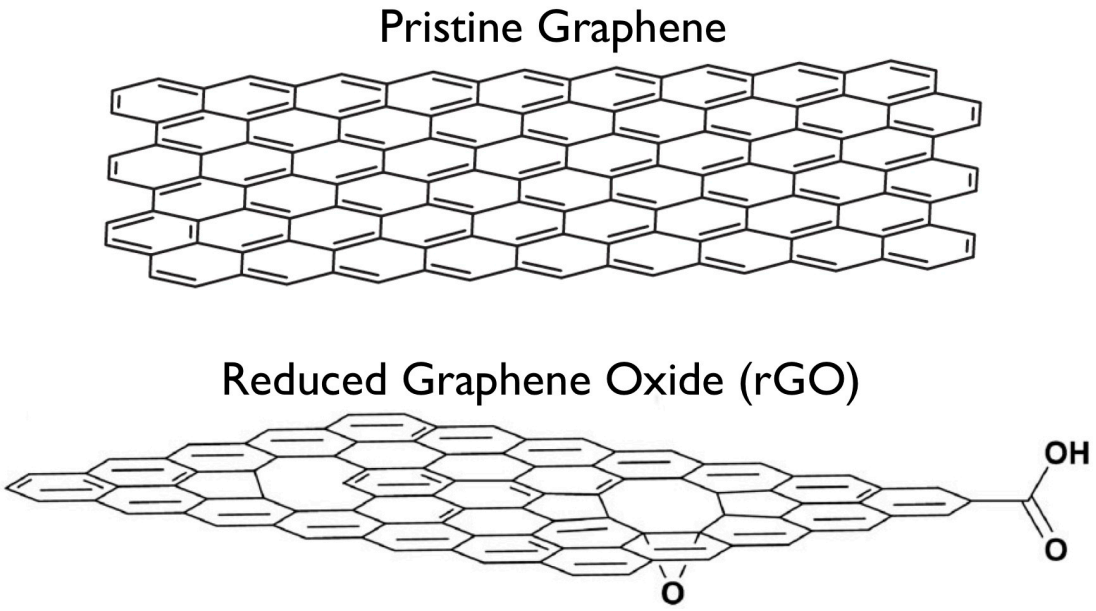

Figure 1.5 Schematic models of pristine graphene and reduced graphene oxide. Figure adapted from references [91] and [92]

Thermal catalytic processes, such as the PrOx (Preferential Oxidation of Carbon Monoxide) reaction, typically employ metal oxides as support materials due to their good chemical and thermal stabilities, large surface areas and high porosities.[96] Common metal oxides for this purpose include aluminum oxide (alumina, Al_2O_3), silicon oxide (silica, SiO_2), and cerium oxide (ceria, CeO_2). In our studies of bimetallic NPs for PrOx activity, as discussed in Chapter 5, we infused alumina with our particles to create the NP catalysts. Alumina's nature as a non-reducible oxide support allowed us to directly correlate the NPs' compositions and architectures with their PrOx activities without influence from the catalytic support.[64]

1.5 Analytical Techniques for Sample Characterization

As noted, the inherent physical and chemical characteristics of the NP catalysts are the principal determinants in their overall catalytic activity. To accurately correlate the observed performance of a catalyst with its chemical and structural makeup, thorough analytical characterization of the catalysts is essential. The following section presents an overview of the many characterization tools used in this dissertation, the chemical and structural information that can be obtained from each, and how the combination of these techniques contributes to forming a clear understanding of a NP's chemical and structural arrangement.

Powder X-ray diffraction (XRD) is a commonly used technique for determining the chemical composition and crystallographic structure of metal nanoparticles.[97] Bragg's law can be used to express X-rays scattered by a crystalline material:

$$n\lambda = 2d \sin\theta \tag{4}$$

Here, n is an integer, λ is the wavelength of the incident X-rays, d is the spacing between crystallographic planes of the material's atomic lattice, and θ is the angle between the incident X-ray and the scattering planes. As the lattice spacing between crystal planes of a given element are unique to that element and it's crystal structure, the elemental composition and crystal structure of a NP can be determined based on the peak positions within its diffraction pattern. This phenomenon can be further exploited when analyzing bimetallic NPs. Vegard's law approximates a linear relationship between the lattice spacing of a bimetallic alloy and the concentration of constituent metals. If the diffraction peak positions of two pure metals are known,

Vegard's law allows for the elemental composition ratio of a bimetallic alloy NP to be determined. The crystal structure sensitive nature of XRD also allows it to distinguish between an alloy and intermetallic of a bimetallic system of identical composition. Alloys and intermetallics often have different crystal structures, which materialize as unique diffraction patterns. If an alloy and intermetallic have similar crystal structures, the additional atomic ordering of the intermetallic typically results in additional diffraction peaks that are not present in the diffraction pattern of the alloy. Figure 1.6 illustrates the elemental determination aspect of XRD analysis by featuring diffraction patterns of Co_xPt_y NPs of varying metal concentrations. Here, the diffraction peak positions shift to higher angles with increasing Co concentration.

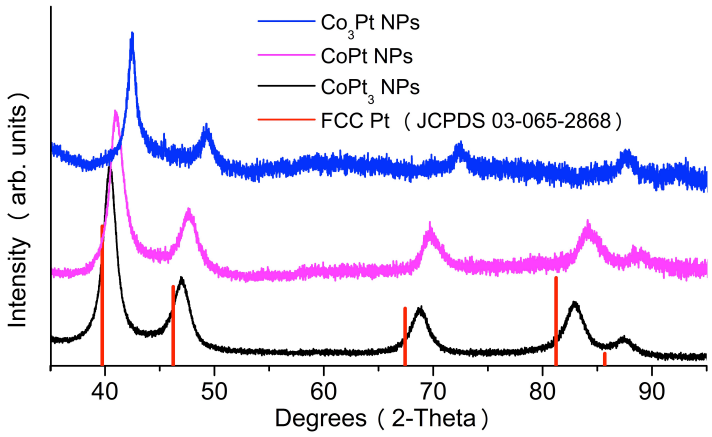

Figure 1.6 XRD patterns of $CoPt_3$ (black), CoPt (magenta), and Co_3Pt (blue) NPs. Red lines indicate the peak positions for FCC phase Pt.

XRD can also provide information on the sizes of the NPs analyzed by use of the Scherrer equation (3):

$$\tau = \frac{K\lambda}{\beta \cos\theta} \tag{5}$$

Here, τ is the crystallite size, *K* is the shape factor (roughly 0.9), β is the full width at half maximum (FWHM) of the diffraction peak, and λ and θ are the same as equation (4). Figure 1.7 demonstrates the rough size estimates XRD provides, where the diffraction peaks corresponding to Au NPs broaden (increasing β values) as the particle size (t value) decreases from 4 nm to 1 nm.

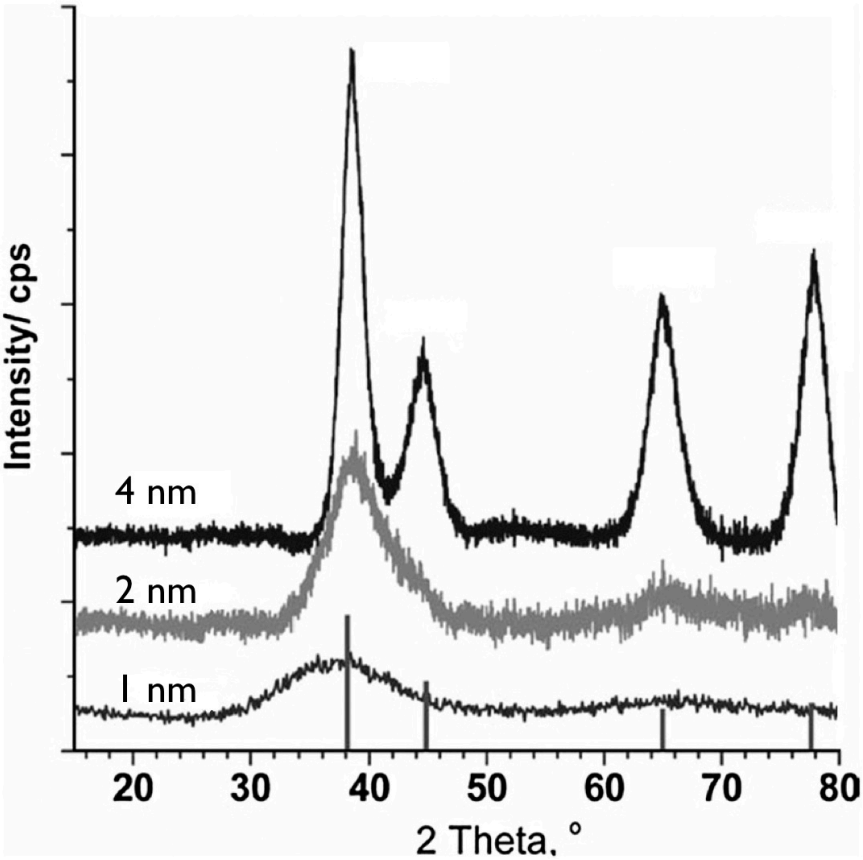

Figure 1.7 XRD patterns of 1, 2, and 4 nm Au NPs. Vertical lines indicate the peak positions for FCC phase Au. Figure modified from Lu and Chen[98]

Transmission electron microscopy (TEM) imaging is the primary technique for obtaining morphological information of a given NP sample. The principles behind TEM operation are similar to that of a traditional light microscope, where a highly

energetic beam of electrons (in place of light) interacts with a specimen to produce an image. Unlike light microscopes, the high energy of the electron beam allows atomic scale resolution, enabling the imaging and analysis of individual NPs. Particle size analysis, performed by counting large numbers of individual particles, is used to determine the average size and size distribution of a NP sample. At high magnifications and resolutions, TEM can also be used to provide structural information on the individual NP level. Crystallographic planes of NP samples can be revealed when the electron beam is scattered, resulting in the appearance of Moiré patterns commonly referred to as lattice fringe images. Performing lattice fringe analysis by measuring the distances between these atomic planes provides crystal structure data for a single NP in a similar fashion as XRD analysis.

When operated in the scanning mode (STEM) and combined with additional analytical tools, such as energy dispersive X-ray spectroscopy (EDS), these TEM analyses become even more informative, especially for bimetallic samples. Initially developed as a stand-alone technique, EDS analysis can be utilized to determine not only the elemental composition of individual NPs, but also the locations of these elements within the NP. This ability is quite useful in distinguishing between two different architectures of identically constituted bimetallic NPs. In EDS, X-rays are given off and enumerated by a detector when the NPs are struck by the TEM's electron beam. The energies of the emitted X-rays are characteristic of the atomic structure of the element from which they originated. When this information is combined with the number of X-rays measured by the EDS detector, the compositional ratio of elements within the sample can be calculated. Figure 1.8 shows

STEM images and EDS line scans of single RuPt alloy (a) and Ru@Pt core-shell NPs (b). While both NPs have a 1:1 ratio of Ru:Pt, the Gaussian distribution of Ru within the core and the bimodal distribution of Pt at the edges clearly illustrate the core-shell architecture of the Ru@Pt particle.

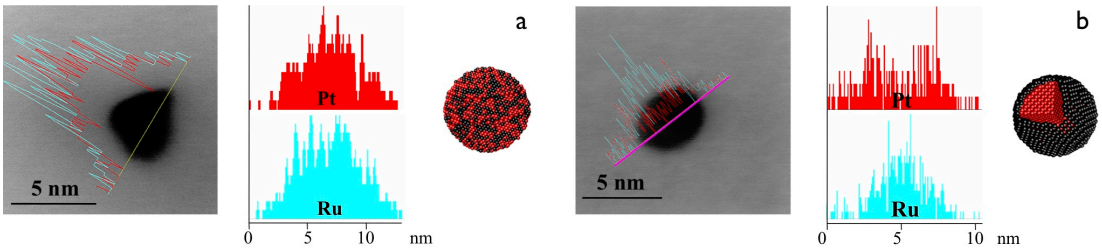

Figure 1.8 Representative STEM-EDS line scans of (a) a RuPt (1:1) alloy NP and (b) a Ru@Pt core-shell NP. Relative atomic % composition values (vertical axis) of Pt (red) and Ru (cyan) are plotted against the line scan probe position (horizontal axis) and are given next to the STEM images. Figure adapted from Alayoglu *et al.*[83]

Information on the elemental composition and architecture of metallic NPs can also be determined from Fourier transform infrared spectroscopy (FTIR) using carbon monoxide (CO) as a probe molecule.[42] Here, FTIR is used to monitor the positions and relative intensities of the CO stretching frequency when bound on a metal surface. CO bonds to transition metal surfaces via σ-bonding, while the transition metal bonds to CO through π-backbonding to the antibonding orbitals of CO. This π-backbonding decreases the CO bond order, resulting in a decrease in the CO stretching frequency. The degree and nature of this π-backdonation is dependent on the d-electron density of the metal and varies for each metal. As such, the band

positions in the CO-FTIR spectra can reveal the elemental identity of the NP surface. This is especially useful when determining if a NP has a core-shell architecture, as the CO-FTIR spectra of a core-shell NP before and after shell formation should be different due to their surfaces containing only one type of metal. The CO-FTIR spectra of Rh, Pt, and Rh@Pt core-shell nanoparticles, as seen in Figure 1.9, illustrate this principle. Here, the CO stretches on Rh and Pt have different frequencies, while the CO stretch of the Rh@Pt particles matches that of monometallic Pt, clearly demonstrating that the original Rh surface has been completely covered by Pt.

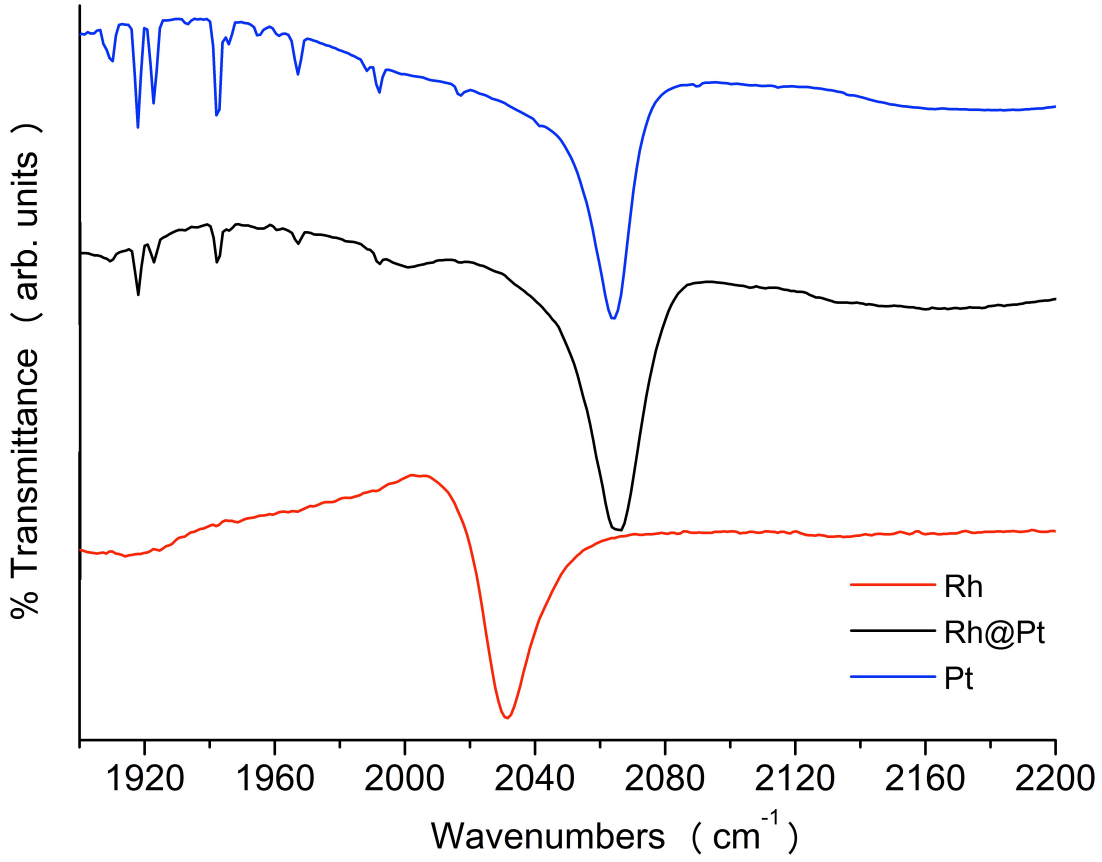

Figure 1.9 CO-FTIR of Rh (red), Pt (blue), and Rh@Pt (black) core-shell NPs. Each colloidal suspension was bubbled with CO for 20 min before measurement and the native colloidal suspension was used as the background

X-ray photoelectron spectroscopy (XPS) is an additional characterization tool that also can be used to evaluate the chemical and structural properties of materials, but it is not used in this work to analyze metallic NPs. Here, XPS is used to study the graphene-like support materials discussed in Chapters 2 and 3. In XPS analysis, the sample is irradiated with x-rays, resulting in the ejection of electrons from the atoms within the sample. The energies of these electrons are unique to the element from which they originate, allowing XPS to provide elemental identification. By quantifying the number of electron of a particular energy, compositional ratios can also be calculated. XPS also has the ability to identify and quantify the chemical and electronic states of the elements within a sample. This information can range from determining the oxidation states of a particular metal, to distinguishing the bonding character within a compound. Figure 1.10 shows the C 1s XPS spectrum of Kevlar fibers. The peak locations are used to identify the different bonding environments of the carbon atoms, while the peak intensity ratios quantify the concentrations of each.

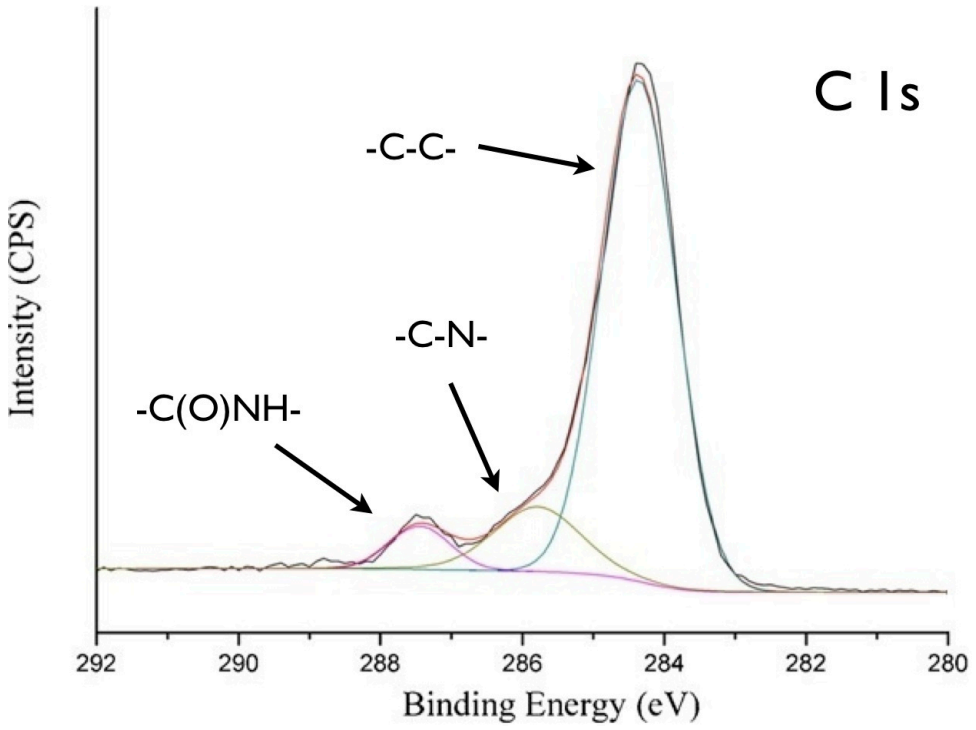

Figure 1.10 Carbon 1s XPS spectrum of Kevlar fibers. Figure modified from Su *et al.*[99]

Each technique described provides useful information on the chemical and structural character of the NP catalysts, yet it is only by uniting the information obtained that a full picture of can be formed. This picture provides the essential information needed to understand how the properties of the NPs (and supports) affect their performance in catalytic applications.

1.6 Overview of the Dissertation

The work described in this dissertation entails the synthesis, characterization, and activity studies of various monometallic and bimetallic NP catalysts. Chapter 2 describes the synthesis and exploratory electrocatalytic studies of graphene-supported

metal NPs. A full study of Pt and PtSn intermetallic NPs supported on four unique rGO materials is presented in Chapter 3. Chapter 4 contains the synthesis, characterization, and electrocatalytic activities of Co_xPt_y NPs with varying sizes, compositions, and architectures. The syntheses, characterizations, and preliminary catalytic evaluations of various bimetallic core-shell NPs appear in Chapter 5. Finally, a brief summary of the results and contributions from this work, as well as a prospective on future studies in the field will be presented in Chapter 6.

Chapter 2: Metal Nanoparticle Templating and Electrocatalytic Modification Using Functionalized Graphene Sheets

2.1 Introduction

Transition-metal nanoparticles (NPs) have received much attention for their use as catalysts for several energy-relevant reactions, including the oxygen reduction reaction (ORR)[100] and hydrogen electrooxidation reaction (HOR).[101] Many of these catalysts, whether mono- or poly- metallic in nature, consist primarily of precious metals such as Pt. However, the expense and scarcity of these metals hinders their long-term usage and has prompted research focused on creating new catalysts with minimal precious metal content. Traditional synthetic routes for producing metal NPs typically use methods such as surface stabilizers to limit surface metal oxidation and control particle size,[102] energy intensive processes,[103] or strong reducing agents.[104] These practices can negatively impact the efficiency of the resultant catalytic system and should be minimized when possible.[105]

For electrochemical applications, nanoparticle catalysts require the use of electronically conductive support materials, such as carbon black (CB), to immobilize the NPs and transport electrons to and from the catalyst particles. Previous research has demonstrated the ability to synthesize nanoparticles in the presence of the support material, however many of these procedures use the aforementioned synthesis methods, such as employing strong reducing agents and/or surfactants.[79,106] In several cases where these methods are not used, the resultant particles are large in size (> 15 nm), consequently reducing the amount of surface area available for catalysis.[107,108]

As such, creating a generic methodology where small, well-dispersed nanoparticles are directly grown on the catalytic support without the use of surfactants and/or strong reducing agents is a worthy endeavor.

Recently, graphene sheets have received considerable attention as a new support material for electrochemical applications. The remarkable properties of graphene, including its high electrical conductivity,[109] large surface area,[110] and mechanical strength[111] have spurred research interest in this area. While a practical large-scale production method for pristine graphene has not yet been realized, graphene oxide (GO) can be produced on a large scale via Hummers' method and its variations.[111-114] Unlike graphene, GO is electronically insulating and hydrophilic[115] and, as such, the resultant GO must be reduced to recover electrical conductivity necessary for electrochemical applications. The degree of reduction, commonly approximated by the C/O ratio, has a dramatic impact on the properties of the resultant graphene-like sheets.[116]

We describe here a generic method of preparing Ni, Ru, Pt and Fe@Fe_2O_3 NPs supported on commercial, electrically conducting reduced GO by way of a "one pot" synthetic route. We show that this method gives electrochemically active materials with modified catalytic activity due to metal-support interactions. In our studies, we used highly reduced GO known as functionalized graphene sheets (FGS) with a C/O ratio of 22 that is produced by the Aksay and Prud'homme method of thermal exfoliation of graphite oxide.[93,117] The distinguishing factor of this method is its rapid heating of fully oxidized GO to 1050 °C, resulting in the production of intercalated CO_2 that quickly expands the graphene layers into individual wrinkled sheets.[117]

Advantages provided by this process include a larger percentage of uniform single layer sheets and a higher degree of GO reduction. Another key feature of this methodology is the ability to control the C/O ratio of the graphene-like product through additional high-temperature annealing in a reducing atmosphere.[117] The properties of FGS are promising for use as a support material for NP based electrocatalysts since prior research has shown FGS to be highly conductive with large surface areas.[116,118-121] The reduced graphene-like electrocatalyst support materials, such as FGS, are presumed to be structurally and electronically distinct from other carbon-based supports, such as Vulcan-XC-72.[93,116,117,121] As a probe of particle-support interactions, we studied the electrooxidation of CO/H_2 gas mixtures on Pt supported FGS. Our studies show that nanoparticle catalysts supported on FGS have distinct activity from other Pt-on-carbon electro catalysts. Thus the FGS can be used as a surfactant and a support material with novel metal-support interactions.

2.2 Experimental

2.2.1 Materials and Methods

2.2.1.1 Materials.

Vor-X graphene (FGS, C/O ratio: 22) was provided by Vorbeck Materials. Iron pentacarbonyl ($Fe(CO)_5$, 99.99%), nickel acetylacetonate ($Ni(acac)_2$, 95%), ruthenium acetylacetonate ($Ru(acac)_3$, 97%), platinum acetylacetonate ($Pt(acac)_2$, 97%), diphenyl ether (Ph_2O, 99%), and acetone (99.5%) were purchased from Aldrich. Tetrahydrofuran (THF, 99%) was purchased from Mallinckrodt. Toluene (99.5%) was purchased from VWR. Isopropanol (99%) was purchased from

Pharmco-AAPER. Sulfuric acid (H_2SO_4, 96.4%) was purchased from Fisher. 5% Nafion® solution was purchased from Fluka. E-TEK Pt (30% HP Pt on Vulcan® XC-72 CB) was purchased from BASF. Ultra-pure water was obtained from deionized water using a Millipore Academic Milli-Q A10 purifier system. $Ni(acac)_2$ was stored in a glove box until ready to use. All materials were used as received without further purification. All reactions were carried out on Schlenk lines under N_2 atmospheres.

2.2.1.2 Solvent Washing of FGS.

FGS (30 mg) was mixed with solvent (acetone or water, 10 mL) in a capped glass vial and sonicated for 60 min in a sonication bath (FS30H, Fisher Scientific). The resultant mixture was transferred to a 50 mL conical centrifuge tube and centrifuged at 6000 rpm for 30 min. The supernatant was discarded and the black solid was allowed to dry in air.

2.2.1.3 Combustion Analysis of FGS.

FGS (30 mg) was placed into a metallic Ni crucible and covered with a ceramic lid that was left slightly ajar to allow air flow. The sample was then placed into a furnace oven (Thermolyne 47900, Thermo Scientific) in air, where it was heated to 650 °C and held for 240 min before cooling to room temperature. The residue, which was brown in color, was collected and used for further analysis.

2.2.1.4 Synthesis of FGS-Fe@Fe_2O_3 NPs.

In a typical synthesis, FGS (20 mg) was mixed with toluene (10 mL) in a capped glass vial and sonicated for 10 min in a sonication bath (FS30H, Fisher Scientific). The resulting mixture was transferred to a three-necked round-bottom flask (RBF) equipped with a magnetic stirrer and a reflux condenser and heated to reflux. $Fe(CO)_5$ (15 μL, 0.111 mmol Fe) was added via a N_2-purged syringe and the reaction was kept at reflux for 60 min. The flask was allowed to cool to room temperature before the black slurry was transferred to a 50 mL conical centrifuge tube and centrifuged at 6000 rpm for 15 min. The supernatant was discarded and the black solid was allowed to dry in air. The resultant material was 52% Fe metal by weight based on the initial amounts of reagents.

2.2.1.5 Synthesis of FGS-Ni NPs.

In a typical synthesis, FGS (20 mg) was mixed with THF (30 mL) in a glass beaker and sonicated for 60 min at 0 °C using an ultrasonic homogenizer (Sonic Ruptor 400, Omni International) equipped with a ¾" processing tip. The resulting mixture was then transferred to a Schlenk flask equipped with a magnetic stirrer that also contained Ph_2O (20 mL). The mixture was heated to 30 °C under vacuum with vigorous stirring to remove the THF. Once the THF was removed, the temperature was increased to 75 °C to degas the system. Once degassed, N_2 was introduced and the temperature was increased to 250 °C. A degassed solution of $Ni(acac)_2$ (9.7 mg, 0.04 mmol Ni) in Ph_2O (2 mL) was then added dropwise via a N_2-purged syringe and allowed to react at 250 °C for 60 min. The flask was allowed to cool to room temperature before the black slurry was transferred to a 50 mL conical centrifuge tube

and centrifuged at 6000 rpm for 15 min. The supernatant was discarded and the black solid was mixed with acetone (20 mL) and vortexed. The resultant mixture was divided amongst 1.5 mL conical centrifuge tubes, then centrifuged at 13000 rpm for 10 min. The supernatant of each tube was discarded and the black solids were mixed with acetone (1 mL), vortexed, then centrifuged at 13000 rpm for 10 min. The acetone washing process was repeated five times. The black solid was then dried under vacuum for 60 min. The resultant material was 10% Ni metal by weight based on the initial amounts of reagents.

2.2.1.6 Synthesis of FGS-Ru NPs.

In a typical synthesis, $Ru(acac)_3$ (4.0 mg, 0.01 mmol Ru) was dissolved in Ph_2O (20 mL) in a RBF equipped with a magnetic stirrer and a reflux condenser. In a glass beaker, FGS (9.5 mg) was mixed with THF (30 mL) and sonicated for 60 min using an ultrasonic homogenizer (Sonic Ruptor 400, Omni International) equipped with a ¾" processing tip placed in an ice bath. The FGS mixture was then transferred to the Ru precursor solution. The resultant mixture was heated to 30 °C under vacuum with vigorous stirring to remove the THF. Once the THF was removed, the temperature was increased to 75 °C to degas the system. Once degassed, N_2 was introduced and the flask was heated to reflux where it was held for 15 min. The flask was allowed to cool to room temperature before the black slurry was transferred to a 50 mL conical centrifuge tube and centrifuged at 6000 rpm for 15 min. The supernatant was discarded and the black solid was mixed with acetone (20 mL) and vortexed. The resultant mixture was divided amongst 1.5 mL conical centrifuge tubes,

then centrifuged at 13000 rpm for 10 min. The supernatant of each tube was discarded and the black solids were mixed with acetone (1 mL), vortexed, then centrifuged at 13000 rpm for 10 min. The acetone washing process was repeated five times. The black solid was then allowed to dry in air. The resultant material was 10% Ru metal by weight based on the initial amounts of reagents.

2.2.1.7 Synthesis of FGS-Pt NPs.

In a typical synthesis, $Pt(acac)_2$ (34.6 mg, 0.09 mmol Pt) was dissolved in Ph_2O (40 mL) in a RBF equipped with a magnetic stirrer and a reflux condenser. In a glass beaker, FGS (40 mg) was mixed with THF (30 mL) and sonicated for 60 min using an ultrasonic homogenizer (Sonic Ruptor 400, Omni International) equipped with a ¾" processing tip placed in an ice bath. The FGS mixture was then transferred to the Pt precursor solution. The resultant mixture was heated to 30 °C under vacuum with vigorous stirring to remove the THF. Once the THF was removed, the temperature was increased to 75 °C to degas the system. Once degassed, N_2 was introduced and the flask was heated to 225 °C where it was held for 60 min. The flask was allowed to cool to room temperature before the black slurry was transferred to a 50 mL conical centrifuge tube and centrifuged at 6000 rpm for 15 min. The supernatant was discarded and the black solid was mixed with acetone (20 mL) and vortexed. The resultant mixture was divided amongst 1.5 mL conical centrifuge tubes, then centrifuged at 13000 rpm for 10 min. The supernatant of each tube was discarded and the black solids were mixed with acetone (1 mL), vortexed, then centrifuged at 13000 rpm for 10 min. The acetone washing process was repeated five

times. The black solid was then dried under vacuum for 60 min. The resultant material was 30% Pt by metal weight based on the initial amounts of reagents.

2.2.1.8 Heat Treatment of NPs.

The FGS-supported NPs were placed in a ceramic boat, which was introduced into a quartz glass tube. The tube was heated in a horizontal solid tube furnace (Thermolyne F21135, Thermo Scientific) under a H_2/Ar atmosphere (5% H_2) at a flow rate of 90 SCCM. The Fe particles were annealed at 450 °C for 120 min, while the Ni and Pt particles were annealed at 400 °C for 240 and 120 min, respectively.

2.2.2 Sample Characterization

2.2.2.1 Transmission Electron Microscopy

Transmission electron microscope (TEM) images were obtained on a JEM 2100F Field Emission TEM operating at 200 kV. The supported NP powders were dispersed in THF, then an aliquot (6 μL) of the resulting dispersion was drop cast on the TEM grids. The TEM grids used were lacey carbon-coated Cu grids (Cu-400LC, Pacific Grid Tech).

2.2.2.2 Powder X-ray Diffraction

Powder X-ray diffraction (XRD) patterns were obtained on a Bruker D8 Advance diffractometer equipped with a LynxEye detector using a monochromatic Cu Kα radiation source biased at 40 kV and 40 mA. The XRD patterns were background corrected.

2.2.2.3 X-ray Photoelectron Spectroscopy

X-ray photoelectron spectroscopy (XPS) data were collected on a Kratos Axis 165 X-ray photoelectron spectrometer operating in the hybrid mode using Al Kα radiation (1486.6 eV) at 300 W. Charge neutralization was used to minimize sample charging. The charge neutralizer settings were: 2.0 A, 1.0 V charge balance, 1.0 V bias. Binding energies were calibrated with respect to the C1s peak at 284.7 eV.

2.2.3 Electrochemical Analysis

iPrOH (159.2 mL), ultra-pure water (40.0 mL) and Nafion® solution (0.80 mL, 5%) were mixed and stored as a stock solution. The catalyst ink was prepared by mixing the supported NP powder with the above stock solution such that the concentration was 1.0 mg/mL of powder in solution. The resultant mixture was then sonicated for 120 min. The catalyst ink (20 μL) was cast on a glassy carbon (GC) electrode (Pine Instruments, 5.0 mm diameter) using a micropipette and allowed to dry in air overnight while covered. Electrochemical studies were performed on a potentiostat (Gamry Instruments) with a standard rotating electrode electrochemical cell. The GC rotating disk electrode (RDE) with dried catalyst ink on its surface was used as the working electrode. Pt wire was used as the counter electrode and a saturated calomel electrode (SCE) was used as the reference electrode. Potentials were recorded with respect to the SCE. The electrolyte was 0.5 M H_2SO_4 in ultra-pure water. Prior to the electrochemical experiments, each catalyst was subjected to 20 potential scan cycles between -0.245 V and 0.5 V (vs. SCE) in 0.5 M H_2SO_4 saturated

with Ar (99.9% pure). To obtain the HOR curves, the catalyst was saturated with H_2 by bubbling the electrolyte with H_2 (99.999% pure) for 15 min, then running potential scans (20 mV/s) under gentle H_2 bubbling at various rotation rates (1600, 900, 400, 100 rpm). To obtain the CO stripping curves, the catalyst was saturated with CO by bubbling CO (99.5% pure, Al tank) in the electrolyte for 15 min, followed by Ar-purging for 30 min. To obtain the polarization curves for the electrooxidation of CO-contaminated H_2, the electrolyte was bubbled with a CO/H_2 gas mixture (1000 ppm CO, balance H_2, 99% pure, Al tank) for 60 min with the electrode potential held at -0.20 V vs. SCE, followed by a potential scan at 1 mV/s with a rotation rate of 1600 rpm.

2.3 Results

2.3.1 Characterization of Functionalized Graphene Sheets (FGS)

While FGS has been previously well characterized,[93,116-121] we performed additional studies to confirm the nature of the commercially produced material. As expected, TEM images of the as-received FGS powder show the tendency of these wrinkled sheets (Figure 2.S1a to form multi-layer stacks (Figure 2.S1b). Analysis of one such stack reveals an average interlayer distance of 0.38 nm, slightly greater than the 0.34 nm seen in pristine graphene (inset of Figure 2.S1b). This result is reasonable given the wrinkled nature of the FGS and is in good agreement with previous reports.[93,117,119] An XRD pattern of the as-received FGS also shows sheet stacking, with the expected broad peaks associated with weakly diffracting graphene sheets

(Figure 2.1a). The XRD pattern of the acetone-washed FGS powder (Figure 2.1b) is similar to that of the as-received FGS powder, but also contains sharper peaks due to a second phase (or phases) in the 30°-40° range. It is possible that the later peaks are due to impurities within the FGS powder, although they could not be indexed to a particular compound. These peaks are consistently present in the XRD patterns of the FGS-supported NP systems (Figures 2.4-2.7) suggesting they are present in the commercial FGS material. The XRD pattern of the water-washed FGS (Figure 2.1c) is quite similar to that of the as-received FGS powder but lacks several of the peaks observed in the acetone-washed sample. This result suggests that some of the extraneous material can be removed through water washing, which is in agreement with the XPS data discussed below.

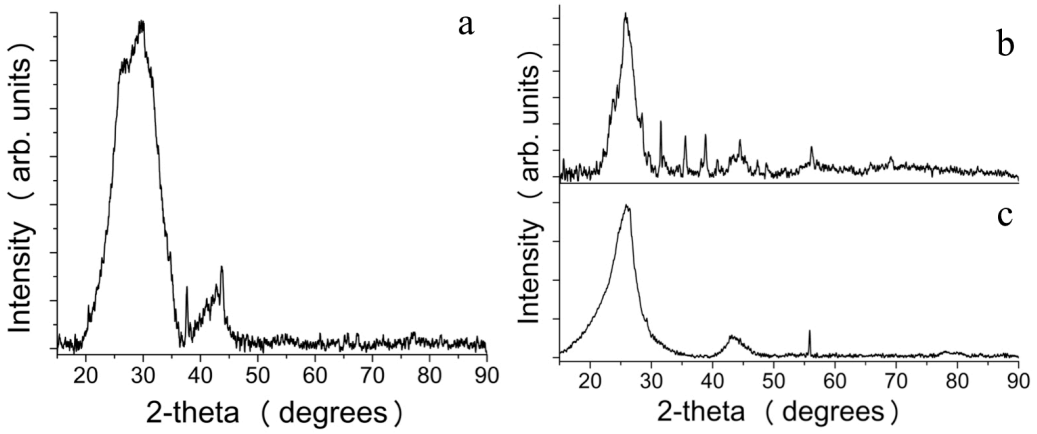

Figure 2.1 XRD patterns of the (a) as-received, (b) acetone-washed, and (c) water-washed FGS powder. The sharp peaks between 30-60° 2θ are due to a secondary phase(s).

The hydration level of the sample after interaction with solvent also affects the FGS' diffraction pattern. Thoroughly dried FGS gives a broad peak centered at the 26°, as expected from its graphene-like structure (Figures 2.5 and 2.7). However, this peak shifts to ca. 20° when the FGS is fully intercalated with solvent, presumably Ph_2O (Figure 2.S2). In some cases, intercalated and non-intercalated aggregates or domains co-exist in partially dried FGS samples (Figure 2.6). Similar results have been reported for graphene oxide, where water molecules intercalate between the sheet layers.[122]

We also performed XPS analysis on the as-received and solvent-washed FGS. The XPS spectrum of the as-received FGS powder (Figure 2.2a) shows the presence of C and O with a C/O ratio of 22.6, in excellent agreement with the C/O ratio stated by the manufacturers, along with small amounts of S ($\leq$ 1%) and Cl ($\leq$ 0.5%). XPS analyses of the acetone-washed (Figure 2.2c) and water-washed (Figure 2.2e) FGS samples gave similar results; however, Cl was absent in the water-washed sample. Because the FGS has a thickness of < 1 nm per layer, the XPS data can be considered a bulk analysis.

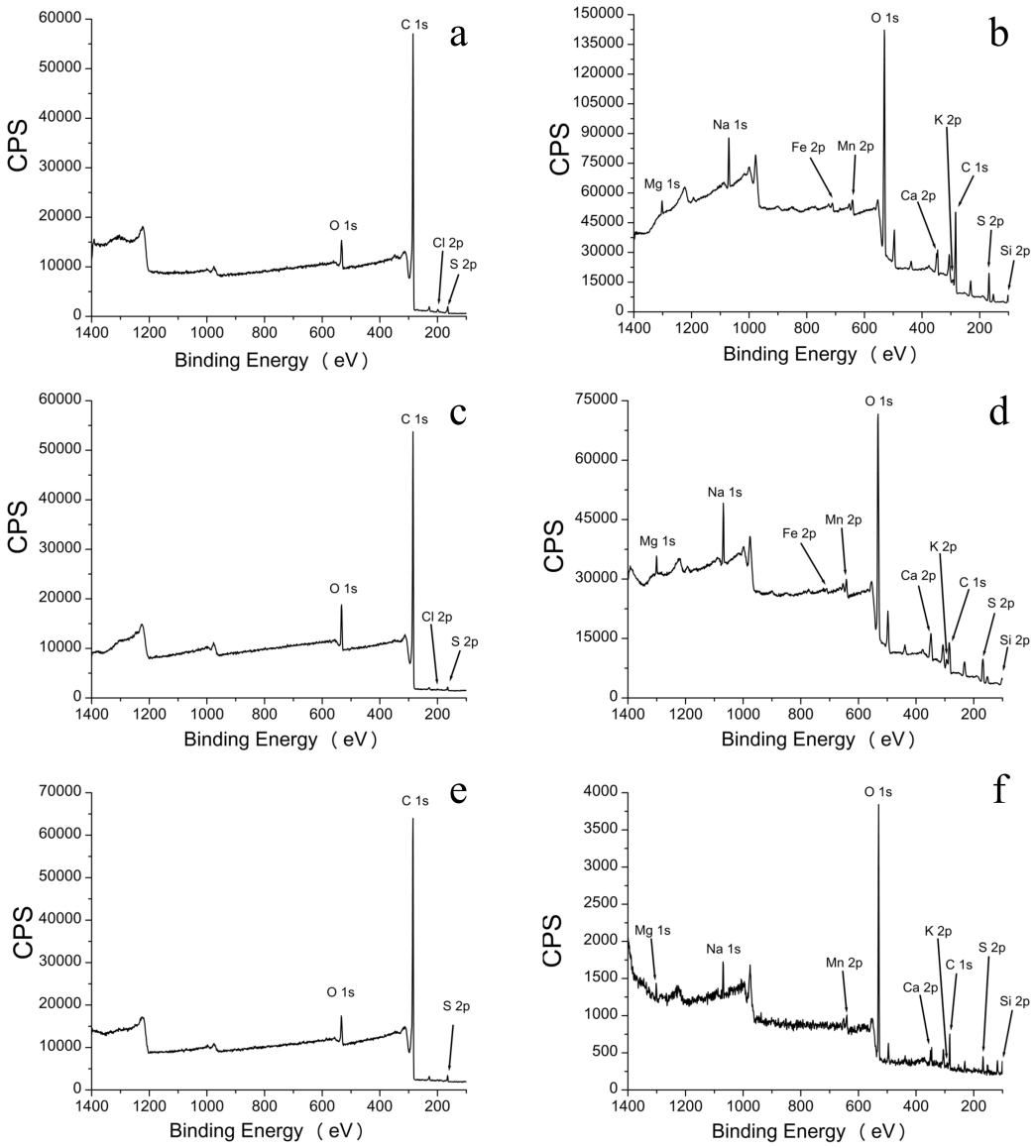

Figure 2.2 XPS spectra of the (a) as-received, (c) acetone-washed, and (e) water-washed FGS powders and the (b) as-received, (d) acetone-washed, and (f) water-washed FGS combustion residues. For clarity, only the most intense XPS peak for each element is indicated

Combustion of the black FGS powder left a dark brown residue, regardless of whether the FGS was washed or unwashed. $CaSO_4$ peaks dominate the XRD patterns of the residues, but the remaining peaks could not be unequivocally identified (Fig 2.3). Elemental compositions of the residues were obtained by using XPS (Figures 2.2b, d, f), which showed the presence of Mn, Fe, Ca, and Mg, with each accounting for less than 0.1% of the original FGS powder. We reason these trace impurities result from the manufacturing process.

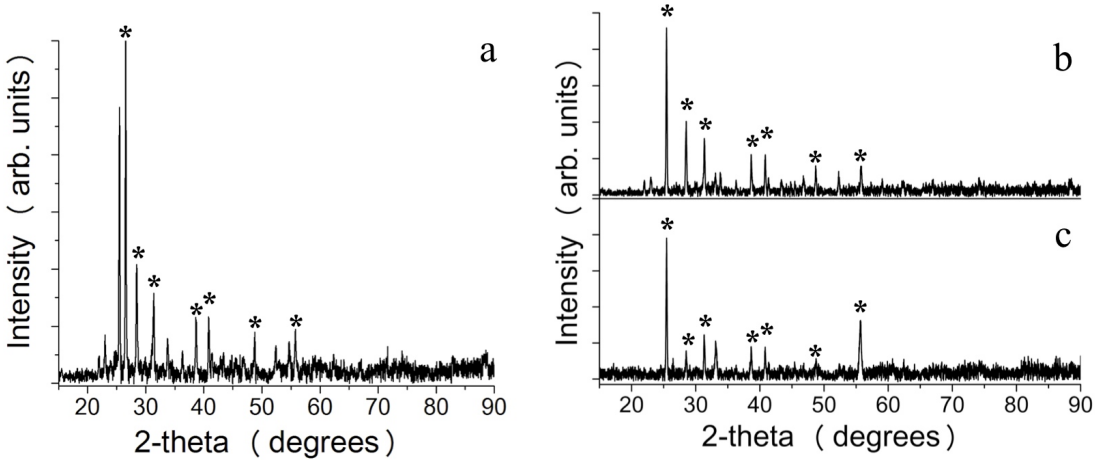

Figure 2.3 XRD patterns of the FGS combustion residues of (a) as-received, (b) acetone-washed, and (c) water-washed samples. Asterisks denote peaks associated with $CaSO_4$ (JCPDS 01-086-2270); the remaining peaks have not been unequivocally identified.

2.3.2 Synthesis and Characterization of FGS-Supported Nanoparticles

$Fe@Fe_2O_3$, Ni, Ru, and Pt NPs supported on FGS were synthesized *in situ* by the decomposition/reduction of common metal precursors[64,123-126] in heated suspensions of FGS under anaerobic conditions. TEM analysis shows that the average sizes of the particles differ with each system, but they all have relatively narrow size

distributions. The observed oxide shell on the Fe NPs (see below) most likely formed as a result of the partial oxidation of the Fe metal when exposed to air. The Ni NPs most likely exist as No after exposure to air but are readily re-reduced to the metallic state as described below.

The heat-treated Fe@Fe_2O_3 NPs have an average diameter of 13.8 ± 2.1 nm (Figure 2.4a). A higher magnification lattice fringe image reveals their crystalline core-shell architecture, with the cores having average diameters of 6.4 ± 1.0 nm and an average shell thickness of 3.7± 0.8 nm (inset of Figure 2.4a). The core has an average lattice separation of 0.20 nm, corresponding to the (110) plane of metallic Fe, while the shell has an average lattice separation of 0.25 nm, which corresponds to the (311) plane of γ-Fe_2O_3. Figure 2.4b shows the XRD pattern of the Fe@Fe_2O_3 NPs, which contains intense peaks centered at 44.7°, 65.1°, and 82.3° due to the BCC iron core, along with several reflections associated with the γ-Fe_2O_3 shell.

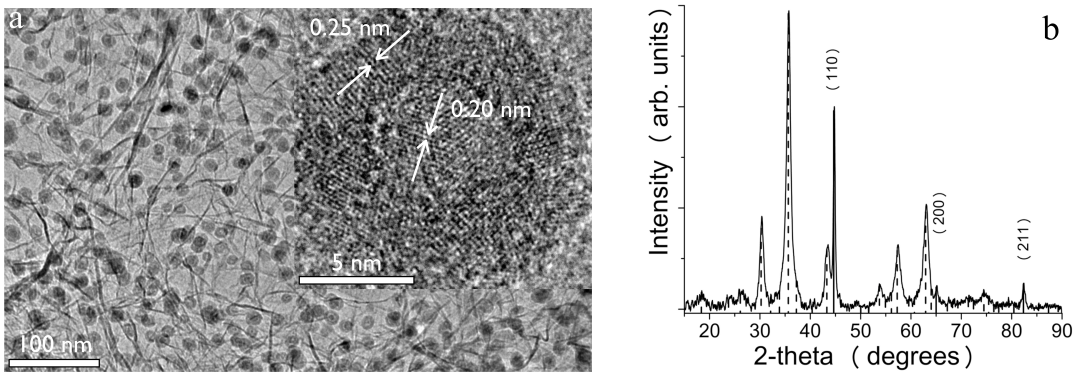

Figure 2.4 (a) TEM image and (b) XRD pattern of the heat-treated Fe@Fe_2O_3 NPs supported on FGS. Peak positions for BCC Fe phase (Solid, JCPDS 03-065-4899) and γ-Fe_2O_3 phase (Dashed, JCPDS 00-039-1346) are also shown. A lattice fringe image of a single particle highlighting the (110) plane of BCC Fe and (311) plane of γ-Fe_2O_3 is inset in Figure 2.4a. The large particle size and highly crystalline nature of the Fe@Fe_2O_3 NPs result in intense diffraction that obscures the diffraction for the nearly amorphous FGS.

The as prepared (AP) Ni particles have an average size of 1.3 ± 0.4 nm and an average lattice separation of 0.20 nm, which may correspond with the (111) Ni or (200) NiO planes (Figure 2.5a). Despite the clear crystallinity of the AP Ni particles, we did not detect any crystalline Ni compounds by XRD, presumably due to the small particle size (Figure 2.5b). After heat-treatment in flowing H_2/Ar at 400 °C for 240 min, the average particle size increases to 6.7 ± 4.2 nm with an average lattice separation of 0.19 nm, corresponding to the (111) Ni plane (Figure 2.5c). The XRD

pattern has broad FCC Ni diffraction peaks along with the broad FGS peaks, which is consistent with small metallic Ni NPs supported on the FGS (Figure 2.5d).

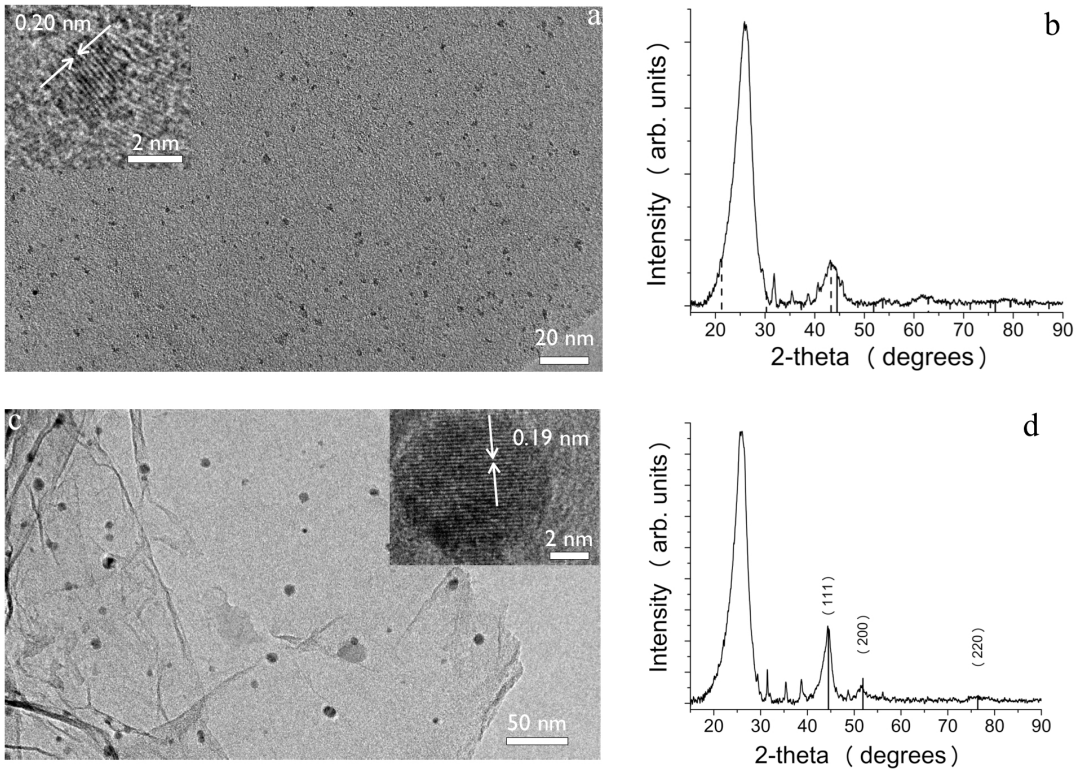

Figure 2.5 (a) TEM image and (b) XRD pattern of the AP Ni NPs supported on FGS. Peak positions for FCC phase Ni (Solid, JCPDS 03-065-2865) and rhombohedra NiO (Dashed, JCPDS 01-089-3080) are also shown. A lattice fringe image of a single particle is inset in Figure 2.5a. (c) TEM image and (d) XRD pattern of heat-treated Ni NPs supported on FGS. A lattice fringe image of a single particle highlighting the (111) plane of FCC Ni is inset in Figure 2.5c.

Similar analyses were performed on the AP Ru and Pt NPs, which have average diameters of 2.0 ± 0.5 nm and 2.6 ± 0.6 nm, respectively (Figures 2.6a and 2.7a). Lattice fringe analysis of the particles show the (101) Ru and (111) Pt planes,

with average lattice separations of 0.20 nm and 0.22 nm, respectively. XRD patterns of the Ru (Figure 2.6b) and Pt (Figure 2.7b) particles clearly show the expected broad peaks associated with metallic HCP Ru and FCC Pt crystallites. Heat-treating the Pt NPs for 120 min at 400 °C in flowing H_2/Ar induces a slight size increase to 2.9 ± 0.8 nm (Figure 2.8a).

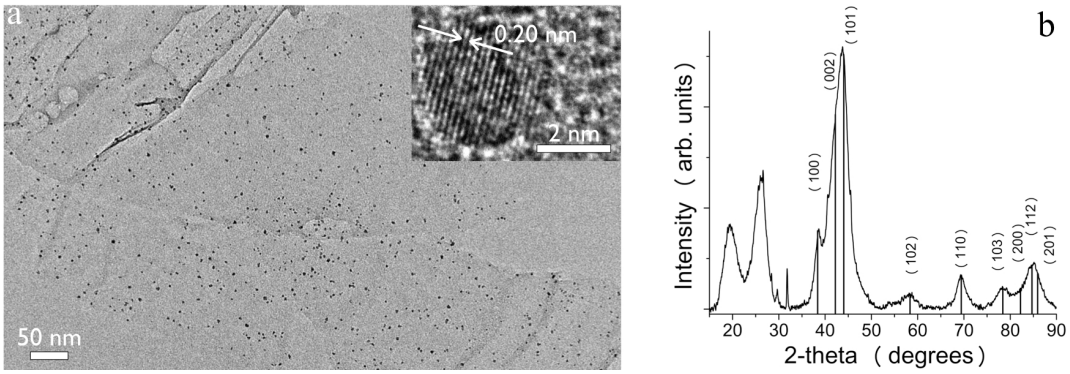

Figure 2.6 (a) TEM image and (b) XRD pattern of the AP Ru NPs supported on FGS. Solid lines indicate the peak positions for HCP Ru (JCPDS 00-006-0663). A lattice fringe image of a single particle highlighting the (101) plane of HCP Ru is inset in Figure 2.6a. The two broad diffraction peaks at 20° and 26° 2θ arise from intercalated and non-intercalated domains of FGS, respectively.

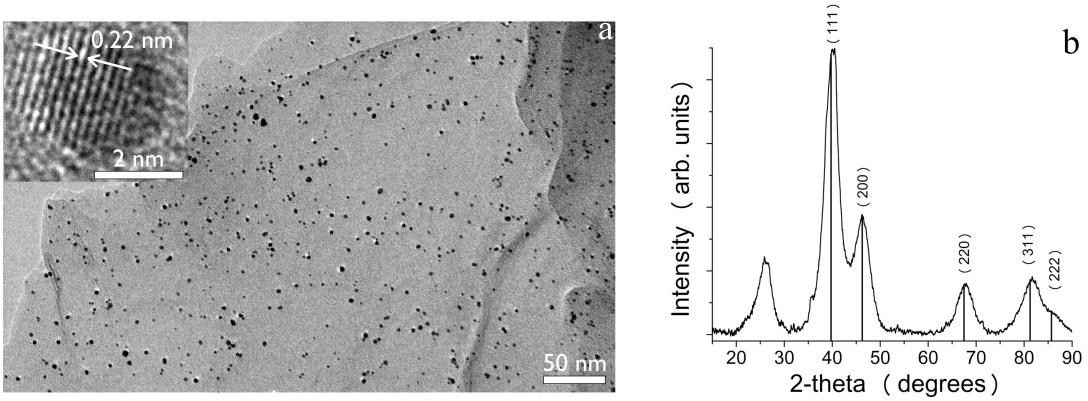

Figure 2.7 (a) TEM image and (b) XRD pattern of the AP Pt NPs supported on FGS. Solid lines indicate the peak positions for FCC Pt (JCPDS 01-089-7382). A lattice fringe image of a single particle highlighting the (111) plane of FCC Pt is inset in Figure 2.7a.

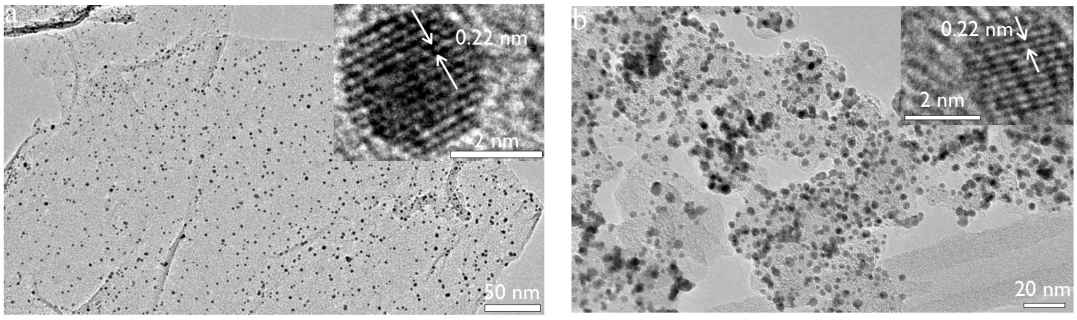

Figure 2.8 TEM images of the (a) heat-treated Pt NPs supported on FGS and (b) E-TEK Pt catalyst. Lattice fringe images of single particles highlighting the (111) plane of FCC Pt are inset.

2.3.3 Electrochemical Analysis of FGS-Supported Pt Nanoparticles

To probe the effect of support material on the catalytic activity of the NPs, electrochemical analyses were performed on our AP and heat-treated FGS-Pt NPs and

compared them with the commercially available E-TEK Pt catalyst (Figure 2.8b). All three catalysts contained a 30% Pt metal loading by weight based on the initial amounts of reagents.

Figure 2.9 shows the CO stripping curves of the FGS-Pt catalyst before and after heat-treatment along with the E-TEK Pt catalyst. Both FGS catalysts have CO stripping peak potentials similar to those of the E-TEK catalyst. The CO oxidation potential of the AP FGS catalyst is markedly higher than that of the E-TEK catalyst, which suggests a much stronger adsorption of CO. Annealing the FGS-Pt catalyst in H_2/Ar atmospheres significantly improves the CO stripping onset potentials but the resulting peak remains somewhat broader than that of the E-TEK catalyst. The integrated areas under the CO stripping regions of both FGS-Pt catalysts are approximately the same as that of the E-TEK catalyst, confirming that all three catalysts have similar electrocatalytically active surface areas and similar Pt metal loadings. The primary differences between the three catalysts are the support material and the resulting metal-support interactions.

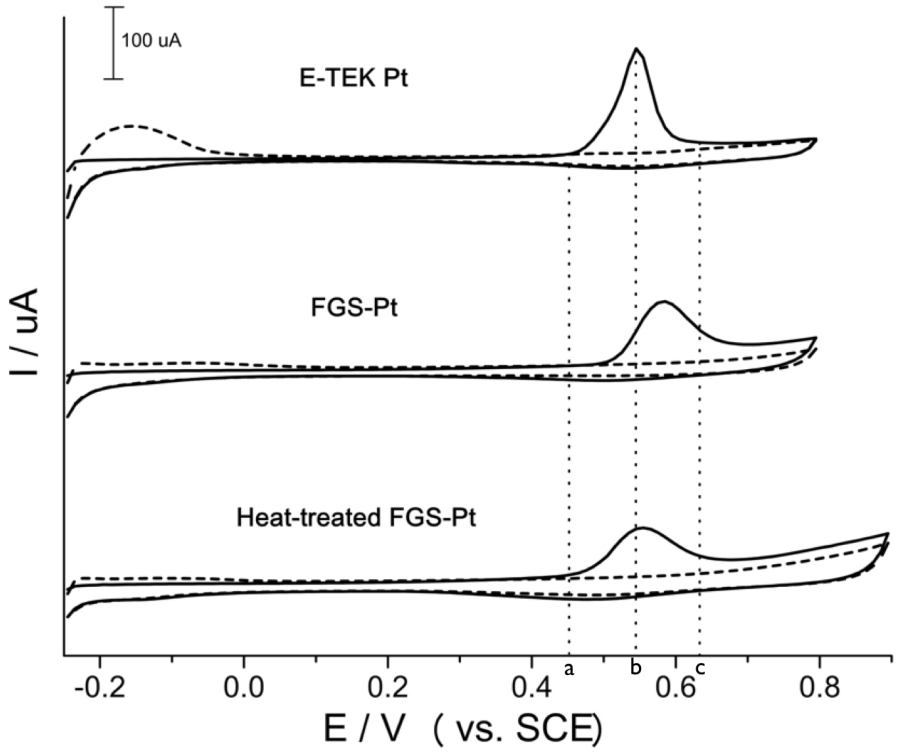

Figure 2.9 CO stripping curves of the E-TEK Pt, FGS-Pt and heat-treated FGS-Pt catalysts in 0.5 M H_2SO_4 solution at 25 °C. Scan rate: 20 mV/s. The dotted curves are the CVs recorded after CO stripping. The vertical dashed lines denote the (a) onset, (b) peak, and (c) terminal CO oxidation potentials of the E-TEK catalyst.

Figure 2.10 shows the RDE polarization curves for the electrooxidation of pure H_2 and CO-contaminated H_2 (1000 ppm CO, balance H_2) for the FGS catalyst before and after heat-treatment and the E-TEK catalyst. All three catalysts show typical HOR behavior for Pt catalyzed electrooxidation of pure H_2 with the expected onset potential. This result suggests the nature of the support does not have an appreciable effect on the NPs' catalytic activity for pure H_2 fuel. However, for CO-contaminated H_2 fuels, the onset potential of each catalyst is significantly different.

The onset potential for the FGS-Pt catalyst decreases by nearly 0.1 V after heat-treatment. However, both FGS catalysts' onset potentials are far higher (at least 0.15 V) than that of the E-TEK catalyst.

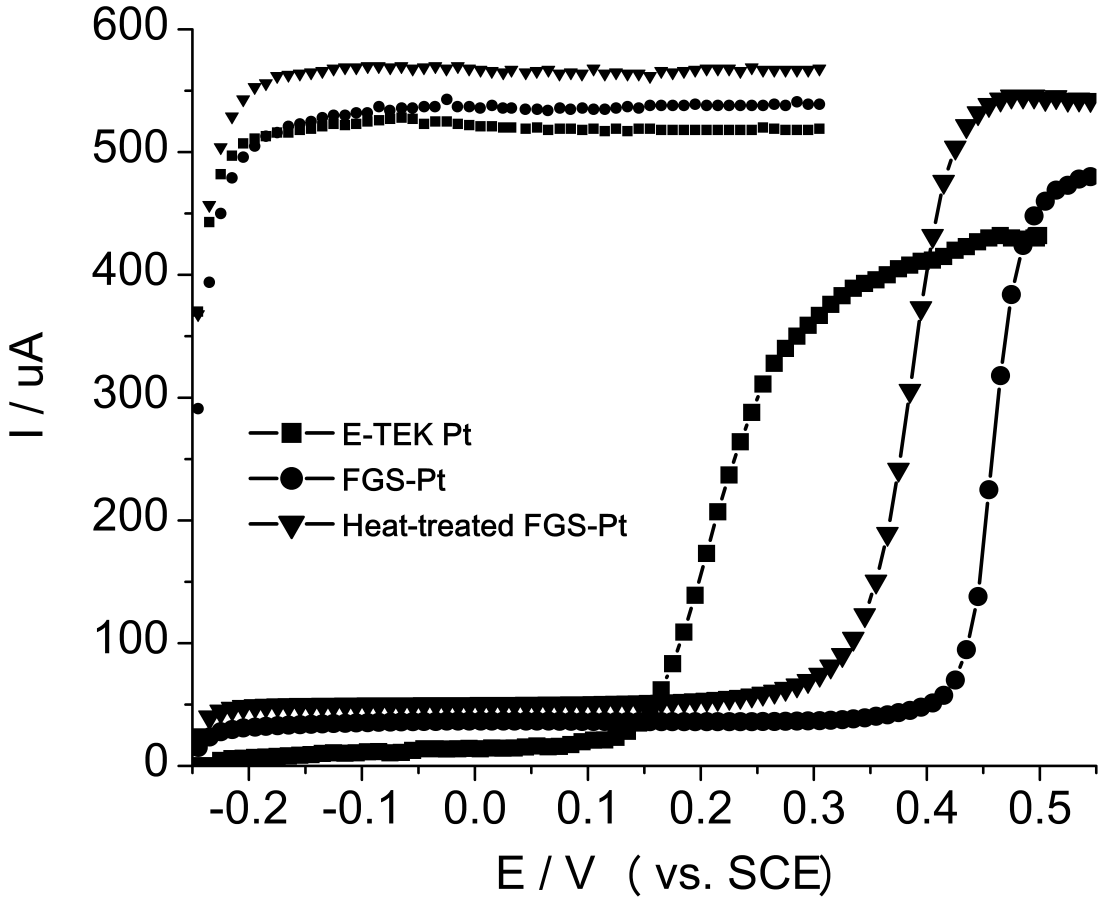

Figure 2.10 Polarization curves for the electrooxidation of H_2 (symbols only) and H_2 containing 1000 ppm CO (symbol + lines) of the E-TEK Pt, FGS-Pt, and heat-treated FGS-Pt catalysts in 0.5 M H_2SO_4 solution. Curves were recorded at 25 °C with 1600 rpm rotation rates and scan rates of 100 mV/s (H_2) and 1mV/s (H_2 + CO).

2.4 Discussions

2.4.1 Synthesis and Characterization of FGS-Supported Nanoparticles

The results above show that well-dispersed, metallic NPs supported on conductive FGS can be conveniently prepared in a simple one-pot method that does not require additional reducing agents or additional surfactants. In most cases (Ni, Ru, Pt), the resulting particles are quite small (<3 nm), which makes them ideally suited for applications where high surface area metallic particles on conductive substrates are required. In contrast to other methods of producing graphene-supported NP composites, our methods employ off-the-shelf reagents in the complete absence of additional reducing agents and surfactants that can impede electrochemical processes. While several reports of Fe and Ni NPs supported on graphene exist,[127-131] non-oxidized particles have only been accessible through the use of strong reagents[132-135] or non-standard synthetic methods.[136-138] Few reports of graphene supported Ru NPs exist, with the only examples employing microwave irradiation in ionic liquids[139] and high-temperature aqueous reduction with GO.[140] Both methods produce particles ~2 nm in diameter, which is comparable to our results. Compared to these other procedures, our method utilizes simple solution heating to easily produce small, well-dispersed Ru NPs on the FGS support with particle sizes similar to well-known surfactant based procedures.[64,141,142] In contrast, Pt is the most studied graphene-supported NP system, with several methodologies existing for the production of small graphene-supported Pt particles.[140,143-153] The Pt NPs described here possess sizes and dispersions in agreement with previous reports.

2.4.2 Electrochemical Analysis of FGS-Supported Pt Nanoparticles

The electrooxidation of H_2 in the presence of CO (i.e. CO tolerance) is very sensitive to the electronic structure of the Pt catalyst.[154] By employing Pt NPs of similar size and loading, we have exploited this sensitivity to probe the metal-support interactions and the resulting changes to the electrocatalytic properties of the Pt NPs. The CO tolerance of the FGS-Pt catalyst is markedly different from that of the E-TEK Pt catalyst, despite the catalysts having similar NP sizes and metal loadings. The ~0.15 V shift in onset potential reveals a significant change in the catalytic properties of FGS-Pt relative to CB-Pt. This difference is surprising in light of the similarities of the RDE results for pure H_2 electrooxidation and the CO stripping for the two catalysts. While the CO stripping peak of the annealed FGS-Pt is somewhat broader than that of the E-TEK catalyst, the onset potentials are almost identical. There is no discernible difference in the electrooxidation of pure H_2 for any of the catalysts.

Theoretical and experimental studies of CO tolerance in Pt-graphene HOR catalysts have suggested graphene and doped graphene supports improved CO tolerance relative to traditional CB based catalysts.[155,156] The lower onset potentials for the graphene based catalysts were attributed to weaker CO binding to the Pt NP surface due to a downshift in the *d*-band center arising from strong Pt-graphene metal-support interactions.[157,158] In contrast, we found that the CO tolerance of FGS-Pt is inferior to the CB based E-TEK control. Although we used somewhat different experimental conditions than Yoo *et al.* (scan rates, reference electrode, etc.), the onset potentials for CO oxidation for the CB-based Pt references from both studies are in agreement, indicating the differences in the graphene-based catalysts were

associated with the graphene itself. The onset potentials for CO electrooxidation on both the heat-treated FGS-Pt and E-TEK Pt were the same (0.44 V vs. SCE), which is in contrast to the small negative shifts in onset potentials for the graphene-supported particles relative to their CB counterparts (0.35 vs. 0.37 V vs. SCE) in the study by Yoo *et al.*[155] For CO-contaminated H_2 electrooxidation, Yoo *et al.* also showed a decrease in onset potential for the graphene-based catalyst compared to its CB-based counterpart, which is consistent with their CO-stripping experiments and the concept of a downshifted Pt *d*-band center. The diminished CO tolerance observed for our FGS-Pt system relative to the CB-based E-TEK control suggests that the Pt *d*-band center is slightly raised for the FGS-Pt system. Correlations between the Pt *d*-band center and thermal CO oxidation have been well established on M@Pt core shell NP catalysts,[75] and may be equally valid in the electrooxidation processes described here.

The FGS-Pt catalysts appear to have markedly different metal-support interactions relative to the graphene-Pt catalysts described by Yoo *et al.* While there are several possible explanations for the differences in the two systems, it is likely that the differences in functional groups and the resulting electronic structures of the graphene substrates are largely responsible for the activity differences. The commercial FGS and the graphene sheets used by Yoo *et al.* were prepared by reducing graphite oxide, yet the methods of reduction are different. The graphene sheets used in the previous studies were prepared from chemical hydrazine reduction of exfoliated GO sheets,[155,156] while the FGSs used here are produced from the dual thermal exfoliation/reduction of graphite oxide.[93,117] These methodologies result in fundamentally different materials, although both are graphene-like.[159] While

hydrazine reduction does not appear to create atomic vacancies, the FGS production method has been shown to induce many structural defects, which would result in different modes of binding with the Pt NPs. The trace impurities within the FGS or its unusual stacking formations may also affect the catalytic activity of the supported Pt NPs, but their concentrations are very low relative to the Pt metal loading. While not much is known about these particle interactions with FGS, understanding their mechanisms is key to discerning its effect on the activity of these and future catalysts. The influence of the graphene-like support's chemical/structural nature on the resultant metal-support interaction and catalytic activity is further explored in Chapter 3.

2.5 Conclusion

In summary, we have developed a simple, one-pot solution method for synthesizing well-dispersed NPs of several different metals supported on FGS. Our method improves on previous reports by eliminating strong reducing agents, surfactants, and/or specialized equipment, while still maintaining a high degree of uniformly small and well-dispersed particles on the electrocatalytic support. Through the use of RDE and CO stripping electrochemical experiments, we have shown that metal-support interactions of Pt NPs on reduced graphene oxide supports can vary dramatically and significantly alter the resulting catalytic activity. While the electrooxidation reactions are only amenable to the Pt-based catalysts due to the highly acidic nature of the system, the results for the Pt-system suggest that the FGS supports can alter catalytic performance. When combined with the studies of Yoo *et*

al., it appears that reduced graphene oxides can be tuned (electron donating vs. electron accepting) to modify the catalytic performance of catalyst composites by controlling the metal-support interactions. This concept is thoroughly investigated in Chapter 3.

2.6 Supplemental Information

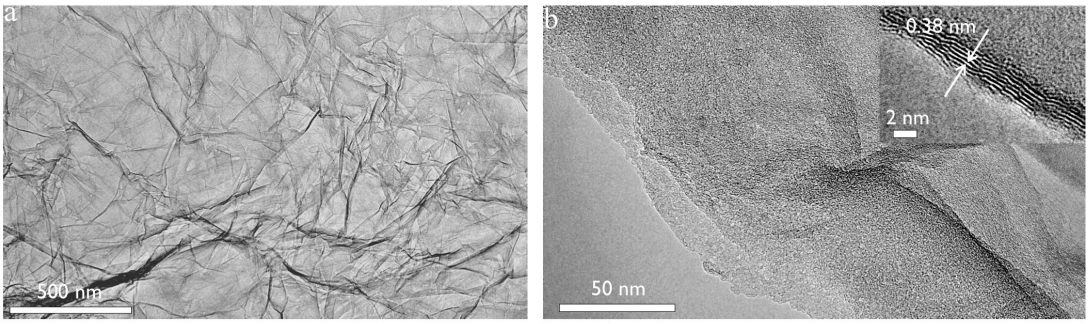

Figure 2.S1 TEM images of as-received FGS powder. Note the wrinkled morphology of the sheets in Figure 2.S1a and the sheet-stacking phenomenon in Figure 2.S1b. The inset in Figure 2.S1b highlights the 0.38 nm average interlayer distance between a single stack of FGS layers, which corresponds to a 2θ of 23.4° in our XRD data.

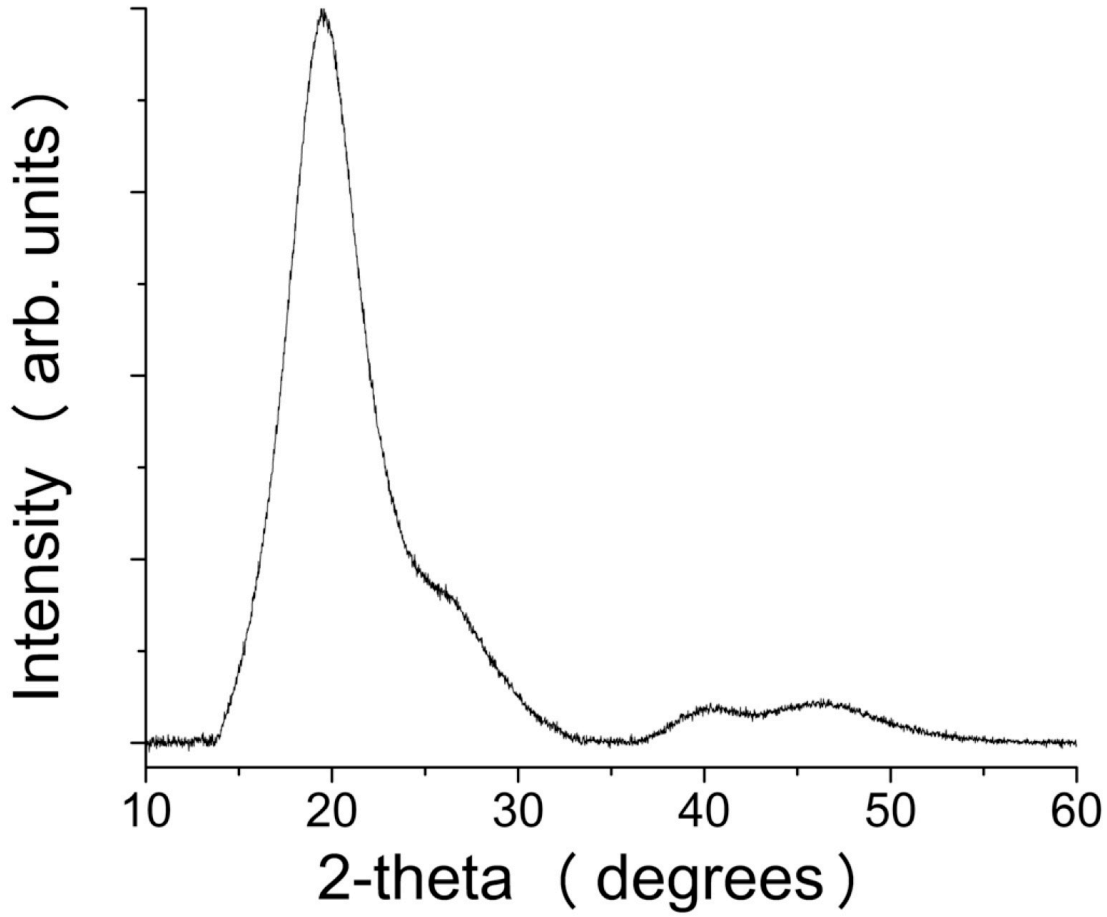

Figure 2.S2 XRD pattern Pt NPs supported on FGS while suspended in Ph_2O. Note that the FGS is primarily intercalated (20°) with some non-intercalated domains (26°)

Chapter 3: CO Tolerance of Pt and PtSn Intermetallic Electrocatalysts on Synthetically Modified Reduced Graphene Oxide Supports

3.1 Introduction

As a carbon-based support material for nanoparticle (NP) electrocatalysts, graphene is thought to be advantageous over traditional carbon black (CB), due to its large surface area[110] and high electronic conductivity,[160] while being relatively easy to produce.[112,113] Although industrial-scale production of pristine graphene sheets is currently impractical, reduced graphene oxides (rGO) are available in large quantities and have been subjected to many studies. In contrast to pristine graphene, rGOs can contain several kinds of functional groups, heteroatoms and defects. Many pathways have been developed for synthesizing rGOs, including one-step thermal exfoliation/reduction,[93,117] high temperature reduction in hydrogen atmosphere,[161] wet chemical reductions,[144,162,163] and various combinations of these techniques.[159,164,165] Different synthetic methods create different functional groups that alter the physical and electronic properties relative to pristine graphene.[93,116,117,119,121,162,166-169] The defects and functional groups in the rGOs alter the interactions between the NP and support and potentially affect the catalytic activity of a system. For example, recent thermal studies have shown that rGO-supported iron-based NP catalysts had markedly better performance in syn-gas conversions relative to the same iron-based NP catalysts on carbon nanotubes.[170]

While many electrochemical studies have been conducted on rGO-supported metal NP catalysts,[80,94,143,145,149,150,155,156,171-177] the influence of rGO on the electrocatalytic activity of NPs is not well understood. In the context of electrooxidation of H_2 in the presence of CO impurities (i.e. CO tolerance), previous studies[155-157] have suggested that rGO-Pt NPs have improved activity relative to CB-Pt catalysts due to Pt electronic structure modification as a result of strong Pt-graphene interactions. The magnitude of this metal-support interaction is thought to be dependent on the amount and types of chemical defects within the graphene structure.[157,178,179] Since the chemistry of functionalizing graphene has advanced significantly in recent years, the ability to tune these metal-support interactions through chemical modification of graphene is potentially powerful. Metal-support interactions between NPs and inorganic supports are well known to have significant influences on catalytic activities, but are not tunable in the same way that a graphene system can be modified.[89,180,181] This research aims to evaluate the influence of different types of modified graphene on electrocatalytic activity with the ultimate goal of developing predictability and control in the design of new electrocatalyst systems.

To evaluate the metal-support interactions between modified graphene and metallic NP catalysts, we describe the full characterization of four different rGOs and their use in preparing rGO-supported Pt and PtSn electrocatalysts. These electrocatalysts were evaluated for their CO electrooxidation and CO/H_2 electrooxidation activities. Our studies show that the nature of the rGO support material affects catalytic performances of the resulting Pt and PtSn NPs. In the case

of nitrogen-doped rGOs, an anomalous metal support interaction was found that caused a marked difference in the behavior of the Pt and PtSn systems for CO/H_2 electrooxidation.

3.2 Experimental

3.2.1 Materials and Synthesis

3.2.1.1 Materials

Vor-X graphene powder (FGS, C:O ratio = 22) was provided by Vorbeck Materials. Single layer graphene (SLG, powder) and single layer graphene oxide (GO, flakes) were purchased from ACS Material. Platinum acetylacetonate ($Pt(acac)_2$, 97%), tin chloride ($SnCl_4$, 99%), sodium triethylborohydride solution ($NaBEt_3H$, 1.0 M in toluene), sodium borohydride ($NaBH_4$, 98%), hydrazine monohydrate (H_2NNH_2, 98%), 1-octadecene (90%), and acetone (99.5%) were purchased from Aldrich. Methanol (MeOH, 99.8%) was purchased from VWR. Tetrahydrofuran (THF, 99%) was purchased from Mallinckrodt. Isopropanol (iPrOH, 99%) was purchased from Pharmco-AAPER. Sulfuric acid (H_2SO_4, 96.4%) was purchased from Fisher. Nafion® (5%) solution was purchased from Fluka. E-TEK Pt (30% HP Pt on Vulcan® XC-72) was purchased from BASF. Ultra-pure water was obtained from deionized water using a Millipore Academic Milli-Q A10 purifier system. All materials were used as received without further purification.

3.2.1.2 Preparation of Borohydride-reduced Graphene Oxide (BGO)

Typically, GO (100 mg) was dissolved in ultra-pure water (40 mL) in a glass beaker in a sonication bath (FS30H, Fisher Scientific) and then transferred into a 100 mL round-bottomed flask. $NaBH_4$ (1 g, 0.026 mol) was added to the solution, which was then heated to 80 °C for 24 hr. After cooling to room temperature, the black precipitate was separated by filtration, washed with 2 L water, air-dried overnight and dried under vacuum for 24 hr.

3.2.1.3 Preparation of Hydrazine-reduced Graphene Oxide (NGO)

The same procedure as above was utilized, except H_2NNH_2 (1 mL, 0.02 mol) was used instead of $NaBH_4$. All other steps were identical.

3.2.1.4 Synthesis of rGO-supported PtSn Intermetallic NPs

In a typical synthesis, rGO (13.3 mg) was mixed with 1-octadecene (10 mL) in a glass vial and sonicated for 120 min in a sonication bath (FS30H, Fisher Scientific). The resultant mixture was then added to a Schlenk flask and degassed at 80 °C while stirring. Once degassed, N_2 was introduced and the temperature was increased to 200 °C. In a separate vial, $Pt(acac)_2$ (10.0 mg, 0.025 mmol Pt) was dissolved in 1-octadecene (1 mL), degassed, and placed under N_2. $SnCl_4$ (3 μL, 0.025 mmol Sn) was then added to the Pt precursor solution while stirring. $NaBEt_3H$ solution (2 mL, 1.0 M in toluene) was injected into the rGO dispersion, immediately followed by the injection of the PtSn precursor solution. All injections were

performed using N_2-purged syringes. The reaction mixture was returned to 200 °C for 60 min before the heating source was removed. The flask was allowed to cool down to room temperature before the black slurry was transferred to a 50 mL conical centrifuge tube. MeOH (2 mL) and acetone (20 mL) were added to the tube and the resultant mixture was sonicated for 10 min. The tube was then centrifuged at 6000 rpm for 15 min. The supernatant was discarded and the black solid was mixed with ultra-pure water (2 mL) and acetone (10 mL) and sonicated for 10 min. The resultant mixture was divided amongst several 1.5 mL conical centrifuge tubes and centrifuged at 13000 rpm for 2 min. The supernatant of each tube was discarded and the black solids were mixed with acetone (1 mL), vortexed, then centrifuged at 13000 rpm for 2 min. The acetone washing process was repeated five times. The black solid was then dried under vacuum for 60 min. The dried solid was placed in a ceramic boat, which was introduced into a quartz glass tube. The tube was heated in a horizontal solid tube furnace (Thermolyne F21135, Thermo Scientific) at 400 °C for 120 min under a 5% H_2/95% Ar atmosphere with a flow rate of 90 SCCM.

3.2.1.5 Synthesis of rGO-supported Pt NPs

The same procedure as above was utilized, except $SnCl_4$ was absent and the amount of $Pt(acac)_2$ was increased to maintain the same weight percent loading of metal on rGO (11.5 mg, 0.029 mmol Pt). All other steps were identical.

3.2.2 Characterization Methods

3.2.2.1 Raman Spectroscopy

Raman spectroscopy data were collected on a Horiba Yvon LabRam ARAMIS Raman microscope using a ~1 mW, 532 nm wavelength laser source. The rGO samples were pressed on a glass slide for analysis.

3.2.2.2 X-ray Photoelectron Spectroscopy

X-ray photoelectron spectroscopy (XPS) data were collected on a Kratos Axis 165 X-ray photoelectron spectrometer operating in the hybrid mode using Al monochromatic radiation (1486.6 eV) at 280 W. Charge neutralization was used to minimize sample charging. Binding energies were calibrated with respect to the C 1s peak at 284.8 eV. Casa XPS software was used for data analysis peak fitting; all peaks were fit after subtraction of a Shirley background. An *ad hoc* asymmetric peak shape (A(0.41,0.36,70)GL(50)) was used to fit the primary graphitic carbon peak for all the rGO samples. The $\pi \rightarrow \pi^*$ shake-up satellites were fitted to have a full width at half maximum (FWHM) value of 3.5 at maximum. All other peaks were fixed to have the same FWHM for each sample. Peak positions for C-N, C-O, C=O, COOH, and the $\pi \rightarrow \pi^*$ shake-up satellites were fixed relative to the graphitic peak with separations of 0.9, 1.7, 3.0, 4.3, 6.4 eV, respectively.

3.2.2.3 Powder X-ray Diffraction

Powder X-ray diffraction (XRD) patterns were obtained on a Bruker C2 Discover diffractometer equipped with a VÅNTEC-500 detector using a

monochromatic Cu Kα radiation source biased at 40 kV and 40 mA. The rGO-supported NP powders were pressed on a glass slide for analysis.

3.2.2.4 Transmission Electron Microscopy with Energy-Dispersive X-Ray Spectroscopy

Transmission electron microscope (TEM) images were obtained on a JEM 2100F Field Emission TEM operating at 200 kV. Energy-dispersive X-ray spectroscopy (EDS) data were collected on the same TEM operating in the scanning (STEM) mode. The rGO-supported NP powders were dispersed in THF, and an aliquot (6 μL) of the resulting dispersion was drop cast on the TEM grids. The TEM grids used were lacey carbon-coated Cu grids (Cu-400LC, Pacific Grid Tech).

3.2.3 Electrochemical Analysis

iPrOH (159.2 mL), ultra-pure water (40.0 mL) and Nafion® solution (0.80 mL, 5%) were mixed and stored as a stock solution. The catalyst ink was prepared by mixing the supported NP powder with the above stock solution such that the concentration was 1.0 mg/mL of powder in solution. The resultant mixture was then sonicated in a sonication bath (FS30H, Fisher Scientific) for 120 min. The catalyst ink (20 μL) was cast on a glassy carbon (GC) electrode (Pine Instruments, 5.0 mm diameter) using a micropipette and allowed to dry in air overnight while covered. Electrochemical studies were performed on a potentiostat (Autolab PGSTAT30) with a standard rotating electrode electrochemical cell. The rotating GC disk electrode with dried catalyst ink on its surface was used as the working electrode. Pt wire was used as the counter electrode and a saturated calomel electrode (SCE) was used as the reference

electrode. All potentials were recorded with respect to the SCE. H_2SO_4 in ultra-pure water (0.5 M) was used as the electrolyte. To obtain the CO stripping curves, the catalyst was saturated with CO by bubbling CO (99.5% pure, Al tank) in the electrolyte for 20 min with the electrode potential held at -0.2 V vs. SCE, followed by Ar-purging for 40 min. Two consecutive potential scans (20 mV/s) were then run to obtain the CO stripping and baseline curves. To obtain polarization curves for the electrooxidation of CO-contaminated H_2, the electrolyte was bubbled with a 1000ppm CO/balance H_2 gas mixture (99% pure, Al tank) for 60 min with the electrode potential held at -0.20 V vs. SCE, followed by a potential scan (1 mV/s) at a rotation rate of 1600 rpm.

3.3 Results

3.3.1 Characterization of Reduced Graphene Oxide (rGO) Supports

To fully evaluate the series of rGOs, we used two commercial rGOs, known as functionalized graphene sheets (FGS) by Vorbeck Materials and single layer graphene (SLG) by ACS Material. In addition, we prepared two synthetic rGOs by reducing a synthetic graphene oxide (GO) with either borohydride or hydrazine. The hydrazine reduction method is known to induce pyrazole-type N-doping at the edges of the resulting graphene sheets whereas borohydride reductions give "pure" graphene without B or N doping.[162,166,167,169] These materials are denoted as NGO (N-doped reduced graphene oxide) and BGO (borohydride-reduced graphene oxide), respectively.

XPS (Figure 3.1) and Raman microscopy studies (Figure 3.2) show that the four rGOs have different degrees of reduction (i.e. graphene-like character) and a range of functional groups. From these data, the degree of graphitic-like character was evaluated using three different criteria: 1) the concentration of functional groups and defects from XPS data, 2) the FWHM value of the graphitic carbon C 1s peak, and 3) the degree of structural disorder through a comparison of the D and G peak intensities obtained from the Raman spectra. The normalized C 1s XPS spectra of the rGOs are shown in Figure 3.1 and the data are summarized in Table 3.1. The comparative structural and spectroscopic data are summarized in Table 3.2.

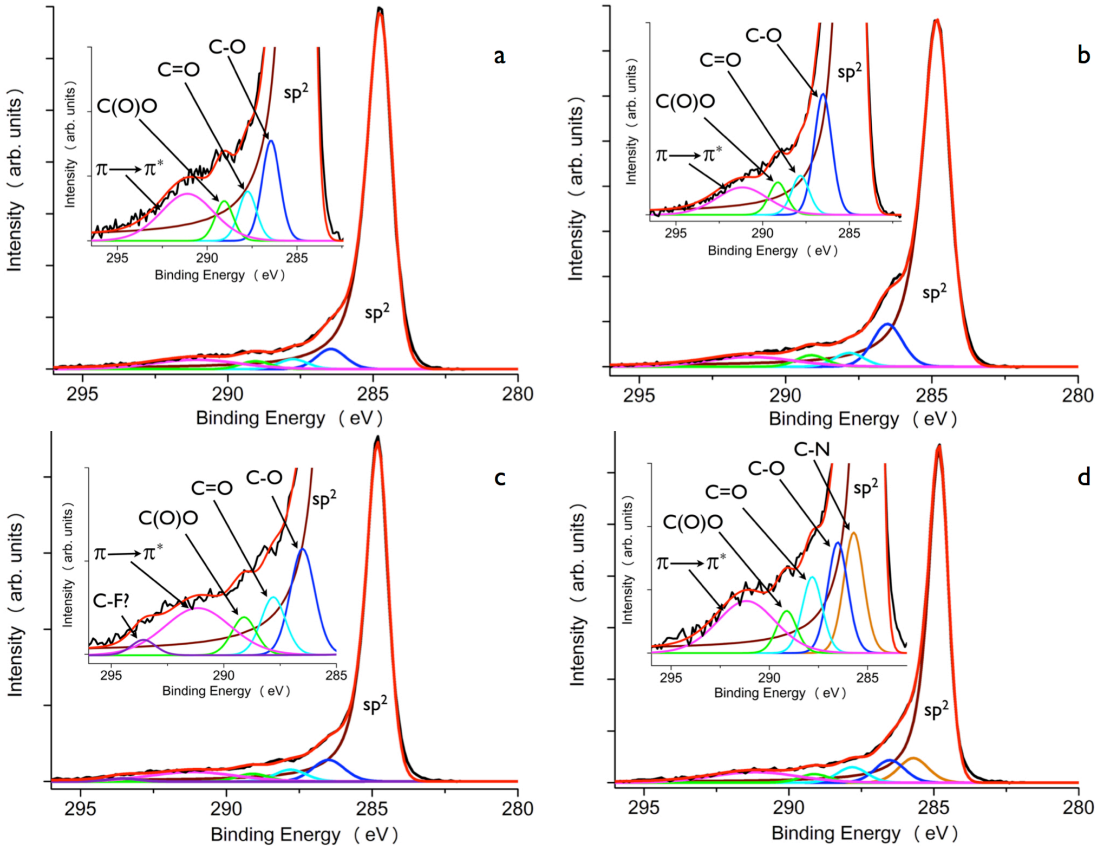

Figure 3.1. Carbon 1s XPS spectra of the (a) FGS, (b) SLG, (c) BGO, and (d) NGO materials. The raw data (black) was fitted (red) according to the following functional groups: graphitic carbon (brown), C-N (orange), C-O (blue), C=O (cyan), C(O)O (light green), π→π* shake-up satellite (magenta). An unknown peak (purple) seen in the BGO sample is believed to arise from a small fluoride impurity (C-F, 1.08%).

Table 3.1. C 1s XPS peak position and relative peak area percentage of various functional groups in the rGOs.

Sample	C-C/C=C	C-N	C-O	C=O	C(O)O	π→π*
FGS	284.8 eV (81.5%)	-	286.5 eV (5.6%)	287.8 eV (2.8%)	289.1 eV (2.2%)	291.1 eV (7.9%)
SLG	284.8 eV (75.5%)	-	286.5 eV (10.9%)	287.8 eV (3.5%)	289.1 eV (2.9%)	291.2 eV (7.2%)
BGO	284.8 eV (75.8%)	-	286.5 eV (7.4%)	287.8 eV (4.1%)	289.1 eV (2.7%)	291.2 eV (9.0%)
NGO	284.8 eV (67.1%)	285.7 eV (7.9%)	286.5 eV (7.3%)	287.8 eV (5.0%)	289.1 eV (2.8%)	291.2 eV (10.0%)

The FGS, BGO, and NGO XPS C 1s spectra are very similar, featuring the expected intense peaks at 284.8 eV associated with graphitic type carbon (Figure 3.1). While all of the rGOs have shoulders at higher binding energies due to various functional groups, the C-O peak for the SLG material is the most pronounced (Figure 3.1b). Previous studies[92,159,162,165,166,182] have shown that hydrazine and borohydride reduction methods leave some unreacted carboxyl and hydroxyl groups, which is consistent with the small C-O, C(O)O and C=O peaks observed in our studies. The NGO spectrum also has a C-N peak consistent with the incorporation of nitrogen into the graphene structure.[165,167,183] The relative concentration of functional groups can be assessed by calculating the area ratio (C_g/C_f) of graphitic-type carbon, including π→π* shake-up satellites (C_g) to total carbon associated with the functional groups (C_f). Excluding NGO, these data suggest that SLG is the most oxygenated, containing a large concentration of C-O moieties. FGS contains the fewest oxygen functionalities, with BGO intermediate between the two. After heat-treatment in H_2 atmosphere, there is a slight decrease in the C-O peaks for the SLG and BGO samples

(Figure 3.S1). Accordingly, the C_g/C_f value for each rGO sample increases (less functional groups) with the exception of FGS (Table 3.S1). Both observations are most likely due to a reduction of some hydroxyl groups during the H_2 atmosphere heat-treatment step.[161]

In addition to the oxygen-containing functional groups described above, NGO also contains 3.1% nitrogen resulting in 7.9% carbon-based C-N functional groups (Table 3.1). The N 1s spectrum of the NGO (Figure 3.S3) shows three types of nitrogen-containing species. The two major components at 399.3 eV and 400.8 eV are consistent with a pyrazole-like moiety whereas the minor peak at 402.7 eV is attributed to a quaternary-like nitrogen.[167,184] Similar results were obtained from analysis of the heat-treated NGO sample (Figure 3.S4). These analyses (along with those below) suggest that the majority of nitrogen is conjugated within the delocalized *p*-system of the graphene structure and remains in this state after high-temperature heat-treatment.

The conductivity of the rGOs can be correlated with the FWHMs of their respective graphitic carbon peak. Previous studies[185,186] have shown that a smaller FWHM value is associated with an increased degree of delocalization within the rGO. Our data (Table 3.2) suggest that the NGO is most conductive material (most graphene-like character), followed by the BGO, FGS, and SLG samples. This trend is essentially maintained after heat-treatment, except FGS appears to have slightly more graphene-like character than BGO after conditioning (Table 3.S2).

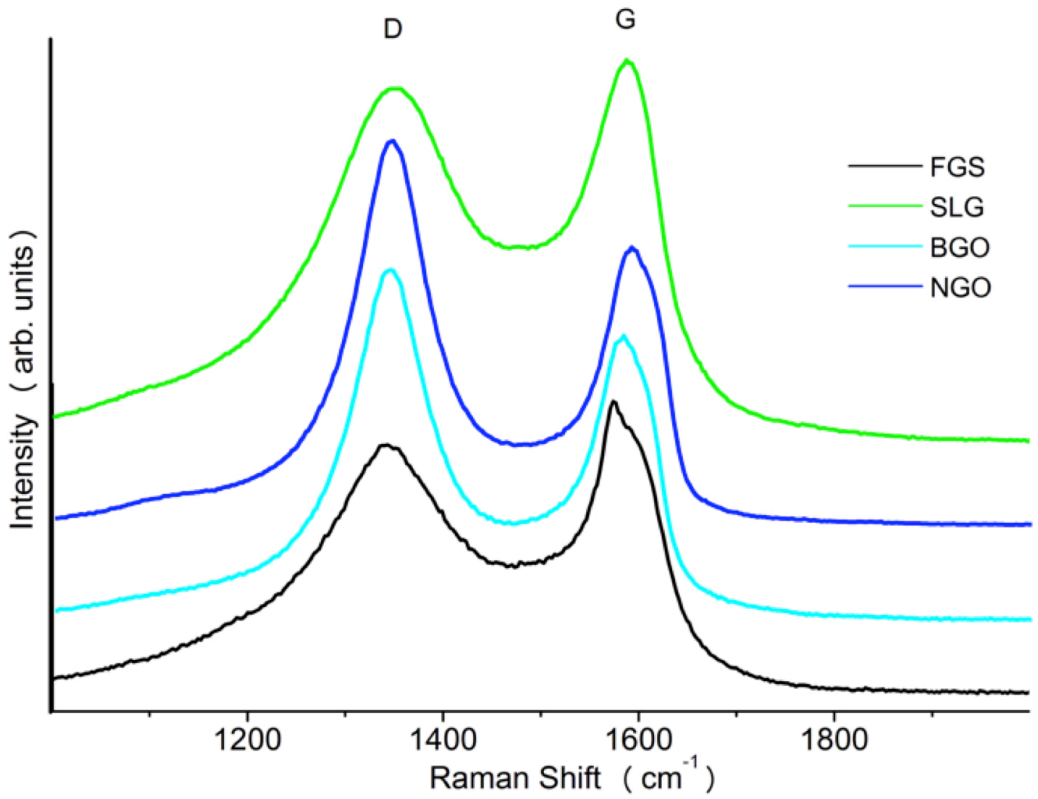

Figure 3.2. Raman spectra of the different rGO materials.

Raman spectroscopy provides a measure of structural disorder in graphene-based materials through a comparison of the graphite-like peak (G peak) to the disorder peak (D peak).[162,165,166,187] The disorder arises from intrinsic functional groups (ethers, epoxides, ketones), as well as atomic vacancies and defects, which affect the interactions with supported nanoparticle catalysts. Figure 3.2 shows the Raman spectra of the rGOs, with the expected prominent D and G bands. The D/G ratios are listed in Table 3.2. Because the peak widths varied among the different rGOs, we calculated the D/G ratios by comparing the areas of the respective peaks and not the peak amplitudes. The rGOs examined here all have D/G ratios significantly greater than 1, which is similar to other graphene-like materials prepared from the reduction

of GO.[166,175,183,188,189] These ratios suggest that BGO is the least defective material, followed by FGS and NGO with identical values whereas SLG has the highest defect concentration. After heat-treatment, all of the rGO samples have smaller D/G ratios, which are all very close to a value of 1 (Table 3.S2). This suggests the H_2 atmosphere heat-treatment induces some slight reduction of functional groups within the different rGO materials, in agreement with the XPS analysis as seen elsewhere.[190]

Table 3.2. Summary of evaluation criteria for the different rGOs

Sample	FWHM[a]	C_g/C_f[b]	D/G[c]
FGS	0.97	8.4	1.6
SLG	1.04	4.8	2.3
BGO	0.85	5.6	1.4
NGO	0.77	5.4	1.6

[a] C 1s XPS graphitic carbon peak FWHM (Figure 3.1) [b] Graphitic carbon and $\pi \rightarrow \pi^*$ shake-up satellites (C_g) and functionalized carbon (C_f) peak area percentages were used to determine C_g/C_f ratios (Table 3.1). [c] D/G ratios determined from integrating the D and G Raman peaks (Figure 3.2).

From these combined analyses (Table 3.2), we summarize the general characteristics of the rGOs as follows: 1) NGO is the most conductive rGO in our series and has few oxygen functional groups; the pyrazole-like nitrogen is presumably localized on the sheet edges[167] and does not appear to impart localizing defects into the structure; 2) FGS is equal to NGO in the level of disorder (D/G ratio) but FGS is less conductive and has the smallest number of oxygen-containing functional groups. The defects are presumably due to atomic vacancies associated with the FGS synthetic method;[93,117] 3) BGO has a greater amount of oxygen functionalities than

FGS, but is more conductive. This ordering is reversed after heat-treatment; 4) SLG is the most defective rGO, with a high concentration of oxygen-containing functional groups and disorder and the lowest conductivity in the series. Overall, BGO is the most graphene-like in character (low FWHM, low D/G ratio, low functional group concentration), whereas NGO is the most conductive (lowest FWHM, low D/G ratio).

3.3.2 Synthesis and Characterization of rGO-Supported Nanoparticles

We prepared surfactant-free Pt and PtSn intermetallic ($P6_3/mmc$) NPs on the rGOs to evaluate the influence of the metal-support interactions. The rGO-supported PtSn intermetallic NPs were synthesized through modifications of our previous methods.[82] Specifically, $Pt(acac)_2$ and $SnCl_4$ were co-reduced in 1-octadecene using $NaBEt_3H$ in the presence of rGO at 200 °C. To transform the disordered PtSn alloy into its ordered intermetallic phase, the supported particles were heat-treated for 120 min at 400 °C under flowing H_2/Ar. While this procedure yielded the target PtSn intermetallic NPs, it also caused varying degrees of particle sintering. Many NPs remained in the sub-10 nm range (Figure 3.3, Table 3.3); however, agglomerates and aggregates of small particles make up a significant portion of the material (Figure 3.S5, Table 3.3). The synthetic procedure was optimized to keep particles as small as possible yet ensure complete transformation to the ordered PtSn intermetallic. High-resolution images of the single particles reveal their intermetallic structure, with lattice fringe analysis showing average lattice separations of 0.21 nm and 0.30 nm, corresponding to the (102) and (101) planes, respectively, of the hexagonal ($P6_3/mmc$) PtSn intermetallic lattice (insets in Figure 3.3). Figure 3.4 shows the XRD patterns of the heat-treated particles, featuring intense diffraction peaks unique to the

hexagonal ($P6_3/mmc$) PtSn intermetallic. EDS analysis of the PtSn intermetallic NPs shows they have an average 1:1 (Pt:Sn) composition, comparable to that of the initial precursor ratio (Figure 3.S6).

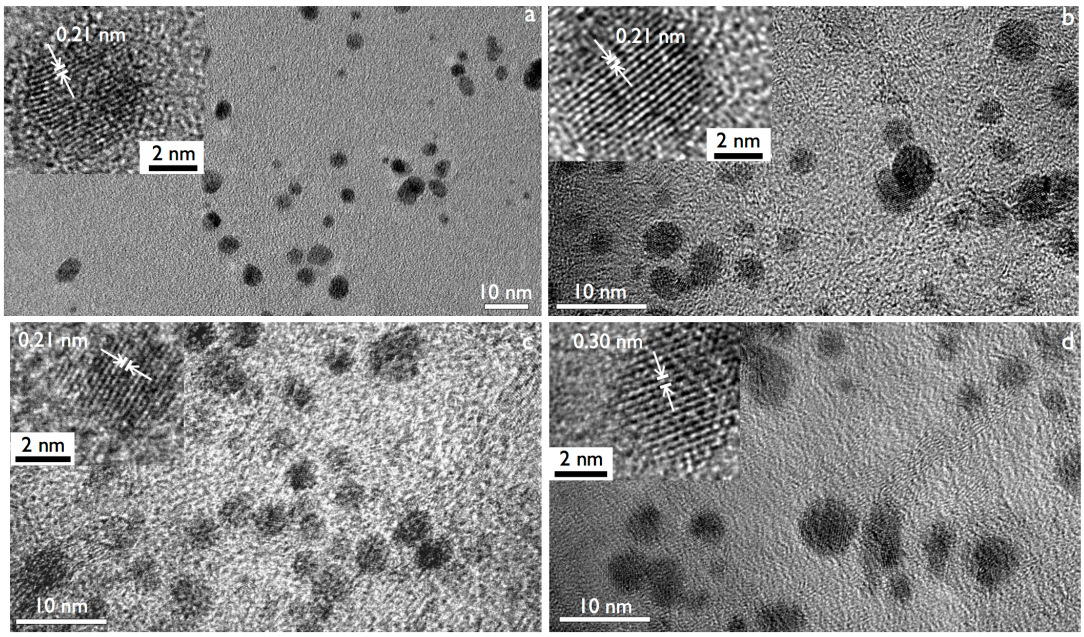

Figure 3.3. TEM images of the heat-treated PtSn intermetallic NPs supported on (a) FGS, (b) SLG, (c) BGO, and (d) NGO. Lattice fringe images of single particles are inset.

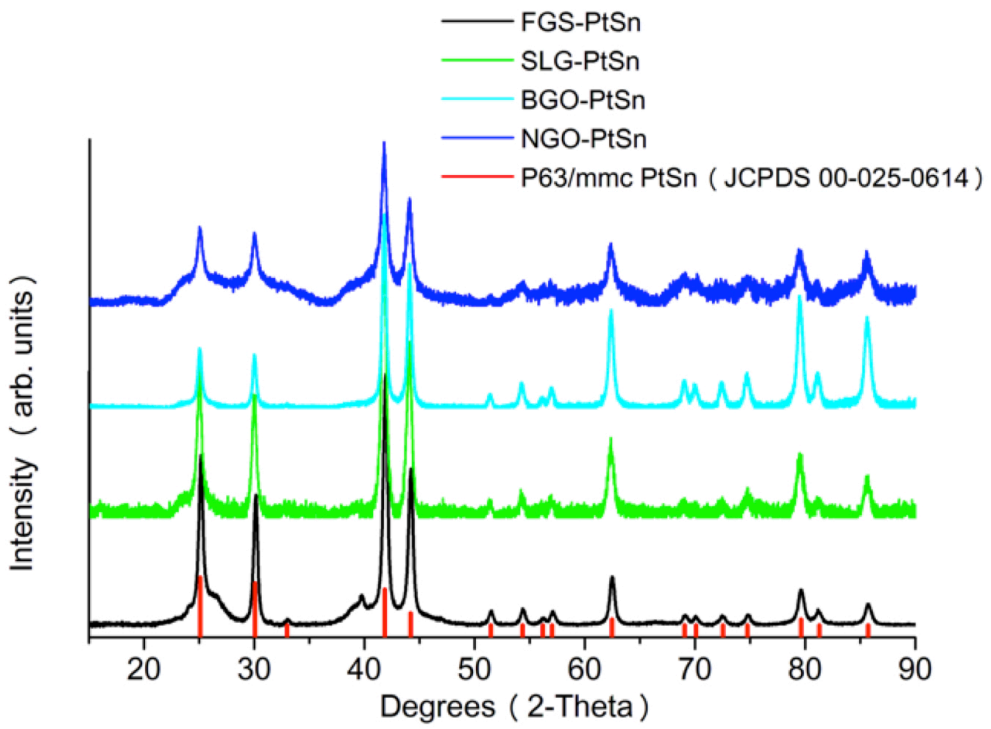

Figure 3.4. XRD patterns of the heat-treated rGO-PtSn intermetallic NPs. Red lines indicate the peak positions for hexagonal ($P6_3/mmc$) PtSn intermetallic (JCPDS 00-025-0614). The small peak at 40° in the FGS-PtSn sample is due to a small Pt_3Sn impurity. The broad low angle peaks (20-35°) are due to the rGOs.

The rGO-supported Pt electrocatalysts were synthesized using the same method as the PtSn NPs, except for the absence of the Sn precursor. These particles were also subjected to the same heat-treatment (400 °C for 120 min under flowing H_2/Ar), with similar particle aggregations. For the SLG, BGO, and NGO supports, significant quantities of sub-10 nm particles are present (Figure 3.5, Table 3.3), but as with the PtSn NPs, significant particle aggregation occurs (Figure 3.S7b-d, Table 3.3). In contrast, particle sintering is minimal in the FGS-Pt sample, which has a

relatively narrow size distribution centered on an average diameter of 2.8 nm (Figure 3.S7a, Table 3.3). Lattice fringe analysis from high-resolution images of the single particles shows average lattice separations of 0.22 nm, corresponding to the (111) planes of FCC Pt (insets in Figure 3.5). The XRD patterns of the heat-treated particles are presented in Figure 3.6, with diffraction peaks matching those of FCC Pt. The XRD pattern of the FGS-Pt sample has broader peaks relative to the other samples, in agreement with the TEM analysis suggesting minimal particle sintering from heat-treatment.

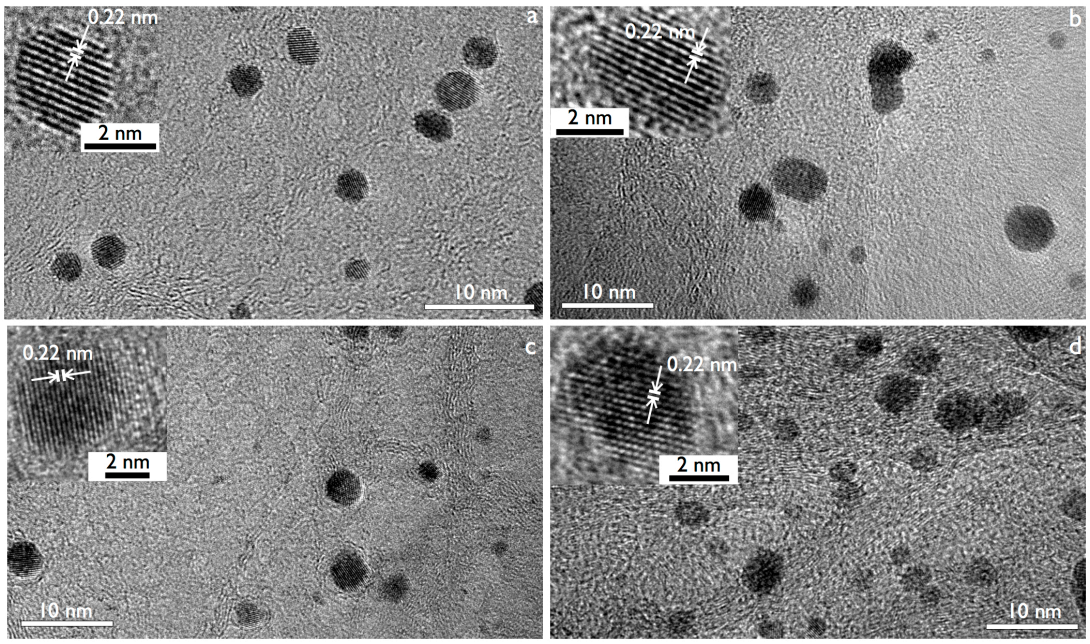

Figure 3.5. TEM images of the heat-treated Pt NPs supported on (a) FGS, (b) SLG, (c) BGO, and (d) NGO. Lattice fringe images of single particles are inset.

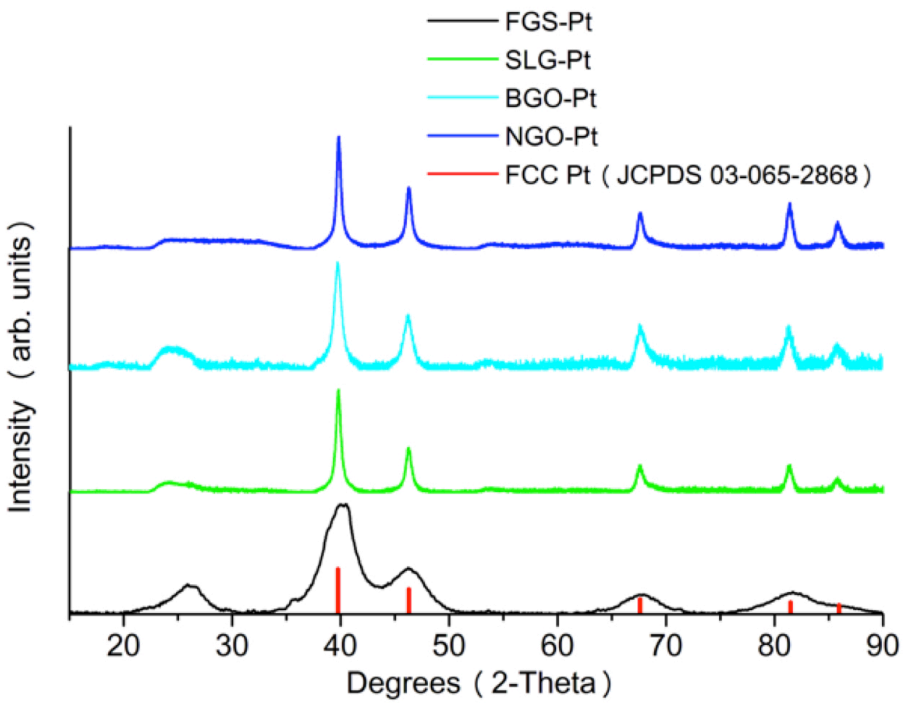

Figure 3.6. XRD patterns of the heat-treated rGO-Pt NPs. Red lines indicate the peak positions for FCC phase Pt (JCPDS 03-065-2868). Broad peaks (20-35°, 52-56°) are due to the rGOs.

3.3.3 Electrochemical Analysis of rGO-Supported Nanoparticles

The electrocatalytic activities of the rGO-supported Pt and PtSn NPs were evaluated by CO stripping cyclic voltammetry (CV) and rotating disk electrochemical (RDE) experiments to probe the metal-support influences on catalytic CO/H_2 electrooxidation. We compared Pt and PtSn catalysts because they are both well known H_2 electrooxidation catalysts and their respective abilities to mitigate CO poisoning effects are well understood.[31,35,82,191-195] By using the same catalysts on different rGO supports, the relative shifts in H_2 oxidation onset with a well-defined CO impurity can be used as a measure of catalytic modification. The results are

benchmarked against the commercial E-TEK Pt catalyst. All catalysts were prepared with a 30% total metal loading by weight based on the initial amounts of reagents. Prior to the electrochemical experiments, each catalyst was subjected to 10 potential scan cycles between -0.2 V and 0.8 V (vs. SCE) in 0.5 M H_2SO_4 saturated with Ar (99.9% pure). Additional details are found in the experimental section.

The CO stripping curves for each of the supported Pt catalysts show the characteristic CO oxidation peak near 0.5 V vs. SCE (Figure 3.7).[25] However, the onset potentials for CO oxidation vary from 0.46 V (SLG-Pt) to 0.53 V for FGS-Pt and E-TEK Pt standard. The BGO-Pt and NGO-Pt catalysts are intermediate. Figure 3.8 shows the RDE polarization curves for the electrooxidation of CO/H_2 mixtures (1000 ppm CO) on the Pt catalysts. The SLG-Pt and BGO-Pt show a 50 mV improvement in onset potentials relative to E-TEK Pt, whereas NGO-Pt and FGS-Pt are somewhat less CO-tolerant than E-TEK Pt. In general, the rGO-Pt catalysts show the expected correlation between CO stripping onset and CO/H_2 electrooxidation onset where lower CO oxidation overpotentials give improved CO tolerance.

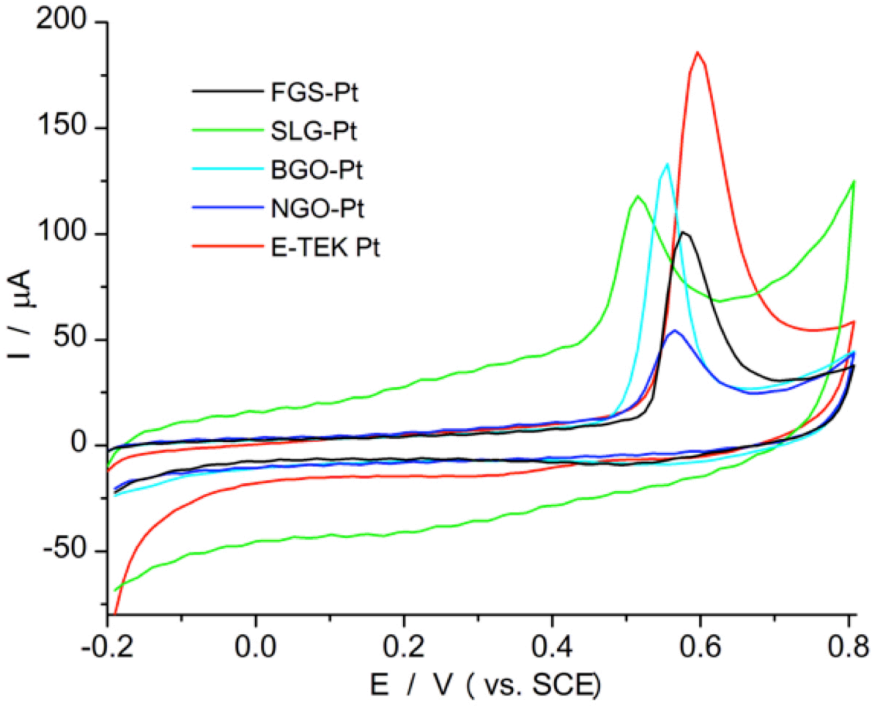

Figure 3.7. CO stripping curves of the rGO-Pt NP catalysts in 0.5 M H_2SO_4 solution at 25 °C. Red line indicates E-TEK Pt catalyst as reference. Scan rate: 20 mV/s.

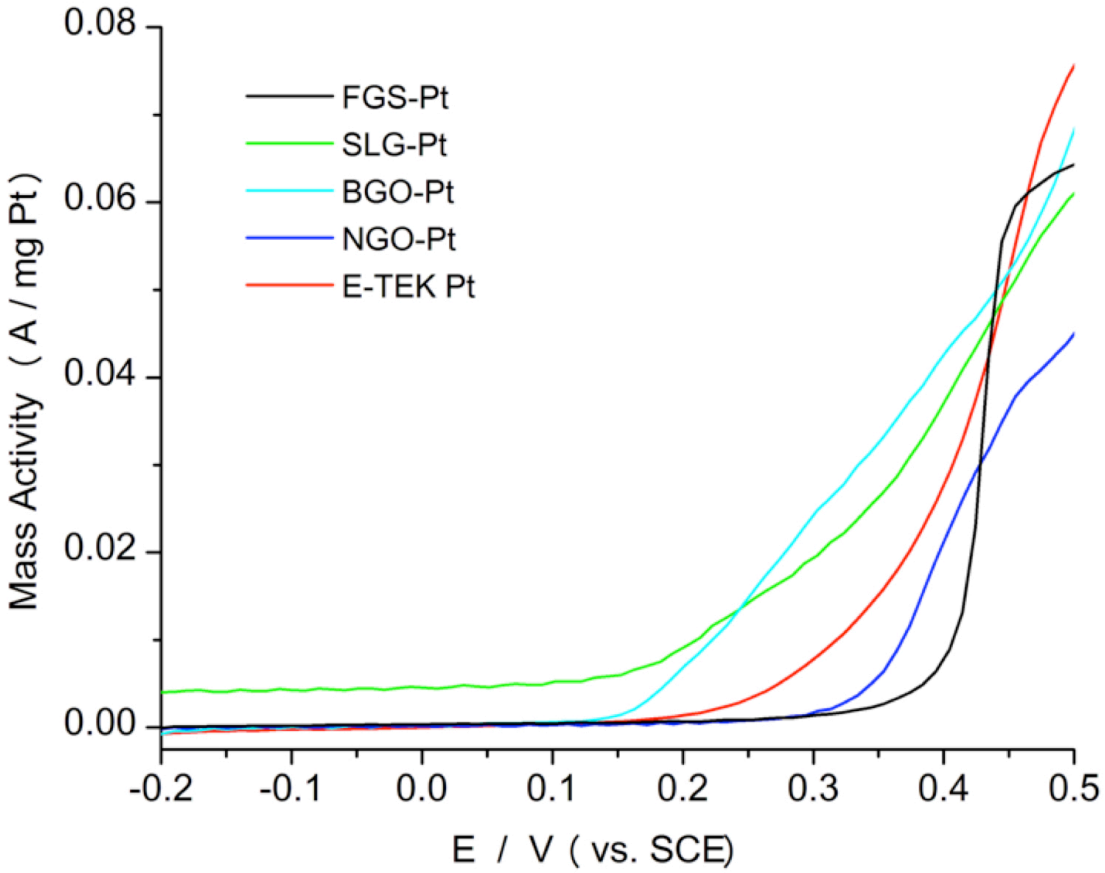

Figure 3.8. Polarization curves for the electrooxidation of CO-contaminated H_2 (1000 ppm CO, balance H_2) of the rGO-Pt NP catalysts in 0.5 M H_2SO_4 solution. Red line indicates E-TEK Pt catalyst as reference. Curves were recorded at 25 °C with 1 mV/s scan rates and 1600 rpm rotation rates.

Since CO has a low affinity for binding to the PtSn surface, their CO stripping curves are typically broad and of low intensity compared to their Pt counterparts (Figure 3.9).[191,192,196,197] The solid lines represent the CO stripping curves while the dashed lines are the baselines recorded after the CO stripping experiments. For the FGS-PtSn sample (Figure 3.9), two distinct peaks are observed at 0.35 V and 0.57 V, from CO oxidation and the oxidation of surface Sn, respectively.[82,194] Small Sn

oxidation peaks are present in the BGO-PtSn and NGO-PtSn samples as well. Despite the ill-defined peak shapes, the onset potentials for CO oxidation can be discerned and varies from 0.08 V (NGO-PtSn) to 0.2 V (FGS-PtSn), with SLG-PtSn and BGO-PtSn intermediate.

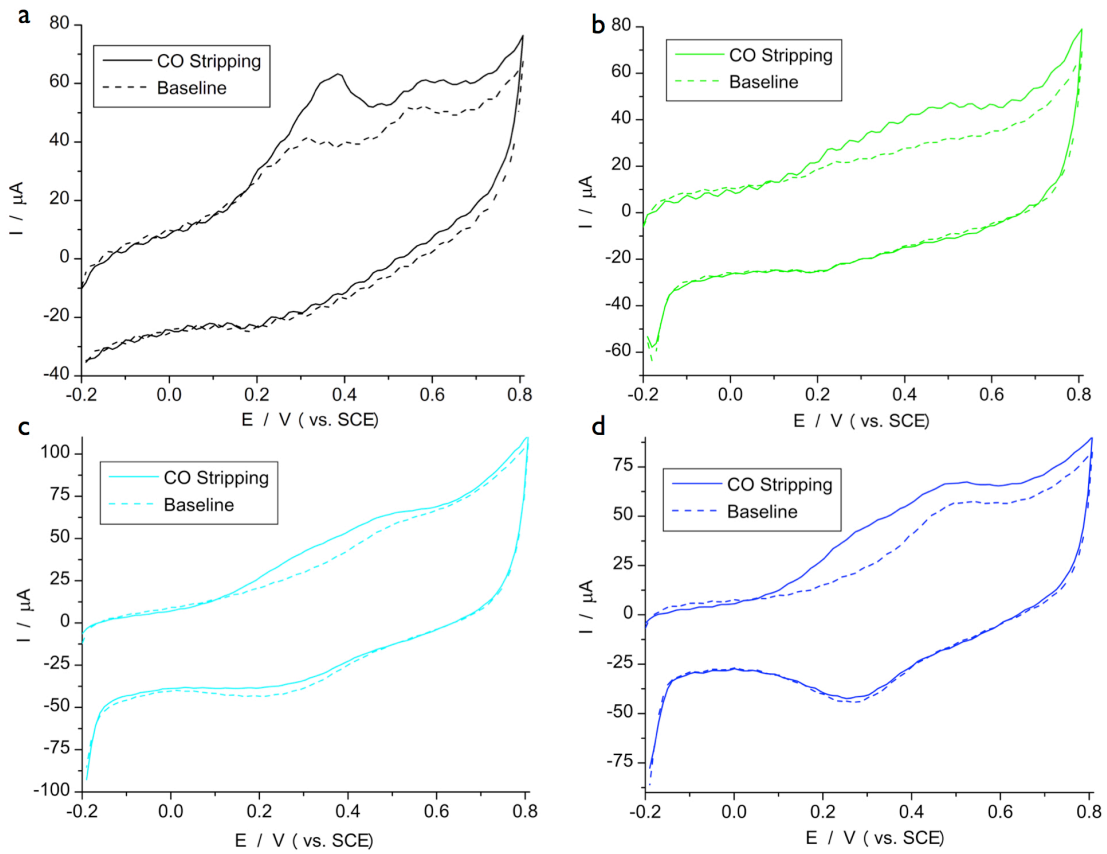

Figure 3.9. CO stripping curves of the (a) FGS, (b) SLG, (c) BGO, and (d) NGO supported PtSn intermetallic NP catalysts in 0.5 M H_2SO_4 solution at 25 °C. Scan rate: 20 mV/s. The dotted curves are the CVs recorded after CO stripping.

Figure 3.10 shows the polarization curves for the electrooxidation of CO/H_2 mixtures (1000 ppm CO) on the PtSn catalysts with the E-TEK Pt reference. The rGO-PtSn polarization onset potentials span 160 mV and are generally 200-400 mV lower than their rGO-Pt counterparts. The improvement in CO tolerance of the PtSn

catalysts compared to the Pt systems is due to the "bifunctional mechanism" of CO oxidation and is consistent with previous studies.[25,28,82,198] The trends within the rGO-PtSn catalysts also follow those of the rGO-Pt samples (SLG > BGO > FGS) with the exception of the NGO-PtSn sample, where the CO tolerance is significantly increased compared to its Pt counterpart. The NGO-PtSn catalyst has the best performance of all the rGO-Pt or rGO-PtSn catalysts and surpasses the CO tolerance of the PtSn intermetallics supported on carbon black.[82] This improved CO tolerance is consistent with the CO stripping results, where NGO-PtSn also had the lowest onset potential for CO oxidation.

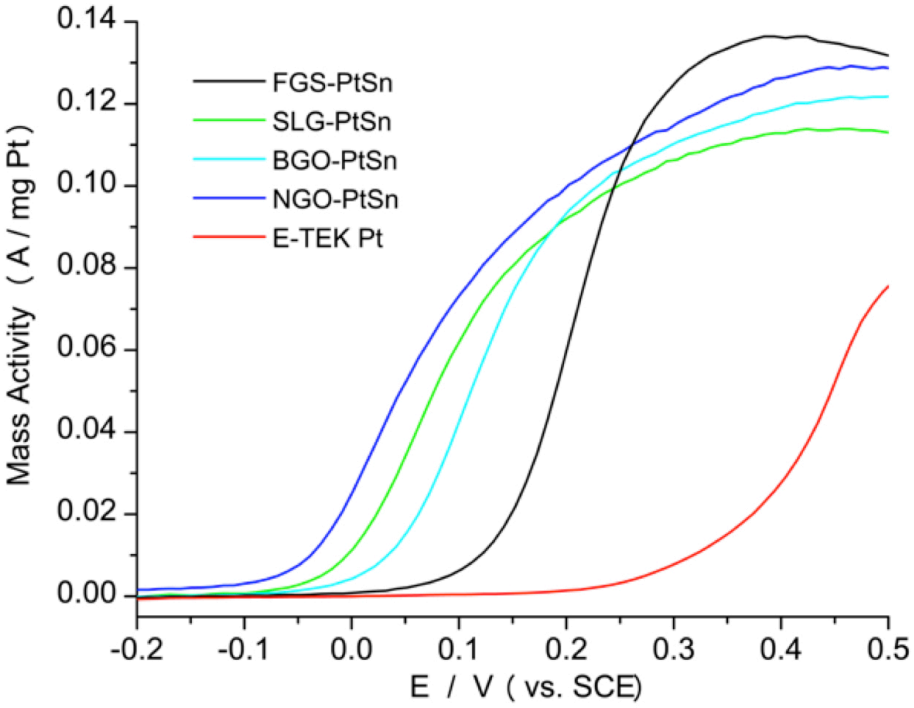

Figure 3.10. Polarization curves for the electrooxidation of CO-contaminated H_2 (1000 ppm CO, balance H_2) of the rGO-PtSn intermetallic NP catalysts in 0.5 M H_2SO_4 solution. Red line indicates E-TEK Pt catalyst as reference. Curves were recorded at 25 °C with 1 mV/s scan rates and 1600 rpm rotation rates.

3.4 Discussion

The synthetic, spectroscopic and electrochemical studies described above show that rGOs that are presumably quite similar in composition show a range of nanoparticle templating properties and can electronically influence electrocatalytic activity. These properties are summarized in Table 3.3. Two major tends emerge from the data.

Table 3.3. Summary of representative experimental data for NP catalysts.

Sample	Avg. NP Size[a] (nm)	CO Stripping E_{Onset}[b]	CO Stripping E_{Peak}[b]	H_2/CO Oxidation E_{Onset}[b]	H_2/CO Oxidation ΔE_{Onset} (E_{PtSn}-E_{Pt})
E-TEK Pt	N/A	0.53	0.59	0.20	-
FGS-Pt	2.8 ± 0.8	0.53	0.58	0.35	-0.27
FGS-PtSn	5.2 ± 3.9	0.20	*	0.08	
SLG-Pt	4.0 ± 2.0	0.46	0.52	0.15	-0.2
SLG-PtSn	4.4 ± 2.2	0.13	*	-0.05	
BGO-Pt	4.6 ± 2.6	0.49	0.56	0.15	-0.18
BGO-PtSn	4.2 ± 1.8	0.15	*	-0.03	
NGO-Pt	5.4 ± 3.0	0.52	0.57	0.33	-0.41
NGO-PtSn	5.6 ± 3.9	0.08	*	-0.08	

[a] Calculated by counting 100 small particles and agglomerates in Figures 3.S5 and 3.S7. [b] Potential vs. SCE. * Not determinable from experimental data.

First, the FGS support gives smaller Pt NPs with less agglomeration and sintering after annealing relative to the other rGO supports tested. This finding is consistent with the high level of defects found in FGS that presumably anchor the Pt seeds and NPs more tightly relative to the other rGO materials. Because we do not employ surfactants or dispersants, there is always some degree of agglomeration after sintering, but the FGS minimizes this sintering to a large degree. The templating effect of FGS extends to other monometallic NPs,[94] but is not apparent in the bimetallic PtSn system. The four rGO supports give similar PtSn particle sizes with no statistical differences in diameter or agglomeration.

Second, there is an apparent catalytic enhancement of the NGO-supported PtSn system relative to the other PtSn electrocatalysts. Previous studies have shown that PtSn electrocatalysts show a *ca.* 200 mV improvement in CO tolerance (ΔE_{onset}) relative to Pt catalysts of the same size on the same supports.[82] The SLG and BGO

systems fall into this category (Table 3.3) showing 200 mV and 180 mV enhancements, respectively. The FGS catalysts show a somewhat larger ΔE_{onset} of 270 mV, but the larger shift most likely resides in the enhanced CO poisoning of the small Pt NPs[199] formed on the FGS support and large particle size differences between the Pt and PtSn particles. Somewhat surprisingly, there is a large 410 mV shift in ΔE_{onset} for the NGO Pt/PtSn system, despite the similarities in particle sizes of the Pt and PtSn NPs on this rGO support. In addition the NGO-supported PtSn NPs have sizes and agglomerates that are similar to the FGS-supported PtSn NPs, but have a 180 mV enhancement in CO tolerance. The possible origins of this enhancement are discussed below.

Previous theoretical studies have suggested that CO binds less tightly to Pt NPs supported on defective graphene (heteroatom inclusions, vacancies and disorder) relative to "pristine" graphene due to a downward shift in *d*-band center, resulting in increased CO tolerance.[157,158] In particular, theoretical studies by Kim and Jhi suggest that doping of graphene with nitrogen weakens the Pt-CO bond on NGO-Pt NPs and improves their CO tolerance relative to un-doped graphene.[157] In contrast to these theoretical predictions, our work shows that the NGO-Pt catalyst has much lower CO tolerance compared to the nitrogen-free SLG and BGO analogues. However, the theoretical model employed by Kim and Jhi[157] analyzed the effects of pyridine-like nitrogen within the graphene structure, which does not appear to match the structure of the NGO used in our experiments. In a recent study, Park *et al.* showed that hydrazine reduction of GO results in the incorporation of pyrazole-like moieties into the graphene structure, which are primarily located on the edges of the graphene

sheets.[167] Our analysis of NGO here is in agreement with their results. Other reports have suggested that the electronic effects of nitrogen incorporation may differ depending on the type of nitrogen substitution *and* the location of this substitution within the graphene structure.[157,167,200-204]

For PtSn intermetallic NPs, the nitrogen incorporation into the rGO support appears to lead to significant improvement in CO tolerance. It appears that the nitrogen or other defects in the NGO support have a substantially different interaction with the PtSn NPs relative to the pure Pt NPs. For example, it is possible that the surface Sn atoms form strong interactions with the NGO defect sites that drain electron density from the PtSn particle relative to the other rGOs. Such electron transfer would reduce Pt-CO bonding and increase CO tolerance. In our earlier work involving PtSn@Pt core-shell NPs, the PtSn intermetallic core modified the electronic structure of the Pt shell by shifting the *d*-band center, which promoted an improvement in CO tolerance.[82] The metal-support interactions in the present system may promote similar electronic modifications.

It is also possible that the anomalous activity enhancement for the NGO-PtSn system is a result of a spillover effect from the nitrogen, which can be viewed as an enhancement of the bifunctional mechanism of CO oxidation. The bifunctional mechanism proceeds via favorable OH binding to Sn surface atoms, which results in enhanced CO oxidation and improved CO tolerance.[26-28,31] A process that involves OH spillover from the NGO support onto the PtSn catalyst could enhance the bifunctional oxidation process. However, the lack of a similar enhancement in the corresponding NGO-Pt system suggests that OH spillover from the NGO support not likely. Rather,

the enhancement is most likely a unique metal-support interaction between the PtSn intermetallic and the NGO support.

Our results here and in earlier experiments show that the CO tolerance enhancement for the PtSn intermetallic over pure Pt is consistently 180-270 mV lower when supported on nitrogen-free carbonaceous supports (CB, SLG, BGO, FGS).[82] Thus it appears that a unique 410 mV enhancement of the CO tolerance observed for NGO-PtSn relative to NGO-Pt results from a combination of electronic modifications due to PtSn intermetallic formation and the NGO-PtSn metal-support interaction. The origin of the enhancement may result from weakened Sn-OH bonding due to the increased electronic donation from the nitrogen dopants in NGO.[172,173,175,205] Such an increase could enhance CO tolerance by way of the bifunctional mechanism. In the pure Pt systems, however, increased donation from the NGO would only strengthen Pt-CO bonding and decrease CO tolerance. These opposing effects on the Pt vs. PtSn systems are consistent with the anomalous ΔE_{onset} in the NGO system (Table 3.3).

3.5 Conclusion

In summary, we have developed a simple method for the production of both Pt and PtSn intermetallic NPs supported on various rGO materials without the use of additional surfactants or dispersants. Through RDE and CO stripping electrochemical experiments, we have shown that the rGO-PtSn catalyst is superior to the rGO-Pt catalyst regardless of the rGO material, in agreement with earlier reports on PtSn NP electrocatalysts. Our results also suggest that the catalytic activity is modulated by the rGO-catalyst support for the nitrogen-doped NGO. It appears that while BGO and

SLG have different levels of functional group incorporation (C_g/C_f) and structural disorder (D/G), they show very similar metal-support interactions and catalytic performances for both the Pt and PtSn intermetallic systems. FGS appears to impart the strongest metal-support interactions, as evidenced by the lowest level of catalyst sintering of all rGOs tested. The NGO support is the most unusual since it seems to shift the CO tolerance in both directions depending on the electrocatalytic mechanism. For the NGO-PtSn system, CO tolerance may be enhanced through weakened Sn-OH bonding whereas CO tolerance from the NGO-Pt system would be reduced due to stronger Pt-CO bonding, both phenomena arising from electronic structure modifications to the NPs induced by the nitrogen-dopants in NGO. Further studies into the nature of these metal-support interactions are ongoing.

3.6 Supplemental Information

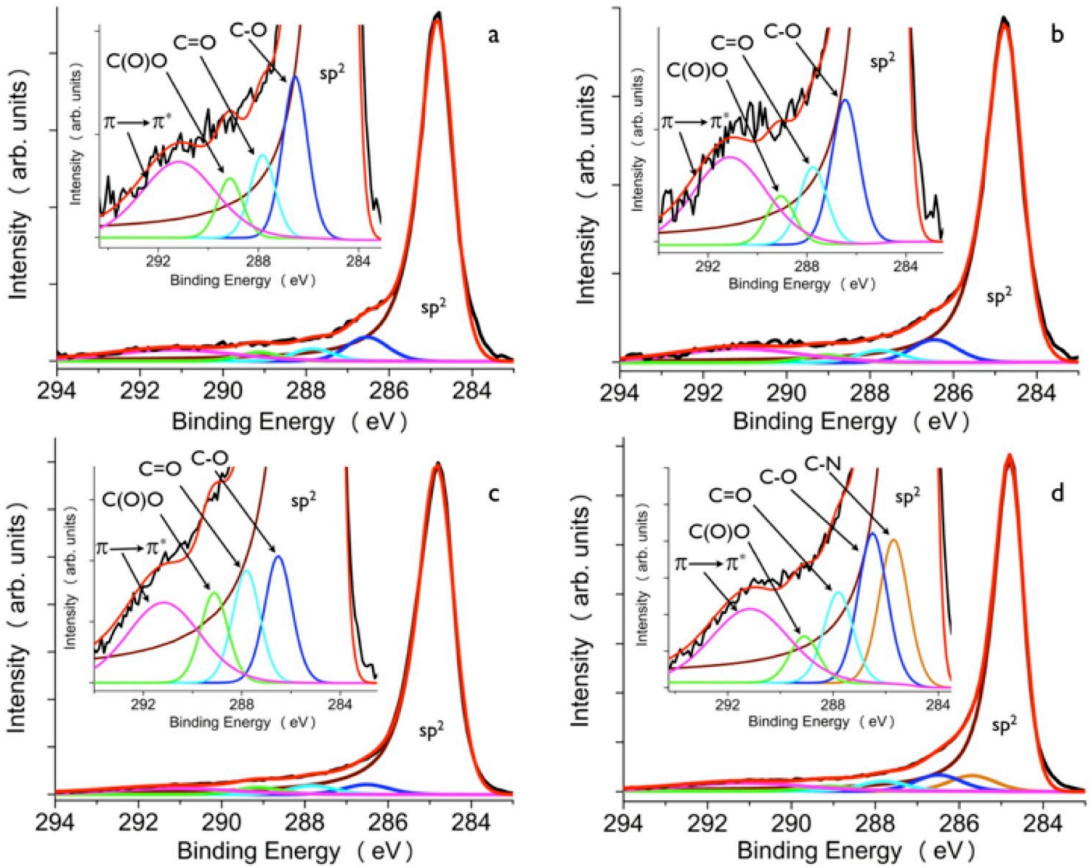

Figure 3.S1. Carbon 1s XPS spectra of the heat-treated (a) FGS, (b) SLG, (c) BGO, and (d) NGO materials. The raw data (black) was fitted (red) according to the following functional groups: graphitic carbon (brown), C-N (orange), C-O (blue), C=O (cyan), C(O)O (light green), π→π* shake-up satellite (magenta).

Table 3.S1. C 1s XPS peak position and relative peak area percentage of various functional groups in the heat-treated rGOs.

Sample	C-C/C=C	C-N	C-O	C=O	C(O)O	π→π*
FGS	284.8 eV (76.5%)	-	286.5 eV (7.2%)	287.8 eV (3.7%)	289.1 eV (2.6%)	291.2 eV (10.0%)
SLG	284.8 eV (75.2%)	-	286.5 eV (7.1%)	287.8 eV (3.8%)	289.1 eV (2.4%)	291.1 eV (11.5%)
BGO	284.8 eV (84.8%)	-	286.5 eV (3.5%)	287.8 eV (3.1%)	289.1 eV (2.5%)	291.2 eV (6.0%)
NGO	284.8 eV (74.2%)	285.7 eV (5.9%)	286.5 eV (6.2%)	287.8 eV (3.7%)	289.1 eV (1.9%)	291.1 eV (8.1%)

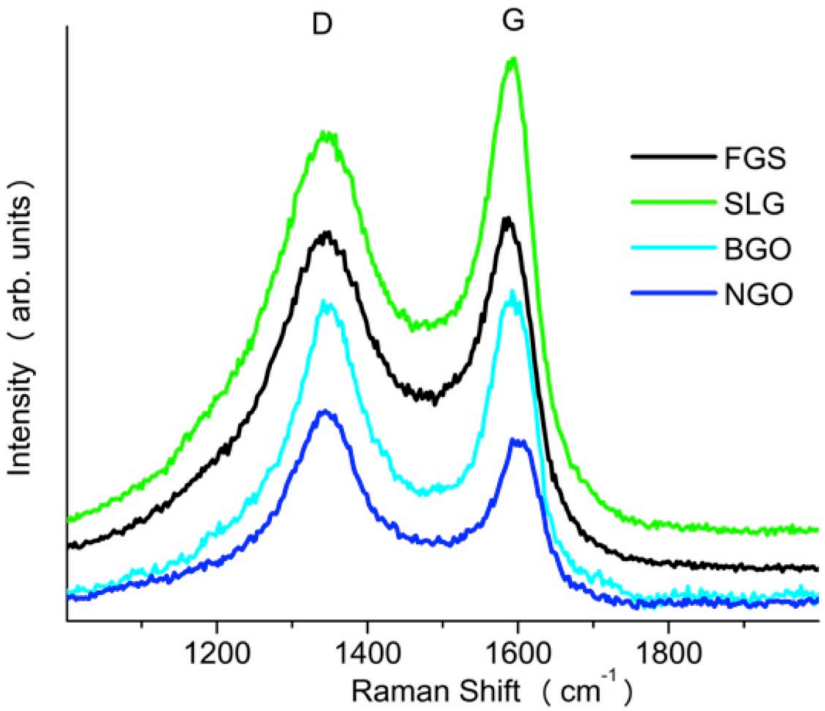

Figure 3.S2. Raman spectra of the different rGO materials after heat-treatment.

Table 3.S2. Summary of evaluation criteria for the different rGOs after heat-treatment.

Sample	FWHM[a]	C_g/C_f[b]	D/G[c]
FGS	0.90	6.4	1.0
SLG	0.96	6.5	0.9
BGO	0.95	9.9	1.0
NGO	0.78	7.5	1.2

[a] C 1s XPS graphitic carbon peak FWHM (Figure 3.S1) [b] Graphitic carbon and $\pi \rightarrow \pi^*$ shake-up satellites (C_g) and functionalized carbon (C_f) peak area percentages were used to determine C_g/C_f ratios (Table 3.S1). [c] D/G ratios determined from integrating the D and G Raman peaks (Figure 3.S2).

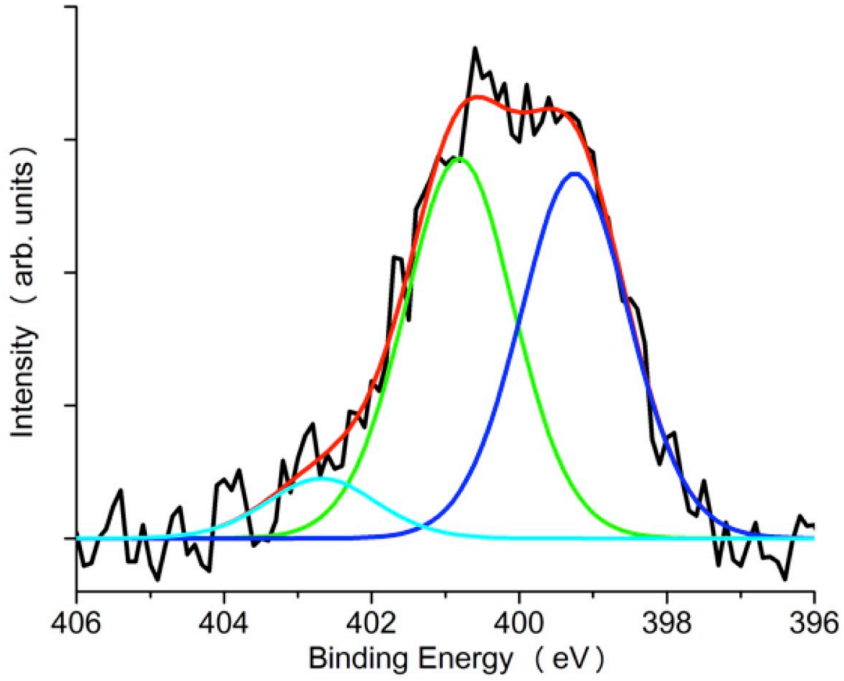

Figure 3.S3. Nitrogen 1s XPS spectrum of NGO. The raw data (black) was fitted (red) accordingly: the two major components, centered at 399.3 eV (blue) and 400.8 eV (green) are consistent with a pyrazole-like moiety, whereas the minor peak at 402.7 eV (cyan) is attributed to quaternary-like nitrogen.

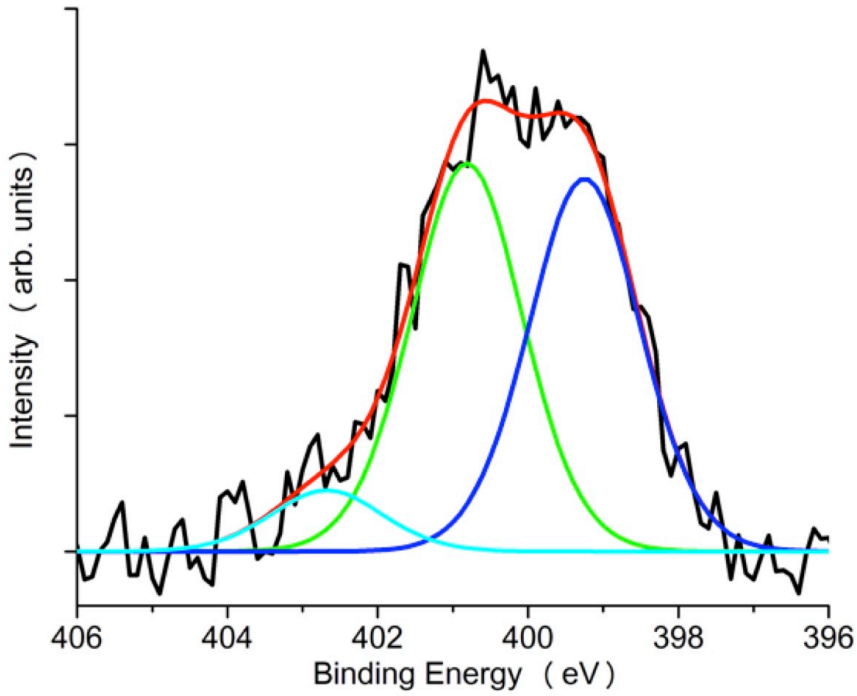

Figure 3.S4. Nitrogen 1s XPS spectrum of heat-treated NGO. The raw data (black) was fitted (red) accordingly: the two major components, centered at 399.3 eV (blue) and 400.8 eV (green) are consistent with a pyrazole-like moiety, whereas the minor peak at 402.7 eV (cyan) is attributed to quaternary-like nitrogen.

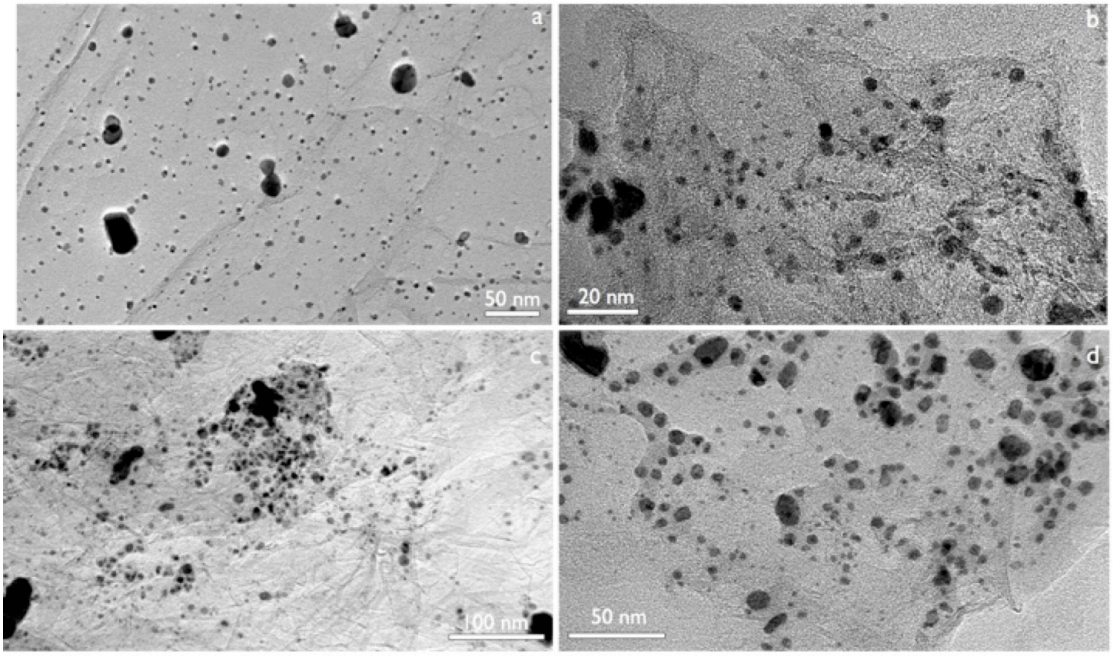

Figure 3.S5. TEM images of the heat-treated PtSn intermetallic NPs supported on (a) FGS, (b) SLG, (c) BGO, and (d) NGO.

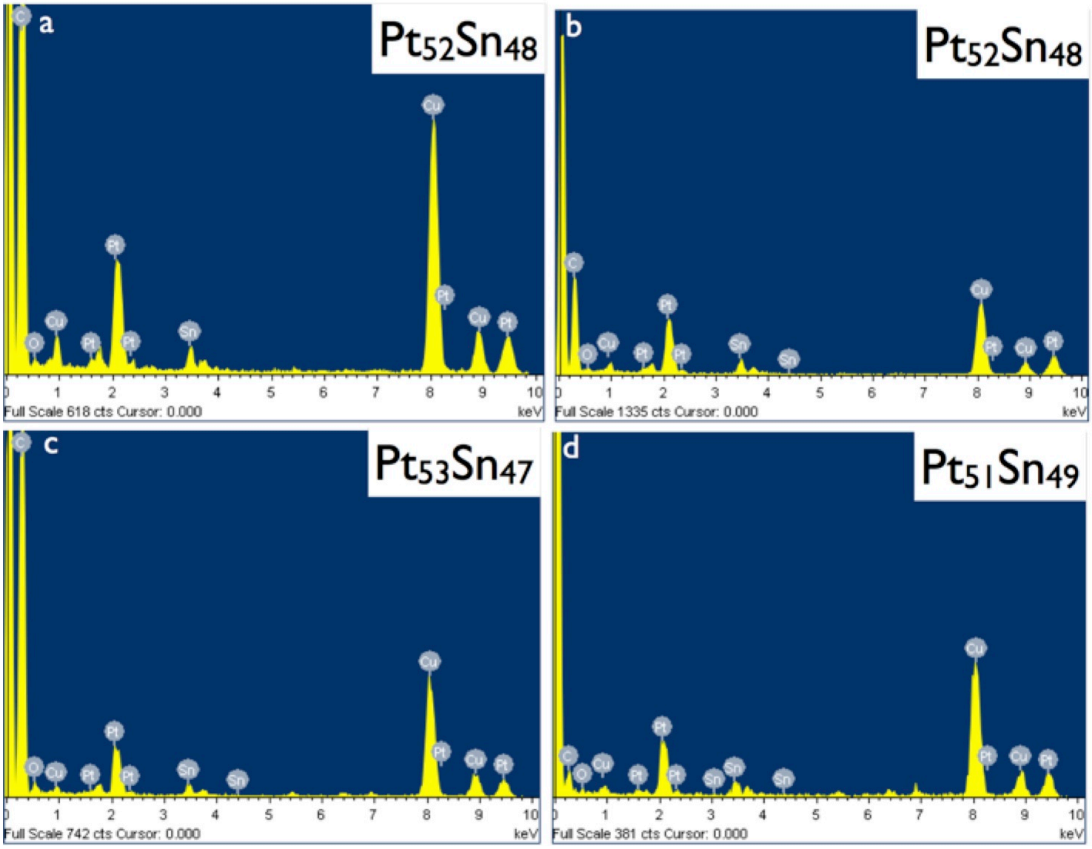

Figure 3.S6. EDS analysis of the (a) FGS, (b) SLG, (c) BGO, and (d) NGO supported PtSn intermetallic NPs.

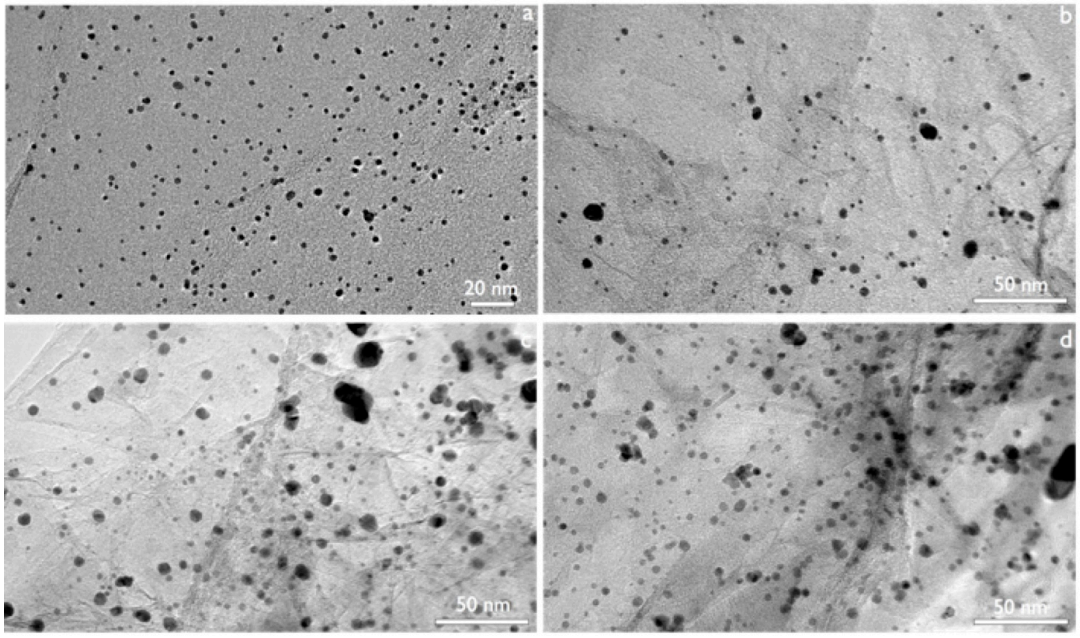

Figure 3.S7. TEM images of the heat-treated Pt NPs supported on (a) FGS, (b) SLG, (c) BGO, and (d) NGO.

Chapter 4: Effects of Size, Composition, and Architecture on the Electrocatalytic Activities of Co_xPt_y Nanoparticles

4.1 Introduction

Proton exchange membrane fuel cells (PEMFCs) are highly regarded as a clean alternative energy technology for motor vehicles, power generators, and many other applications. Unfortunately, several factors limit their commercial viability, including the high expense of their catalytic materials, the poisoning of the hydrogen oxidation reaction (HOR) electrocatalyst at the anode by carbon monoxide (CO), and the inefficiency of the oxygen reduction reaction (ORR) electrocatalyst at the cathode. To mitigate these issues, researchers have developed new Pt-based bimetallic nanoparticles (NPs) by alloying Pt with cheaper metals such as Cr,[206,207] Fe,[208,209] or Cu.[56,210] Use of these bimetallic NPs has led to reduced catalyst costs, improved CO tolerance for the HOR, and increased catalytic efficiencies for the ORR.

The Co-Pt bimetallic system has been extensively studied for ORR catalysis, with high catalytic activities predicted by theoretical models and demonstrated in the literature.[57,70,206,207,211-219] In general, Pt-rich Pt-Co alloy catalysts, such as $CoPt_3$, were reported to have the highest activity for the ORR.[69,70,206,217,220,221] More recently, research has shifted towards determining if the sizes, compositions, and architectures of the Co-Pt NPs could be modified to enhance their activity for the ORR. Co-Pt

alloys of varying composition have been studied, with some reports supporting a shift towards more Co-rich Co-Pt alloys for cost interests, despite the mild observed decrease in catalytic activity.[210] However, Co-Pt alloys, especially those of increased Co content, are vulnerable to dissolution in the acidic environment of the PEMFC, leading to concerns over durability. To address this issue, studies have looked into pre-treated "dealloyed" Co-Pt NPs, which were found to maintain the high ORR activity associated with the bimetallic Co-Pt system.[56,58] Curiously, there are few reports where the more stable Co-Pt intermetallic system is discussed.[57,216,222,223] The results of these studies were conflicting, with results suggesting the atomic ordering and enhanced stability induced by intermetallic phase formation to be both detrimental[57,216] and beneficial[223] to ORR catalytic activity. As such, further studies are needed to understand the influence of composition and architecture on the ORR activity of bimetallic Co-Pt NPs.

In contrast to the wealth of studies performed on Co-Pt NPs for ORR catalysis, research into the use of Co-Pt NPs, regardless of composition and/or architecture, for CO-tolerant HOR are quite limited.[224-226] While these previous studies reported mild improvements in CO tolerance from Co-alloying, the Pt-rich $CoPt_3$ alloy was again the focus of research,[224-226] with little discussion of other compositions or architectures.[224] In our previous work, the CO tolerance of the analogous Fe-Pt bimetallic system was found to vary significantly with respect to differing NP architectures, despite the particles' having similar elemental compositions.[227] Studies such as this highlight the importance of compositional *and*

structural control of bimetallic NPs, due to their essential roles in determining the ultimate performance of a catalytic system.

Here, we present the synthesis of $CoPt_3$, CoPt, and Co_3Pt (Co_xPt_y) alloy and intermetallic NPs, which were extensively characterized by powder X-ray diffraction (XRD), transmission electron microscopy (TEM), and energy dispersive spectroscopy (EDS) analyses. We conduct a full systematic evaluation of the well-characterized Co_xPt_y NPs for CO-tolerant HOR and ORR catalysis to probe the influences of size, composition, and architecture on these energy conversion processes. For HOR catalysis, the Co_xPt_y alloy catalysts were found to have similar performance to monometallic Pt catalysts, but the structural and electronic modifications induced by intermetallic formation were found to be detrimental to their ability to tolerate CO. For ORR catalysis, Co-alloying was found to have minimal impact on the overall catalytic performance, with modifications to the NP composition providing improvements in the specific activity of the Co_xPt_y catalysts. In general, the Co_xPt_y NPs studied here have HOR and ORR catalytic performance comparable to monometallic Pt, but have improved mass activities and are far more cost-effective as electrocatalysts for PEMFCs.

4.2 Experimental

4.2.1 Materials and Synthesis

4.2.1.1 Materials

Cobalt acetylacetonate ($Co(acac)_3$, 99.99%), platinum acetylacetonate ($Pt(acac)_2$, 97%), 1-octadecene (90%), sodium triethylborohydride solution

($NaBEt_3H$, 1.0 M in toluene), oleic acid (OA, 90%), acetone (99.5%) and perchloric acid ($HClO_4$, 70%) were purchased from Aldrich. Methanol (MeOH, 99.8%) was purchased from VWR. Oleylamine (OAm, >70%) and Nafion® solution (5%) were purchased from Fluka. Isopropanol (iPrOH, 99%) was purchased from Pharmco-AAPER. Hexanes (99.9%) and sulfuric acid (H_2SO_4, 96.4%) were purchased from Fisher. Vulcan XC-72 carbon black powder (CB) was purchased from Cabot Corporation. E-TEK Pt (30% HP Pt on Vulcan XC-72) was purchased from BASF. Ultra-pure water was obtained from deionized water using a Millipore Academic Milli-Q A10 purifier system. All materials were used as received without further purification. All reactions were carried out on Schlenk lines under N_2 atmosphere.

4.2.1.2 Synthesis of Co_xPt_y Alloy and Intermetallic NPs

In a typical synthesis, $Co(acac)_3$ and $Pt(acac)_2$ in the appropriate molar ratios (0.075 mmol total metal, Co:Pt ratios: 3:1, 1:1, 1:3), OA (50 μL), and OAm (50 μL) were mixed in 1-octadecene (5 mL) in a 50 mL round-bottom flask. The resultant mixture was heated to 80 °C under vacuum to degas the system, placed under a flowing N_2 atmosphere and held at 100 °C for 60 min to ensure full dissolution of the precursors. In a separate Schlenk flask, 1-octadecene (15 mL) was added and degassed at 80 °C under vacuum, placed under flowing N_2 and heated to 200 °C. At this temperature, $NaBEt_3H$ solution (3 mL, 1.0 M in toluene) was injected into the Schlenk flask, followed by the immediate injection of the Co_xPt_y precursor solution into the Schlenk flask. The reaction solution instantly turned black with the precursor injection, and the resultant mixture was returned to 200 °C. After being held at 200

°C for 60 min, the heating source was removed and the reaction was allowed to cool down to room temperature. The black colloidal solution was transferred to a 50 mL conical centrifuge tube, where a 1:1 MeOH/acetone mixture (40 mL) was added to the tube, which was sonicated in a sonication bath (FS30H, Fisher Scientific) for 10 min before centrifugation at 6000 rpm for 15 min. The supernatant was discarded and the washing procedure was repeated an additional two times. The black solid was dried overnight, before re-suspension in hexanes (20 mL).

To make carbon-supported Co_xPt_y electrocatalysts with 30 wt % total metal loading, the AP NPs dispersed in hexanes were mixed with a suitable amount of CB powder and sonicated in a sonication bath (FS30H, Fisher Scientific) for 180 min. The hexanes were evaporated in air overnight and the resultant CB-supported NPs were vacuum-dried. The dried solids were placed in a ceramic boat, which was introduced into a quartz glass tube. To remove the surfactants from the NPs, the tube was heated in a horizontal solid tube furnace (Thermolyne F21135, Thermo Scientific) at 400 °C for 90 min under a 5% H_2/95% Ar atmosphere with a flow rate of 90 SCCM. To convert the alloy particles into their intermetallic counterparts, the annealing tube was instead heated at 550 °C for 90 min. Intermetallic particles were also obtained by heating the annealing tube at 700 °C for 90 min.

4.2.2 Characterization of Co_xPt_y Nanoparticles

4.2.2.1 Powder X-ray Diffraction

Powder X-ray diffraction (XRD) patterns of samples were obtained on a Bruker C2 Discover diffractometer equipped with a VÅNTEC-500 detector using a

monochromatic Cu Kα radiation source biased at 40 kV and 40 mA. The supported NP powders were pressed on a glass slide for analysis.

4.2.2.2 Transmission Electron Microscopy with Energy-Dispersive X-Ray Spectroscopy

Transmission electron microscope (TEM) images were obtained on a JEM 2100F Field Emission TEM operating at 200 kV. Energy dispersive spectroscopy (EDS) data were collected on the same TEM operating in the scanning (STEM) mode. The supported NP powders were dispersed in MeOH, and an aliquot (10 μL) of the resulting dispersion was drop cast on the TEM grids. The TEM grids used were carbon-coated Cu grids (CF400-Cu, Electron Microscopy Sciences).

4.2.3 Electrochemical Analysis of Co_xPt_y Nanoparticles

iPrOH (159.2 mL), ultra-pure water (40.0 mL), and Nafion® solution (0.80 mL, 5%) were mixed and stored as a stock solution. The catalyst ink was prepared by mixing the supported NP powder with the above stock solution such that the concentration was 1.0 mg/mL of powder in solution. The resultant mixture was sonicated in a sonication bath (FS30H, Fisher Scientific) for 120 min. The catalyst ink (20 μL) was cast on a glassy carbon (GC) electrode (Pine Instruments, 5.0 mm diameter) using a micropipette and allowed to dry in air overnight while covered. Electrochemical experiments were performed on a potentiostat (Autolab PGSTAT30) with a standard three-electrode electrochemical cell. The rotating GC disk electrode with dried catalyst ink on its surface was used as the working electrode. Pt wire was used as the

counter electrode and a saturated calomel electrode (SCE) was used as the reference electrode. H_2SO_4 in ultra-pure water (0.5 M) was used as the electrolyte for the HOR and CO oxidation studies, while $HClO_4$ in ultra-pure water (0.1 M) was used as the electrolyte for the ORR studies. In both systems, the catalysts were subjected to 50 potential scan cycles at 50 mV/s between -0.22 V and 0.8 V while Ar-saturated as a conditioning procedure. After catalyst conditioning, fresh electrolyte was used during the collection of experimental data. To obtain the H adsorption curves, the catalyst was saturated with Ar by bubbling Ar (99.9% pure) in the electrolyte for 30 min followed by a 50 mV/s potential scan between -0.22 V and 0.8 V. To perform the CO stripping experiment, the catalyst was saturated with CO by bubbling CO (99.5% pure, Al tank) in the electrolyte for 20 min followed by Ar-purging for 40 min. To obtain polarization curves for the electrooxidation of CO-contaminated H_2, the electrolyte was bubbled with a 1000 ppm CO/balance H_2 gas mixture (99% pure, Al tank) for 90 min with the electrode potential held at -0.20 V, followed by a potential scan (1 mV/s) at a rotation rate of 1600 rpm. To obtain polarization curves for the reduction of O_2, the electrolyte was bubbled with O_2 (99.999% pure) for 30 min followed by consecutive potential scans (5 mV/s) at various rotation rates (400, 600, 900, 1200, 1600, and 2000 rpm). These polarization curves were used to calculate kinetic currents. The kinetic current (I_k) can be calculated using the Koutecky–Levich equation:

$$\frac{1}{I} = \frac{1}{I_k} + \frac{1}{I_d} \tag{6}$$

where I is the measured current and I_d the diffusion limited current. The I_d term can be obtained from the Levich equation:

$$I_d = 0.62nFAD^{2/3}\upsilon^{-1/6}\omega^{1/2}C_{O_2} \quad (7)$$

where n is the number of electrons transferred; F is Faraday's constant (96,485 C/mol); A is the area of the electrode (0.196 cm^2); D is the diffusion coefficient of O_2 in 0.1 M $HClO_4$ solution (1.93×10^{-5} cm^2/s); υ is the kinematic viscosity of the electrolyte (1.01×10^{-2} cm^2/s); ω is the angular frequency of rotation, $\omega = (2\pi f)/60$, f is the RDE rotation rate in rpm; C_{O_2} is the concentration of molecular oxygen in 0.1 M $HClO_4$ solution (1.26×10^{-6} mol/cm^3).[223]

Electrochemically active surface area (ECSA) values were calculated from the integrated charges obtained from the H adsorption experiments in 0.1 M $HClO_4$ electrolyte. The integrated charges were obtained by integrating the area under the hydrogen desorption region between 0.15 V and -0.2 V on the reverse sweep of the H adsorption experiment using a conversion factor of 200 μC/cm^2.[228,229]

4.3 Results and Discussions

4.3.1 Synthesis and Characterization of Co_xPt_y Nanoparticles

Bimetallic Co_xPt_y NPs were synthesized with a procedure comparable to, but distinct from previously reported methods.[72,218,230-233] Specifically, appropriate amounts of $Co(acac)_3$ and $Pt(acac)_2$ were co-reduced in 1-octadecene using $NaBEt_3H$ in the presence of an OA/OAm surfactant mixture at 200 °C. The three different as prepared (AP) Co_xPt_y samples ($CoPt_3$, CoPt, and Co_3Pt) were annealed at three different temperatures (400 °C, 550 °C, and 700 °C) to convert the disordered alloys into ordered intermetallic phases. The results of our experiments are in good agreement with previous reports.[218,230-233] A summary of the experimental data to

follow, as determined from XRD, TEM, and EDS analyses of the NPs, is shown in Table 4.1.

Table 4.1. Summary of representative experimental data for NPs

Sample	Space Group (Crystal Structure)[a]	Lattice Parameter(s)[a]	Crystallite Size[a]	Avg. NP Size[b]	Avg. NP Composition[c]
E-TEK Pt	Fm-3m (FCC)	a = 0.392 nm	3.8 nm	3.2 ± 0.8 nm	--
$CoPt_3$-AP	Fm-3m (FCC)	a = 0.390 nm	2.3 nm	2.2 ± 0.4 nm	Co:Pt 24:76
$CoPt_3$-400 °C	Fm-3m (FCC)	a = 0.386 nm	6.5 nm	2.8 ± 1.3 nm	
$CoPt_3$-550 °C	Pm-3m (Primitive)	a = 0.386 nm	12.1 nm	6.0 ± 3.8 nm	
$CoPt_3$-700 °C	Pm-3m (Primitive)	a = 0.386 nm	20.9 nm	6.9 ± 4.0 nm	
CoPt-AP	Fm-3m (FCC)	a = 0.389 nm	2.0 nm	2.1 ± 0.3 nm	Co:Pt 45:55
CoPt-400 °C	Fm-3m (FCC) P4/mmm (FCT)	a = 0.381 nm a = 0.269 nm c = 0.383 nm	6.3 nm 6.6 nm	2.7 ± 0.7 nm	
CoPt-550 °C	P4/mmm (FCT)	a = 0.270 nm c = 0.383 nm	13.8 nm	4.7 ± 3.2 nm	
CoPt-700 °C	P4/mmm (FCT)	a = 0.270 nm c = 0.383 nm	30.3 nm	6.0 ± 3.9 nm	
Co_3Pt-AP	Fm-3m (FCC)	a = 0.425 nm	1.5 nm	1.7 ± 0.4 nm	Co:Pt 70:30
Co_3Pt-400 °C	Fm-3m (FCC)	a = 0.394 nm	2.6 nm	2.2 ± 0.6 nm	
Co_3Pt-550 °C	Fm-3m (FCC)	a = 0.369 nm	9.0 nm	3.9 ± 2.5 nm	
Co_3Pt-700 °C	Fm-3m (FCC)	a = 0.369 nm	22.7 nm	4.9 ± 3.9 nm	

[a] Determined from XRD analysis. [b] Calculated by counting 100 small particles and agglomerates. [c] Determined from EDS analysis

The XRD patterns of the $CoPt_3$ NPs are shown in Figure 4.1. Relative to monometallic Pt, the diffraction peaks in the $CoPt_3$ samples are shifted to slightly

higher angles due to lattice contraction resulting from Co incorporation (Table 4.1). Superlattice reflections are present in the XRD patterns of the 550 °C and 700 °C samples, illustrating their transition from an alloy into the intermetallic phase. The peaks become sharper with increasing annealing temperature, resulting from increased crystallinity consistent with larger particle sizes. Debye-Scherrer analysis gives crystallite sizes of 2.3, 6.5, 12.1, and 20.9 nm for the AP, 400 °C, 550 °C, and 700 °C $CoPt_3$ NPs, respectively (Table 4.1). TEM images of the AP, 400 °C, 550 °C, and 700 °C $CoPt_3$ NPs show the average sizes to be 2.2, 2.8, 6.0, and 6.9 nm, respectively (Figure 4.2). High-resolution lattice fringe images of the single particles show average lattice separations of 0.221 nm, which corresponds to the (111) plane of the cubic (Pm-3m) $CoPt_3$ intermetallic lattice (insets of Figure 4.2) and is supported by the XRD data.

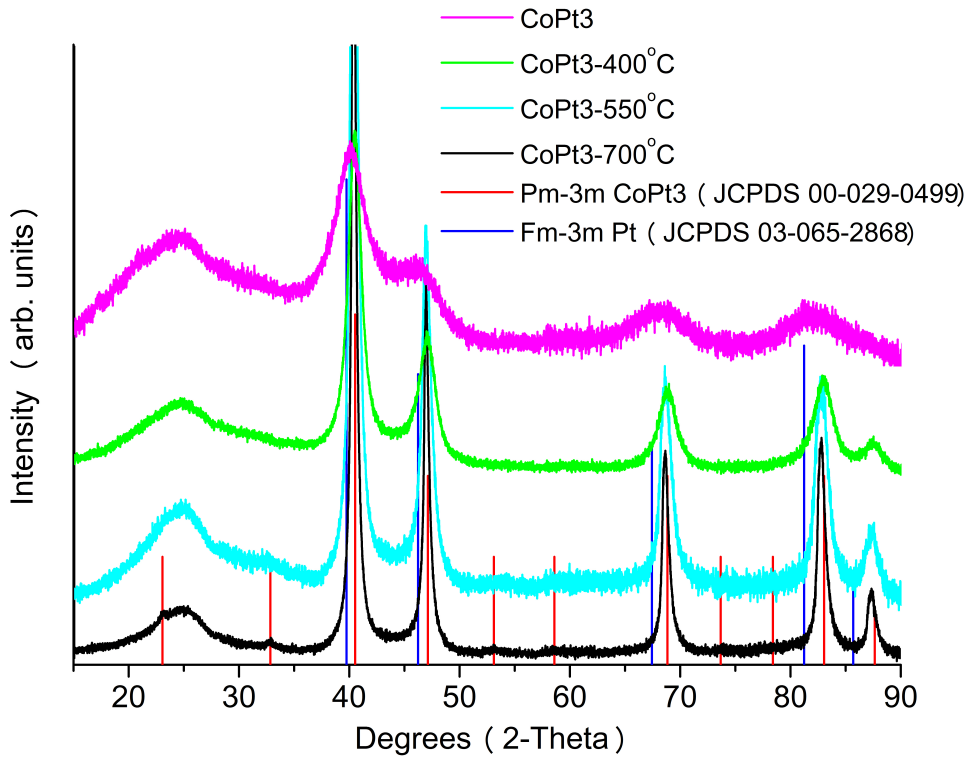

Figure 4.1. XRD patterns of the $CoPt_3$ NPs. Red lines indicate the peak positions for the cubic (Pm-3m) $CoPt_3$ intermetallic (JCPDS 00-029-0499). Blue lines indicate the peak positions for FCC phase Pt (JCPDS 03-065-2868). The broad low angle peaks are due to the glass slide.

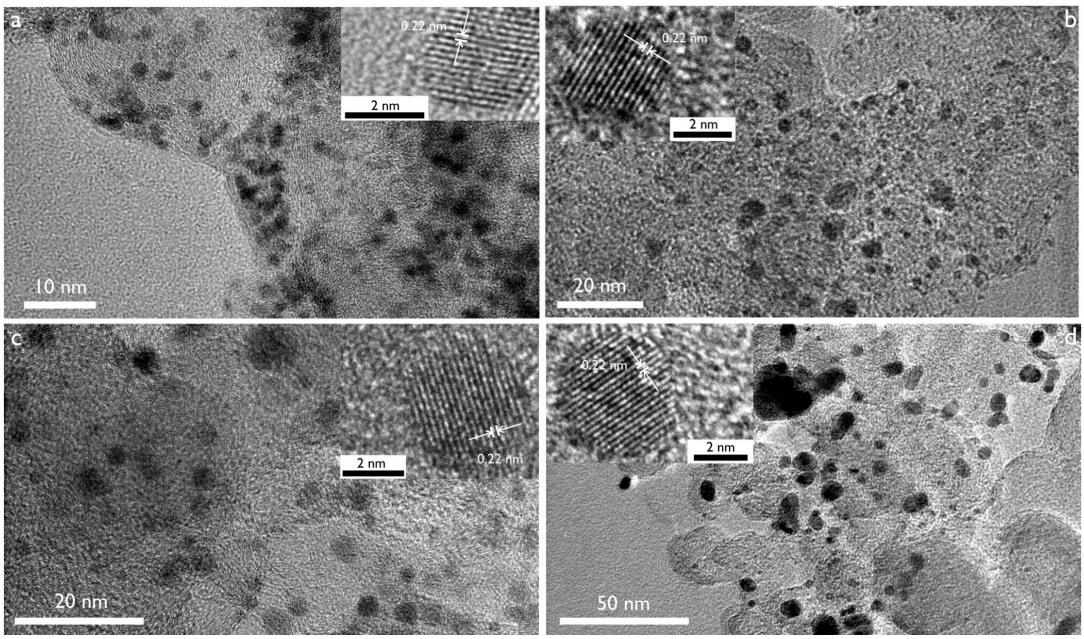

Figure 4.2. TEM images of the (a) AP, (b) 400 °C, (c) 550 °C, and (d) 700 °C $CoPt_3$ NPs. Lattice fringe images of single particles are inset.

Figure 4.3 shows the XRD patterns of the CoPt samples. The increased Co content induces additional lattice contraction (and peak shifting) relative to the $CoPt_3$ samples (Table 4.1). As with the $CoPt_3$ samples, increasing the annealing temperature converts the CoPt alloy into its intermetallic phase and is illustrated here by the appearance of the unique CoPt superlattice reflections in the XRD patterns of the 550 °C and 700 °C samples. The diffraction peaks also increase in intensity, indicating larger particle sizes. Debye-Scherrer analysis of the diffraction pattern gives crystallite sizes of 2.0, 6.5, 13.8, and 30.8 nm for the AP, 400 °C, 550 °C, and 700 °C CoPt samples, respectively (Table 4.1). TEM images of the CoPt particles show their respective average sizes to be 2.1, 2.7, 4.7, and 6.0 nm (Figure 4.4). High-resolution lattice fringe images of the single particles are inset in Figure 4.4. The average lattice

separation of 0.219 nm in the annealed NPs matches the (101) plane of the FCT (P4/mmm) CoPt intermetallic lattice (insets of Figure 4.4), in agreement with the XRD analysis.

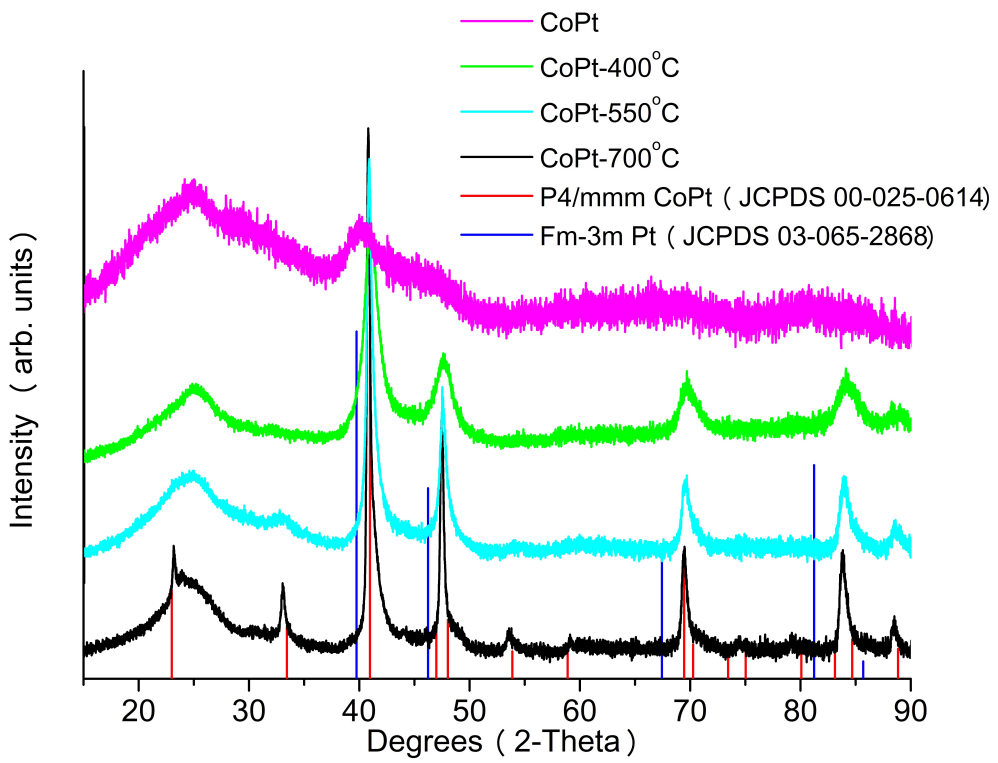

Figure 4.3. XRD patterns of the CoPt NPs. Red lines indicate the peak positions for the tetragonal (P4/mmm) CoPt intermetallic (JCPDS 00-025-0614). Blue lines indicate the peak positions for FCC phase Pt (JCPDS 03-065-2868). The broad low angle peaks are due to the glass slide.

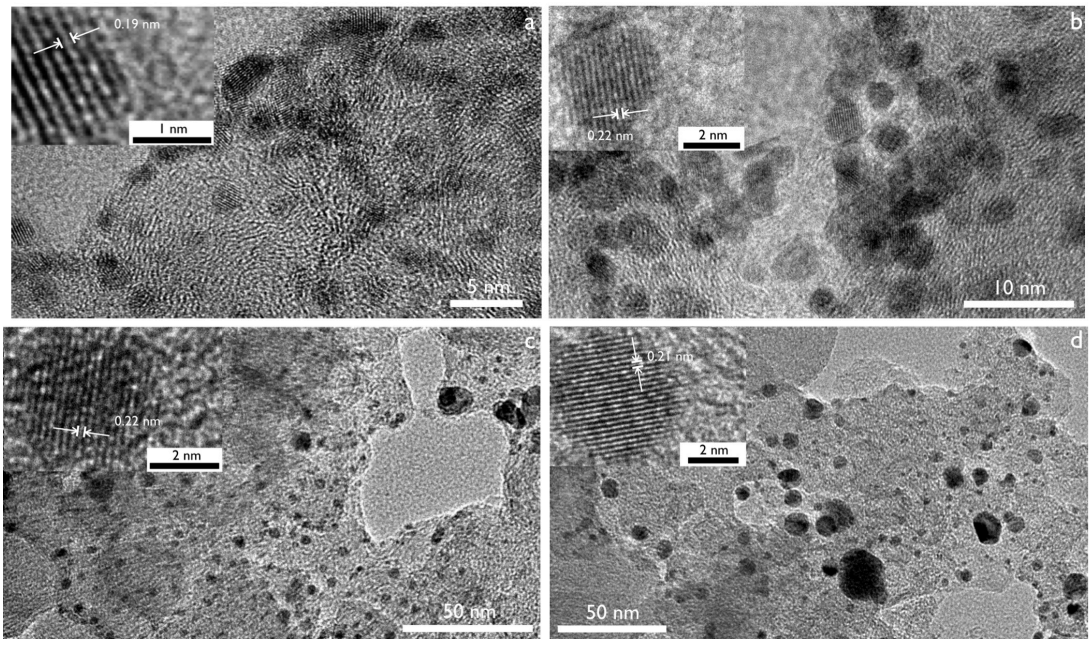

Figure 4.4. TEM images of the (a) AP, (b) 400 °C, (c) 550 °C, and (d) 700 °C CoPt NPs. Lattice fringe images of single particles are inset.

The XRD patterns of the Co_3Pt NPs are clearly distinct from the other Co_xPt_y samples (Figure 4.5). Compared to the $CoPt_3$ and CoPt samples, the additional Co content causes the diffraction peaks of the Co_3Pt NPs to shift to even higher angles due to further lattice contraction. However, the diffraction peaks appear at slightly lower angles relative to the Co_3Pt reference, which suggests the Co:Pt ratio of the Co_3Pt NPs is less than the expected 3:1. The XRD patterns of the Co_3Pt NPs are also distinguished by the absence of superlattice reflections in the 550 °C and 700 °C samples, which would indicate intermetallic formation. This is because the Co_3Pt NPs remain in the alloy phase under heat-treatment, unlike their $CoPt_3$ and CoPt counterparts, which form intermetallic phases at elevated temperatures. Like the other samples, the Co_3Pt NPs increase in size with increased annealing temperature,

resulting in increasingly sharper diffraction peaks. Debye-Scherrer analysis gives crystallite sizes of 1.5, 2.6, 9.0, and 22.7 nm for the AP, 400 °C, 550 °C, and 700 °C Co_3Pt samples, respectively. TEM images of the Co_3Pt NPs show the respective average sizes to be 1.7, 2.2, 3.9, and 4.9 nm (Figure 4.6). The average lattice separation of 0.213 nm in the annealed NPs is slightly larger than the literature data value (0.211 nm) for the (111) plane of FCC Co_3Pt alloy NPs (insets of Figure 4.6). These observations suggest the Co_3Pt NPs have disordered FCC structures and have Co:Pt ratios less than the expected 3:1, in agreement with the earlier XRD analysis. To approximate the Co:Pt ratio of the Co_3Pt NPs, Vegard's law calculations were performed. Using literature lattice parameter data of several Co_xPt_y samples (Pt, $CoPt_3$, CoPt, Co_3Pt, and Co), the Co:Pt ratio of the Co_3Pt NPs was found to be 7:3, which is supported by EDS analysis.

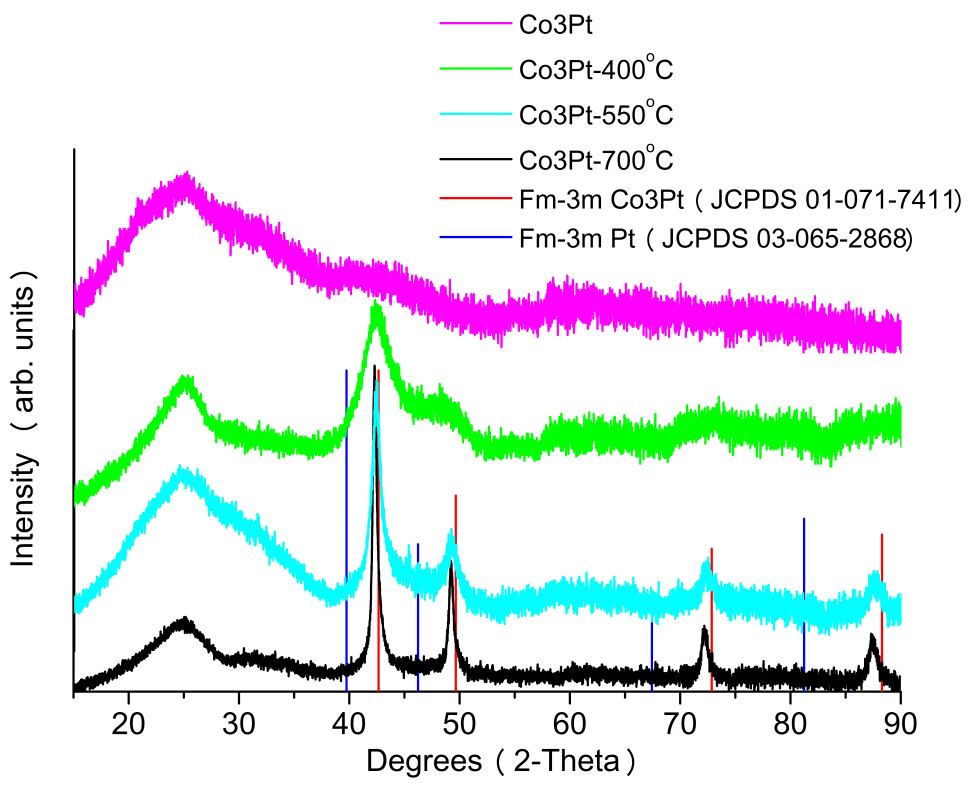

Figure 4.5. XRD patterns of the Co_3Pt NPs. Red lines indicate the peak positions for FCC phase Co_3Pt (JCPDS 01-071-7411). Blue lines indicate the peak positions for FCC phase Pt (JCPDS 03-065-2868). The broad low angle peaks are due to the glass slide.

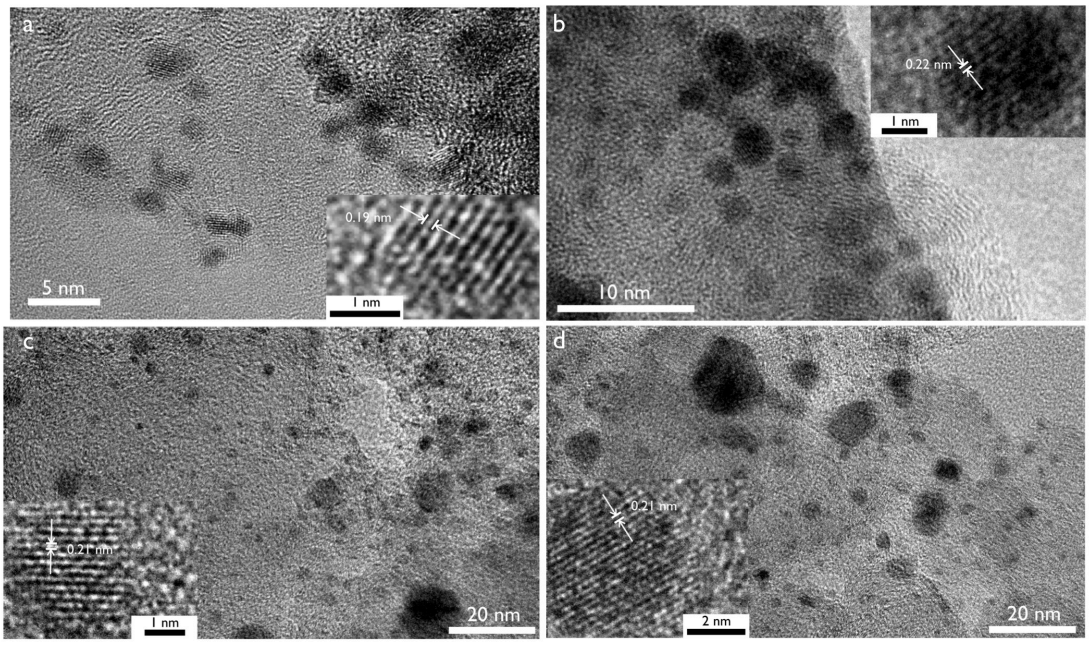

Figure 4.6. TEM images of the (a) AP, (b) 400 °C, (c) 550 °C, and (d) 700 °C Co_3Pt NPs. Lattice fringe images of single particles are inset.

Each of the Co_xPt_y NPs samples were analyzed with EDS (Figures 4.S1-4.S3), where the average compositions are in good agreement with the precursor ratios used. EDS analysis also shows that the compositions of the NPs do not change with respect to the different annealing temperatures, with the $CoPt_3$, CoPt, and Co_3Pt NPs having average Co:Pt composition ratios of 24:76 (Figure 4.S1), 45:55 (Figure 4.S2), and 70:30 (Figure 4.S3), respectively. These results also support the XRD analysis, where the diffraction peak positions for each sample within a given composition set ($CoPt_3$, CoPt, Co_3Pt) do not shift (indicating consistent Co:Pt ratios) with respect to annealing temperature.

Comparing the different Co_xPt_y NPs shows that the particles generally increase in size with increasing Pt content. All of the AP samples are roughly 2 nm in

size, but the $CoPt_3$ particles are slightly larger than the CoPt NPs, followed by the Co_3Pt particles. This result is primarily influenced by the metal-surfactant ratio. Each Co_xPt_y synthesis contained the same amount of surfactant with equal moles of total metal. Only the Co:Pt ratios changed between the different Co_xPt_y syntheses. Increasing the Pt content (but maintaining equal moles of metal) within a synthesis results in slightly increased surface area due to the larger size of Pt atoms relative to Co. Since surfactants control NP size with respect to surface area, the increased surface area effectively increases the metal-surfactant ratio, which leads to a slight increase in NP size.

While the Co-Pt phase diagram shows that the $CoPt_3$ and CoPt NPs should exist as intermetallics, the rapid reduction and nucleation of Co and Pt results in the formation of Co_xPt_y alloy particles. Annealing the $CoPt_3$ and CoPt NPs induces their transformation into their thermodynamically stable intermetallic phases, while the Co_3Pt NPs maintain the expected alloy structure. While high temperature annealing is necessary to induce the transformation from alloy to intermetallic, it also results in the growth and agglomeration of the NPs. It is this phenomenon that causes the discrepancy in NP size as determined by XRD (Debye-Scherrer) vs. TEM analyses. XRD size analysis is volume weighted, so a few large, highly crystalline agglomerates can skew the resulting calculation. Since the number and sizes of these agglomerates increase with higher annealing temperature, the size discrepancy between the two experiment techniques also increases.

4.3.2 Electrochemical Characterization of Co_xPt_y Alloy and Intermetallic NPs

To assess the effects of size, composition and architecture on the NPs' catalytic activities, we evaluated the catalytic activities of all nine annealed (400 °C, 550 °C, and 700 °C) Co_xPt_y catalysts for CO-tolerant HOR and the ORR. As a reference, the commercially available E-TEK Pt catalyst was tested under the same conditions. All catalysts were prepared with a 30% total metal loading by weight based on the initial amounts of reagents. Given the similar metal loadings of the Co_xPt_y NP catalysts, we focus our analysis on how the different sizes, compositions and architectures of the NPs impact their resultant catalytic activities.

For the oxidative electrochemical processes occurring at the anode (CO stripping and CO-tolerant HOR), potentials are reported with respect to the SCE. Enhanced catalytic activity for these processes are associated with *lower* onset potential (E_{Onset}) values.

For the reductive electrochemical processes occurring at the cathode (ORR), potentials are reported with respect to the reversible hydrogen electrode (RHE). Enhanced catalytic activity for these processes are associated with *higher* onset potential (E_{Onset}) values.

4.3.3 Evaluation of Co_xPt_y Nanoparticles for CO-Tolerant Hydrogen Electrooxidation

The CO stripping curves for the Co_xPt_y catalysts are seen in Figures 4.S4 ($CoPt_3$), 4.S5 (CoPt), and 4.S6 (Co_3Pt). The onset potentials for CO oxidation are all

in the range of 0.4 - 0.55 V (Table 4.2), which is similar to the 0.53 V onset potential for the E-TEK Pt reference (Figure 4.S7). When comparing the composition sets ($CoPt_3$ vs. CoPt vs. Co_3Pt), two trends emerge: 1) the onset potential tends to decrease with increasing Co content; 2) the integrated charge below the CO stripping peak decreases with increasing Co content. In addition, the integrated charge below the CO stripping peak within a particular Co_xPt_y composition set tends to decrease with increasing annealing temperature. These data show that the CO adsorption and oxidation efficiencies are directly correlated to the Pt surface area, which decreases with increasing particle size and increasing Co concentration, in agreement with previous studies.[8,35,234,235]

Figures 4.S8 ($CoPt_3$), 4.S9 (CoPt), and 4.S10 (Co_3Pt) show the polarization curves for the electrooxidation of CO/H_2 mixtures (1000 ppm CO) for the Co_xPt_y catalysts, along with the E-TEK Pt reference. The onset potentials range from 0.27 - 0.4 V, which is lower than the pure CO oxidation onset potentials as expected. Only the Co_3Pt-700 °C catalyst shows improved CO tolerance over E-TEK Pt, with the other Co_3Pt catalysts featuring similar activity. The $CoPt_3$-400 °C catalyst behaves almost identically to E-TEK Pt, while the remaining Co_xPt_y catalysts have noticeably lower CO tolerance. Unlike other studies where lower CO stripping onset potentials are correlated with lower CO/H_2 onset potentials and increased CO tolerance, there is no clear correlation between the CO oxidation and onset potentials in the Co_xPt_y catalysts.[63,194] For example, the CO oxidation onset potentials for the $CoPt_3$-400 °C and Co_3Pt-700 °C samples differ by 90 mV, yet have comparable onset potentials for CO/H_2 oxidation.

Changing the reference point by comparing the different catalysts within an annealing temperature set is more informative. Figures 4.7 (400 °C), 4.8 (550 °C), and 4.9 (700 °C) show the same CO/H_2 polarization curves except they are now grouped by annealing temperature rather than NP composition. With this perspective change, new trends are now apparent. All three Co_xPt_y catalysts annealed at 400 °C have CO tolerance comparable to E-TEK Pt. The CoPt catalyst is less CO-tolerant, while the $CoPt_3$ and Co_3Pt catalysts have nearly identical onset potentials as the E-TEK Pt reference. However, in the 550 °C and 700 °C sets, the CoPt and $CoPt_3$ catalysts are less CO-tolerant than their Co_3Pt counterparts and E-TEK Pt. NP size is expected to play a role in the CO tolerance of the Co_xPt_y catalysts, as illustrated by the CoPt and $CoPt_3$ catalysts, where CO tolerance decreases with increasing particle size induced by high temperature annealing. However, the Co_3Pt-700 °C catalyst has the highest CO tolerance of all the studied catalysts despite having larger particles than the other Co_3Pt or 400 °C annealed catalysts. This observation suggests that the NP composition and architecture have more influence on the catalyst's CO tolerance than the particle size.

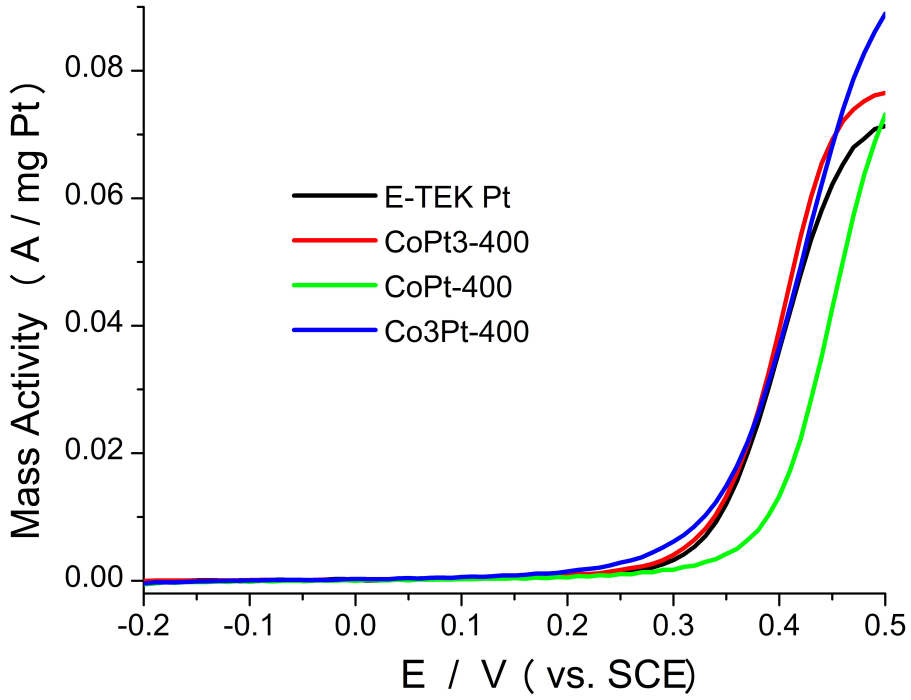

Figure 4.7. Polarization curves for the electrooxidation of CO-contaminated H_2 (1000 ppm CO, balance H_2) of the 400 °C Co_xPt_y NP catalysts in 0.5 M H_2SO_4 solution. Black line indicates E-TEK Pt catalyst as reference. Curves were recorded at 25 °C with 1 mV/s scan rates and 1600 rpm rotation rates.

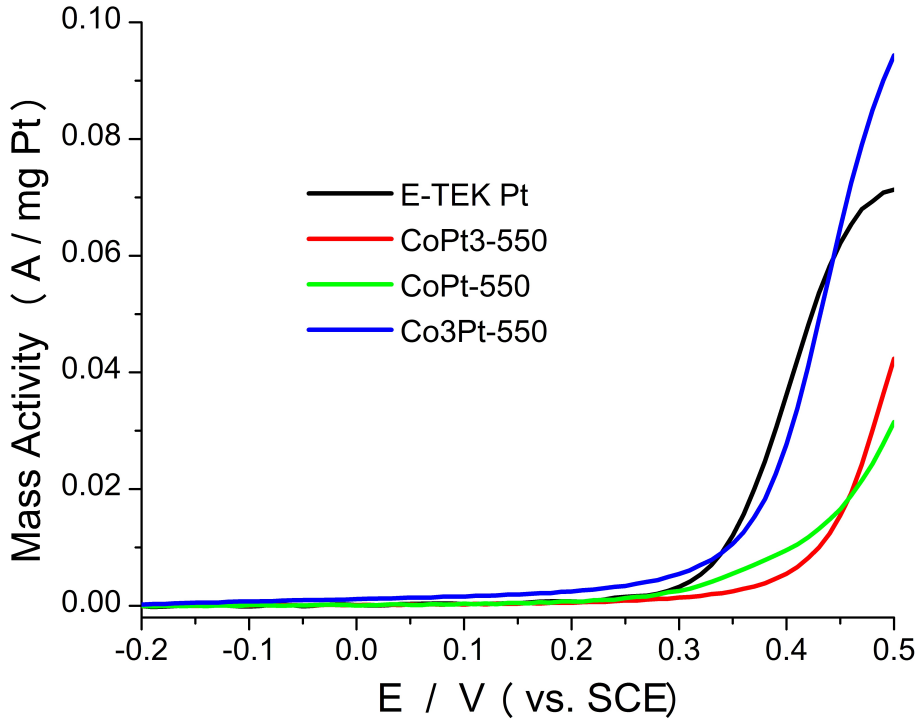

Figure 4.8. Polarization curves for the electrooxidation of CO-contaminated H_2 (1000 ppm CO, balance H_2) of the 550 °C Co_xPt_y NP catalysts in 0.5 M H_2SO_4 solution. Black line indicates E-TEK Pt catalyst as reference. Curves were recorded at 25 °C with 1 mV/s scan rates and 1600 rpm rotation rates.

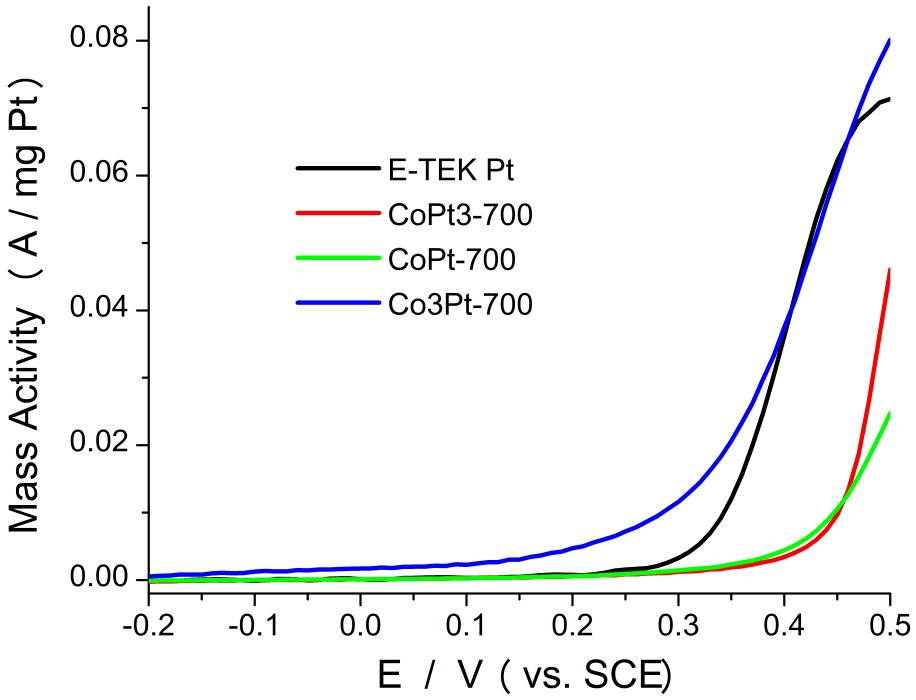

Figure 4.9. Polarization curves for the electrooxidation of CO-contaminated H_2 (1000 ppm CO, balance H_2) of the 700 °C Co_xPt_y NP catalysts in 0.5 M H_2SO_4 solution. Black line indicates E-TEK Pt catalyst as reference. Curves were recorded at 25 °C with 1 mV/s scan rates and 1600 rpm rotation rates.

To help illustrate this point, a summary of the structural and anodic electrochemical properties of the different catalysts is given in Table 4.2.

Table 4.2. Summary of representative experimental data for NP CO/H_2 electrocatalysts

Sample	Space Group (Crystal Structure)	Avg. NP Size[a]	CO Stripping E_{Onset}[b]	CO Stripping E_{Peak}[b]	CO/H_2 Oxidation E_{Onset}[b]
E-TEK Pt	Fm-3m (FCC)	3.2 ± 0.8 nm	0.53	0.59	0.29
$CoPt_3$-400 °C	Fm-3m (FCC)	2.8 ± 1.3 nm	0.50	0.55	0.29
$CoPt_3$-550 °C	Pm-3m (Primitive)	6.0 ± 3.8 nm	0.47	0.54	0.38
$CoPt_3$-700 °C	Pm-3m (Primitive)	6.9 ± 4.0 nm	0.54	0.60	0.40
CoPt-400 °C	Fm-3m (FCC) P4/mmm (FCT)	2.7 ± 0.7 nm	0.48	0.55	0.34
CoPt-550 °C	P4/mmm (FCT)	4.7 ± 3.2 nm	0.45	0.54	0.37
CoPt-700 °C	P4/mmm (FCT)	6.0 ± 3.9 nm	0.45	0.54	0.39
Co_3Pt-400 °C	Fm-3m (FCC)	2.2 ± 0.6 nm	0.47	0.56	0.29
Co_3Pt-550 °C	Fm-3m (FCC)	3.9 ± 2.5 nm	0.42	0.51	0.31
Co_3Pt-700 °C	Fm-3m (FCC)	4.9 ± 3.9 nm	0.41	0.52	0.27

[a] Calculated by counting 100 small particles and agglomerates. [b] Potential vs. SCE.

As shown in Table 4.2 and described above, the $CoPt_3$-400 °C and all three Co_3Pt catalysts have CO/H_2 onset potentials very similar to E-TEK Pt. Each of these catalysts also has a FCC disordered alloy structure. Previous studies have shown that ordered intermetallic structures are typically more stable than the corresponding disordered alloy. In the acidic environment, Co dissolution occurs from the alloy samples during the potential cycling conditioning procedure. This dissolution phenomenon reduces the effects of Co-alloying, resulting in NP catalysts that behave similarly to monometallic Pt catalysts due to the Pt-rich surface. The $CoPt_3$-400 °C catalyst already has a Pt-rich surface due to its high Pt content, but will experience some Co dissolution due to its alloy structure. As the Co_3Pt catalysts adopt an alloy

architecture at all annealing temperatures, they are also subject to the Co dissolution process, which should also result in a Pt-rich surface. Accordingly, the $CoPt_3$-400 °C and Co_3Pt catalysts studied here most likely have Pt-rich surfaces and should function similarly to monometallic Pt.

Likewise, Table 4.2 shows that the 550 °C and 700 °C annealed CoPt and $CoPt_3$ catalysts have similar CO tolerances, which are much lower than the other catalysts discussed. XRD analysis shows the 550 °C and 700 °C annealed CoPt and $CoPt_3$ catalysts exist as intermetallics, and not alloys like the aforementioned samples. As a result, these samples should be more resistant to Co dissolution and have more Co on their surfaces. Previous reports have suggested that the HOR only occurs on the Pt sites of bimetallic catalysts and that Co-alloying does not appear to impact the ability of the Pt-based catalyst to perform the HOR.[193,224] Given that hypothesis, increasing the amount of surface Co, as in the intermetallic CoPt and $CoPt_3$ catalysts, will result in fewer of the Pt surface sites needed for H_2 adsorption and the resultant HOR. These intermetallic Co_xPt_y catalysts would have lower CO tolerance compared to their alloy counterparts as a result.

However, the lack of correlation between CO oxidation onset potential and CO tolerance suggests the diminished CO tolerance in the intermetallic NPs is most likely due to modified electronic structures that negatively impact their ability to tolerate CO relative to the alloy particles. As previously seen in $FePt_3$ catalysts, this loss of CO tolerance would most likely manifest through reduced H_2 adsorption and activity for HOR.[227] This explanation would also account for the CO tolerance of the

CoPt-400 °C catalyst, which is of mixed alloy/intermetallic state and behaves intermediate of the two architectures.

To summarize, previous studies have demonstrated that the electronic structure modifications induced by alloying Pt catalysts with Co improves their ability to oxidize CO in the absence of H_2. The results of these previous CO stripping experiments are reproduced here. Traditional reasoning implies lower onset potentials for CO oxidation should also result in improved CO tolerance for HOR, but no correlation was found in our experiments. The most likely explanation is that Co-alloying also impacts the Co_xPt_y NPs' ability to perform the HOR. In the case of the alloy NPs, the Co-alloying effect is minimal, resulting in their CO tolerances being quite similar to monometallic Pt. In the intermetallic NPs however, the effects of Co-alloying are increased, resulting in a decrease in CO-tolerant HOR activity.

4.3.4 Evaluation of Co_xPt_y Nanoparticles for the Oxygen Reduction Reaction

Table 4.3 summarizes the ORR electrochemical data to follow, along with selected structural data, for the different catalysts.

Table 4.3. Summary of representative experimental data for ORR NP electrocatalysts

Sample	Space Group (Crystal Structure)	Avg. NP Size[a]	ORR E_{Onset}[b]	ORR E_{Inf}[b]	Kinetic Current (mA)[c]	Specific Activity (mA/cm^2 Pt)[d]
E-TEK Pt	Fm-3m (FCC)	3.2 ± 0.8 nm	0.98	0.89	1.10	2.58
$CoPt_3$-400 °C	Fm-3m (FCC)	2.8 ± 1.3 nm	0.97	0.87	1.09	6.76
$CoPt_3$-550 °C	Pm-3m (Primitive)	6.0 ± 3.8 nm	0.97	0.88	1.01	9.60
$CoPt_3$-700 °C	Pm-3m (Primitive)	6.9 ± 4.0 nm	0.96	0.86	0.78	7.00
CoPt-400 °C	Fm-3m (FCC) P4/mmm (FCT)	2.7 ± 0.7 nm	0.96	0.86	0.64	4.23
CoPt-550 °C	P4/mmm (FCT)	4.7 ± 3.2 nm	0.94	0.84	0.40	4.48
CoPt-700 °C	P4/mmm (FCT)	6.0 ± 3.9 nm	0.93	0.81	*	*
Co_3Pt-400 °C	Fm-3m (FCC)	2.2 ± 0.6 nm	0.96	0.85	0.60	3.56
Co_3Pt-550 °C	Fm-3m (FCC)	3.9 ± 2.5 nm	0.96	0.85	0.60	4.07
Co_3Pt-700 °C	Fm-3m (FCC)	4.9 ± 3.9 nm	0.95	0.84	0.48	4.35

[a] Calculated by counting 100 small particles and agglomerates. [b] Potential vs. RHE. [c] Kinetic current at 0.8 V calculated from Koutecky-Levich plots [d] Specific activity at 0.8 V calculated from kinetic current values. * Not determinable from experimental data.

Polarization curves for the ORR on the Co_xPt_y catalysts, along with the E-TEK Pt reference, are seen in Figures 4.10 ($CoPt_3$), 4.11 (CoPt) and 4.12 (Co_3Pt). Immediately observable are the diffusion-limited mass activities of the Co_xPt_y NPs, which increase with decreased Co content within the NPs ($CoPt_3$ > CoPt > Co_3Pt) and remain reasonably consistent irrespective of annealing temperature. The onset potentials of the Co_xPt_y catalysts are similar, with the $CoPt_3$ and Co_3Pt catalysts having almost identical onset potentials to each other and to that of E-TEK Pt; the CoPt catalysts have slightly lower onset potentials (Table 4.3). Within each composition set, the onset potentials slightly decrease with increased annealing temperature due to the larger NP sizes and decreased surface areas induced by the annealing process. Using the inflection potentials (E_{Inf}) of the ORR polarization curves as a measure of catalytic activity reveals the same general trend: E-TEK Pt > $CoPt_3$ > Co_3Pt > CoPt (Table 4.3).

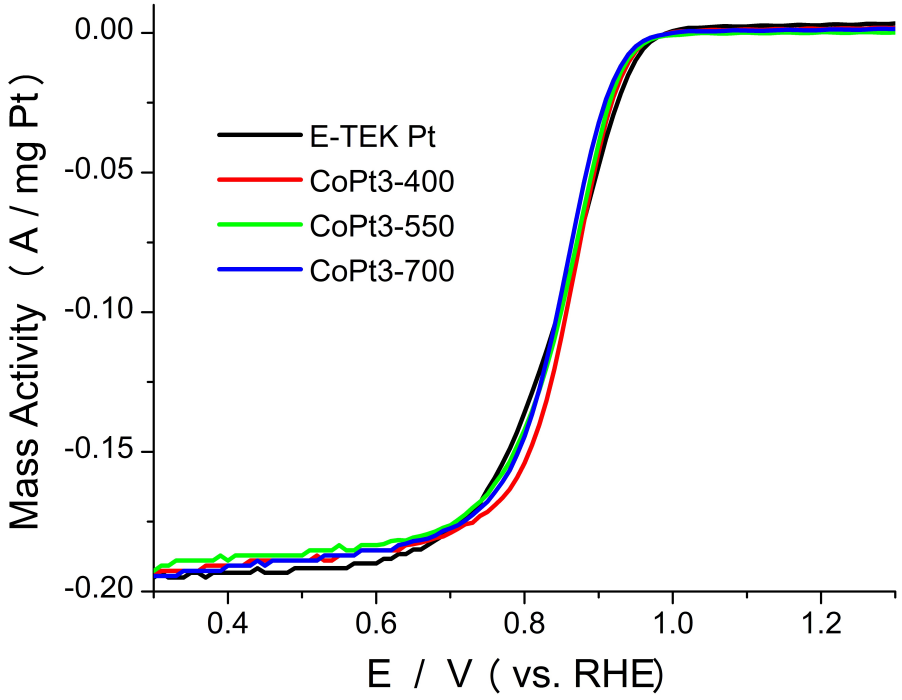

Figure 4.10. ORR polarization curves of the $CoPt_3$ NP catalysts in 0.1 M $HClO_4$ solution. Black line indicates E-TEK Pt catalyst as reference. Curves were recorded at 25 °C with 5 mV/s scan rates and 1600 rpm rotation rates.

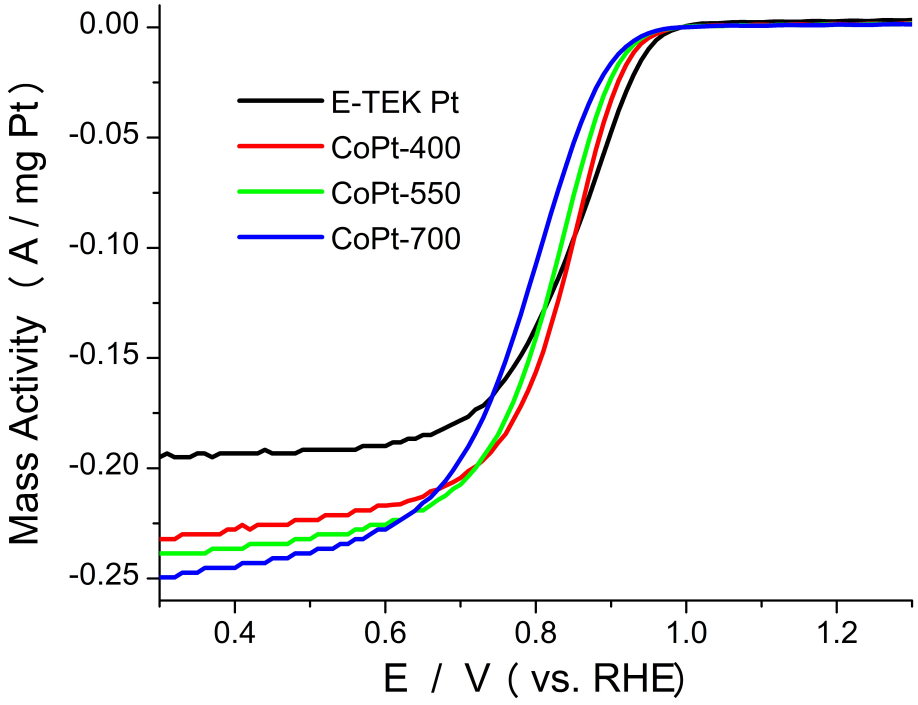

Figure 4.11. ORR polarization curves of the CoPt NP catalysts in 0.1 M $HClO_4$ solution. Black line indicates E-TEK Pt catalyst as reference. Curves were recorded at 25 °C with 5 mV/s scan rates and 1600 rpm rotation rates.

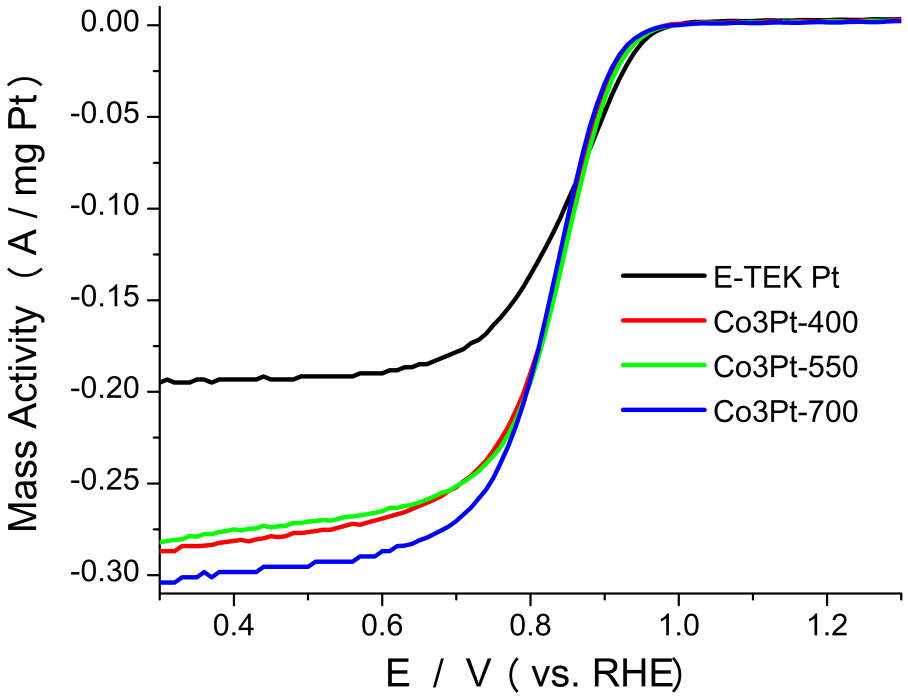

Figure 4.12. ORR polarization curves of the Co_3Pt NP catalysts in 0.1 M $HClO_4$ solution. Black line indicates E-TEK Pt catalyst as reference. Curves were recorded at 25 °C with 5 mV/s scan rates and 1600 rpm rotation rates.

To obtain additional information on the electrocatalytic activities of the Co_xPt_y catalysts, kinetic currents and specific activities at 0.8 V (within the mixed kinetic/diffusion region) were derived from the ORR polarization curves and the ECSAs of the catalysts. The kinetic currents are calculated directly from Koutecky-Levich plots (Figure 4.S11), while the specific activities use the kinetic current data in conjunction with the ECSAs determined from H_2-adsorption curves (Figure 4.S12).[223] These results are also listed in Table 4.3. From the slopes of the Koutecky-Levich plots, the number of electrons transferred during the ORR experiment at 0.8 V

was calculated to be roughly 4 for the E-TEK Pt, $CoPt_3$, and Co_3Pt catalysts. This value indicates the complete reduction of O_2 to H_2O, a 4-electron process, on these catalysts. 4-electron reduction could not be confirmed for the CoPt catalysts at 0.8 V. Only in the diffusion-limited region (below 0.65 V), could the 4-electron reduction on each of the CoPt catalysts be unequivocally calculated.

As shown in Table 4.3, the ORR kinetic currents of the E-TEK Pt reference and the $CoPt_3$ catalysts are much greater than those of the CoPt and Co_3Pt catalysts, whose kinetic currents are very similar. However, when normalizing with respect to ECSA, all of the Co_xPt_y catalysts have higher specific activities than the E-TEK Pt, in agreement with previous reports.[57,206,207,214,216,223] Within a given composition set, the kinetic currents appear to decrease somewhat with increasing annealing temperature, but the specific activities are fairly constant and represent a more reliable reference for catalytic activity. We now consider the effects of particle size, composition and architecture on each of these experimental results.

The NP sizes have minimal influence on the ORR onset potentials in agreement with the studies by Koh *et al.*[57,216] Although the ORR onset potentials within a composition set decrease with increasing annealing temperature and increasing particle size, these differences are miniscule. The $CoPt_3$ and Co_3Pt catalysts have nearly identical onset potentials despite having varying particle sizes. This observation also shows that the onset potentials are minimally affected by NP composition. The one property shared by each of the $CoPt_3$ and Co_3Pt catalysts is that they all have cubic crystal structures. Only the CoPt-400 °C catalyst, which was earlier shown to have a mixed cubic-tetragonal structure, has comparable onset

potentials to the $CoPt_3$ and Co_3Pt catalysts. Furthermore, the onset potentials of the CoPt catalysts decrease with increased annealing temperature, accompanied by further transformation into a stable FCT intermetallic. This suggests that the crystal structure of the Co_xPt_y catalysts primarily influence their ORR activity, in agreement with earlier reports.[57,216,236]

The kinetic data obtained from the Koutecky-Levich plots can also be used to distinguish the different Co_xPt_y catalysts. As shown in Table 4.3, the specific activities of the $CoPt_3$ catalysts are noticeably greater than the CoPt and Co_3Pt catalysts. This suggests that the ORR proceeds faster on these Pt-rich catalysts vs. their counterparts containing more Co, as expected from previous studies demonstrating improved ORR kinetics on a Pt surface vs. those of earlier transition metals.[206,237,238] In the case of these $CoPt_3$ catalysts, any alteration in electronic structure or surface identity resulting from architectural changes appears to have minimal impact on the kinetics of the ORR, as the specific activities remain relatively constant regardless of these changes.

The kinetic currents of the CoPt and Co_3Pt catalysts are quite similar to each other despite their differing sizes, compositions, and architectures. Assuming some amount of Co dissolution occurs in the alloy Co_3Pt catalysts, it is possible for them to have similar amounts of Pt and Co on their surfaces such that they have similar amounts of active Pt sites as the CoPt catalysts. It could be argued that the intermetallic structure seen in the CoPt catalysts prohibits the level of Co dissolution experienced by the alloy particles. Assuming Co dissolution occurs such that the CoPt

and Co_3Pt catalysts have similar surfaces (in terms of surface metal ratios), then the similar kinetic results are quite reasonable.

To summarize, XRD analysis has shown the CoPt catalysts to primarily exist as tetragonal intermetallics, while the $CoPt_3$ and Co_3Pt have cubic structures in both alloy and intermetallic phase. Previous studies have shown the cubic structure to be uniquely active of ORR catalysis and support the results reported here. With respect of specific ORR activity, the $CoPt_3$ catalysts are already Pt-rich regardless of architecture and have the highest values of the Co_xPt_y catalysts studied here. The low stability of the alloy phase results in the dissolution of Co from the Co_3Pt catalysts, thereby increasing the amount of active Pt sites to numbers near that of the more stable CoPt catalysts. As a result, the specific activities of these two catalysts are roughly the same.

4.4 Conclusion

In summary, a series of Co_xPt_y NPs with controlled compositions and architectures were synthesized through a simple co-reduction method. The Co_xPt_y electrocatalysts were tested for their activities towards CO-tolerant HOR and ORR electrochemical reactions to probe the influences of size, composition, and architecture. The Co_xPt_y catalysts were found to have similar or less CO tolerance relative to monometallic Pt, with the modifications induced by atomic ordering of Co and Pt found to negatively impact their activity for the HOR. Each of the Co_xPt_y catalysts have similar activity for the ORR, with improvements in specific activity arising from modifying the NPs' composition. Overall, the Co_3Pt NPs have HOR and ORR catalytic activities comparable to monometallic Pt, but utilize far less Pt to

achieve this result, leading to a significant reduction in the overall cost of the electrocatalyst.

4.5 Supplemental Information

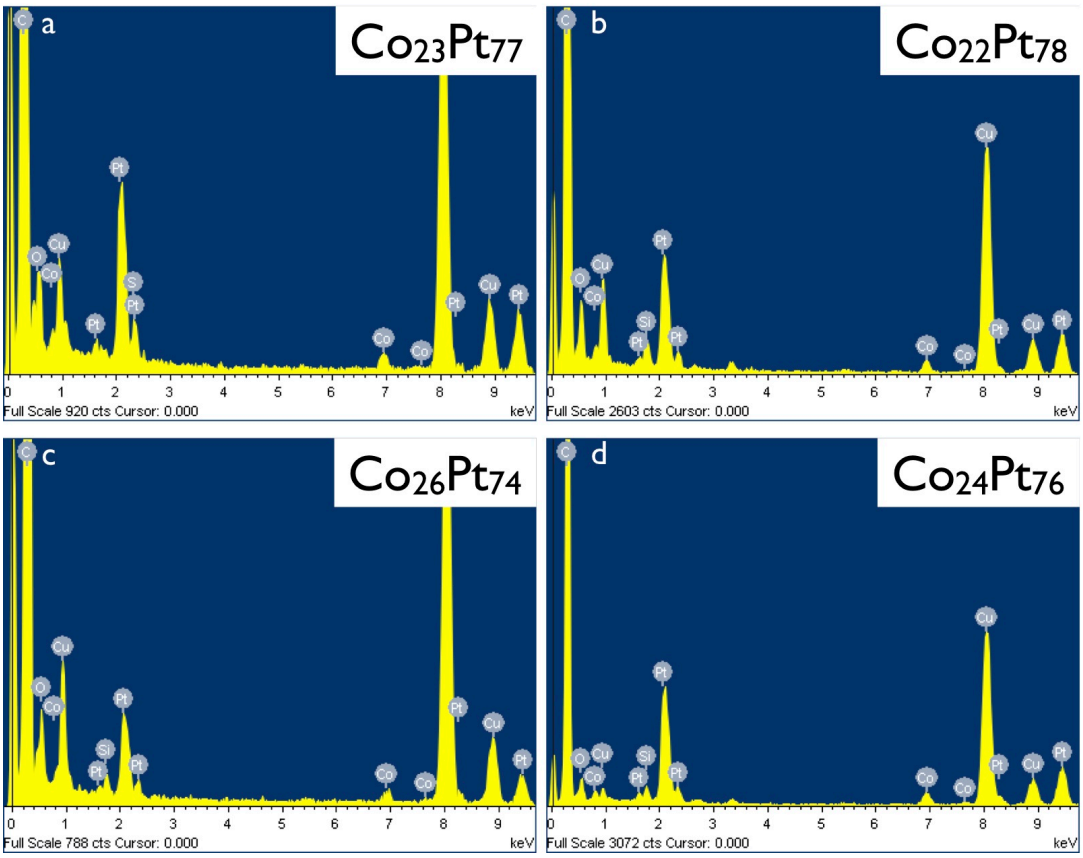

Figure 4.S1. EDS analysis of the (a) AP, (b) 400 °C (c) 550 °C, and (d) 700 °C $CoPt_3$ NPs.

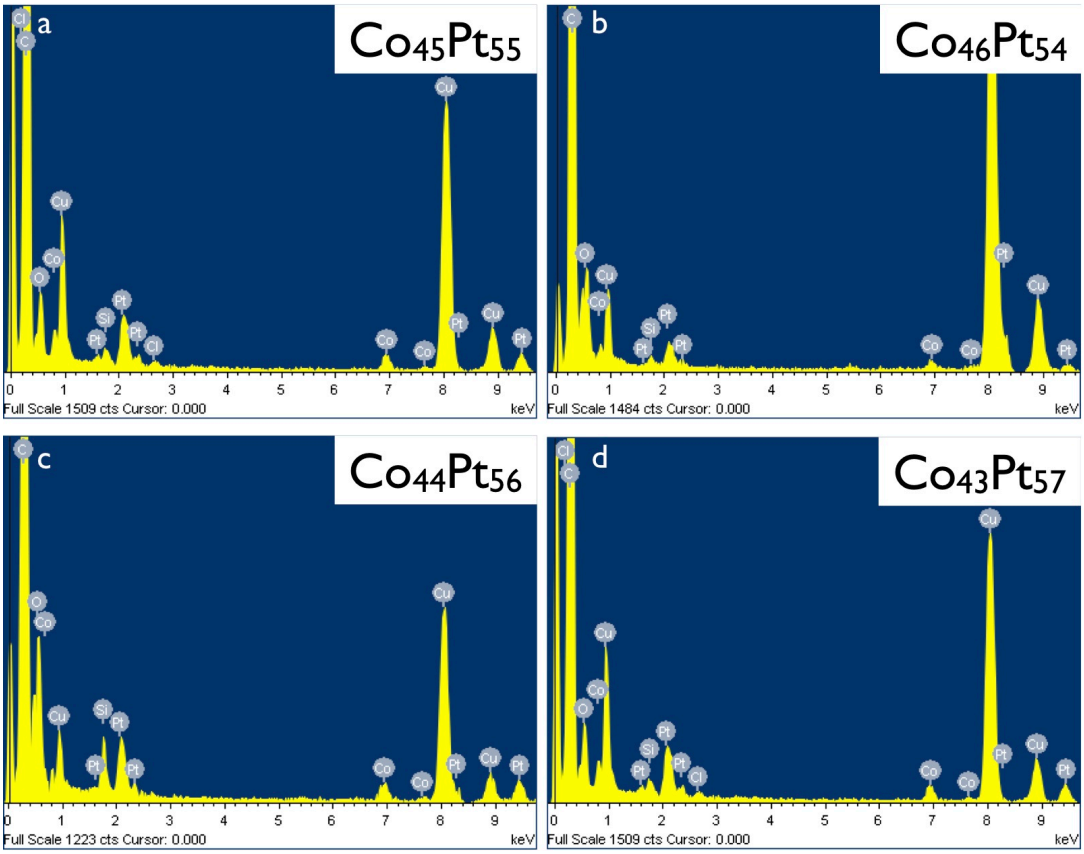

Figure 4.S2. EDS analysis of the (a) AP, (b) 400 °C, (c) 550 °C, and (d) 700 °C CoPt NPs.

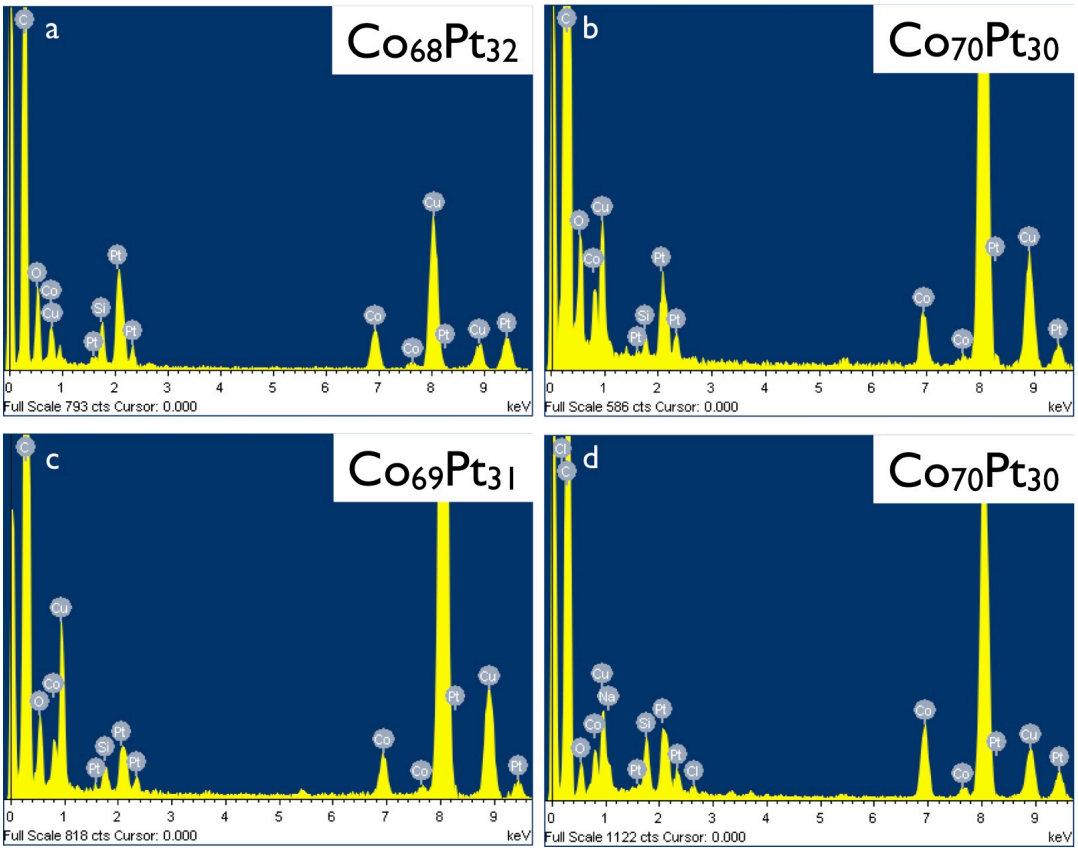

Figure 4.S3. EDS analysis of the (a) AP, (b) 400 °C, (c) 550 °C, and (d) 700 °C Co_3Pt NPs.

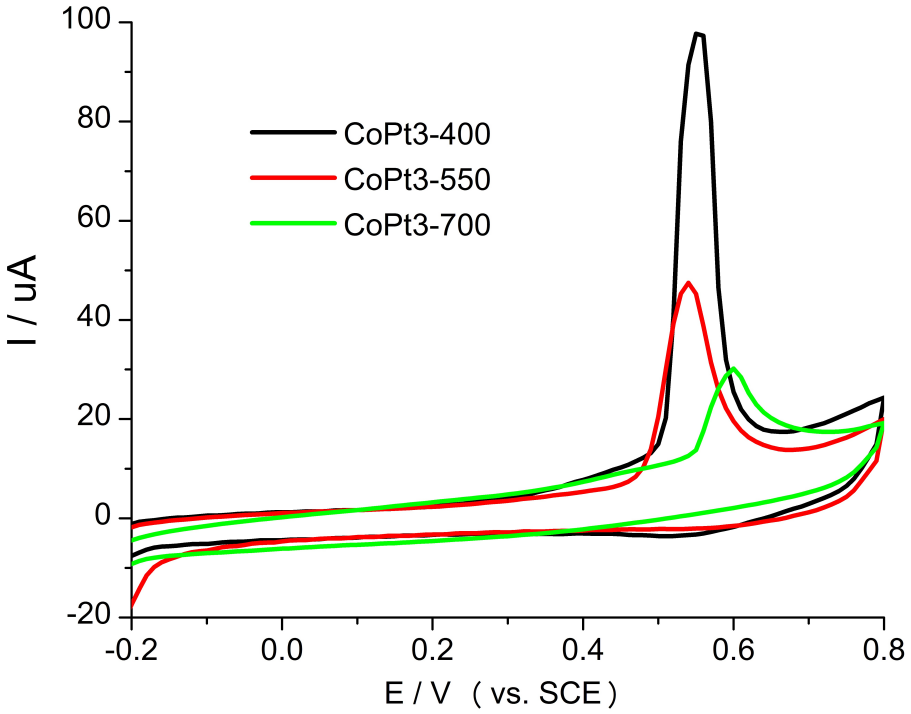

Figure 4.S4. CO stripping curves of the $CoPt_3$ NP catalysts in 0.5 M H_2SO_4 solution at 25 °C. Scan rate: 20 mV/s.

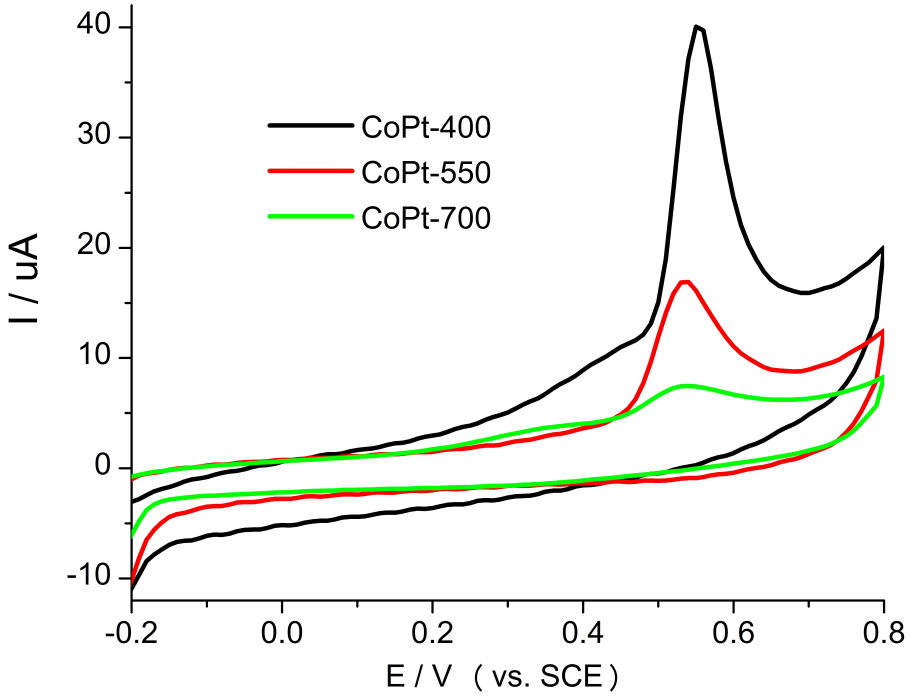

Figure 4.S5. CO stripping curves of the CoPt NP catalysts in 0.5 M H_2SO_4 solution at 25 °C. Scan rate: 20 mV/s.

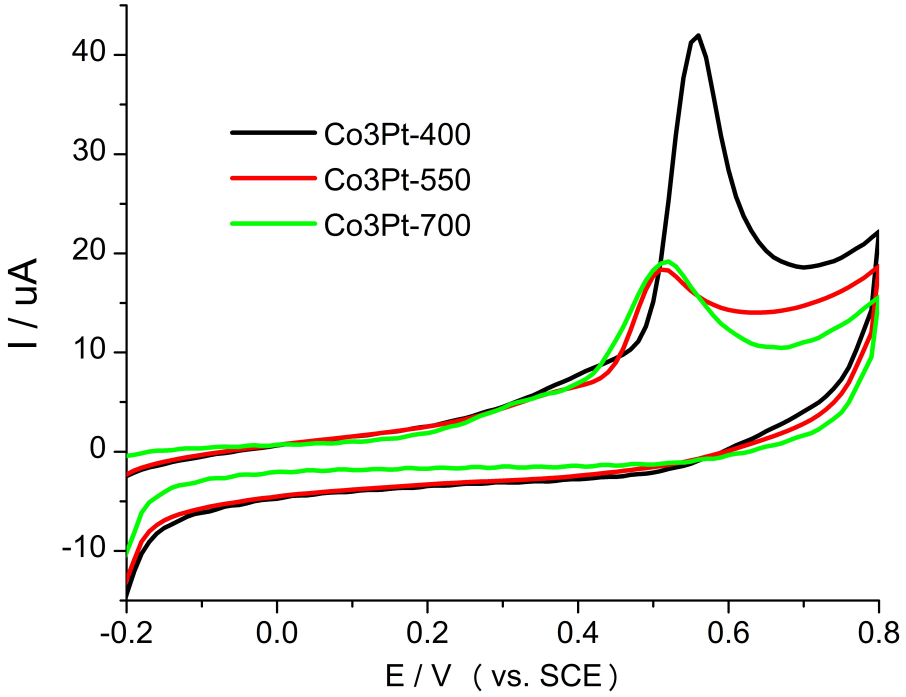

Figure 4.S6. CO stripping curves of the Co_3Pt NP catalysts in 0.5 M H_2SO_4 solution at 25 °C. Scan rate: 20 mV/s.

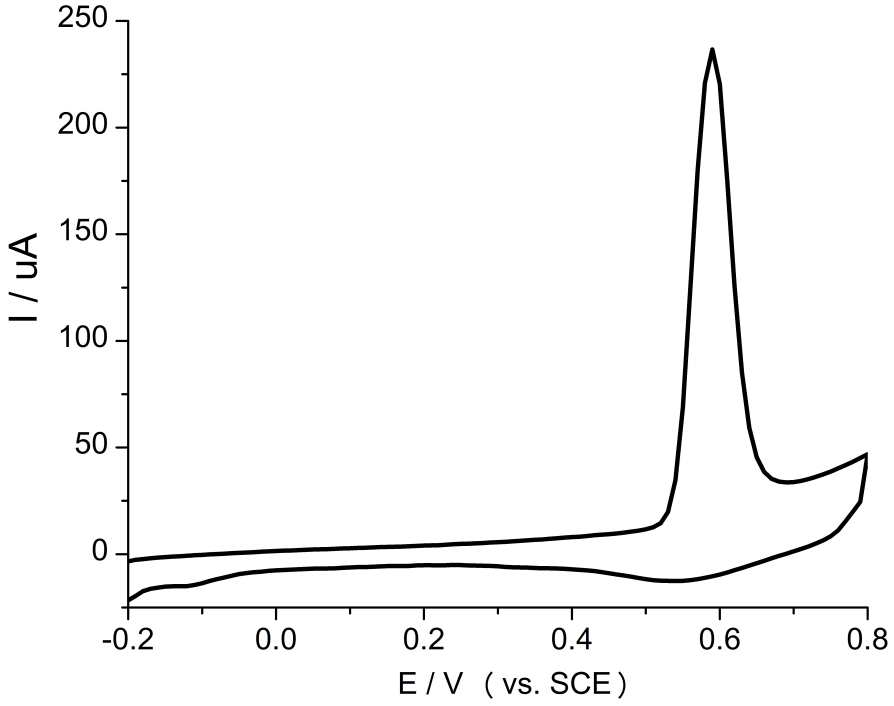

Figure 4.S7. CO stripping curve of the E-TEK Pt catalyst in 0.5 M H_2SO_4 solution at 25 °C. Scan rate: 20 mV/s.

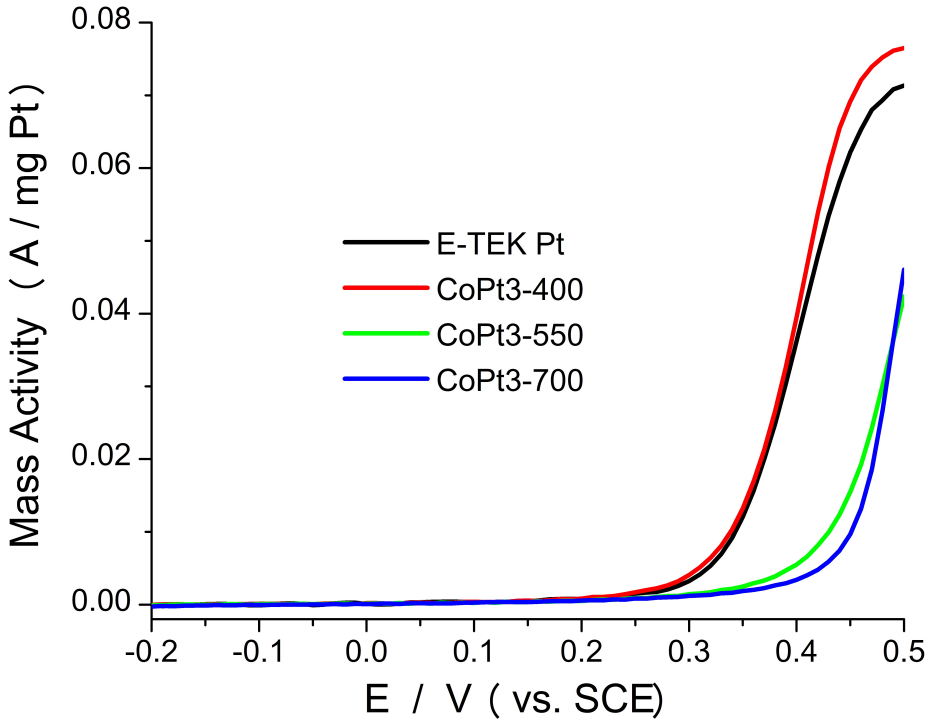

Figure 4.S8. Polarization curves for the electrooxidation of CO-contaminated H_2 (1000 ppm CO, balance H_2) of the $CoPt_3$ NP catalysts in 0.5 M H_2SO_4 solution. Black line indicates E-TEK Pt catalyst as reference. Curves were recorded at 25 °C with 1 mV/s scan rates and 1600 rpm rotation rates.

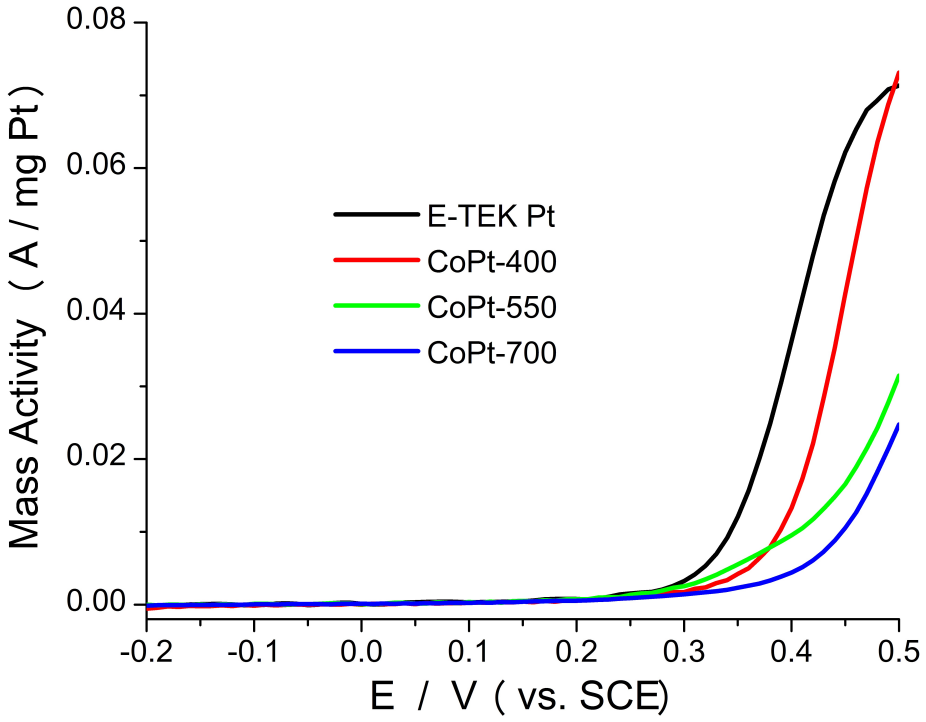

Figure 4.S9. Polarization curves for the electrooxidation of CO-contaminated H_2 (1000 ppm CO, balance H_2) of the CoPt NP catalysts in 0.5 M H_2SO_4 solution. Black line indicates E-TEK Pt catalyst as reference. Curves were recorded at 25 °C with 1 mV/s scan rates and 1600 rpm rotation rates.

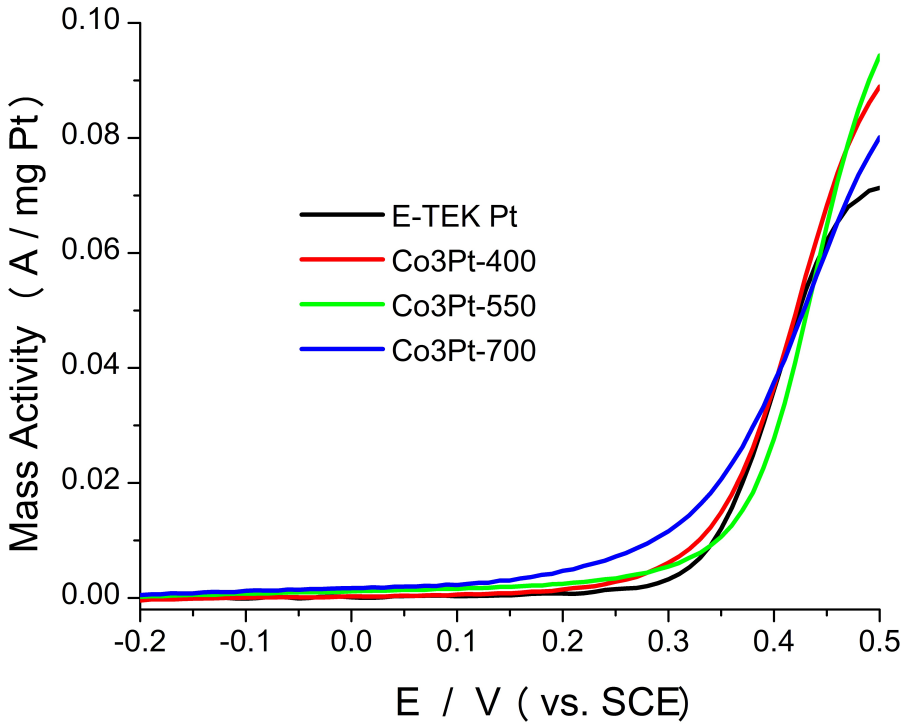

Figure 4.S10. Polarization curves for the electrooxidation of CO-contaminated H_2 (1000 ppm CO, balance H_2) of the Co_3Pt NP catalysts in 0.5 M H_2SO_4 solution. Black line indicates E-TEK Pt catalyst as reference. Curves were recorded at 25 °C with 1 mV/s scan rates and 1600 rpm rotation rates.

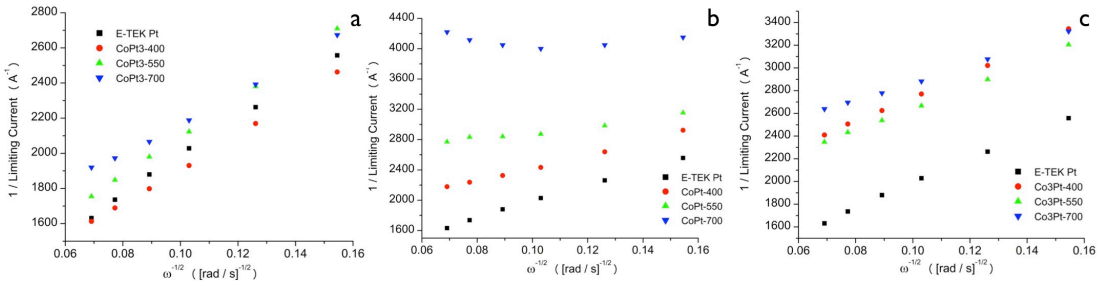

Figure 4.S11. Koutecky-Levich plots derived from ORR data for the (a) $CoPt_3$, (b) CoPt, and (c) Co_3Pt catalysts at 0.8 V (vs. RHE), along with the E-TEK Pt reference.

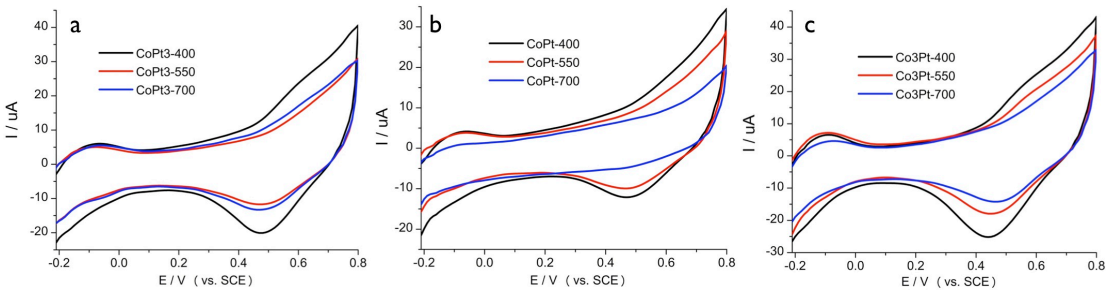

Figure 4.S12. H_2-adsoprtion curves for the (a) $CoPt_3$, (b) CoPt, and (c) Co_3Pt catalysts in Ar-saturated 0.1 M $HClO_4$ solution at 25 °C. Scan rate: 50 mV/s.

Chapter 5: Bimetallic Core-Shell Nanoparticles for Preferential Oxidation of Carbon Monoxide in the Presence of Hydrogen

5.1 Introduction

The primary means of producing H_2 fuel for proton exchange membrane fuel cell (PEMFC) devices is through the hydrocarbon steam reformation and the water gas-shift (WGS) processes.[6] Unfortunately, the resultant H_2 fuel contains a significant amount of unconverted CO, which poisons the Pt-based catalysts within the PEMFCs.[5] This catalyst poisoning is one of the major obstacles preventing the commercialization of PEMFCs.[239] To reduce the amount of CO to acceptable levels for PEMFC operation, it is oxidized to CO_2 through a catalytic process known as preferential oxidation (PrOx).[240,241] Selectively converting CO to CO_2 at a high rate, while minimizing the conversion of H_2 fuel to H_2O represents the ideal for a PrOx catalyst. Traditionally, this process requires expensive catalysts operating under very specific conditions.[242]

Previously, our group studied Rh-Pt bimetallic NPs with alloy and core-shell (C@S) architectures to compare their structure-dependent properties and catalytic activities.[61] It was shown that the Rh@Pt core-shell NPs had superior activity for PrOx relative to their alloy or monometallic counterparts, despite the NPs having the same sizes, shapes, and atomic ratios. The enhancements in catalytic activity of the core-shell architecture can be explained using theoretical models.

In their theoretical studies of single layer metal surfaces laid over metal substrates, the Norskov and Mavrikakis groups used density functional theory (DFT) calculations to show that the underlying metal can induce strain on the surface metal.[154,243] This strain results in a shifting of the surface metal's *d*-band center, which impacts the binding energy of molecular and atomic adsorbates.[244] By correlating the *d*-band center of a particular bimetallic surface-substrate combination with these adsorbate binding energies, core-shell NP catalysts can now be predicted to have specific activity for a given catalytic process.

Using DFT calculations provided by Nilekar and Mavrikakis, our group later synthesized a series of M@Pt (M = Ru, Rh, Ir, Pd, Pt) NPs, which were tested for PrOx activity.[75] The modeling studies predicted the following activity trend based on calculated binding energies of CO onto Pt surfaces: Ru@Pt > Rh@Pt > Ir@Pt > Pd@Pt > Pt. Remarkably, the experimental results directly matched the predictions, with the Ru@Pt NPs in particular having very high PrOx activity These enhancements in activity were credited to a lowering of the Pt *d*-band center by the core metal (Ru, Rh, Pd, or Ir), thereby reducing the CO-metal interaction and facilitating its catalytic oxidation to CO_2. This study represented one of the first demonstrations of "catalysts by design", where theoretical models were used to predict catalytic performance and guide the development of NP catalysts.

Unfortunately, the PrOx catalysts described above are fully comprised of precious metals, causing them to be quite expensive. While use of the core-shell architecture can decrease costs by limiting the precious metal only to the NP surface, employing earth-abundant metals would further reduce the costs of the PrOx catalyst.

However, PrOx catalysts using non-precious metals tend to have lower activities and often require higher operating temperatures (>150 °C) than precious metal catalysts, including the core-shell NP catalysts mentioned earlier.[241,245] An efficient catalyst using earth-abundant metals (such as Ni) would combine the ideals of low cost and high performance and represents the ultimate goal of PrOx catalyst design.

Towards this goal, we aimed to synthesize Ni-shell NPs with various metal cores in an effort to improve the catalytic activity of Ni. Using relatively electron-rich substrate metals (Ru, Pd, Pt) should result in a heightened *d*-band center for the Ni surface layer.[40] This electronic modulation may enhance or hinder the binding of reactive species, but should definitely result in modified catalytic activity. These preliminary studies will pave the way for future catalysts comprised of only earth-abundant materials.

Here, we present the synthesis of a series of bimetallic core-shell NPs of varying compositions, including unique M@Ni (M = Ru, Pd, Pt) NPs with near-monolayer Ni shells. The NPs were fully characterized by a combination of XRD, TEM, EDS, and CO-FTIR techniques to elucidate their structures. Preliminary catalytic studies were performed on the Ru@Ni and Pt@Ni NPs, where they were compared to each other and to monometallic Ni particles. It was found that the Ru@Ni and Pt@Ni NPs had higher catalytic performance for CO and H_2 oxidation relative to monometallic Ni particles. The differences in catalytic activity are attributed to electronic structure modifications of the Ni surface, as induced by the Ru and Pt cores, which change the nature of its interactions with reactant gases and intermediates.

5.2 Experimental

5.2.1 Materials

Ruthenium acetylacetonate ($Ru(acac)_3$, 97%), palladium acetylacetonate ($Pd(acac)_2$, 99%), sodium borohydride ($NaBH_4$, 98%), ethylene glycol (EG, 99%), polyvinylpyrrolidone (PVP, Typical M_w: 55,000), acetone (99.5%), and methanol (MeOH, 99.9%) were purchased from Aldrich. Nickel acetylacetonate ($Ni(acac)_2$, anhydrous, 95%) was purchased from Strem Chemical. Palladium chloride ($PdCl_2$, 60.0% Pd) and platinum chloride ($PtCl_2$, 73.09% Pt) were purchased from Engelhard. Sodium Bromide (NaBr, 99%) was purchased from Baker. Aluminum Oxide (alumina, γ-Al_2O_3, 99.97%) was purchased from Alfa Aesar. Ethanol (EtOH, 99.98%) was purchased from Pharmco-AAPER. Diethyl Ether (Et_2O, anhydrous, 99.9%) and hexanes (99.97%) were purchased from Fisher Scientific. Ultra-pure water was obtained from deionized water using a Millipore Academic Milli-Q A10 purifier system. $Ni(acac)_2$ was stored in a glove box until ready to use. All materials were used as received without further purification. All reactions were carried out on Schlenk lines under N_2 atmosphere.

5.2.2 Synthesis of Monometallic Nanoparticles

5.2.2.1 Synthesis of Monometallic Ru NPs

In a typical synthesis, $Ru(acac)_3$ (40.0 mg, 0.1 mmol Ru) was mixed with PVP (28.0 mg, 0.51 mmol) and EG (20 mL) in a RBF equipped with a magnetic stirrer and a reflux condenser. The mixture was stirred and heated to ~70 °C under vacuum to

degas the system. Once degassed, the mixture was placed under N_2 atmosphere and then held at ~70 °C for 30 min to dissolve the contents. The red solution was then rapidly brought to reflux (~10 min), where it was held for 90 min, before being quenched over ice water. The solution turned black and colloidal in the 150-180 °C temperature range. This procedure leads to Ru NPs 3.0 nm in diameter.

5.2.2.2 Synthesis of Monometallic Pd NPs

In a typical synthesis, $Pd(acac)_2$ (28.0 mg, 0.9 mmol Pd) was mixed with PVP (40.0 mg, 0.72 mmol), NaBr solution (500 μL, 0.02 M in EG), and EG (20 mL) in a RBF equipped with a magnetic stirrer and a reflux condenser. The mixture was stirred and heated to ~70 °C under vacuum to degas the system. Once degassed, the mixture was placed under N_2 atmosphere and then held at ~70 °C for 30 min to dissolve the contents. The yellow/gold solution was then rapidly brought to reflux (~10 min), where it was held for 60 min, before being quenched over ice water. The solution turned black and colloidal in the 90-120 °C temperature range. This procedure leads to Pd NPs 5.2 nm in diameter.

5.2.2.3 Synthesis of Monometallic Pt NPs

In a typical synthesis, $PtCl_2$ (18.0 mg, 0.07 mmol Pt) was mixed with PVP (60.0 mg, 1.1 mmol) and EG (20 mL) in a RBF equipped with a magnetic stirrer and a reflux condenser. The mixture was stirred and heated to ~70 °C under vacuum to degas the system. Once degassed, the mixture was placed under N_2 atmosphere and then held at ~70 °C for 30 min to dissolve the contents. The dark brown solution was

then rapidly brought to reflux (~10 min), where it was held for 60 min, before being quenched over ice water. The solution turned black and colloidal in the 130-160 °C temperature range. This procedure leads to Pt NPs 4.5 nm in diameter.

5.2.2.4 Synthesis of Monometallic Ni NPs

Ni NPs can be synthesized using the same EG reduction method used for the Ru, Pd, and Pt NPs. In a typical synthesis, $Ni(acac)_2$ (25.0 mg, 0.1 mmol Ni) was mixed with PVP (80.0 mg, 1.45 mmol) and EG (20 mL) in a RBF equipped with a magnetic stirrer and a reflux condenser. The mixture was stirred and heated to ~70 °C under vacuum to degas the system. Once degassed, the mixture was placed under N_2 atmosphere and then held at ~70 °C for 30 min to dissolve the contents. The light green solution was then rapidly brought to reflux (~10 min), where it was held for 5 min, before being quenched over ice water. The light green solution begins to lighten at 140 °C and becomes completely yellow by 180 °C. The solution gradually becomes darker and turns black and colloidal in the 190-195 °C temperature range. This procedure leads to Ni NPs 43.8 nm in diameter.

To produce small Ni NPs, Ni^{2+} reduction using $NaBH_4$ can be employed. In a typical synthesis, $Ni(acac)_2$ (25.0 mg, 0.1 mmol Ni) was mixed with PVP (80.0 mg, 1.45 mmol) and EG (20 mL) in a RBF equipped with a magnetic stirrer and a reflux condenser. The mixture was stirred and heated to ~70 °C under vacuum to degas the system. Once degassed, the mixture was placed under N_2 atmosphere and then held at 140 °C for 15 min to dissolve the contents. Excess $NaBH_4$ (55.0 mg) was then added to the light green solution, which instantly became black and colloidal with the

evolution of H_2 gas. The reaction was maintained at 140 °C for 60 min, before being quenched over ice water. This procedure leads to Ni NPs 2.6 nm in diameter.

5.2.3 Synthesis of Bimetallic Nanoparticles

5.2.3.1 Synthesis of Ru@Ni Core-Shell NPs

In a typical synthesis, $Ni(acac)_2$ (30.0 mg, 0.12 mmol Ni) was added to 10 mL of Ru NP colloidal suspension along with additional EG (10 mL). The mixture was stirred and heated to ~70 °C under vacuum to degas the system, then placed under N_2 atmosphere. The mixture was then brought to 160 °C, where it was held for 90 min, before being quenched over ice water. This procedure leads to Ru@Ni NPs 3.6 nm in diameter, with ~1 layer thick Ni shells coating the Ru core. To increase the shell thickness to ~2-3 layers (4.6 nm NPs), 40 mg (0.16 mmol Ni) of $Ni(acac)_2$ was used instead.

5.2.3.2 Synthesis of Pd@Ni Core-Shell NPs

In a typical synthesis, $Ni(acac)_2$ (32.0 mg, 0.125 mmol Ni) was added to 10 mL of Pd NP colloidal suspension along with additional EG (10 mL). The mixture was stirred and heated to ~70 °C under vacuum to degas the system, then placed under N_2 atmosphere. The mixture was heated to 110 °C, where it was held for 30 min, then heated to 115 °C and held there for 90 min. The reaction was finally quenched over ice water. This procedure leads to Pd@Ni NPs 5.7 nm in diameter, with ~1 layer thick Ni shells coating the Pd core.

5.2.3.3 Synthesis of Pt@Ni Core-Shell NPs

In a typical synthesis, $Ni(acac)_2$ (16.0 mg, 0.06 mmol Ni) was added to 10 mL of Pt NP colloidal suspension along with additional EG (10 mL). The mixture was stirred and heated to ~70 °C under vacuum to degas the system, then placed under N_2 atmosphere. The mixture was heated to 120 °C, where it was held for 60 min, then heated to 125 °C and held there for 60 min. The reaction was finally quenched over ice water. This procedure leads to Pt@Ni NPs 5.1 nm in diameter, with ~1 layer thick Ni shells coating the Pt core.

5.2.3.4 Synthesis of Ru@Pd Core-Shell NPs

In a typical synthesis, $PdCl_2$ (9.5 mg, 0.05 mmol Pd) and PVP (7.5 mg, 0.14 mmol) were added to 10 mL of Ru NP colloidal suspension along with additional EG (10 mL). The mixture was stirred and heated to ~60 °C under vacuum to degas the system, then placed under N_2 atmosphere. The mixture was then brought to 100 °C, where it was held for 120 min. The reaction was slowly ramped to 120 °C at an average rate of 1 °C/min, then to reflux at an average rate of 1.5 °C/min. The reaction was held at reflux for 90 min before being quenched over ice water. This procedure leads to Ru@Pd NPs 3.9 nm in diameter, with ~1 layer thick Pd shells coating the Ru core.

5.2.3.5 Synthesis of Ru@Pt Core-Shell NPs

In a typical synthesis, $PtCl_2$ (14.0 mg, 0.05 mmol Pt) was added 10 mL of Ru NP colloidal suspension along with additional EG (10 mL). The mixture was stirred and heated to ~80 °C under vacuum to degas the system, then placed under N_2 atmosphere. The mixture was quickly (~ 5 min) brought to 125 °C, then slowly ramped to 170 °C at an average rate of 1 °C/min. Once at 170 °C, the reaction was brought to reflux, where it was held for 60 min, before being quenched over ice water. This procedure leads to Ru@Pt NPs 3.7 nm in diameter, with ~1 layer thick Pt shells coating the Ru core.

5.2.3.6 Synthesis of Pt@Pd Core-Shell NPs

In a typical synthesis, $PdCl_2$ (5.0 mg, 0.03 mmol Pd) was added to 10 mL of Pt NP colloidal suspension along with additional EG (10 mL). The mixture was stirred and heated to ~70 °C under vacuum to degas the system, then placed under N_2 atmosphere and held for 60 min. The mixture was then slowly brought to 90 °C at an average rate of 0.33 °C/min and held at 90 °C for 60 min. The reaction was finally quenched over ice water. This procedure leads to Pt@Pd NPs 5.1 nm in diameter, with ~1 layer thick Pd shells coating the Pt core.

5.2.3.7 Synthesis of Pd@Pt Core-Shell NPs

In a typical synthesis, $PtCl_2$ (6.0 mg, 0.02 mmol Pt) was added to 10 mL of Pd NP colloidal suspension along with additional EG (10 mL). The mixture was stirred

and heated to ~80 °C under vacuum to degas the system, then placed under N_2 atmosphere. The mixture was then brought to 120 °C at a rate of 1.5 °C/min and held at 120 °C for 120 min, before being quenched over ice water. This procedure leads to Pd@Pt NPs 5.7 nm in diameter, with ~1 layer thick Pt shells coating the Pd core.

5.2.3.8 Synthesis of NiRu Alloy NPs

In a typical synthesis, $Ni(acac)_2$ (22.0 mg, 0.085 mmol Ni) and $Ru(acac)_3$ (34.0 mg 0.085 mmol Ru) were mixed with PVP (60.0 mg, 1.1 mmol) and EG (20 mL) in a RBF equipped with a magnetic stirrer and a reflux condenser. The mixture was stirred and heated to ~70 °C under vacuum to degas the system. Once degassed, the mixture was placed under N_2 atmosphere and then held at 130 °C for 15 min. Excess $NaBH_4$ (100.0 mg, 2.64 mmol) was then added to the dark red solution, which instantly became black and colloidal with the evolution of gas. The reaction was maintained at 130 °C for 60 min, before being quenched over ice water. This procedure leads to NiRu NPs 2.1 nm in diameter.

5.2.4 Characterization of Nanoparticles

5.2.4.1 Powder X-ray Diffraction

Powder X-ray diffraction (XRD) patterns of samples were obtained on a Bruker C2 Discover diffractometer equipped with a VÅNTEC-500 detector using a monochromatic Cu Kα radiation source biased at 40 kV and 40 mA. The NP solutions (2 mL) were washed with acetone (10 mL) and centrifuged at 13000 rpm to precipitate the NPs and the supernatant was discarded. This washing process was

repeated multiple times. After the final wash, the precipitated NP powders were dried under vacuum. The dried NP powders were pressed on a glass slide for analysis.

5.2.4.2 CO-Probe Fourier Transform Infrared Spectroscopy

CO-probe Fourier transform infrared spectra (CO-FTIR) were collected on a Thermo Scientific Nexus 870 FT-IR spectrometer. The NP solutions were bubbled with CO using a stainless steel needle submerged in the solution at a 30 SCCM flow rate for 20 min. An aliquot (100 μL) of the CO-saturated NP solution was placed into a liquid IR cell consisting of a 0.5 mm Teflon spacer sandwiched between two rectangular-shaped CaF_2 windows. The NP solution prior to CO bubbling was used for the background spectra.

5.2.4.3 Transmission Electron Microscopy with Energy-Dispersive X-Ray Spectroscopy

Transmission electron microscope (TEM) images were obtained on a JEM 2100F Field Emission TEM operating at 200 kV. Energy dispersive spectroscopy (EDS) data were collected on the same TEM operating in STEM mode. The NP solutions were dispersed in MeOH, and an aliquot (10 μL) of the resulting dispersion was drop cast on the TEM grids. The TEM grids used were carbon-coated Cu grids (CF400-Cu, Electron Microscopy Sciences).

5.2.5 Preparation and Evaluation of Nanoparticle Catalysts

5.2.5.1 Preparation of NP Loaded Al_2O_3 Catalysts

The metal loading of each Al_2O_3 catalyst varies with respect to the surface metal given the different atomic sizes and densities of the metals used. This was done in an effort to maintain roughly equal numbers of metal surface atoms for each catalyst system. The intention is to correlate any differences in catalytic activities with the composition/arrangement (rather than size, loading, etc.) of the NPs. All metal NP loadings were based on the initial amounts of reagents. Ru NPs are supported onto Al_2O_3 such that the Ru metal loading is ~0.47% by weight. For Ni and Ni shells, the Ni metal loading is ~0.22% by weight. For Pd and Pd shells, the loading is ~0.53% Pd by weight. For Pt and Pt shells, the loading is ~1% Pt by weight.

To prepare the catalysts, EtOH was placed into a 50 mL conical centrifuge tube. An appropriate amount of Al_2O_3 (to achieve the desired metal loading) was slowly added, while being physically mixed and sonicated in a sonication bath (FS30H, Fisher Scientific) until it was fully dispersed. Separately and concurrently, an appropriate amount of NP colloidal solution (to achieve the desired metal loading) was sonicated with an equal amount of EtOH in a glass vial. Once the Al_2O_3 was fully dispersed (~30 min), the NP solution was added to the tube. The resulting mixture was then sonicated and physically mixed for 60 min. Centrifuging at 6000 rpm for 20 min precipitated the catalyst powder and the supernatant was discarded. The powder was redispersed in a 1:1 EtOH:Hexanes solution (30 mL), then sonicated/physically mixed for 60 min, before again being precipitated. This process

was repeated with a 2:1 Et_2O:Hexanes solution and then just Et_2O. After the final precipitation from Et_2O, the catalyst powder was allowed to dry in air.

5.2.5.2 Evaluation of NP Loaded Al_2O_3 Catalysts for CO Oxidation and PrOx Reaction

Catalytic tests were carried out using alumina-supported NP catalysts (100 ± 1 mg) in temperature programmed reaction (TPR) setup similar to one described elsewhere.[60] Catalysts were loaded into a fixed bed reactor consisting of a quartz tube (12 mm internal diameter). The reactor bed composition was the following: quartz wool, quartz sand (5 g), quartz wool for gas homogenization, evenly loaded catalyst (3.5 ± 0.2 mm bed height), then additional quartz wool and quartz sand for support. The temperature was monitored and controlled with a K-type thermocouple placed at the tailing edge of the catalyst bed to ensure no disruption to the reactor flow. The catalysts were pretreated in 1% O_2-H_2 mixture at 300°C prior to catalytic testing. During the tests, the temperature was set to 300 °C and the heating ramp was 0.5 °C/min. The total inlet flow rate was fixed at 200 SCCM, to give a gas hourly space velocity of 100,000/hr. The gas mixture for the CO oxidation tests was composed of 1% CO (99.5% pure, Al tank), 1% O_2 (99.999% pure), 98% He (99.999% pure). The gas mixture for the PrOx reaction tests was composed of 1% CO (99.5% pure, Al tank), 1% O_2 (99.999% pure), 98% H_2 (99.999% pure). Reactor effluent was monitored using an online gas chromatograph (Varian CP-3800, Hayesep D column, Helium carrier gas) equipped with a single thermal conductivity detector (TCD).

5.3 Results and Discussions

5.3.1 Synthesis and Characterization of Monometallic Nanoparticles

The preparations of monometallic Ru, Pd, and Pt NPs via the polyol reduction method are well known and were prepared according to previous reports or through slight modifications of known methods.[78,141,246] Briefly, the chosen metal precursor salt ($Ru(acac)_3$, $Pd(acac)_2$, or $PtCl_2$) was reduced in refluxing EG in the presence of PVP stabilizers. XRD, TEM, and CO-FTIR characterizations were performed to confirm the synthesis of the Ru, Pd, and Pt NPs. The results of our experiments are consistent with previous reports.

A representative XRD pattern, TEM image, and CO-FTIR spectrum of the Ru NPs are shown in Figures 5.1 and 5.2. As expected, the XRD pattern contains a broad peak near 42°, consistent with the formation of small Ru NPs with a poorly crystalline HCP structure (Figure 5.1a). TEM analysis shows the average NP size to be 3.0 nm (Figure 5.2), while lattice fringe analysis of a single particle shows an average lattice separation of 0.20 nm, corresponding to the (101) plane of HCP Ru (inset of Figure 5.2). Finally, the peak at 2020 cm^{-1} in the CO-FTIR spectra corresponds to CO bound to Ru sites on the nanoparticle surface (Figure 5.1b).

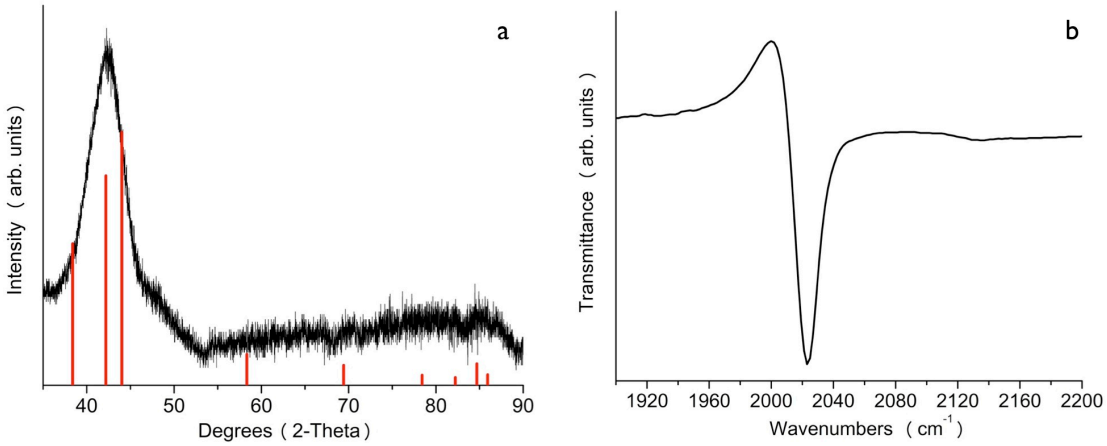

Figure 5.1. Representative (a) XRD pattern and (b) CO-FTIR spectrum of the Ru NPs. Red vertical lines indicate the peak positions for HCP phase Ru (JCPDS 01-070-0274)

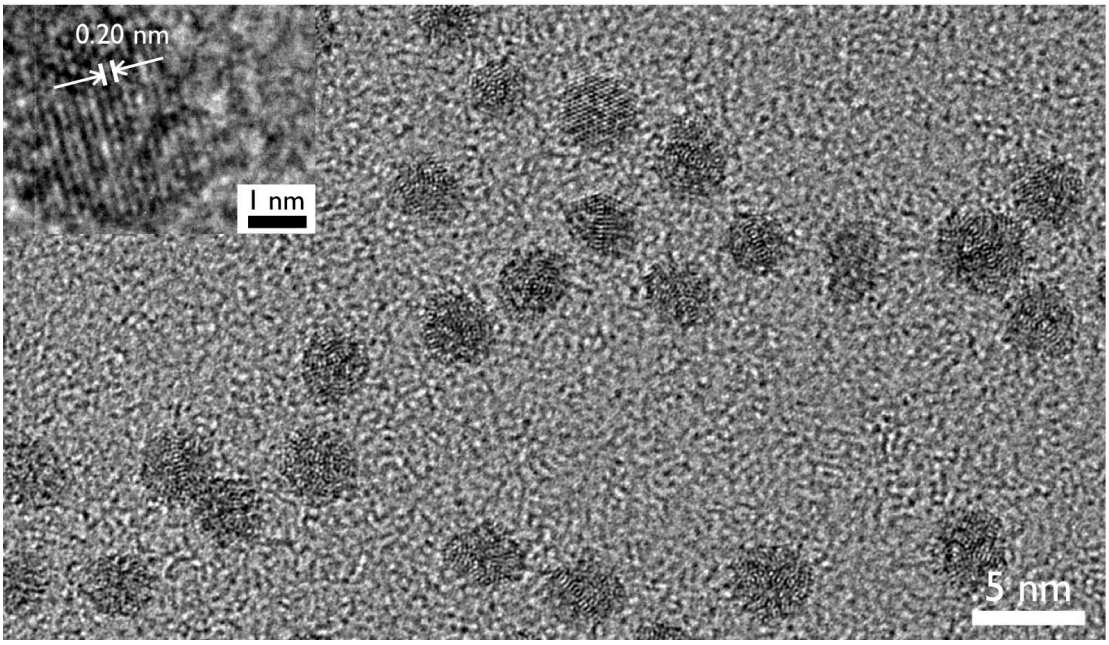

Figure 5.2. Representative TEM image of the Ru NPs. A lattice fringe image of a single particle highlighting the (101) plane of HCP Ru is inset

A representative XRD pattern, TEM image, and CO-FTIR spectrum of the Pd NPs are shown in Figures 5.3 and 5.4. The XRD pattern shows the expected broad peaks associated with metallic FCC Pd crystallites (Figure 5.3a). TEM analysis shows

the average NP size to be 5.2 nm (Figure 5.4), while lattice fringe analysis of a single particle shows an average lattice separation of 0.22 nm, corresponding to the (111) plane of FCC Pd (inset of Figure 5.4). The CO-FTIR spectra has two bands: the first peak at 2060 cm^{-1} is assigned to CO bound atop to Pd, while the second peak at 1950 cm^{-1} corresponds to CO bound to the Pd surface in the bridging mode (Figure 5.3b).

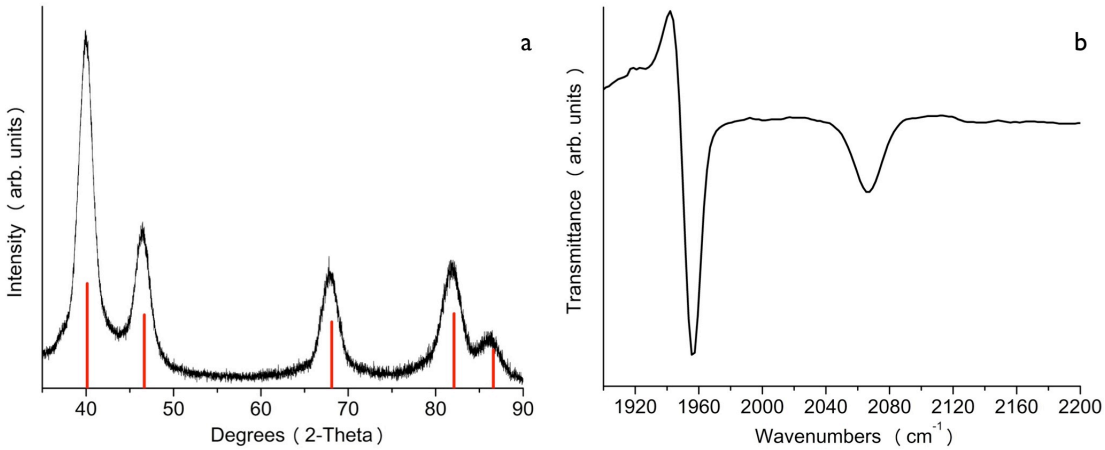

Figure 5.3. Representative (a) XRD pattern and (b) CO-FTIR spectrum of the Pd NPs. Red vertical lines indicate the peak positions for FCC phase Pd (JCPDS 01-071-3757)

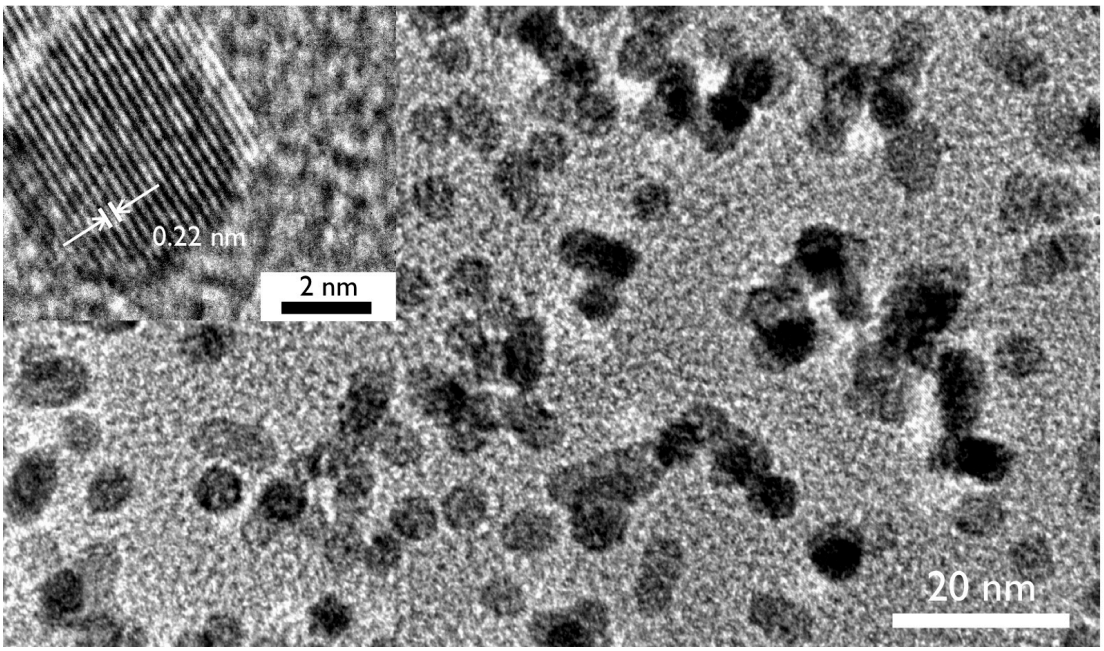

Figure 5.4. Representative TEM image of the Pd NPs. A lattice fringe image of a single particle highlighting the (111) plane of FCC Pd is inset

A representative XRD pattern, TEM image, and CO-FTIR spectrum of the Pt NPs are shown in Figures 5.5 and 5.6. Intense broad peaks, associated with highly crystalline FCC Pt NPs, appear in the XRD pattern as expected (Figure 5.5a). TEM analysis shows the average NP size to be 4.5 nm (Figure 5.6), while lattice fringe analysis of a single particle displays the (111) plane of FCC Pt, with an average lattice separation of 0.22 nm (inset of Figure 5.6). The CO-FTIR spectrum contains a peak at 2065 cm^{-1} that corresponds to Pt-bound CO (Figure 5.5b).

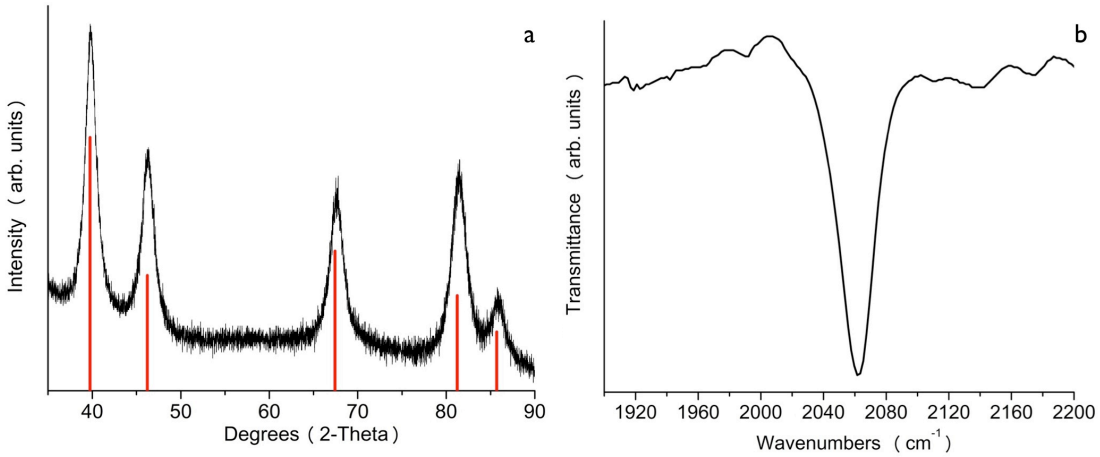

Figure 5.5. Representative (a) XRD pattern and (b) CO-FTIR spectrum of the Pt NPs. Red vertical lines indicate the peak positions for FCC phase Pt (JCPDS 03-065-2868)

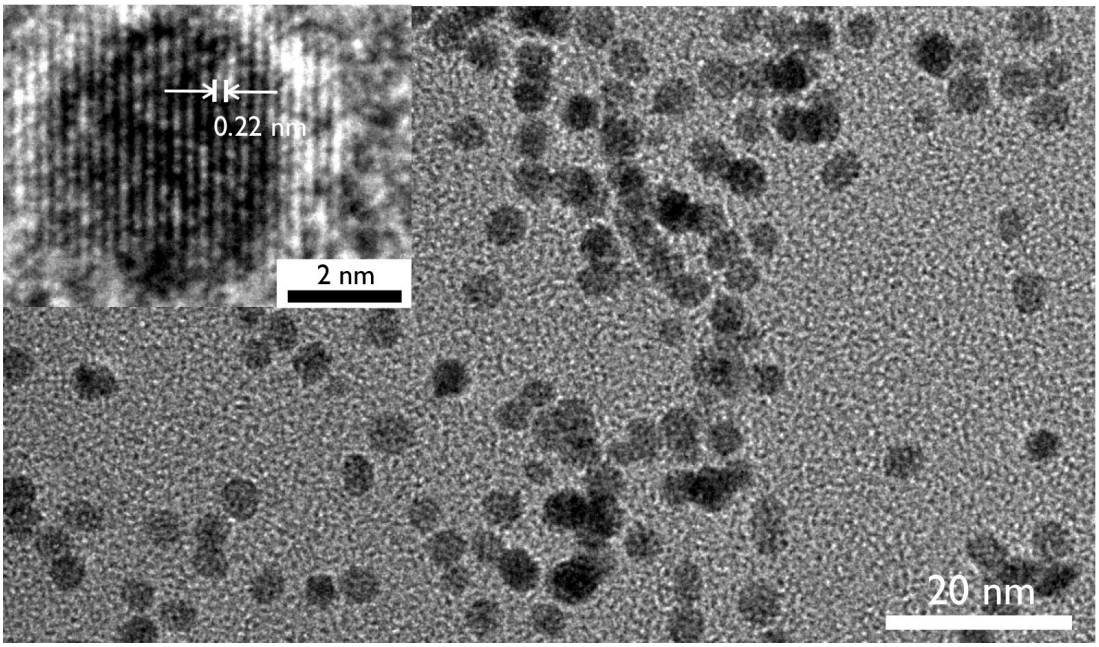

Figure 5.6. Representative TEM image of the Pt NPs. A lattice fringe image of a single particle highlighting the (111) plane of FCC Pt is inset

Monometallic Ni NPs were synthesized using two different methods to reduce $Ni(acac)_2$ in EG in the presence of PVP stabilizers. One method uses EG as both solvent and mild reducing agent, while the second method uses the stronger reducing agent $NaBH_4$. As in previous work, the use of strong reducing agents in the synthesis

of Ni NPs resulted in smaller, more monodispersed particles relative to the more common polyol methods.[107,247-249] The results shown here are in agreement with previous studies.

The size difference resultant from the two methods is clearly seen in their XRD patterns, where intense sharp peaks are seen in EG-reduced NPs, while the peaks of the $NaBH_4$-reduced NPs are very broad and of low intensity (Figure 5.7a). Both samples' diffraction patterns are consistent with metallic FCC Ni, yet given the high oxophilicity of Ni, an amorphous oxide shell is very likely to form. TEM characterization reveals average particle sizes of 43.9 and 2.5 nm for the EG and $NaBH_4$-reduced NPs (Figures 5.8a and 5.8b), while lattice fringe analysis of the $NaBH_4$-reduced NPs gives an average lattice separation of 0.18 nm, corresponding to the 200 plane of FCC Ni (inset of Figure 5.8b). The CO-FTIR spectrum of the $NaBH_4$-reduced Ni particles has two major peaks: the more intense peak from atop bound CO centered at 2050 cm^{-1} and a less intense peak associated with bridging CO binding near 1930 cm^{-1} (Figure 5.7b). The CO-FTIR spectrum of the EG-reduced Ni particles is similar, maintaining the primary atop CO peak at 2050 cm^{-1}, but the bridging CO peak at 1930 cm^{-1} is essentially absent (Figure 5.7b). The bridging CO binding mode intensity is typically associated with edge and terrace sites on the NP surface. The number of these sites is expected to dramatically decrease given the large sizes of the EG-reduced Ni particles, hence the absence of this peak in the CO-FTIR spectrum.

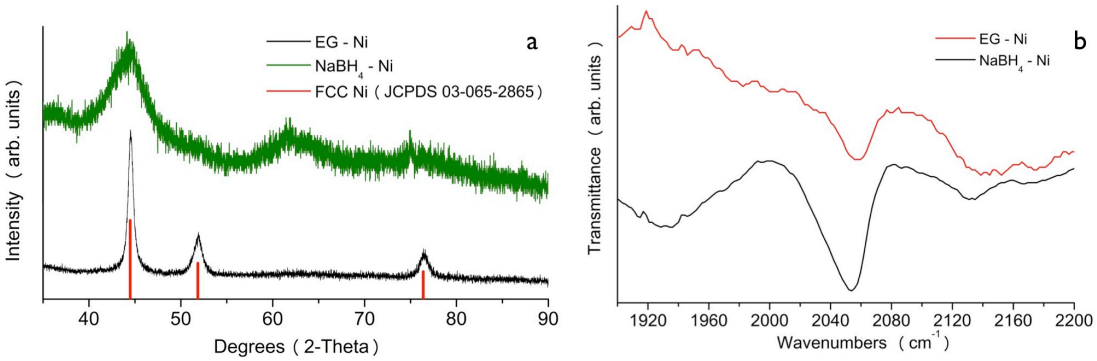

Figure 5.7. Representative (a) XRD patterns and (b) CO-FTIR spectra of the EG and $NaBH_4$ reduced Ni NPs. Red vertical lines indicate the peak positions for FCC phase Ni (JCPDS 03-065-2865)

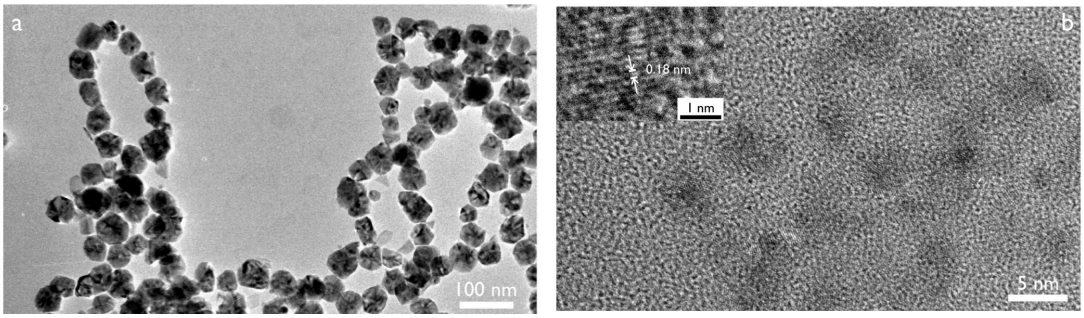

Figure 5.8. Representative TEM images of the (a) EG and (b) $NaBH_4$ reduced Ni NPs. A lattice fringe image of a single particle highlighting the (200) plane of FCC Ni is inset in Figure 5.8b

5.3.2 Synthesis and Characterization of Bimetallic Nanoparticles

5.3.2.1 Synthesis and Characterization of M@Ni (M = Ru, Pd, Pt) Core-Shell NPs

The Ru@Ni NPs were prepared by depositing Ni onto 3.0 nm Ru NPs in EG, with the precursor ratios modified to adjust the shell thickness. Ni deposition was accomplished by reducing $Ni(acac)_2$ with EG at 160 °C in the presence of the pre-formed Ru cores. TEM images of both the thin-shelled and thick-shelled Ru@Ni samples are shown in Figure 5.9. Size analysis reveals their respective sizes to be 3.6

nm and 4.6 nm, while their Ru:Ni elemental ratios were respectively found to be 6:4 and 4:6 by EDS analysis (Figure 5.10). The XRD patterns of both the monometallic Ru and 3.6 nm Ru@Ni NPs contain a single broad peak near 42°, which is typical of small Ru crystallites, but peaks from Ni diffraction are not seen in these samples (Figure 5.11a). When the Ni shell is thickened, as in the 4.6 nm Ru@Ni NPs, broad peaks from Ni diffraction are clearly visible in the XRD pattern (Figure 5.11a). CO-FTIR spectra of both Ru@Ni samples show the disappearance of the Ru-CO peak (2020 cm^{-1}), with the appearance of new peaks at 1930 and 2040 cm^{-1}, assigned to the bridging and atop modes of CO bound to a Ni surface (Figure 5.11b). The thicker Ni shell of the larger Ru@Ni NPs allows for STEM-EDS line scan analysis, which confirms the formation of a Ni shell around the Ru core (Figure 5.12). Here, the Gaussian distribution of Ru within the core and the bimodal distribution of Ni at the particle edges clearly illustrate the core-shell architecture.

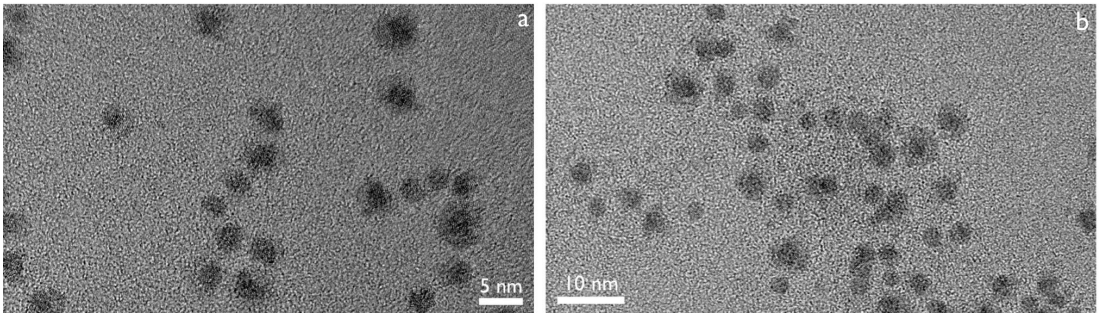

Figure 5.9. Representative TEM images of the (a) thin-shell and (b) thick-shell Ru@Ni NPs

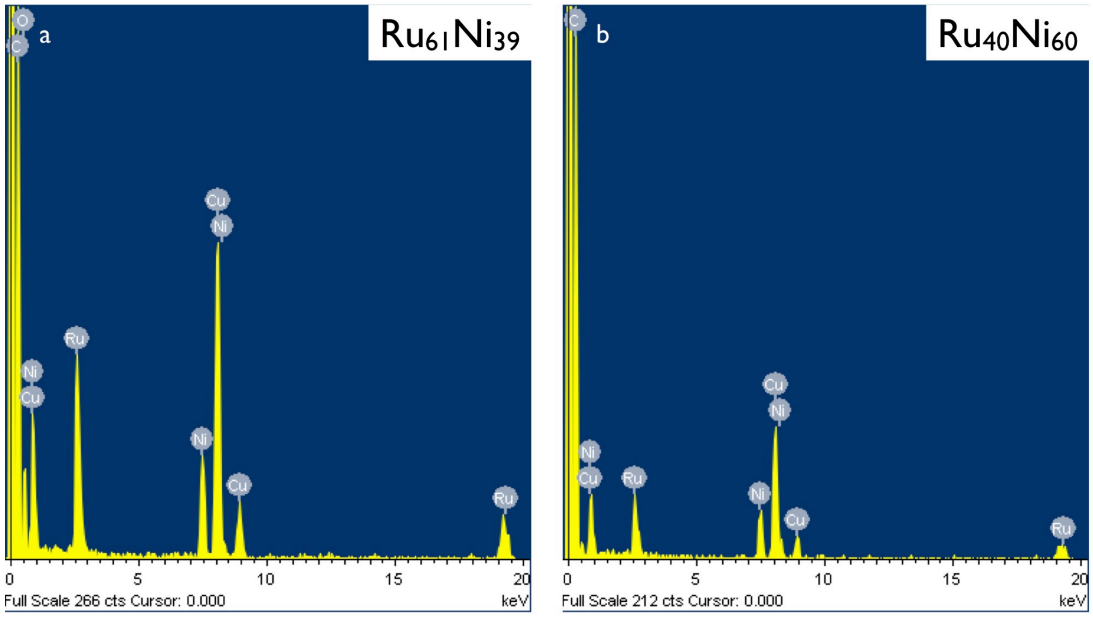

Figure 5.10. EDS analysis of the (a) thin-shell and (b) thick-shell Ru@Ni NPs

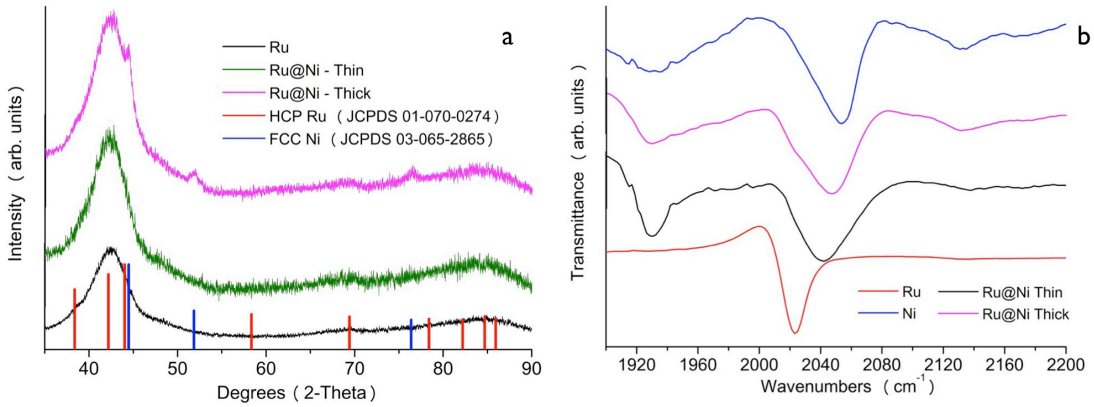

Figure 5.11. Representative (a) XRD patterns and (b) CO-FTIR spectra of the thin shell and thick shell Ru@Ni NPs. Data for monometallic Ru and Ni NPs are shown for comparison. Red vertical lines indicate the peak positions for HCP phase Ru (JCPDS 01-070-0274), while blue vertical lines indicate the peak positions for FCC phase Ni (JCPDS 03-065-2865)

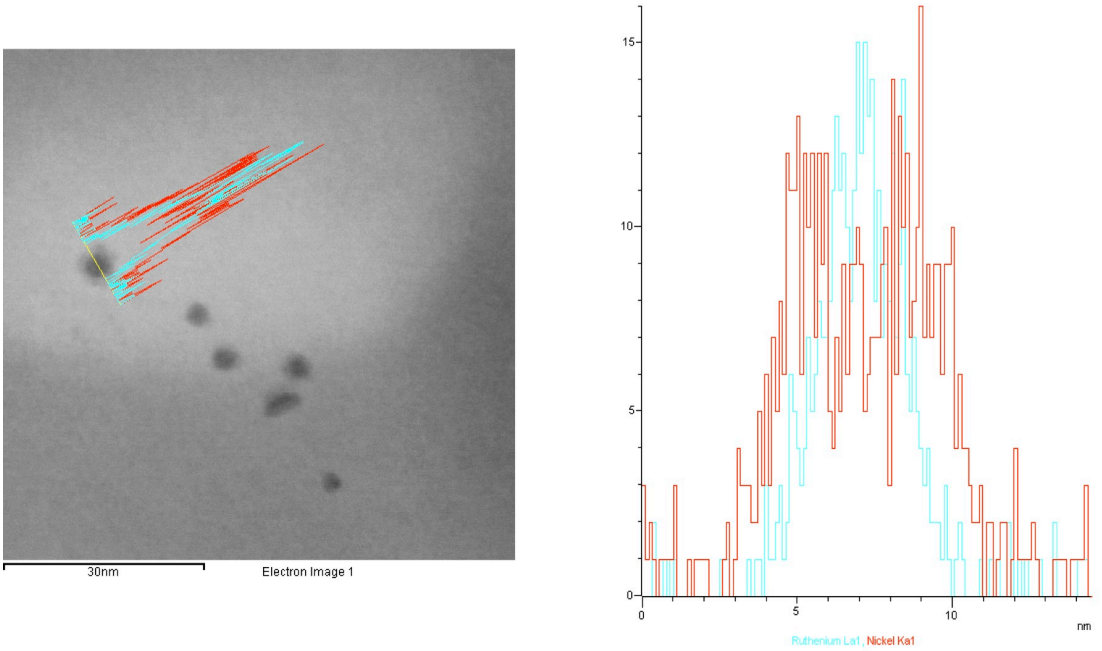

Figure 5.12. STEM-EDS line scan analysis of a single thick-shell Ru@Ni NP. Note the bimodal distribution of Ni (red) at the edges and the Gaussian distribution of Ru (cyan) within the center

Given that the Ru NP seeds are 3.0 nm in size and Ni has a FCC lattice constant of 0.352 nm, the thin-shelled 3.6 nm Ru@Ni particles are expected to have a single layer of Ni on their surfaces. This is easily seen from the increase in average particle size from the Ru seeds and the surface analysis provided by the CO-FTIR spectroscopy. Since the Ni shells of these particles were too thin to provide distinct diffraction peaks, thicker Ni shells were synthesized by increasing the amount of Ni precursor for the Ni shell deposition process. These thicker shell Ru@Ni NPs are noticeably large, with average sizes of 4.6 nm. Again, considering that the Ru seeds are 3.0 nm in diameter and the lattice parameter of Ni, it could be inferred that roughly 2-3 layers of Ni cover the 4.6 nm Ru@Ni particles, whose pure Ni surface is

also supported by the CO-FTIR spectrum. The thicker Ni shell is now observable by both XRD and STEM-EDS line scan analyses, which support the TEM and CO-FTIR characterizations in confirming the Ru@Ni core-shell architecture.

To our knowledge, Ru@Ni core-shell NPs have been reported only once before in the literature.[250] Those particles were formed by atomizing Ru and Ni precursors in a flowing spray-pyrolysis reactor operating at high temperatures (600-800 °C). However, the synthesis method results in large particles, with little control over the NPs' architecture and minimal characterization. Conversely, the Ru@Ni core-shell NPs discussed here are very well characterized, with precise control of size, composition and architecture.

Pd@Ni and Pt@Ni NPs were prepared using a similar synthetic protocol except Ni deposition on Pd was carried out at 115 °C. The temperature was increased to 125 °C to deposit Ni onto the pre-formed Pt NPs. Due to the lower deposition temperatures (compared to the Ru@Ni synthesis), longer reaction times were necessary to coat the core with Ni shells. The XRD pattern (Figure 5.13a) of the Pd@Ni NPs is similar to that of monometallic Pd, but additional faint and broad peaks (most noticeable at 44.5° and 52°) suggest the presence of poorly crystalline Ni. The average sizes of the NPs increase from 5.2 nm to 5.7 nm upon Ni deposition, while EDS analysis gives a Pd:Ni ratio of 3:1, in agreement with the precursor ratios (Figure 5.14). CO-FTIR analysis of the Pd@Ni particles gives a unique spectrum different from those of monometallic Pd and Ni. Compared to Pd, both CO binding peaks in Pd@Ni are shifted to lower wavenumbers, showing that the NP surface is modified by the presence of Ni, suggesting the formation of a Ni shell around the Pd

core (Figure 5.13b). However, the spectrum of the Pd@Ni NPs has more in common with the spectrum of monometallic Pd particles, rather than monometallic Ni, Ru@Ni, and Pt@Ni NPs. The peak assigned to atop bound CO in the CO-FTIR spectrum of the Pd@Ni NPs is of much lower intensity than those in the spectra of the monometallic Ni, Ru@Ni and Pt@Ni NPs. Likewise, the peak assigned to bridging CO in the Pd@Ni spectrum is sharper and of increased intensity compared to the spectra of the monometallic Ni, Ru@Ni and Pt@Ni NPs. Two possibilities emerge from this observation: 1) the Pd seed modifies the CO adsorption properties on the Ni surface such that the spectrum of the Pd@Ni NPs begins to resemble that of pure Pd; 2) the Pd core is incompletely covered by Ni, leaving Pd sites available for CO adsorption.

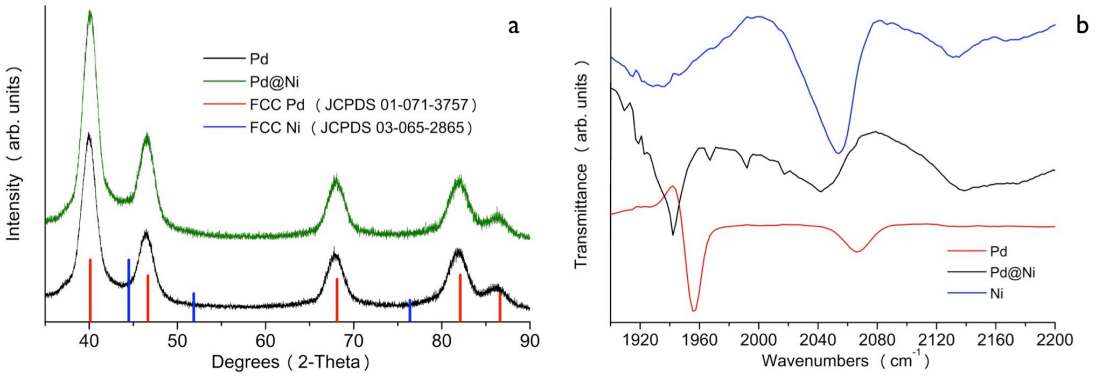

Figure 5.13. Representative (a) XRD pattern and (b) CO-FTIR spectrum of the Pd@Ni NPs. Data for monometallic Pd and Ni NPs are shown for comparison. Red vertical lines indicate the peak positions for FCC phase Pd (JCPDS 01-071-3757) while the blue vertical lines indicate the peak positions for FCC phase Ni (JCPDS 03-065-2865)

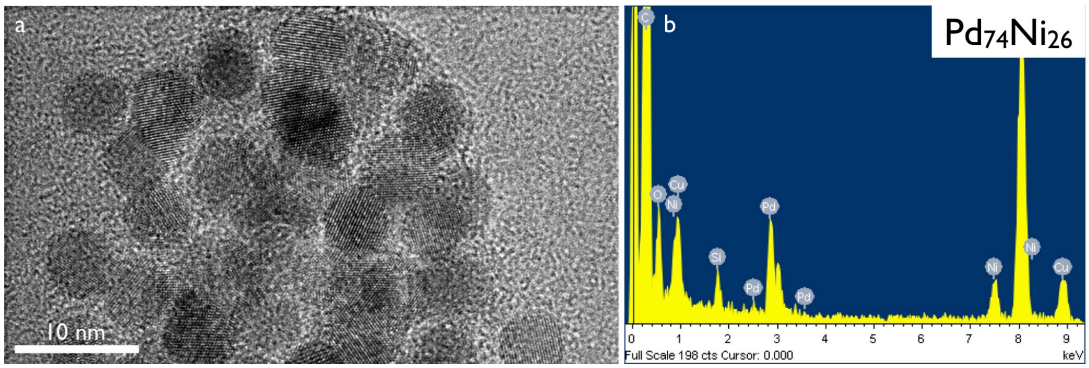

Figure 5.14. Representative (a) TEM image and (b) EDS analysis of the Pd@Ni NPs

Pt@Ni core-shell NPs were produced similarly to the Pd@Ni particles, with the exception of using 4.5 nm Pt NPs as the seeds. The intense peaks of the Pt core remain in the XRD pattern of the Pt@Ni NPs in addition to new faint peaks (at 44.5°, 52°, and 76.5°) consistent with Ni diffraction (Figure 5.15a). TEM analysis shows the average NP size to have increased to 5.1 nm, while EDS analysis shows the Pt:Ni ratio to be 7:3 (Figure 5.16). Compared to that of the initial Pt particles, the CO-FTIR spectrum of the Pt@Ni NPs contains a new secondary peak, associated with bridging CO, at 1925 cm^{-1}, while the atop CO peak has shifted from 2060 cm^{-1} to 2050 cm^{-1} (Figure 5.15b). The Pd@Ni spectrum closely resembles that of monometallic Ni, further illustrating full coverage of a Ni shell onto the Pt NP seeds.

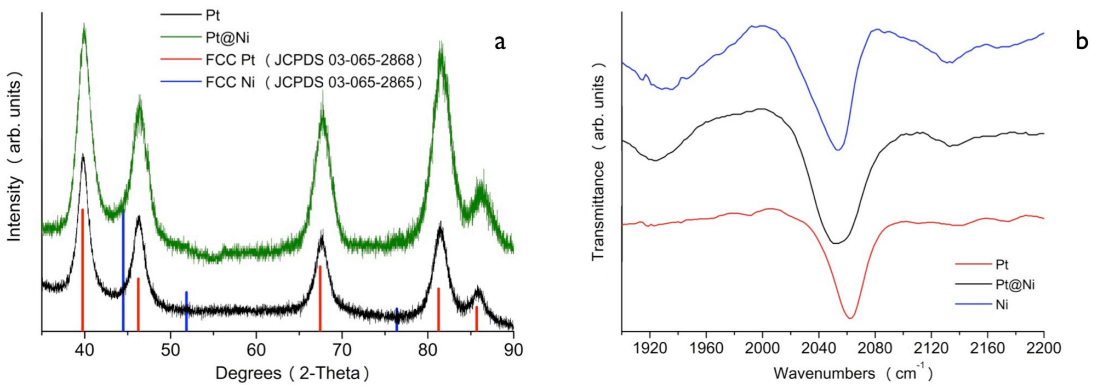

Figure 5.15. Representative (a) XRD pattern and (b) CO-FTIR spectrum of the Pt@Ni NPs. Data for monometallic Pt and Ni NPs are shown for comparison. Red vertical lines indicate the peak positions for FCC phase Pt (JCPDS 03-065-2868) while the blue vertical lines indicate the peak positions for FCC phase Ni (JCPDS 03-065-2865)

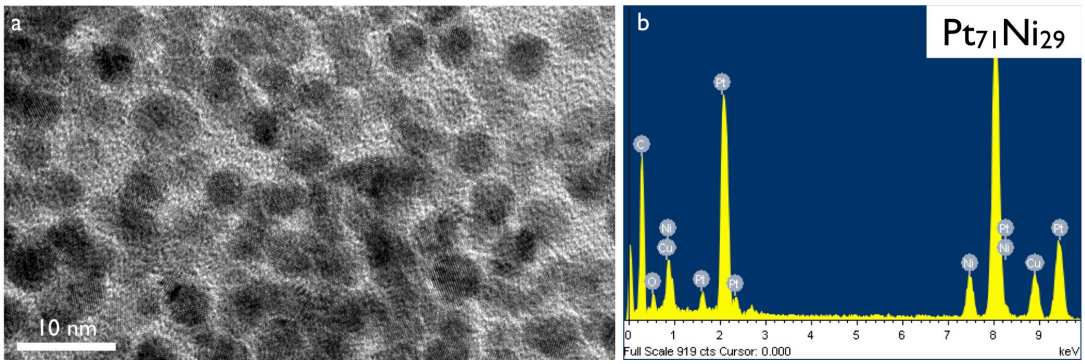

Figure 5.16. Representative (a) TEM image and (b) EDS analysis of the Pt@Ni NPs

Given the lattice parameter of FCC Ni (0.352 nm as previously discussed), the 5.7 nm Pd@Ni core-shell NPs are calculated to have a little less than a single monolayer of Ni on their surface (5.2 nm Pd core). This result is in agreement with the CO-FTIR experiments, which also suggest a submonolayer Ni surface on the Pd core NPs. Unlike the Pd@Ni NPs, the 5.1 nm Pt@Ni NPs are fully coated by Ni. The

CO-FTIR spectrum resembling monometallic Ni and the expected size increase (~0.6-0.7 nm) over the Pt cores (4.5 nm Pt NPs) give weight to this result. While faint Ni diffraction peaks are seen in the XRD patterns for the Pd@Ni and Pt@Ni, the low intensities are inconclusive. Attempts to create thicker Ni shells on these particles, to obtain conclusive XRD patterns and the ability to perform STEM-EDS analysis, were unsuccessful, primarily due to the low reaction temperatures proving insufficient for further Ni deposition onto the Ni shell. Additional trials where the reaction temperature was increased led to the formation of Pd-Ni and Pt-Ni heteroaggregates (data not shown). Further experiments are needed to obtain full control of Ni layer thickness over monometallic Pd and Pt seeds.

Pd@Ni and Pt@Ni core-shell NPs are uncommon in the literature, with the few examples primarily featuring larger particle sizes or existing as intermediates before further surface modification, such as additional shell coatings.[251-253] The particles discussed here are smaller, with thinner Ni shells. Despite the smaller particles produced here, the experimental results are in general agreement with other reports. Previous Pd@Ni NP reports featured particles roughly 15 nm in size, with Ni shell thicknesses sufficient for the observation of Ni via XRD and EDS mapping/line scan analyses. Similar results were seen for Pt@Ni NPs reported in the literature.

5.3.2.2 Synthesis and Characterization of Ru@Pd and Ru@Pt Core-Shell NPs

Ru@Pd and Ru@Pt NPs were prepared as previously described by depositing Pd or Pt over Ru NPs.[246] To confirm their synthesis, the core-shell NPs were

characterized using XRD, TEM, and CO-FTIR analyses, whose results are in agreement with the previous reports.

Bimetallic Ru@Pd core-shell NPs were synthesized according to our previous methods, where Pd from $PdCl_2$ was deposited over 3.0 nm Ru NPs in EG. A representative XRD pattern of the Ru@Pd NPs is shown in Figure 5.17a, where it is compared to the pattern of the Ru NP seeds. The similarity of the patterns is quite evident, with the large, broad peak near 42° indicative of the poorly crystalline Ru core, as discussed earlier. However, the Ru@Pd pattern has faint peaks (most noticeable at 40° and 46.5°) consistent with Pd diffraction. TEM imaging and EDS analysis provide additional evidence of Pd shell formation. Size analysis of a representative TEM image, seen in Figure 5.18a, gives an average NP size of 3.9 nm for the Ru@Pd NPs, which is noticeably larger than the 3.0 nm Ru NP seeds. EDS analysis shows these particles to have an elemental ratio of roughly 1:1 Ru:Pd, as expected from the initial precursor ratios (Figure 5.18b). Finally, the CO-FTIR spectrum of the Ru@Pd NPs is compared to those of monometallic Ru and Pd in Figure 5.17b. The peak associated with CO bound to Ru sites (2020 cm^{-1}) disappears, accompanied by the appearance of peaks associated with both Pd-CO binding modes (1950 and 2060 cm^{-1}). From the lattice parameter value of Pd (0.389 nm), the 3.9 nm Ru@Pd NPs prepared here should have a single layer of Pd coating the 3.0 nm Ru core, in agreement with previous work.

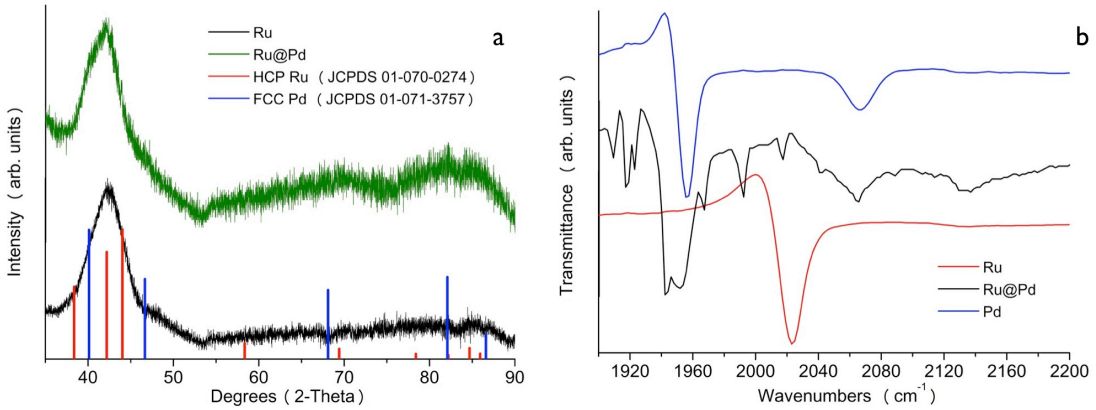

Figure 5.17. Representative (a) XRD pattern and (b) CO-FTIR spectrum of the Ru@Pd NPs. Data for monometallic Ru and Pd NPs are shown for comparison. Red vertical lines indicate the peak positions for HCP phase Ru (JCPDS 01-070-0274) while the blue vertical lines indicate the peak positions for FCC phase Pd (JCPDS 01-071-3757)

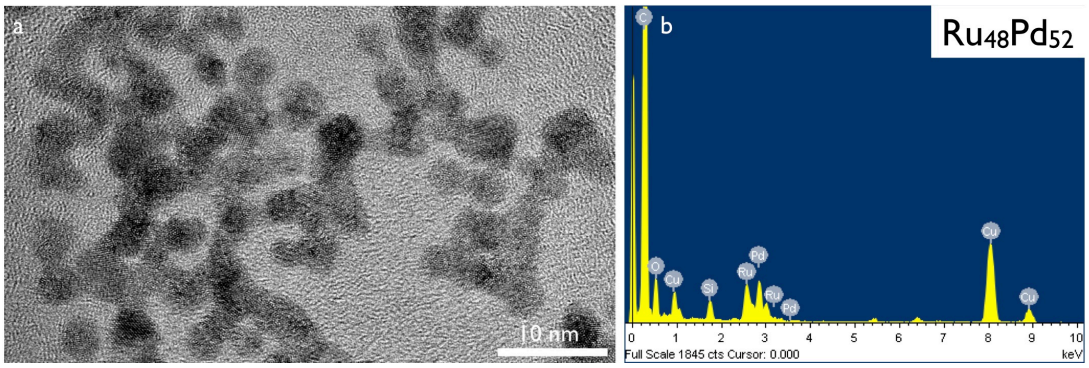

Figure 5.18. Representative (a) TEM image and (b) EDS analysis of the Ru@Pd NPs

Bimetallic Ru@Pt core-shell NPs were synthesized by coating 3.0 nm Ru NPs with Pt by reducing $PtCl_2$ in EG. A representative XRD pattern of the Ru@Pt NPs is shown in Figure 5.19a, where the broad peaks associated with Pt diffraction are clearly seen. The (111) Pt peak (centered near 39°) appears asymmetrical due to faint diffraction from the Ru core near 42°. Figure 5.20a shows a representative TEM image, with the particles having an average size of 3.7 nm. Similar to the Ru@Pd

system, EDS analysis gives an elemental ratio of roughly 1:1 Ru:Pt. (Figure 5.20b). The CO-FTIR spectrum of the Ru@Pt NPs has a peak at 2055 cm^{-1} in Figure 5.19b. This peak is distinct from those associated with CO bound to monometallic Ru (2020 cm^{-1}) or Pt (2065 cm^{-1}) sites. The Ru@Pt CO-FTIR spectrum also has a shoulder near 2030 cm^{-1} off the primary 2055 cm^{-1} peak, suggesting a small number of Ru sites are exposed on the particle surface. From previous data (including the 0.392 nm lattice parameter for Pt), full monolayer coverage of the 3.0 nm Ru core with Pt should result in Ru@Pt particles roughly 4.0 nm in size. The lower than expected size increase in the 3.7 nm Ru@Pt NPs produced here have submonolayer coverage of Pt, in agreement with previous data and the CO-FTIR analysis.

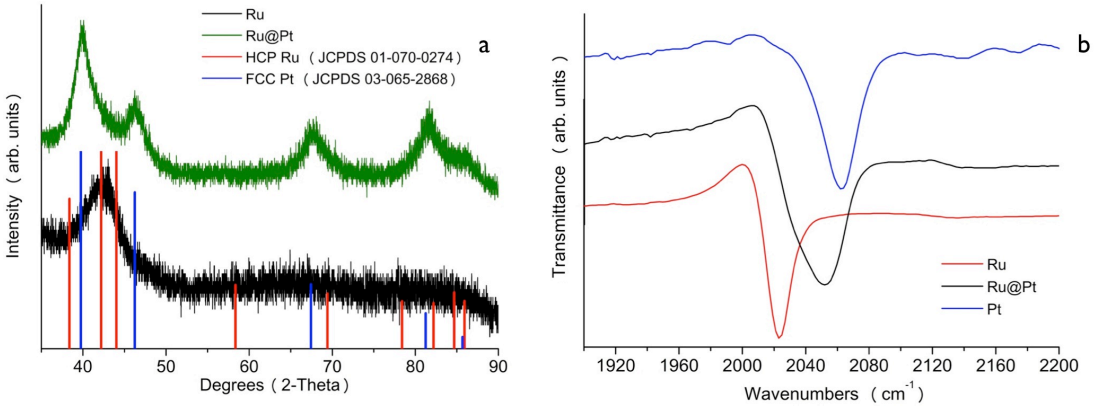

Figure 5.19. Representative (a) XRD pattern and (b) CO-FTIR spectrum of the Ru@Pt NPs. Data for monometallic Ru and Pt NPs are shown for comparison. Red vertical lines indicate the peak positions for HCP phase Ru (JCPDS 01-070-0274) while the blue vertical lines indicate the peak positions for FCC phase Pt (JCPDS 03-065-2868)

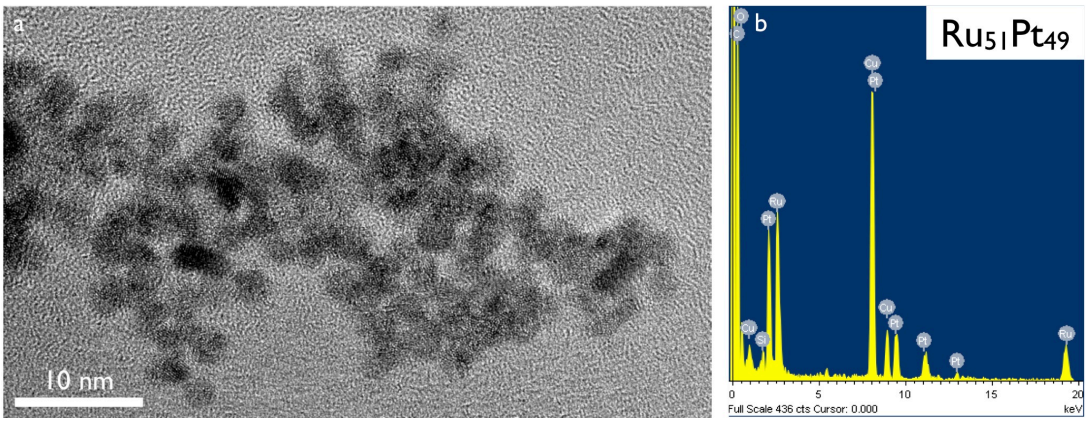

Figure 5.20. Representative (a) TEM image and (b) EDS analysis of the Ru@Pt NPs

5.3.2.3 Synthesis and Characterization of Pt@Pd and Pd@Pt Core-Shell NPs

Pt@Pd and Pd@Pt core-shell NPs are well known and were prepared here using modified versions of our previously reported methods.[42,246,254] Given the nearly identical lattice parameters of FCC Pd (0.389 nm) and Pt (0.392 nm), XRD analysis is a poor tool for distinguishing monometallic, alloy, and core-shell NPs comprised of the two elements. As such, TEM, EDS, and CO-FTIR analyses were utilized to confirm the formation of thin metal shells over the monometallic NPs used as seeds.

Bimetallic Pt@Pd core-shell NPs were synthesized using a modified version of our technique for producing Ru@Pt@Pd particles.[246,254] Specifically, Pd from $PdCl_2$ was deposited over 4.5 nm Pt NPs in EG. Size analysis of a representative TEM image, seen in Figure 5.21a, gives an average NP size of 5.1 nm for the Pt@Pd NPs, while EDS analysis (Figure 5.21b) shows these particles to have an elemental ratio of roughly 6:4 Pt:Pd. While both the Pt and Pt@Pd NPs have peaks near 2060 cm^{-1} in their CO-FTIR spectra, the Pt@Pd spectrum has an additional broad peak centered at 1945 cm^{-1}, which is typical for CO bound to Pd in the bridging mode

(Figure 5.22). The atop CO binding mode peak at 2060 cm^{-1} is also of lower intensity, which is also indicative of a Pd surface.

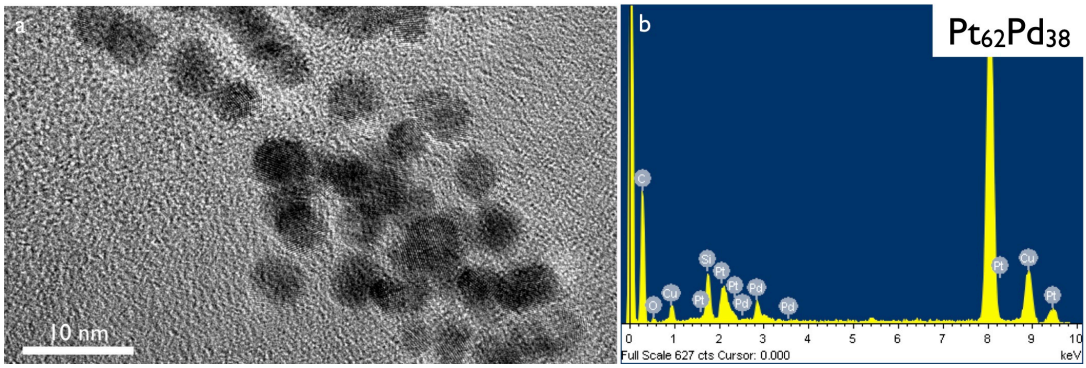

Figure 5.21. Representative (a) TEM image and (b) EDS analysis of the Pt@Pd NPs

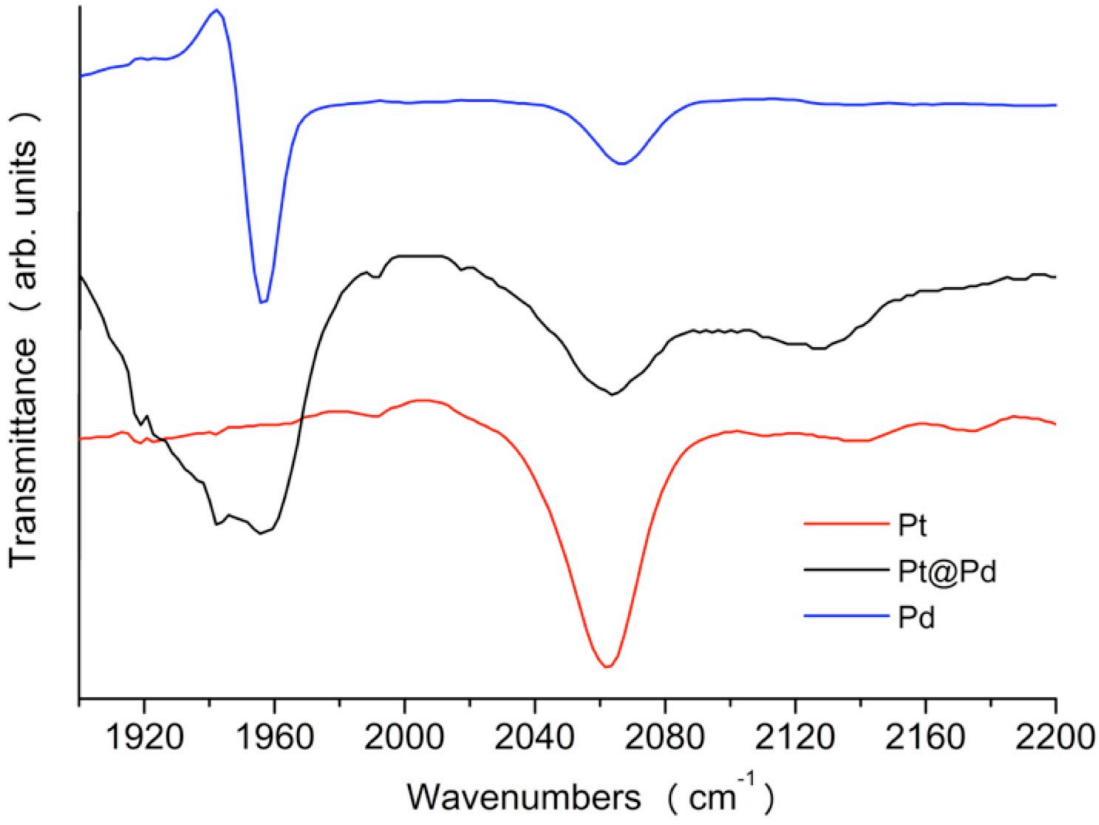

Figure 5.22. CO-FTIR spectrum of the Pt@Pd NPs. Data for monometallic Pt and Pd NPs are shown for comparison.

Bimetallic Pd@Pt core-shell NPs were synthesized similarly to existing methods.[41] 5.2 nm Pd NP seeds were coated with Pt, reduced from $PtCl_2$, in EG. Figure 5.23a is a representative TEM image of the Pd@Pt particles, where size analysis shows the NPs to be 5.7 nm, while EDS analysis gives an elemental ratio of roughly 3:1 Pd:Pt (Figure 5.23b). In the CO-FTIR spectrum of Pd@Pt NPs, not only does the atop CO mode peak at 2065 cm^{-1} increase in intensity, but also the bridging mode peak typically seen at 1955 cm^{-1} is not present (Figure 5.24). These observations show the absence of Pd on the NP surface.

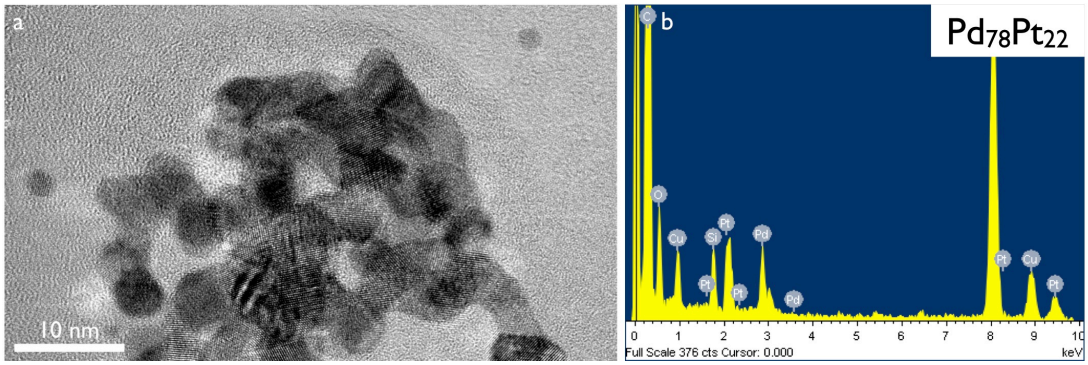

Figure 5.23. Representative (a) TEM image and (b) EDS analysis of the Pd@Pt NPs

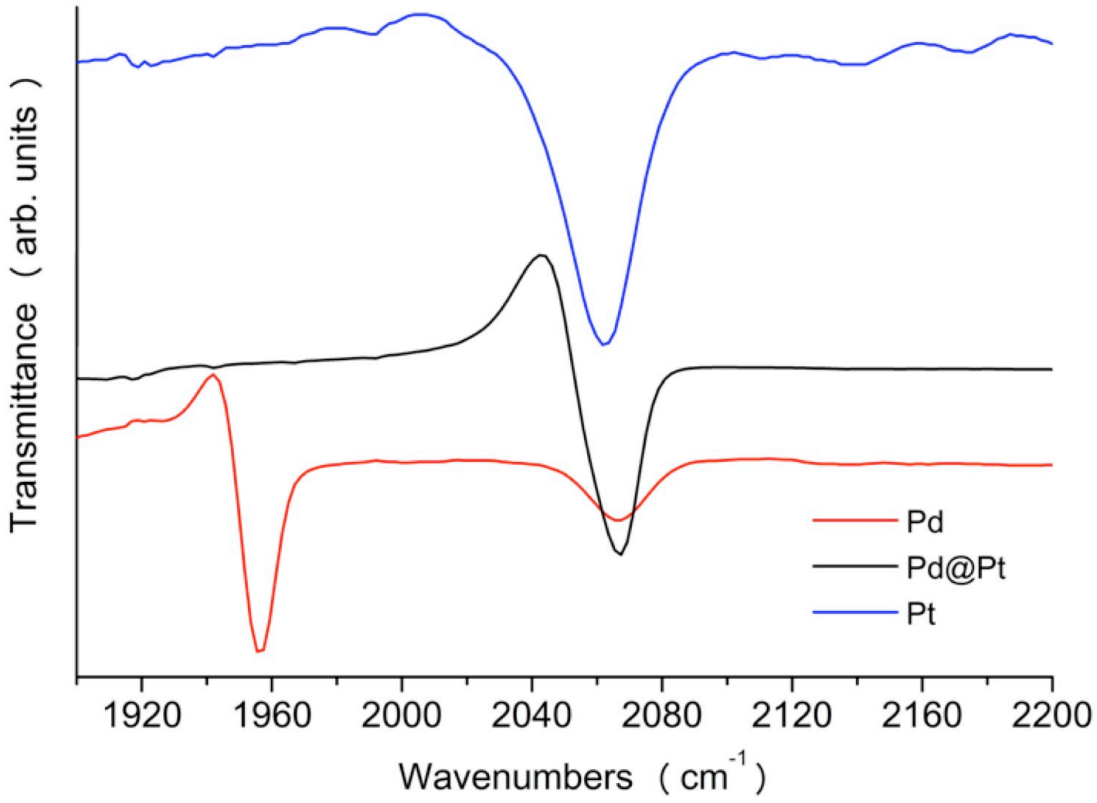

Figure 5.24. CO-FTIR spectrum of the Pd@Pt NPs. Data for monometallic Pd and Pt NPs are shown for comparison.

The experimental data obtained for Pt@Pd and Pd@Pt NPs synthesized here compare well with previous studies.[41] The particle sizes of the core-shell particles are clearly shown to increase upon shell deposition and EDS analysis confirms their bimetallic nature. CO-FTIR analysis confirms Pt@Pd and Pd@Pt NPs have monometallic surfaces.

5.3.2.4 Synthesis and Characterization of NiRu Alloy NPs

Bimetallic NiRu NPs were synthesized by using $NaBH_4$ to co-reduce $Ni(acac)_2$ and $Ru(acac)_3$ at 130 °C in EG in the presence of PVP stabilizer. TEM

analysis shows the average size of the NiRu particles to be 2.1 nm (Figure 5.25a), while EDS analysis gives an elemental ratio of roughly 1:1 Ni:Ru, as expected from the precursor ratios and simultaneous reduction synthesis method (Figure 5.25b). The XRD pattern of the NiRu alloy is similar to that of monometallic Ru, suggesting a poorly crystalline HCP structure, however, the broad primary peak is shifted to a slightly higher angle (43.5° vs. 42°) due to the incorporation of smaller Ni atoms into the lattice (Figure 5.26). Comparing the CO-FTIR spectra of the NiRu alloy to other types of Ni/Ru samples confirms the homogenous distribution of Ni and Ru throughout the NP. The NiRu alloy spectrum is similar to that of the mixture of monometallic Ni and Ru particles as it contains CO bound to both Ni (2045 cm^{-1}) and Ru (2010 cm^{-1}) sites (Figure 5.27). Both are clearly distinct from the Ru@Ni core-shell and monometallic Ni and Ru spectra.

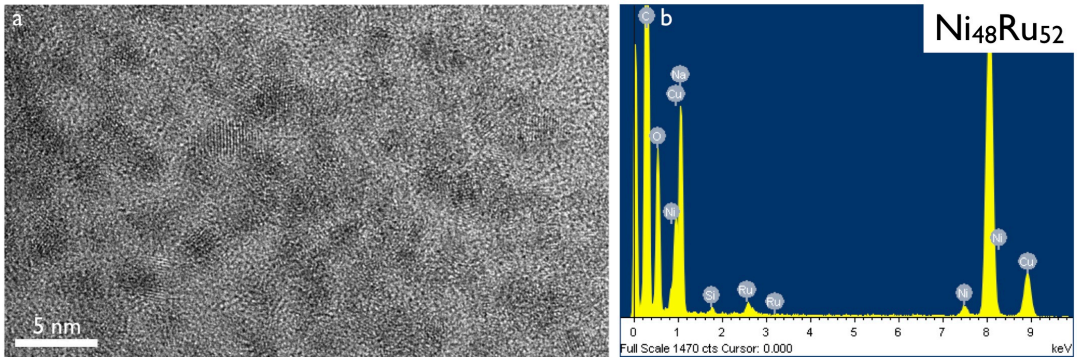

Figure 5.25. Representative (a) TEM image and (b) EDS analysis of the NiRu alloy NPs

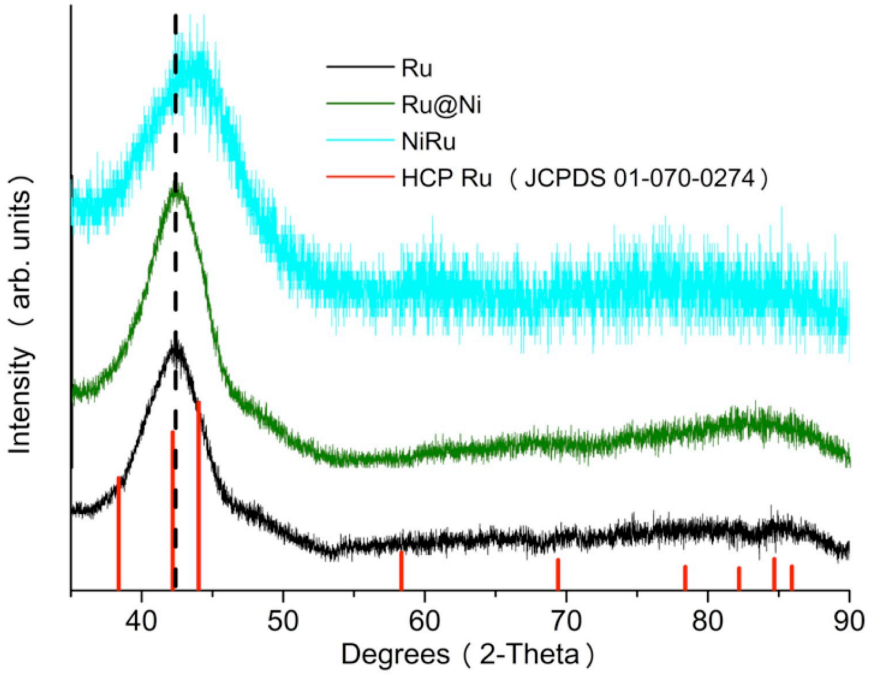

Figure 5.26. Representative XRD pattern of the NiRu alloy NPs. Data for monometallic Ru and Ru@Ni core-shell NPs are shown for comparison. Red vertical lines indicate the peak positions for HCP phase Ru (JCPDS 01-070-0274). The vertical dashed line denotes the angle of maximum peak intensity for the monometallic Ru sample. Note how the peak position does not shift in the Ru@Ni core-shell sample, but does shift for the NiRu alloy sample

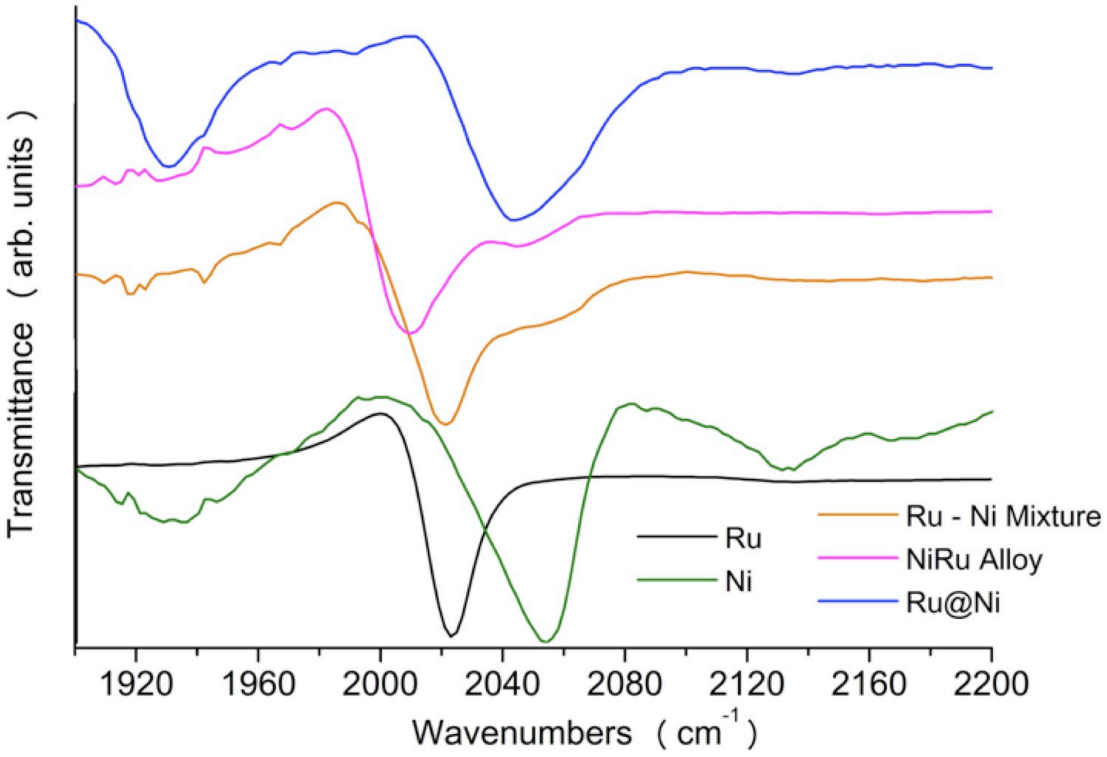

Figure 5.27. CO-FTIR spectrum of various Ni and Ru NP samples. Note the similarity of the NiRu alloy spectrum to that of the mixture of monometallic Ni and Ru NPs.

Few reports of NiRu alloy NPs exist due to the immiscibility of their constituents under standard conditions. These previous studies utilized either high temperature[255] or impregnation methods[256] to produce NiRu alloy particles, requiring either specialized equipment with high complexity and cost, or increased difficulty in controlling NP size and composition. Only one other report of NiRu alloy NPs used a colloidal approach as seen here, with methodical differences including the use of a stronger reducing agent ($LiBEt_3H$), organic solvents and capping agents (Ph_2O; OA, OAm), and higher reaction temperature (250 °C), resulting in ~9 nm NiRu particles.[81]

Despite these synthetic differences, the methodology used here also produces NiRu alloy NPs, but with smaller sizes.

While the NiRu particles described here were synthesized and characterized differently to the ~9 nm NiRu particles from the literature, they are quite similar in constitution and are very different from other Ru-Ni bimetallic architectures (monometallic mixture or core-shell). Despite the size differences, both NiRu alloys have XRD patterns with similar shape. These XRD patterns, while visually similar to those of monometallic Ru particles, have peaks that are shifted to slightly higher angles due to the presence of Ni within the crystal lattice. EDS analyses show the homogenous distribution of Ni and Ru throughout both sets of NiRu NPs, with similar composition ratios of roughly 1:1. This observation is confirmed by the CO-FTIR analysis performed here, where the spectrum of the NiRu alloy is very similar, but slightly different from that of the mixture of monometallic Ni and Ru particles. The CO binding stretches associated with Ni and Ru are shifted to slightly lower wavenumbers in the alloy, while the mixture has peaks at wavenumbers almost identical to monometallic Ni and Ru NPs. This shows that the Ni and Ru components in the alloy NPs have been electronically modified, clearly showcasing their bimetallic nature.

5.3.3 Evaluation of Nanoparticles for Heterogeneous Catalysis

Preliminary catalytic evaluations for CO oxidation and the PrOx reaction were performed on the thin-shelled Ru@Ni, Pt@Ni, and monometallic Ni NPs to probe the influence of metal substrate on the catalytic activity of Ni surfaces. CO oxidation tests were run using a gas mixture composed of 1% CO, 1% O_2, and 98% He. PrOx

evaluations were run similar conditions, except He was replaced with H_2. Although these experiments are exploratory in nature, the preliminary results demonstrate improvement in Ni catalytic activity via core metal-induced electronic structure modification, with the general performance trend Ru@Ni > Pt@Ni > Ni.

TPR plots for CO oxidation on the Ru@Ni, Pt@Ni, and monometallic Ni NP catalysts are shown in Figure 5.28. The variations in catalytic activity are readily apparent, with the Ru@Ni catalyst having CO oxidation begin (light-off) at ~90 °C and complete CO conversion to CO_2 by 170 °C. Following is the Pt@Ni catalyst, with CO oxidation light-off and full conversion at ~120 °C and 215 °C, respectively. The Ni catalyst has very low activity for CO oxidation, requiring temperatures to reach ~230 °C before any CO is converted and then barely reaching full conversion by the end of the catalytic run (~280 °C).

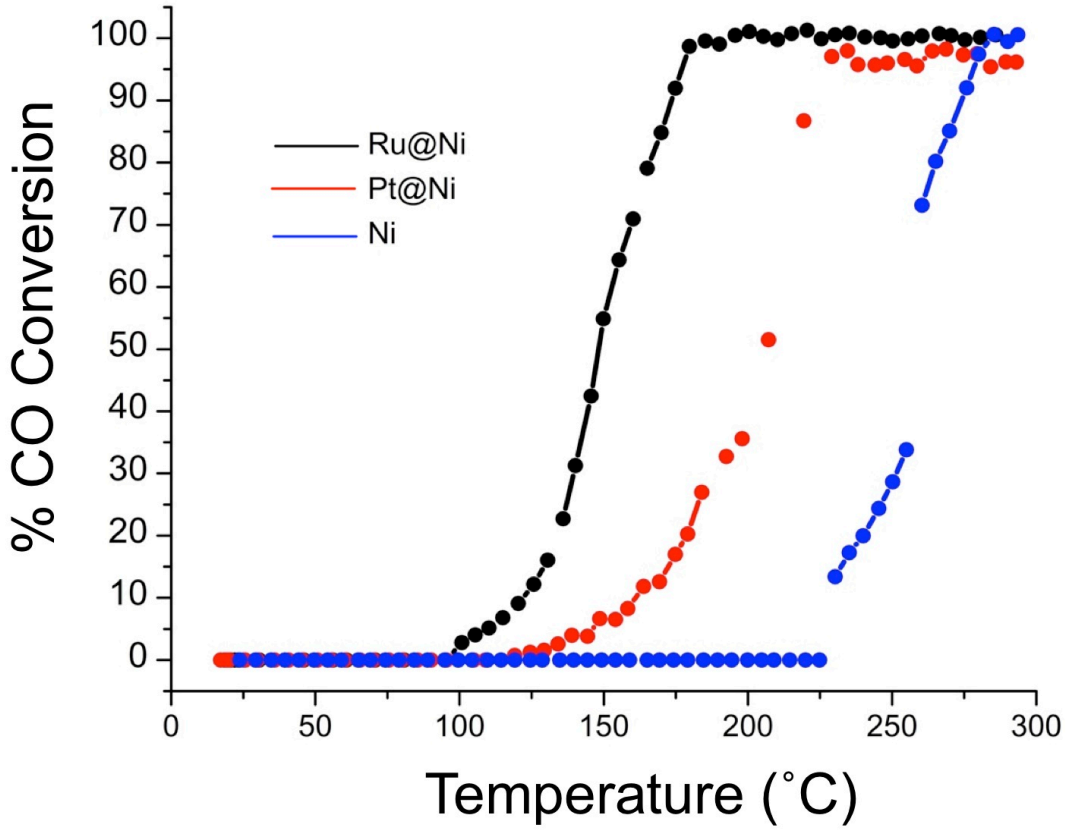

Figure 5.28. TPR plots for CO oxidation showing % CO conversion for the Ru@Ni, Pt@Ni, and monometallic Ni catalysts. The gas mixture was comprised of 1% CO, 1% O_2, and 98% He

Figure 5.29 shows preliminary PrOx catalysis results for all three catalysts. Here, the competing CO_2 and H_2O formation reactions are shown on the same plot for each catalyst to simplify comparisons of temperature light-offs and initiate selectivity discussions. The light-off temperatures for CO_2 and H_2O formation are almost simultaneous for all three catalysts, signifying low PrOx selectivity. This observation is confirmed when the H_2O formation reaction reaches its maximum conversion (due to O_2 being the limiting reagent). At this temperature, the formation of CO_2 begins to

decrease, signifying that most of the charged O_2 is being consumed for H_2 oxidation and not CO oxidation. In this respect, the catalysts tested thus far are poor PrOx catalysts.

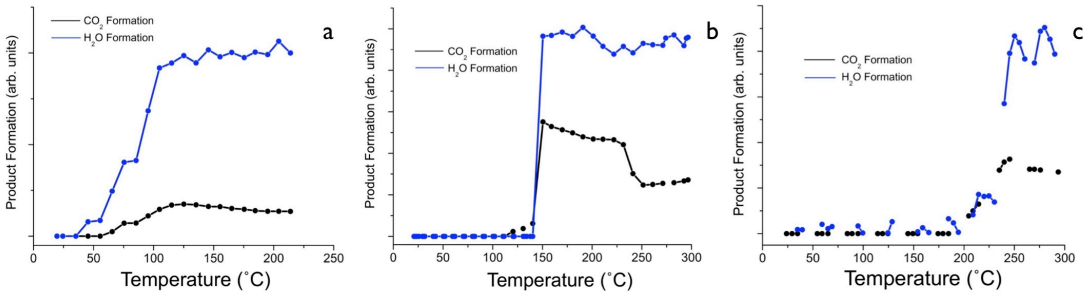

Figure 5.29. TPR plots for the PrOx reaction showing CO_2 formation (black) and H_2O formation (blue) for the (a) Ru@Ni, (b) Pt@Ni, and (c) monometallic Ni catalysts. The gas mixture was comprised of 1% CO, 1% O_2, and 98% H_2

Comparing each catalyst's activity for CO_2 formation under PrOx conditions (Figure 5.29) and in the absence of H_2 (Figure 5.28) shows that the CO oxidation light-off temperatures drop by ~10-30 °C in the presence of H_2. This suggests that under PrOx conditions, the CO oxidation process is mediated by H_2. A similar phenomenon was observed in previous PrOx catalytic studies involving Ru@Pt core-shell NPs.[64] In that study, the unique core-shell arrangement created Ru-induced electronic modifications to the Pt surface. This in turn allowed the CO oxidation reaction to proceed via a H-assisted mechanism, whereby O_2 disassociation (the rate-limiting step) was accelerated, leading to an overall increase in catalytic performance.

Similar electronic modifications appear to be occurring here, with the bimetallic core-shell NPs having improved performance for both CO and H_2 oxidation relative to monometallic Ni particles. The Ru@Ni catalyst in particular

shows much improved performance over its monometallic Ni counterpart. Both Ru and Pt are more electron-rich than Ni and would likely raise the Ni *d*-band center, as seen in surface science studies and predicted by DFT calculations.[24,40] This perturbation should result in increased electron density on the Ni surface, facilitating improved binding of the adsorbates involved in the oxidation reactions. However, in conjunction with *d*-band theory, these electronic shifts will vary with respect to the underlying metal. Compared to Ru, Pt is more electron-rich, and may actually hinder desorption of reactive species from the Ni surface. To better correlate catalytic activity and electronic effects with NP structure, future catalytic studies will include the NiRu alloy and monometallic Ru NPs, along with mixtures of monometallic Ni and Ru. Similar studies will be performed with the Ni-Pd and Ni-Pt systems to further develop our understanding of the factors behind the observed structure-activity relationships.

5.4 Summary

We have presented the synthesis of a series of bimetallic core-shell NPs of varying compositions. The near-single layer Ni-shell particles (M@Ni, M= Ru, Pd, Pt) are among the first reported syntheses of their type. All of the presented NPs were fully characterized by a combination of XRD, TEM, EDS, and CO-FTIR techniques to elucidate or confirm their structures. Preliminary catalytic studies were performed on the Ru@Ni and Pt@Ni core-shell NPs, where they were compared to each other and to monometallic Ni particles. It was found that the Ru@Ni and Pt@Ni NPs showed improved performance for both CO and H_2 oxidation compared to monometallic Ni NPs. This result was ascribed to electronic structure modifications

of the Ni surface by the more electron-rich substrate metal, raising the Ni *d*-band center and thus improving its ability to bind and transform reactant gases. Further catalytic studies involving the remaining NP catalysts are ongoing.

Chapter 6: Summary of Results and Prospective

6.1 Summary of Results

The work described in this dissertation entails the synthesis, characterization, and activity studies of various monometallic and bimetallic NP catalysts. Our studies aimed to better understand the physical and chemical relationships that govern the catalytic activities of the NPs, which were probed by varying the NPs' compositions, structures, and electronic environments.

In Chapter 2 we described the development of a simple one-pot method to synthesize graphene-supported metal NPs. Exploratory electrocatalytic studies using graphene-supported Pt NPs suggested the ability to tune the NPs' catalytic activity by modifying the metal-support interactions.

This proposal was confirmed by the research discussed in Chapter 3, which presented a full study of Pt and PtSn intermetallic NPs supported on four unique rGO materials. Our studies show how the chemical nature of the rGO support impacts the catalytic behavior of the NP catalysts due to unique metal-support interactions, which differ depending on the chemical identity of the NP substrate.

Chapter 4 presented the synthesis and characterization of Co_xPt_y NPs and how their inherent characteristics impact their catalytic activities for electrochemical reactions. Co_xPt_y NPs with intermetallic architectures were found to have diminished CO tolerance compared to their alloy counterparts, while the specific activity of Pt NPs for ORR catalysis was shown to be improved by Co-alloying.

The synthesis, characterization, and preliminary catalytic studies of bimetallic core-shell NPs were described in Chapter 5. Preliminary data illustrated how subsurface metals modify the electronic structure of Ni and enhance its catalytic performance for CO oxidation and the PrOx reaction. Additional CO oxidation and PrOx catalysis studies will be performed on the remaining NPs, which have been synthesized and fully characterized. Findings from these catalytic evaluations will be correlated to the NPs' compositions and architectures and contrasted with existing catalysts.

6.2 Prospective on the Field

The work presented in this dissertation and in recent literature showcase several advances towards the goal of highly active, yet stable catalytic materials with reduced reliance on precious metals. New NP catalysts are being produced with unique assemblies utilizing lesser amounts of precious metal, often having the dual positive outcomes of cutting costs and increasing catalytic performances. Further progress towards these goals will require the development of innovative compounds that, while increasingly intricate in nature, are directed by continually improving design and synthetic techniques. Many avenues exist for these new materials.

There is still much untapped potential from modifying carbon-based electrochemical supports, including carbon black powder, carbon nanotubes, and graphenes. While each support material has its own inherent physical characteristics that influence their interactions with NP catalysts, research has shown how controlling the concentrations and types of heteroatoms within their structures can also have dramatic effects on the catalytic activities of their substrate NPs, as shown

in Chapters 2 and 3. Heteroatom modification has advanced beyond oxygen (C/O ratio control) to where doping of nitrogen atoms and control of specific functional groups (including further modification of said functional groups) are becoming more common. Boron-containing materials are being investigated alongside the emerging interest in doping carbon-based materials with sulfur and phosphorus. Multi-element doping also shows much promise and showcases the wealth of possibilities remaining to be discovered in this field.[202]

Metal oxide materials used as catalyst supports are also being studied at both the physical and chemical levels. Doping of these materials with other metals is quite pervasive in materials science, where the identity and concentrations of these dopants can result in massive changes to their inherent properties. Taking ceria for example, gadolinium doping results in increased ionic conductivity and lower operating temperatures when functioning as a fuel cell electrode.[257-259] While research on the effects of doping these materials is primarily focused towards applications such as optics,[260] or as catalysts themselves,[261] many of the learned principles can also be applied to their role as NP catalyst supports.

The primary research thrust concerns the NP catalysts themselves. Many of the advances made in the past several years owe their discovery to the fruitful partnership between theory and experiment. With this increased understanding of systemic models and improvements in synthetic capabilities, increasingly complex NP catalyst designs are appearing at a rapid rate. For example, intermetallic core-shell (IMCS) NPs, a type of core-shell NP where a metal shell coats an intermetallic core, are receiving increased focus from the catalytic community. No doubt inspired by

surface segregated alloy systems, these IMCS NPs, including Pt_3Co@Pt,[223] Pt_3Fe_2@Pt,[262] and Pt_3Pb@PtPb,[263] generally have enhanced catalytic performance vs. their counterparts due to the unique electronic structures and high stabilities afforded by their robust intermetallic cores.

Multimetallic NP systems are also receiving much attention, with unique physical and chemical properties arising from their complex structures. Multi-shell Pd@Ni@Pt nanocubes reported by Sneed et al employ Pd nanocubes to selectively create a Ni shell primarily consisting of (100) facets before further deposition of Pt.[252] Here, the (100) Ni surface imparts strain on Pt shell, giving rise to an altered electronic structure resulting in increased catalytic activity. Multi-shell NPs can also have bimetallic cores, as seen in the Ir_xRe_y@Pd@Pt NPs reported by the Adzic group.[264] In this case, the catalytic activities of the NPs depend not only on the composition ratio of the alloy core, but also on the presence and thickness of the Pd interlayer. Given the variety of metals and architectures, the possible combinations of future NPs are quite vast.

Ideally, research will yield the eventual creation of precious metal-free NP catalysts for processes where they are traditionally inactive. These NPs are likely to be complex materials and would represent the culmination of the "catalyst by design" process. As seen in Chapter 5 and elsewhere, earth abundant metals can be "activated" by modifying their electronic structures, much like their precious metal counterparts. In practice, these earth abundant NP catalysts would "mimic" their precious metal containing analogues with respect to electronic structure, which could be realized by combining certain metals and/or their oxides in a particular structural

arrangement. These undiscovered combinations could also drive reaction processes through yet unexplored catalytic mechanisms. Theoretical studies will drive the design and synthesis of new NP catalysts, produced through the combination of new support materials, transition metals and their oxides, and controlled reaction processes, necessary to create a new, more sustainable energy infrastructure.

Bibliography

(1) *FuelCellToday*. http://fuelcelltoday.com/technologies/pemfc/ (accessed December 22, 2014)
(2) Steele, B. C.; Heinzel, A. *Nature* **2001**, *414*, 345.
(3) Sarkar, A.; Murugan, A. V.; Manthiram, A. *J. Phys. Chem. C* **2008**, *112*, 12037.
(4) Shao, M.; Liu, P.; Zhang, J.; Adzic, R. *J. Phys. Chem. B* **2007**, *111*, 6772.
(5) Santiago, E. I.; Batista, M. S.; Assaf, E. M.; Ticianelli, E. A. *J. Electrochem. Soc.* **2004**, *151*, A944.
(6) Besenbacher, F.; Chorkendorff, I.; Clausen, B.; Hammer, B.; Molenbroek, A.; Norskov, J.; Stensgaard, I. *Science* **1998**, *279*, 1913.
(7) Liu, Z.; Ada, E. T.; Shamsuzzoha, M.; Thompson, G. B.; Nikles, D. E. *Chem. Mater.* **2006**, *18*, 4946.
(8) García, G.; Silva-Chong, J. A.; Guillén-Villafuerte, O.; Rodríguez, J. L.; González, E. R.; Pastor, E. *Catal. Today* **2006**, *116*, 415.
(9) Sinfelt, J. H. *P. Am. Philos. Soc.* **1999**, *143*, 388.
(10) Sinfelt, J. H. *Surf. Sci.* **2002**, *500*, 923.
(11) Sinfelt, J. H. *Acc. Chem. Res.* **1977**, *10*, 15.
(12) Christmann, K.; Schober, O.; Ertl, G. *J. Chem. Phys.* **1974**.
(13) Ertl, G.; Neumann, M.; Streit, K. M. *Surf. Sci.* **1977**, *64*, 393.
(14) Christmann, K.; Ertl, G.; Pignet, T. *Surf. Sci.* **1976**, *54*, 365.
(15) Conrad, H.; Ertl, G.; Küppers, J. *Surf. Sci.* **1978**, *76*, 323.
(16) Christmann, K.; Schober, O.; Ertl, G. *J. Chem. Phys.* **1974**, *60*, 4719.
(17) Morgan, A. E.; Somorjai, G. A. *Surf. Sci.* **1968**, *12*, 405.
(18) Lang, B.; Joyner, R. W.; Somorjai, G. A. *Surf. Sci.* **1972**, *30*, 454.
(19) Castner, D. G.; Sexton, B. A.; Somorjai, G. A. *Surf. Sci.* **1978**, *71*, 519.
(20) Morgan, A. E. *J. Chem. Phys.* **1969**, *51*, 3309.
(21) Rodriguez, J. A.; Campbell, R. A.; Goodman, D. W. *J. Phys. Chem.* **1990**, *94*, 6936.
(22) Campbell, R. A.; Rodriguez, J.; Goodman, D. W. *Surf. Sci. Lett.* **1991**, *256*, A539.
(23) Rodriguez, J. A.; Campbell, R. A.; Goodman, D. W. *J. Vac. Sci. Technol. A* **1991**, *9*, 1698.
(24) Rodriguez, J. A.; Goodman, D. W. *J. Phys. Chem.* **1991**, *95*, 4196.
(25) Gasteiger, H.; Markovic, N.; Ross, P.; Cairns, E. J. *J. Phys. Chem.* **1994**, *98*, 617.
(26) Gasteiger, H. A.; Marković, N. M.; Ross, P. N., Jr. *J. Phys. Chem.* **1995**, *99*, 8945.
(27) Gasteiger, H. A.; Marković, N. M.; Ross, P. N. *Catal. Lett.* **1996**, *36*, 1.
(28) Wang, K.; Gasteiger, H.; Markovic, N.; Ross, P. *Electrochim. Acta* **1996**, *41*, 2587.
(29) McBreen, J.; Mukerjee, S. *J. Electrochem. Soc.* **1995**, *142*, 3399.
(30) Mukerjee, S.; McBreen, J. *J. Electrochem. Soc.* **1999**, *146*, 600.

(31) Lee, S.; Mukerjee, S.; Ticianelli, E.; McBreen, J. *Electrochim. Acta* **1999**, *44*, 3283.
(32) Mukerjee, S.; Lee, S.; Ticianelli, E.; McBreen, J.; Grgur, B.; Markovic, N.; Ross, P.; Giallombardo, J.; De Castro, E. *Electrochem. Solid-State Lett.* **1999**, *2*, 12.
(33) Mukerjee, S.; Urian, R. C. *Electrochim. Acta* **2002**, *47*, 3219.
(34) Mukerjee, S.; Urian, R. C.; Lee, S. J.; Ticianelli, E. A.; McBreen, J. *J. Electrochem. Soc.* **2004**, *151*, A1094.
(35) Igarashi, H.; Fujino, T.; Zhu, Y.; Uchida, H.; Watanabe, M. *Phys. Chem. Chem. Phys.* **2001**, *3*, 306.
(36) Nørskov, J. K. *Prog. Surf. Sci.* **1991**, *38*, 103.
(37) Hammer, B.; Norskov, J. *Surf. Sci.* **1995**, *343*, 211.
(38) Hammer, B.; Morikawa, Y.; Norskov, J. *Phys. Rev. Lett.* **1996**, *76*, 2141.
(39) Hammer, B.; Norskov, J. *Nature* **1995**, *376*, 238.
(40) Ruban, A.; Hammer, B.; Stoltze, P.; Skriver, H. L.; Nørskov, J. K. *J. Mol. Catal. A* **1997**, *115*, 421.
(41) Wang, Y.; Toshima, N. *J. Phys. Chem. B* **1997**, *101*, 5301.
(42) Toshima, N.; Yonezawa, T. *New J. Chem.* **1998**, *22*, 1179.
(43) Bradley, J. S.; Hill, E. W.; Klein, C.; Chaudret, B.; Duteil, A. *Chem. Mater.* **1993**, *5*, 254.
(44) Bradley, J. S.; Hill, E. W.; Chaudret, B.; Duteil, A. *Langmuir* **1995**, *11*, 693.
(45) Park, J.-I.; Cheon, J. *J. Am. Chem. Soc.* **2001**, *123*, 5743.
(46) Park, J.-I.; Kim, M. G.; Jun, Y.-W.; Lee, J. S.; Lee, W.-R.; Cheon, J. *J. Am. Chem. Soc.* **2004**, *126*, 9072.
(47) Lee, W.; Kim, M.; Choi, J.; Park, J.; Ko, S.; Oh, S.; Cheon, J. *J. Am. Chem. Soc.* **2005**, *127*, 16090.
(48) Sra, A.; Schaak, R. *J. Am. Chem. Soc.* **2004**, *126*, 6667.
(49) Cable, R. E.; Schaak, R. E. *Chem. Mater.* **2007**, *19*, 4098.
(50) Schaak, R.; Sra, A.; Leonard, B.; Cable, R.; Bauer, J.; Han, Y.; Means, J.; Teizer, W.; Vasquez, Y.; Funck, E. *J. Am. Chem. Soc.* **2005**, *127*, 3506.
(51) Roychowdhury, C.; Matsumoto, F.; Zeldovich, V.; Warren, S.; Mutolo, P.; Ballesteros, M.; Wiesner, U.; Abruna, H.; DiSalvo, F. *Chem. Mater.* **2006**, *18*, 3365.
(52) Alden, L. R.; Roychowdhury, C.; Matsumoto, F.; Han, D. K.; Zeldovich, V. B.; Abruna, H. D.; DiSalvo, F. J. *Langmuir* **2006**, *22*, 10465.
(53) Roychowdhury, C.; Matsumoto, F.; Mutolo, P.; Abruna, H.; DiSalvo, F. *Chem. Mater.* **2005**, *17*, 5871.
(54) Leonard, B. M.; Zhou, Q.; Wu, D.; DiSalvo, F. J. *Chem. Mater.* **2011**, *23*, 1136.
(55) Chen, H.; Wang, D.; Yu, Y.; Newton, K. A.; Muller, D. A.; Abruña, H.; DiSalvo, F. J. *J. Am. Chem. Soc.* **2012**, *134*, 18453.
(56) Oezaslan, M.; Strasser, P. *J. Power Sources* **2011**.
(57) Koh, S.; Yu, C.; Mani, P.; Srivastava, R.; Strasser, P. *J. Power Sources* **2007**, *172*, 50.
(58) Mani, P.; Srivastava, R.; Strasser, P. *J. Power Sources* **2011**, *196*, 666.

(59) Zhou, S.; McIlwrath, K.; Jackson, G.; Eichhorn, B. *J. Am. Chem. Soc.* **2006**, *128*, 1780.
(60) Zhou, S.; Varughese, B.; Eichhorn, B.; Jackson, G.; McIlwrath, K. *Angew. Chem. Int. Ed.* **2005**, *44*, 4539.
(61) Alayoglu, S.; Eichhorn, B. *J. Am. Chem. Soc.* **2008**, *130*, 17479.
(62) Zhou, S.; Jackson, G. S.; Eichhorn, B. *Adv. Funct. Mater.* **2007**, *17*, 3099.
(63) Liu, Z.; Hu, J. E.; Wang, Q.; Gaskell, K.; Frenkel, A. I.; Jackson, G. S.; Eichhorn, B. *J. Am. Chem. Soc.* **2009**, *131*, 6924.
(64) Alayoglu, S.; Nilekar, A. U.; Mavrikakis, M.; Eichhorn, B. *Nat. Mater.* **2008**, *7*, 333.
(65) Mazumder, V.; Chi, M.; More, K. L.; Sun, S. *J. Am. Chem. Soc.* **2010**, *132*, 7848.
(66) Liu, Y.; Li, D.; Stamenkovic, V. R.; Soled, S.; Henao, J. D.; Sun, S. *ACS Catal.* **2011**, *1*, 1719.
(67) Guo, S.; Sun, S. *J. Am. Chem. Soc.* **2012**, *134*, 2492.
(68) Mun, B. S.; Watanabe, M.; Rossi, M.; Stamenkovic, V.; Markovic, N. M.; Ross, P. N. *J. Chem. Phys.* **2005**, *123*, 204717.
(69) Stamenkovic, V.; Mun, B. S.; Mayrhofer, K. J. J.; Ross, P. N.; Markovic, N. M.; Rossmeisl, J.; Greeley, J.; Norskov, J. K. *Angew. Chem. Int. Ed.* **2006**, *45*, 2897.
(70) Stamenkovic, V. R.; Mun, B. S.; Mayrhofer, K. J. J.; Ross, P. N.; Markovic, N. M. *J. Am. Chem. Soc.* **2006**, *128*, 8813.
(71) Wang, C.; Chi, M.; Wang, G.; van der Vliet, D.; Li, D.; More, K.; Wang, H.-H.; Schlueter, J. A.; Markovic, N. M.; Stamenkovic, V. R. *Adv. Funct. Mater.* **2010**, *21*, 147.
(72) Alayoglu, S.; Beaumont, S. K.; Zheng, F.; Pushkarev, V. V.; Zheng, H.; Iablokov, V.; Liu, Z.; Guo, J.; Kruse, N.; Somorjai, G. A. *Top. Catal.* **2011**, *54*, 778.
(73) Tao, F.; Grass, M. E.; Zhang, Y.; Butcher, D. R.; Aksoy, F.; Aloni, S.; Altoe, V.; Alayoglu, S.; Renzas, J. R.; Tsung, C.-K.; Zhu, Z.; Liu, Z.; Salmeron, M.; Somorjai, G. A. *J. Am. Chem. Soc.* **2010**, *132*, 8697.
(74) Tao, F.; Grass, M. E.; Zhang, Y.; Butcher, D. R.; Renzas, J. R.; Liu, Z.; Chung, J. Y.; Mun, B. S.; Salmeron, M.; Somorjai, G. A. *Science* **2008**, *322*, 932.
(75) Nilekar, A.; Alayoglu, S.; Eichhorn, B.; Mavrikakis, M. *J. Am. Chem. Soc.* **2010**.
(76) Aiken, J.; Finke, R. *J. Mol. Catal. A* **1999**, *145*, 1.
(77) Watzky, M.; Finke, R. *J. Am. Chem. Soc.* **1997**, *119*, 10382.
(78) Roucoux, A.; Schulz, J.; Patin, H. *Chem. Rev.* **2002**, *102*, 3757.
(79) Jiang, Z.-J.; Liu, C.-Y. *J. Phys. Chem. B* **2003**, *107*, 12411.
(80) Bai, S.; Shen, X.; Zhu, G.; Li, M.; Xi, H.; Chen, K. *ACS Appl. Mater. Interfaces* **2012**, *4*, 2378.
(81) Chen, G.; Desinan, S.; Rosei, R.; Rosei, F.; Ma, D. *Chem. Eur. J.* **2012**, *18*, 7925.
(82) Liu, Z.; Jackson, G. S.; Eichhorn, B. W. *Angew. Chem. Int. Ed.* **2010**, *49*, 3173.

(83) Alayoglu, S.; Zavalij, P.; Eichhorn, B.; Wang, Q.; Frenkel, A. I.; Chupas, P. *ACS Nano* **2009**, *3*, 3127.
(84) Jun, C.-H.; Park, Y. J.; Yeon, Y.-R.; Choi, J.-R.; Lee, W.-R.; Ko, S.-J.; Cheon, J. *Chem. Commun.* **2006**, 1619.
(85) Tsai, C. W.; Chen, H. M.; Liu, R. S.; Lee, J. F.; Chang, S. M.; Weng, B. J. *Int. J. Hydrogen Energ.* **2012**, *37*, 3338.
(86) Guo, H.; Chen, Y.; Chen, X.; Wen, R.; Yue, G.-H.; Peng, D.-L. *Nanotechnology* **2011**, *22*, 195604.
(87) Tran, T.-H.; Nguyen, T.-D. *Colloids Surf., B* **2011**, *88*, 1.
(88) Read, C. G.; Biacchi, A. J.; Schaak, R. E. *Chem. Mater.* **2013**, *25*, 4304.
(89) Joyner, R. W.; Pendry, J. B.; Saldin, D. K.; Tennison, S. R. *Surf. Sci.* **1984**, *138*, 84.
(90) Ralph, T. R.; Hards, G. A.; Keating, J. E.; Campbell, S. A.; Wilkinson, D. P.; Davis, M.; St Pierre, J.; Johnson, M. C. *J. Electrochem. Soc.* **1997**, *144*, 3845.
(91) Compton, O. C.; Nguyen, S. T. *Small* **2010**, *6*, 711.
(92) Singh, V.; Joung, D.; Zhai, L.; Das, S.; Khondaker, S. I.; Seal, S. *Prog. Mater. Sci.* **2011**, *56*, 1178.
(93) Schniepp, H. C.; Li, J.-L.; McAllister, M. J.; Sai, H.; Herrera-Alonso, M.; Adamson, D. H.; Prud'homme, R. K.; Car, R.; Saville, D. A.; Aksay, I. A. *J. Phys. Chem. B* **2006**, *110*, 8535.
(94) Kou, R.; Shao, Y.; Wang, D.; Engelhard, M. H.; Kwak, J. H.; Wang, J.; Viswanathan, V. V.; Wang, C.; Lin, Y.; Wang, Y.; Aksay, I. A.; Liu, J. *Electrochem. Commun.* **2009**, *11*, 954.
(95) Zhang, S.; Shao, Y.; Liao, H.-G.; Liu, J.; Aksay, I. A.; Yin, G.; Lin, Y. *Chem. Mater.* **2011**, *23*, 1079.
(96) Trueba, M.; Trasatti, S. P. *Eur. J. Inorg. Chem.* **2005**, *2005*, 3393.
(97) Pecharsky, V. K.; Zavalij, P. Y. *Fundamentals of Powder Diffraction and Structural Characterization of Materials*; Springer Science & Business Media, 2005.
(98) Lu, Y.; Chen, W. *Chem. Soc. Rev.* **2012**, *41*, 3594.
(99) Su, M.; Gu, A.; Liang, G.; Yuan, L. *Appl. Surf. Sci.* **2011**, *257*, 3158.
(100) Antoine, O.; Bultel, Y.; Durand, R. *J. Electroanal. Chem.* **2001**, *499*, 85.
(101) Chen, S.; Kucernak, A. *J. Phys. Chem. B* **2004**, *108*, 13984.
(102) Li, M.; Schnablegger, H.; Mann, S. *Nature* **1999**, *402*, 393.
(103) Rao, N.; Girshick, S.; Heberlein, J.; McMurry, P.; Jones, S.; Hansen, D.; Micheel, B. *Plasma Chem. Plasma Process.* **1995**, *15*, 581.
(104) Hou, Y.; Kondoh, H.; Ohta, T.; Gao, S. *Appl. Surf. Sci.* **2005**, *241*, 218.
(105) Narayanan, R.; El-Sayed, M. A. *J. Phys. Chem. B* **2005**, *109*, 12663.
(106) Lee, J.-M.; Kim, D.-W.; Jun, Y.-D.; Oh, S.-G. *Mater. Res. Bull.* **2006**, *41*, 1407.
(107) Wu, Z. G.; Munoz, M.; Montero, O. *Adv. Powder Technol.* **2010**, *21*, 165.
(108) Fajaroh, F.; Setyawan, H.; Widiyastuti, W.; Winardi, S. *Adv. Powder Technol.* **2011**, *23*, 328.
(109) Bolotin, K. I.; Sikes, K. J.; Jiang, Z.; Klima, M.; Fudenberg, G.; Hone, J.; Kim, P.; Stormer, H. L. *Solid State Commun.* **2008**, *146*, 351.

(110) Peigney, A.; Laurent, C.; Flahaut, E.; Bacsa, R.; Rousset, A. *Carbon* **2001**, *39*, 507.
(111) Lee, C.; Wei, X.; Kysar, J. W.; Hone, J. *Science* **2008**, *321*, 385.
(112) Hummers, W. S., Jr; Offeman, R. E. *J. Am. Chem. Soc.* **1958**, *80*, 1339.
(113) Fan, X.; Peng, W.; Li, Y.; Li, X.; Wang, S.; Zhang, G.; Zhang, F. *Adv. Mater.* **2008**, *20*, 4490.
(114) Kovtyukhova, N. I.; Ollivier, P. J.; Martin, B. R.; Mallouk, T. E.; Chizhik, S. A.; Buzaneva, E. V.; Gorchinskiy, A. D. *Chem. Mater.* **1999**, *11*, 771.
(115) Gómez-Navarro, C.; Weitz, R. T.; Bittner, A. M.; Scolari, M.; Mews, A.; Burghard, M.; Kern, K. *Nano Lett.* **2007**, *7*, 3499.
(116) Roy-Mayhew, J. D.; Bozym, D. J.; Punckt, C.; Aksay, I. A. *ACS Nano* **2010**, *4*, 6203.
(117) McAllister, M. J.; Li, J.-L.; Adamson, D. H.; Schniepp, H. C.; Abdala, A. A.; Liu, J.; Herrera-Alonso, M.; Milius, D. L.; Car, R.; Prud'homme, R. K.; Aksay, I. A. *Chem. Mater.* **2007**, *19*, 4396.
(118) Kudin, K. N.; Ozbas, B.; Schniepp, H. C.; Prud'homme, R. K.; Aksay, I. A.; Car, R. *Nano Lett.* **2008**, *8*, 36.
(119) Schniepp, H. C.; Kudin, K. N.; Li, J.-L.; Prud'homme, R. K.; Car, R.; Saville, D. A.; Aksay, I. A. *ACS Nano* **2008**, *2*, 2577.
(120) Ramanathan, T.; Abdala, A. A.; Stankovich, S.; Dikin, D. A.; Herrera-Alonso, M.; Piner, R. D.; Adamson, D. H.; Schniepp, H. C.; Chen, X.; Ruoff, R. S.; Nguyen, S. T.; Aksay, I. A.; Prud'Homme, R. K.; Brinson, L. C. *Nat. Nanotechnol.* **2008**, *3*, 327.
(121) Pope, M. A.; Punckt, C.; Aksay, I. A. *J. Phys. Chem. C* **2011**, *115*, 20326.
(122) Acik, M.; Mattevi, C.; Gong, C.; Lee, G.; Cho, K.; Chhowalla, M.; Chabal, Y. J. *ACS Nano* **2010**, *4*, 5861.
(123) Huber, D. L. *Small* **2005**, *1*, 482.
(124) Chen, Y.; Peng, D.-L.; Lin, D.; Luo, X. *Nanotechnology* **2007**, *18*, 505703.
(125) Mayer, A. B. R.; Mark, J. *Colloid Polym. Sci.* **1997**, *275*, 333.
(126) Silvert, P.-Y.; Herrera-Urbina, R.; Duvauchelle, N.; Vijayakrishnan, V.; Elhsissen, K. T. *J. Mater. Chem.* **1996**, *6*, 573.
(127) Wang, G.; Liu, T.; Luo, Y.; Zhao, Y.; Ren, Z.; Bai, J.; Wang, H. *J. Alloys Compd.* **2011**, *509*, L216.
(128) Wang, H.; Liang, Y.; Gong, M.; Li, Y.; Chang, W.; Mefford, T.; Zhou, J.; Wang, J.; Regier, T.; Wei, F.; Dai, H. *Nat. Commun.* **2012**, *3*, 917.
(129) Kottegoda, I. R. M.; Idris, N. H.; Lu, L.; Wang, J.-Z.; Liu, H.-K. *Electrochim. Acta* **2011**, *56*, 5815.
(130) Qian, W.; Chen, Z.; Cottingham, S.; Merrill, W. A.; Swartz, N. A.; Goforth, A. M.; Clare, T. L.; Jiao, J. *Green Chem.* **2012**, *14*, 371.
(131) Hwang, S.-G.; Kim, G.-O.; Yun, S.-R.; Ryu, K.-S. *Electrochim. Acta* **2012**, *78*, 406.
(132) Zhang, L.-R.; Zhao, J.; Li, M.; Ni, H.-T.; Zhang, J.-L.; Feng, X.-M.; Ma, Y.-W.; Fan, Q.-L.; Wang, X.-Z.; Hu, Z.; Huang, W. *New J. Chem.* **2012**, *36*, 1108.
(133) Hudson, R.; Rivière, A.; Cirtiu, C. M.; Luska, K. L.; Moores, A. *Chem. Commun.* **2012**, *48*, 3360.

(134) Fang, M.; Chen, Z.; Wang, S.; Lu, H. *Nanotechnology* **2012**, *23*, 085704.
(135) Guo, J.; Wang, R.; Tjiu, W. W.; Pan, J.; Liu, T. *J. Hazard. Mater.* **2012**, *225-226*, 63.
(136) Lin, Y.; Baggett, D. W.; Kim, J.-W.; Siochi, E. J.; Connell, J. W. *ACS Appl. Mater. Interfaces* **2011**, *3*, 1652.
(137) Stein, M.; Wieland, J.; Steurer, P.; Tölle, F.; Mülhaupt, R.; Breit, B. *Adv. Synth. Catal.* **2011**, *353*, 523.
(138) Bajpai, R.; Roy, S.; kulshrestha, N.; Rafiee, J.; Koratkar, N.; Misra, D. S. *Nanoscale* **2012**, *4*, 926.
(139) Marquardt, D.; Vollmer, C.; Thomann, R.; Steurer, P.; Mülhaupt, R.; Redel, E.; Janiak, C. *Carbon* **2011**, *49*, 1326.
(140) Gotoh, K.; Kawabata, K.; Fujii, E.; Morishige, K.; Kinumoto, T.; Miyazaki, Y.; Ishida, H. *Carbon* **2009**, *47*, 2120.
(141) Yan, X.; Liu, H.; Liew, K. *J. Mater. Chem.* **2001**, *11*, 3387.
(142) Jansat, S.; Picurelli, D.; Pelzer, K.; Philippot, K.; Gómez, M.; Muller, G.; Lecante, P.; Chaudret, B. *New J. Chem.* **2006**, *30*, 115.
(143) Xu, C.; Wang, X.; Zhu, J. *J. Phys. Chem. C* **2008**, *112*, 19841.
(144) Seger, B.; Kamat, P. V. *J. Phys. Chem. C* **2009**, *113*, 7990.
(145) Guo, S.; Wen, D.; Zhai, Y.; Dong, S.; Wang, E. *ACS Nano* **2010**, *4*, 3959.
(146) Li, Y.; Gao, W.; Ci, L.; Wang, C.; Ajayan, P. M. *Carbon* **2010**, *48*, 1124.
(147) Sharma, S.; Ganguly, A.; Papakonstantinou, P.; Miao, X.; Li, M.; Hutchison, J. L.; Delichatsios, M.; Ukleja, S. *J. Phys. Chem. C* **2010**, *114*, 19459.
(148) Ha, H.-W.; Kim, I. Y.; Hwang, S.-J.; Ruoff, R. S. *Electrochem. Solid-State Lett.* **2011**, *14*, B70.
(149) Kundu, P.; Nethravathi, C.; Deshpande, P. A.; Rajamathi, M.; Madras, G.; Ravishankar, N. *Chem. Mater.* **2011**, *23*, 2772.
(150) Nethravathi, C.; Anumol, E. A.; Rajamathi, M.; Ravishankar, N. *Nanoscale* **2011**, *3*, 569.
(151) Choi, S. M.; Seo, M. H.; Kim, H. J.; Kim, W. B. *Carbon* **2011**, *49*, 904.
(152) Wang, Y.; Liu, J.; Liu, L.; Sun, D. D. *Nanoscale Res. Lett.* **2011**, *6*, 241.
(153) Moussa, S.; Abdelsayed, V.; El-Shall, M. S. *Chem. Phys. Lett.* **2011**, *510*, 179.
(154) Greeley, J.; Norskov, J.; Mavrikakis, M. *Annu. Rev. Phys. Chem.* **2002**, *53*, 319.
(155) Yoo, E.; Okada, T.; Akita, T.; Kohyama, M.; Honma, I.; Nakamura, J. *J. Power Sources* **2011**, *196*, 110.
(156) He, D.; Cheng, K.; Li, H.; Peng, T.; Xu, F.; Mu, S.; Pan, M. *Langmuir* **2012**, *28*, 3979.
(157) Kim, G.; Jhi, S.-H. *ACS Nano* **2011**, *5*, 805.
(158) Fampiou, I.; Ramasubramaniam, A. *J. Phys. Chem. C* **2012**, *116*, 6543.
(159) Gao, X.; Jang, J.; Nagase, S. *J. Phys. Chem. C* **2010**, *114*, 832.
(160) Bolotin, K. I.; Sikes, K. J.; Hone, J.; Stormer, H. L.; Kim, P. *Phys. Rev. Lett.* **2008**, *101*, 096802.
(161) Bagri, A.; Grantab, R.; Medhekar, N. V.; Shenoy, V. B. *J. Phys. Chem. C* **2010**, *114*, 12053.

(162) Gao, W.; Alemany, L. B.; Ci, L.; Ajayan, P. M. *Nat. Chem.* **2009**, *1*, 403.
(163) Park, S.; An, J.; Potts, J. R.; Velamakanni, A.; Murali, S.; Ruoff, R. S. *Carbon* **2011**, *49*, 3019.
(164) Long, D.; Li, W.; Ling, L.; Miyawaki, J.; Mochida, I.; Yoon, S.-H. *Langmuir* **2010**, *26*, 16096.
(165) Yang, D.; Velamakanni, A.; Bozoklu, G.; Park, S.; Stoller, M.; Piner, R. D.; Stankovich, S.; Jung, I.; Field, D. A.; Ventrice, C. A.; Ruoff, R. S. *Carbon* **2009**, *47*, 145.
(166) Luo, D.; Zhang, G.; Liu, J.; Sun, X. *J. Phys. Chem. C* **2011**, *115*, 11327.
(167) Park, S.; Hu, Y.; Hwang, J. O.; Lee, E.-S.; Casabianca, L. B.; Cai, W.; Potts, J. R.; Ha, H.-W.; Chen, S.; Oh, J.; Kim, S. O.; Kim, Y.-H.; Ishii, Y.; Ruoff, R. S. *Nat. Commun.* **2012**, *3*, 638.
(168) Punckt, C.; Pope, M. A.; Liu, J.; Lin, Y.; Aksay, I. A. *Electroanal.* **2010**, *22*, 2834.
(169) Shin, H.-J.; Kim, K. K.; Benayad, A.; Yoon, S.-M.; Park, H. K.; Jung, I.-S.; Jin, M. H.; Jeong, H.-K.; Kim, J. M.; Choi, J.-Y.; Lee, Y. H. *Adv. Funct. Mater.* **2009**, *19*, 1987.
(170) Moussa, S. O.; Panchakarla, L. S.; Ho, M. Q.; El-Shall, M. S. *ACS Catal.* **2014**, *4*, 535.
(171) Bong, S.; Kim, Y.-R.; Kim, I.; Woo, S.; Uhm, S.; Lee, J.; Kim, H. *Electrochem. Commun.* **2010**, *12*, 129.
(172) Gao, L.; Yue, W.; Tao, S.; Fan, L. *Langmuir* **2013**, *29*, 957.
(173) Han, F.; Wang, X.; Lian, J.; Wang, Y. *Carbon* **2012**, *50*, 5498.
(174) He, W.; Jiang, H.; Zhou, Y.; Yang, S.; Xue, X.; Zou, Z.; Zhang, X.; Akins, D. L.; Yang, H. *Carbon* **2012**, *50*, 265.
(175) Ji, Z.; Shen, X.; Zhu, G.; Chen, K.; Fu, G.; Tong, L. *J. Electroanal. Chem.* **2012**, *682*, 95.
(176) Rao, C. V.; Reddy, A. L. M.; Ishikawa, Y.; Ajayan, P. M. *Carbon* **2011**, *49*, 931.
(177) Zhou, X.; Huang, X.; Qi, X.; Wu, S.; Xue, C.; Boey, F. Y. C.; Yan, Q.; Chen, P.; Zhang, H. *J. Phys. Chem. C* **2009**, *113*, 10842.
(178) Okamoto, Y. *Chem. Phys. Lett.* **2006**, *420*, 382.
(179) Yoo, E.; Okata, T.; Akita, T.; Kohyama, M.; Nakamura, J.; Honma, I. *Nano Lett.* **2009**, *9*, 2255.
(180) Tauster, S. J. *Acc. Chem. Res.* **1987**, *20*, 389.
(181) *Catalysis and Electrocatalysis at Nanoparticle Surfaces*; Wieckowski, A.; Savinova, E. R., Eds.; 1st ed.; CRC Press, 2003.
(182) Ren, P.-G.; Yan, D.-X.; Ji, X.; Chen, T.; Li, Z.-M. *Nanotechnology* **2011**, *22*, 055705.
(183) Moon, I. K.; Lee, J.; Ruoff, R. S.; Lee, H. *Nat. Commun.* **2010**, *1*, 1.
(184) Katrib, A.; El-Rayyes, N. R.; Al-Kharafi, F. M. *J. Electron. Spectrosc. Relat. Phenom.* **1983**, *31*, 317.
(185) Rozada, R.; Paredes, J. I.; Villar-Rodil, S.; Martínez-Alonso, A.; Tascón, J. M. D. *Nano Res.* **2013**, *6*, 216.
(186) Villar-Rodil, S.; Paredes, J. I.; Martínez-Alonso, A.; Tascón, J. M. *J. Mater. Chem.* **2009**, *19*, 3591.

(187) Ferrari, A. C. *Solid State Commun.* **2007**, *143*, 47.
(188) Geng, D.; Chen, Y.; Chen, Y.; Li, Y.; Li, R.; Sun, X.; Ye, S.; Knights, S. *Energy Environ. Sci.* **2011**, *4*, 760.
(189) Liang, Y. T.; Vijayan, B. K.; Gray, K. A.; Hersam, M. C. *Nano Lett.* **2011**, *11*, 2865.
(190) Bagri, A.; Mattevi, C.; Acik, M.; Chabal, Y. J.; Chhowalla, M.; Shenoy, V. B. *Nat. Chem.* **2010**, *2*, 581.
(191) Arenz, M.; Stamenkovic, V.; Blizanac, B. B.; Mayrhofer, K. J.; Marković, N. M.; Ross, P. N. *J. Catal.* **2005**, *232*, 402.
(192) Boucher, A. C.; Alonso-Vante, N.; Dassenoy, F.; Vogel, W. *Langmuir* **2003**, *19*, 10885.
(193) Camara, G. A.; Ticianelli, E. A.; Mukerjee, S.; Lee, S. J.; McBreen, J. *J. Electrochem. Soc.* **2002**, *149*, A748.
(194) Liu, Z.; Reed, D.; Kwon, G.; Shamsuzzoha, M.; Nikles, D. E. *J. Phys. Chem. C* **2007**, *111*, 14223.
(195) Schmidt, T.; Gasteiger, H.; Stab, G.; Urban, P.; Kolb, D.; Behm, R. *J. Electrochem. Soc.* **1998**, *145*, 2354.
(196) Crabb, E. M.; Marshall, R.; Thompsett, D. *J. Electrochem. Soc.* **2000**, *147*, 4440.
(197) Lee, D.; Hwang, S.; Lee, I. *J. Power Sources* **2005**, *145*, 147.
(198) Hayden, B. E.; Rendall, M. E.; South, O. *J. Am. Chem. Soc.* **2003**, *125*, 7738.
(199) Guerin, S.; Hayden, B. E.; Lee, C. E.; Mormiche, C.; Owen, J. R.; Russell, A. E.; Theobald, B.; Thompsett, D. *J. Comb. Chem.* **2004**, *6*, 149.
(200) Luo, Z.; Lim, S.; Tian, Z.; Shang, J.; Lai, L.; MacDonald, B.; Fu, C.; Shen, Z.; Yu, T.; Lin, J. *J. Mater. Chem.* **2011**, *21*, 8038.
(201) Mahmood, N.; Zhang, C.; Liu, F.; Zhu, J.; Hou, Y. *ACS Nano* **2013**, *7*, 10307.
(202) Paraknowitsch, J. P.; Thomas, A. *Energy Environ. Sci.* **2013**, *6*, 2839.
(203) Pylypenko, S.; Borisevich, A.; More, K. L.; Corpuz, A. R.; Holme, T.; Dameron, A. A.; Olson, T. S.; Dinh, H. N.; Gennett, T.; O'Hayre, R. *Energy Environ. Sci.* **2013**, *6*, 2957.
(204) Reddy, A. L. M.; Srivastava, A.; Gowda, S. R.; Gullapalli, H.; Dubey, M.; Ajayan, P. M. *ACS Nano* **2010**, *4*, 6337.
(205) Zhou, W.-P.; An, W.; Su, D.; Palomino, R.; Liu, P.; White, M. G.; Adzic, R. R. *J. Phys. Chem. Lett.* **2012**, *3*, 3286.
(206) Jeon, M. K.; Zhang, Y.; McGinn, P. J. *Electrochim. Acta* **2010**, *55*, 5318.
(207) Jeon, M. K.; McGinn, P. J. *Electrochim. Acta* **2012**, *64*, 147.
(208) Antolini, E.; Salgado, J. R. C.; Gonzalez, E. R. *J. Power Sources* **2006**, *160*, 957.
(209) Di Noto, V.; Negro, E. *Fuel Cells* **2010**, *10*, 234.
(210) Jayasayee, K.; Van Veen, J. A. R.; Manivasagam, T. G.; Celebi, S.; Hensen, E. J. M.; de Bruijn, F. A. *Appl. Catal., B* **2012**, *111-112*, 515.
(211) Marković, N. M.; Schmidt, T. J.; Stamenkovic, V.; Ross, P. N. *Fuel Cells* **2001**, *1*, 105.
(212) Yu, P.; Pemberton, M.; Plasse, P. *J. Power Sources* **2005**, *144*, 11.

(213) Greeley, J.; Stephens, I. E. L.; Bondarenko, A. S.; Johansson, T. P.; Hansen, H. A.; Jaramillo, T. F.; Rossmeisl, J.; Chorkendorff, I.; Nørskov, J. K. *Nat. Chem.* **2009**, *1*, 552.
(214) Koh, S.; Leisch, J.; Toney, M. F.; Strasser, P. *J. Phys. Chem. C* **2007**, *111*, 3744.
(215) Lima, F. H. B.; de Castro, J. F. R.; Santos, L. G. R. A.; Ticianelli, E. A. *J. Power Sources* **2009**, *190*, 293.
(216) Koh, S.; Toney, M. F.; Strasser, P. *Electrochim. Acta* **2007**, *52*, 2765.
(217) Stamenkovic, V. R.; Mun, B. S.; Arenz, M.; Mayrhofer, K. J. J.; Lucas, C. A.; Wang, G.; Ross, P. N.; Markovic, N. M. *Nat. Mater.* **2007**, *6*, 241.
(218) He, Q.; Mukerjee, S. *Electrochim. Acta* **2010**, *55*, 1709.
(219) Salgado, J. R. C.; Antolini, E.; Gonzalez, E. R. *J. Phys. Chem. B* **2004**, *108*, 17767.
(220) Brushett, F. R.; Duong, H. T.; Wei, J.; Behrens, R. L.; Wieckowski, A.; Kenis, P. J. *J. Electrochem. Soc.* **2010**, *157*, B837.
(221) Qian, Y.; Wen, W.; Adcock, P. A.; Jiang, Z.; Hakim, N.; Saha, M. S.; Mukerjee, S. *J. Phys. Chem. C* **2008**, *112*, 1146.
(222) Watanabe, M.; Tsurumi, K.; Mizukami, T.; Nakamura, T.; Stonehart, P. *J. Electrochem. Soc.* **1994**, *141*, 2659.
(223) Wang, D.; Xin, H. L.; Hovden, R.; Wang, H.; Yu, Y.; Muller, D. A.; DiSalvo, F. J.; Abruna, H. D. *Nat. Mater.* **2012**, *12*, 81.
(224) Cheah, S. K.; Sicardy, O.; Marinova, M.; Guetaz, L.; Lemaire, O.; Gélin, P.; Franco, A. A. *J. Electrochem. Soc.* **2011**, *158*, B1358.
(225) Uchida, H.; Izumi, K.; Aoki, K.; Watanabe, M. *Phys. Chem. Chem. Phys.* **2009**, *11*, 1771.
(226) Ehteshami, S. M. M.; Jia, Q.; Halder, A.; Chan, S. H.; Mukerjee, S. *Electrochim. Acta* **2013**, *107*, 155.
(227) Liu, Z.; Jackson, G. S.; Eichhorn, B. W. *Energy Environ. Sci.* **2011**, *4*, 1900.
(228) Vidal-Iglesias, F. J.; Arán-Ais, R. M.; Solla-Gullón, J.; Herrero, E.; Feliu, J. M. *ACS Catal.* **2012**, *2*, 901.
(229) Chen, Q.-S.; Solla-Gullón, J.; Sun, S.-G.; Feliu, J. M. *Electrochim. Acta* **2010**, *55*, 7982.
(230) Mourdikoudis, S.; Shavel, A.; Rodríguez-González, B.; Serra, C.; Simeonidis, K.; Angelakeris, M.; Dendrinou-Samara, C.; Kalogirou, O. *Polyhedron* **2010**, *28*, 3284.
(231) Favry, E.; Wang, D.; Fantauzzi, D.; Anton, J.; Su, D. S.; Jacob, T.; Alonso-Vante, N. *Phys. Chem. Chem. Phys.* **2011**, *13*, 9201.
(232) Karoui, S.; Amara, H.; Legrand, B.; Ducastelle, F. *J. Phys.: Condens. Matter* **2013**, *25*, 056005.
(233) Shevchenko, E. V.; Talapin, D. V.; Schnablegger, H.; Kornowski, A.; Festin, Ö.; Svedlindh, P.; Haase, M.; Weller, H. *J. Am. Chem. Soc.* **2003**, *125*, 9090.
(234) Xu, Y.; Yuan, Y.; Ma, A.; Wu, X.; Liu, Y.; Zhang, B. *ChemPhysChem* **2012**, *13*, 2601.

(235) Xu, C.; Hou, J.; Pang, X.; Li, X.; Zhu, M.; Tang, B. *Int. J. Hydrogen Energ.* **2012**, *37*, 10489.
(236) Choi, S.-I.; Choi, R.; Han, S. W.; Park, J. T. *Chem. Eur. J.* **2011**, *17*, 12280.
(237) Yano, H.; Kataoka, M.; Yamashita, H.; Uchida, H.; Watanabe, M. *Langmuir* **2007**, *23*, 6438.
(238) Gasteiger, H. A.; Kocha, S. S.; Sompalli, B.; Wagner, F. T. *Appl. Catal., B* **2005**, *56*, 9.
(239) Carrette, L.; Friedrich, K. A.; Stimming, U. *ChemPhysChem* **2000**, *1*, 162.
(240) Wootsch, A.; Descorme, C.; Duprez, D. *J. Catal.* **2004**, *225*, 259.
(241) Liu, Y.; Fu, Q.; Stephanopoulos, M. F. *Catal. Today* **2004**, *93-95*, 241.
(242) Mishra, A.; Prasad, R. *Bull. Chem. React. Eng. Catal.* **2011**, *6*, 1.
(243) Mavrikakis, M.; Hammer, B.; Nørskov, J. K. *Phys. Rev. Lett.* **1998**, *81*, 2819.
(244) Hammer, B.; Nørskov, J. K. *Adv. Catal.* **2000**, *45*, 71.
(245) Laguna, O. H.; Ngassa, E. M.; Oraá, S.; Álvarez, A.; Domínguez, M. I.; Romero-Sarria, F.; Arzamendi, G.; Gandía, L. M.; Centeno, M. A.; Odriozola, J. A. *Catal. Today* **2012**, *180*, 105.
(246) Alayoglu, S. Core/Shell and Alloy Nanoparticles of Transition Metals for Heterogeneous Catalysis: Bridging the Gap between Experiment and Theory, University of Maryland, 2008.
(247) Hinotsu, T. *J. Appl. Phys.* **2004**, *95*, 7477.
(248) Chen, D.-H.; Hsieh, C.-H. *J. Mater. Chem.* **2002**, *12*, 2412.
(249) Couto, G. G.; Klein, J. J.; Schreiner, W. H.; Mosca, D. H.; de Oliveira, A. J. A.; Zarbin, A. J. G. *J. Colloid Interface Sci.* **2007**, *311*, 461.
(250) Pingali, K. C.; Deng, S.; Rockstraw, D. A. *Powder Technol.* **2008**, *183*, 282.
(251) Liu, R.; Zhao, Q.; Li, Y.; Zhang, G.; Zhang, F.; Fan, X. *J. Nanomater.* **2013**, *2013*, 1.
(252) Sneed, B. T.; Young, A. P.; Jalalpoor, D.; Golden, M. C.; Mao, S.; Jiang, Y.; Wang, Y.; Tsung, C.-K. *ACS Nano* **2014**, *8*, 7239.
(253) Xiang, J.; Li, P.; Chong, H.; Feng, L.; Fu, F.; Wang, Z.; Zhang, S.; Zhu, M. *Nano Res.* **2014**, *7*, 1337.
(254) Zhou, S. Architecturally Controlled Bimetallic Nanoparticles for Heterogeneous Catalysis, University of Maryland, 2007.
(255) El-Gendy, A. A.; Khavrus, V. O.; Hampel, S.; Leonhardt, A.; Büchner, B.; Klingeler, R. *J. Phys. Chem. C* **2010**, *114*, 10745.
(256) Braos-García, P.; García-Sancho, C.; Infantes-Molina, A.; Rodríguez-Castellón, E.; Jiménez-López, A. *Appl. Catal., A* **2010**, *381*, 132.
(257) Chourashiya, M. G.; Bhardwaj, S. R.; Jadhav, L. D. *J. Solid State Electrochem.* **2010**, *14*, 1869.
(258) Bocchetta, P.; Santamaria, M.; Di Quarto, F. *J. Electrochem. Soc.* **2012**, *159*, E108.
(259) Dolgopolova, E. A.; Ivanova, O. S.; Ivanov, V. K.; Sharikov, F. Y.; Baranchikov, A. E.; Shcherbakov, A. B.; Trietyakov, Y. D. *Russ. J. Inorg. Chem.* **2012**, *57*, 1303.
(260) Sun, C.; Li, H.; Chen, L. *Energy Environ. Sci.* **2012**, *5*, 8475.

(261) Gibbons, W. T.; Venstrom, L. J.; De Smith, R. M.; Davidson, J. H.; Jackson, G. S. *Phys. Chem. Chem. Phys.* **2014**, *16*, 14271.
(262) Prabhudev, S.; Bugnet, M.; Bock, C.; Botton, G. A. *ACS Nano* **2013**, *7*, 6103.
(263) Gunji, T.; Tanabe, T.; Jeevagan, A. J.; Usui, S.; Tsuda, T.; Kaneko, S.; Saravanan, G.; Abe, H.; Matsumoto, F. *J. Power Sources* **2015**, *273*, 990.
(264) Karan, H. I.; Sasaki, K.; Kuttiyiel, K.; Farberow, C. A.; Mavrikakis, M.; Adzic, R. R. *ACS Catal.* **2012**, 817.